Towards Integrated Pixel Modelling

Maynooth University
National University of Ireland Maynooth

Presented by

Joseph Brennan, B.Sc.

Thesis submitted for the degree of

Doctor of Philosophy

Terahertz Space Optics Group,

Department of Experimental Physics,

National University of Ireland Maynooth,

Maynooth, Co. Kildare,

Ireland

February 2021

Research Supervisors

Dr. Marcin Gradziel

Dr. Neil Trappe

Head of Department

Dr. Créidhe O'Sullivan

Contents

Abstract

The primary focus of this thesis is the re-formulation and extension of traditional mode-matching methods, and the development of the software package SCATTER-TNG (S-TNG) to incorporate them. The foundations of this software are built on the legacy of mode matching routines developed by the Terahertz Group at Maynooth University. This new adaptation aims to enable continued contributions to the design, analysis, and efficient characterisation of the sensitive pixel (feed, cavity, and absorber) structures of future far-infrared instruments. Contemporary waveguide technologies increasingly rely on the exploitation of multi-moded behaviour and operation in higher frequency bands. In these scenarios a more comprehensive approach is required to correctly predict their behaviour as the assumption of ideal surfaces may no longer be entirely valid.

In S-TNG, the fundamental description of fields within waveguides and at discontinuities relies on auxiliary vector potentials rather than their measurable electric and magnetic field quantities. Moreover, the necessary mode matching integrals are derived in terms of contour rather than surface integrals. The reformulations offer an alternative, somewhat more flexible, mathematical representation of the mode matching problem. Furthermore, mode matching methods are extended to allow for non-PEC (Perfect Electrically Conductive) treatment of the boundary walls. These non-PEC boundary walls consider mechanisms for loss which are generally not included in the modal analysis of guide structures. In particular, losses may manifest themselves more significantly in multi-moded structures, as field distributions for increasing higher order modes are localised to a greater extent at the boundary walls.

The motivation for this body of work stemmed from ESA contracted work focused on "New Technology High Efficiency Horn Antennas for Cosmic Microwave Background Experiments and Far-Infrared Astronomy" – fulfilling the requirement to model multi-moded pixel devices for THz space instruments. This included the ability to easily model arbitrary shaped absorbers in an infinitely thin absorber layer model achieved via the contour integral implementation. The software tools developed have since been applied to the design and analysis of some proposed pixel and feed designs for the SPICA/SAFARI instrument. In particular, there is great interest in the non-PEC treatment of the boundary walls for the analysis of prototype designs.

Acknowledgements

Firstly, I would like to express my sincere gratitude to my research supervisor, Dr. Marcin Gradziel, for his patience, enthusiasm and support over the last four years. Without out your dedication and resolve the work presented in this thesis would not have been possible. I'm forever grateful for those long meetings and even longer debugging sessions. A special thanks to my co-supervisor, Dr. Neil Trappe, for all the constructive chats both research and career related, and for always getting me involve in interesting odd-projects.

I would also like to express my thanks to Prof. Anthony Murphy, Dr. Créidhe O'Sullivan and Dr. Frank Mulligan whose guidance and encouragement during both my postgraduate and undergraduate was very much appreciated. I am also grateful to the other academic staff who always made me feel welcome and were never short of conversation over tea and biscuits!

A massive thanks to the administrative and technical staff for all their help over the last few years. To Mr. Derek Gleeson for his help with all things financial and for the odd round of golf. To Mr. John Kelly, Mrs. Marie Galligan, Mr. Pat Seery, Mr. David Watson and not forgetting Dr. Ian McAuley for their assistance with my own research and teaching in the laboratories. Finally, a special thanks to Ms. Gráinne Roche for her kindness and hard work keeping this whole operation running!

To my fellow postgraduates: Aisling, Andrew, Daithí, Darren, Dave, Donnacha, Jack, James, Julianne, Matthew, Noah and former postgraduates: Adam, Eoin, Eimantė, Mark, Melissa, Michael, Rory and Sharon. You have all been such a massive part of my life for the last few years. Thank you for your friendship and for always offering a welcome distraction when work got the better of us.

I would also like to thank my family for their support, encouragement and patience over the course of my time in Maynooth. I know it must not have been easy at times! Finally, to Aoife thank you for your love and support even during challenging periods of our studies. I'm grateful to have shared this journey with you so far and look forward to having more time together.

Chapter 1 – Introduction

Terahertz (THz) radiation is a form of electromagnetic radiation which covers the frequency range of 0.1 to 10 THz. Effectively this portion of the spectrum bridges the gap between short-microwave (3.0 mm) and far-infrared (0.03 mm) radiation. Antennas which operate in this portion of the spectrum require specialised techniques to accurately model and characterise their response to external stimulus. In fact, to model complete terahertz instruments a number of different modelling techniques may be used in tandem: Physical Optics (PO) (Hecht 2001), Ray Tracing (Hecht 2001), Gaussian Beam Mode-Analysis (GBMA) (Goldsmith 1998), Finite Element Methods (FEM) (C. A. Balanis 2012) and Mode Matching (Olver et al. 2011) routines.

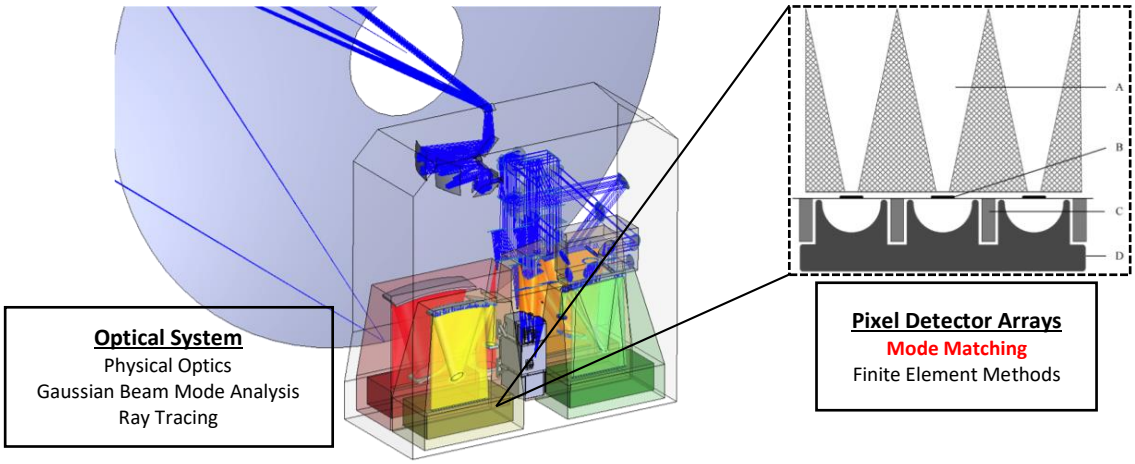

Figure 1-1: Shows the modelling techniques applied to the optics and focal plane of a terahertz instrument. The optical system is composed of the mirrors, lenses, polarisers and other intermediate optics (Roelfsema 2018). The pixel is broken down into the following key components A) multi-mode feed horn B) absorber layer C) Si wafer support beams and D) back-short cavity section (Korte et al. 2012).

The primary focus of this thesis is the development of mode matching routines for the accurate and efficient analysis of the sensitive pixels (feed, cavity, and absorber sections) which make up the detector plane of terahertz instruments as shown in Figure 1-1. Modal analysis of pixel structures is critical for the development of terahertz instruments, these methods offer much improved simulation times compared to FEM especially for electrically large structures. The Experimental Physics Department at Maynooth University has a legacy in the development and application of mode matching routines, most notably contributing to the millimetre and sub-millimetre instruments on board the Planck and Herschel space telescopes. This thesis aims to present the advances made in mode matching techniques over the last number of years which are captured in the newly developed software package SCATTER-TNG.

Much of this development fed into ESA (European Space Agency) contracted work, with the aim to facilitate the design and analysis of feed structures for use in future far-infrared missions. One such mission was SPICA (Space Infrared Telescope for Cosmology and Astrophysics) (Roelfsema 2018), an infrared space observatory collaboration between ESA and JAXA (Japanese Aerospace Exploration Agency). In October 2020 ESA and JAXA announced their decision to not proceed with SPICA as a candidate for the M5 Cosmic Visions Programme. More directly, the developed mode matching methods would have been applied to the SAFARI (SPICA Far-Infrared Instrument) instrument, with the aim of aiding in the design and analysis of its detector arrays being developed by Cambridge, Cardiff and SRON (Netherlands Institute for Space Research).

In this chapter, an effort is made to provide context to the mathematical and modelling focused content of the thesis. Here, the significant applications of terahertz imaging to the astronomical and wider fields are presented, along with a review of the state of the art in terahertz technologies. Finally, a proposed future terahertz space mission (SPICA) is discussed, to which the SCATTER-TNG software will be applied in later chapters.

1.1 Astronomical Observations at GHz – THz Frequencies

Astronomical observations at terahertz frequencies are vital to answering a number of key questions in cosmology. By observing the terahertz radiation arriving from astronomical sources such as the Interstellar Medium (ISM), the Cosmic Microwave Background (CMB), Young Stellar Objects (YSO) and Active Galactic Nuclei (AGN), information about the formative processes and evolution of solar systems, galaxies and even the Universe itself can be uncovered (Walker 2015). Terahertz photons are emitted via changes to a molecule's thermal or vibrational state, or by bending of molecular state (De Maagt 2007). Due to the nature of terahertz emissions observations at these frequencies provide a unique window into the very cold Universe (Withington et al. 2014):

- Objects with physical temperatures of $4 - 100$ K have a blackbody spectrum which peaks in the terahertz range.
- Diffuse molecular gases have rotational and vibrational transitions in the terahertz range which are excited by low temperature collisions.

- Observations can be made through particulate matter, such as grains of graphite, which are generally opaque to shorter wavelengths e.g. proto-planetary disc and star forming regions.

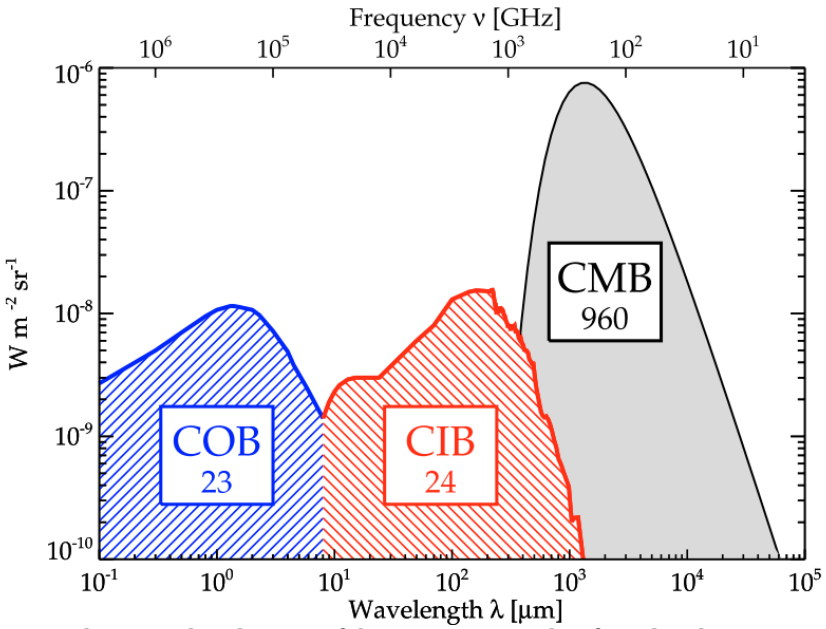

Figure 1-2: Spectral Energy distributions of the Cosmic Optical, Infrared and Microwave Backgrounds (Dole et al. 2006).

By observing terahertz emissions, information about the molecular concentrations and the physical condition (temperature, pressure and dynamics) of the imaged source can be determined (De Maagt 2007). As such, observations in the terahertz range provide a unique point of view and complementary data to observations in other spectral ranges. This is critical to further understanding many astronomical phenomenon and the Universe itself. It is thought that much of the matter in the Universe is cold, with studies indicating that approximately half of the total luminosity and 98% of photons emitted since the big bang fall into the sub-millimetre and far-infrared range (Siegel 2002). In Figure 1-2, the GHz – THz range covers most of the Cosmic Infrared Background (CIB) where many of these astronomical sources can be observed.

Two contributing factors have meant that observations in this GHz-THz regime have been limited up until the late 20th century (Walker 2015). Firstly, it is well understood that water is a very efficient absorber of electromagnetic energy across the spectrum and this is particularly true for GHz – THz photons, see Figure 1-3 (Yang, Shutler, and Grischkowsky 2011). Atmospheric absorption of terahertz photons is a limiting factor to where terahertz instruments may be located. As a result, observations are limited to either space based telescopes or a select number of ground based sites such as Atacama, Chile and Mauna Kea, Hawaii. These sites

offer a relatively unimpaired window for frequencies ranging from 100 GHz – 1.2 THz the requirement being that these be "high and dry". Transmission at these sites range from 95% at the lowest band to 30% at the highest band (Withington et al. 2014).

Secondly, the emission process associated with terahertz photons means that their energies are ~100 times less than typical optical photons emitted via relaxation processes between atomic states (De Maagt 2007). Thus, the sensitivity requirement for observing in the terahertz regime is much more demanding. A lack of commercial viability and serious investment meant that the necessary technology threshold was only met towards the end of the 20th century (Wiltse 1984). Enabled by advances in material sciences, the development of powerful coherent terahertz sources and sensitive terahertz detectors opened up the region to experimentation (Walker 2015). These advances have been driven by astronomy and Earth science demands. Here the focus has been on the development of high-resolution spectroscopy and remote sensing technologies. Heterodyne and Fourier transform techniques have allowed for the mapping of thermal emission lines for light-weight molecules (Siegel 2002).

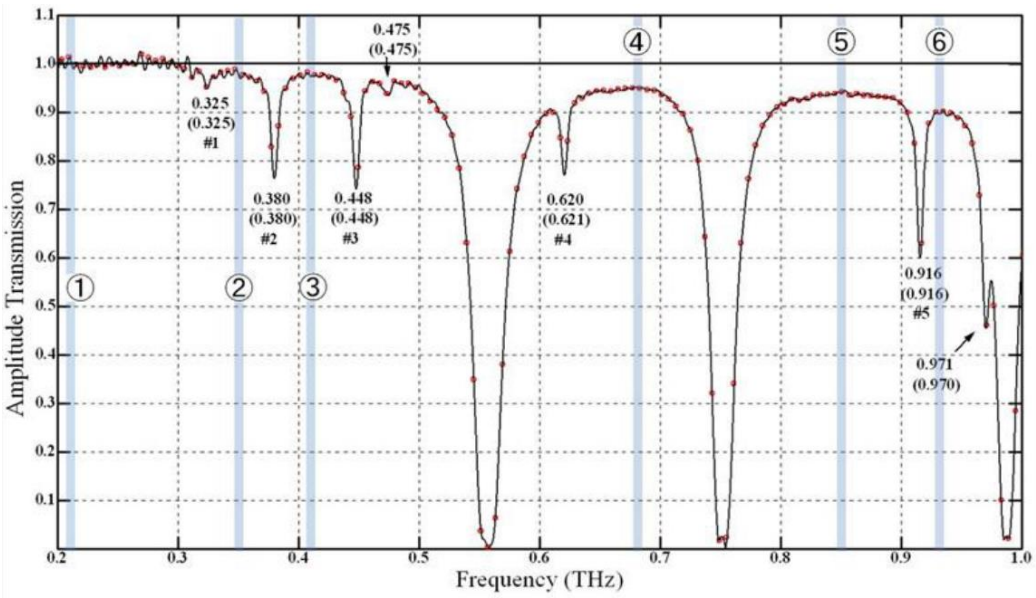

Figure 1-3: Atmospheric transmission levels of terahertz radiation. Here the circled numbers 1-6 indicate 'water windows'- regions which provide relative transparency to terahertz radiation (Yang, Shutler, and Grischkowsky 2011)

Since the 1980s there have been a number of highly successfully millimetre and sub-millimetre missions which have enabled remarkable science. By considering a select few of these instruments, both legacy and currently active, the science case for future instruments to further explore the terahertz spectrum is presented. In the following section, the ALMA (Atacama Large Millimetre Array) and Herschel telescopes are studied to provide an overview of the unique observations which can be made at this portion of the electromagnetic spectrum. Future

terahertz based mission must have science drivers which complement the capabilities of ground based measurements and expand on the legacy of past missions. Understanding the limitations of legacy instruments also highlights the necessary developments of terahertz technologies to obtain the required sensitivity and achieve space qualification.

1.1.1 Atacama Large Millimetre Array – ALMA

The Atacama Desert, Chile is home to the Atacama Large Millimetre Array (ALMA) and is one of the few locations on Earth where terahertz observations can be made relatively unimpaired. Atacama is an arid region with little precipitation year round; on average the regions sees ~ 15 mm of rainfall per year and in some locations as little as 3 mm. Combined with an elevation of 5000 m above sea level, the Atacama region provides an ideal high and dry site which minimises atmospheric attenuation at terahertz frequencies ('ALMA - ESO' 2013).

ALMA facilitates excellent science which can be achieved with ground based terahertz observations, with over 1000 per-reviewed papers published using ALMA data since becoming fully operational in 2013. The main array consists of 50 mobile-antennas of 12 m in diameter, allowing for different observation configurations and spatial resolutions. Furthermore, an additional 12 antennas of 7 m in diameter, combined with 4 of the main array antennas make-up the Atacama Compact Array (ACA) which facilitates auxiliary measurements to the main array ('ALMA - ESO Receiver Bands' 2016). ALMA spans a wide-range of frequencies (35 – 950 GHz) with a total of 10 distinct bands covering millimetre and sub-millimetre wavelengths, each with a focus on different astronomy goals. An overview of each band is presented in the following table.

Table 1-1: Overview of the ALMA bands including their operating range, manufacture, receiver technology and year of first light ('ALMA - ESO Receiver Bands' 2016).
HEMT - High-Electron-Mobility Transistor, SIS - Superconductor–Insulator–Superconductor

ALMA Band	Wavelength coverage (mm)	Noise Temperature (K) Specification	Frequency (GHz)	Produced by	Receiver Technology	First light
1	6–8.5	26	35 – 50	ASIAA	HEMT	2021
2	3.3–4.5	47	65 – 90	TBD	HEMT	TBD
3	2.6–3.6	60	84 – 116	HIA	SIS	2009
4	1.8–2.4	82	125 – 163	NAOJ	SIS	2013
5	1.4–1.8	105	163 – 211	OSO / NOVA	SIS	2016
6	1.1–1.4	136	211 – 275	NRAO	SIS	2009
7	0.8–1.1	219	275 – 373	IRAM	SIS	2009
8	0.6–0.8	292	385 – 500	NAOJ	SIS	2013
9	0.4–0.5	261	602 – 720	NOVA	SIS	2011
10	0.3–0.4	344	787 – 950	NAOJ	SIS	2012

The receiver technologies of ALMA's bands (bands 1-2: HEMT - High-Electron-Mobility Transistor, bands 3-10: SIS - Superconductor–Insulator–Superconductor) which are both types of coherent detectors and are discussed in section 1.2. These bands span ALMA's spectral range, each enabling a host of different observations to be made ('ALMA - ESO Receiver Bands' 2016):

- Band 1 ($35 - 50$ GHz): formal development of the Band 1 receivers was announced in 2016 with first light planned for 2020. Band 1 aims to detail the evolution of grains in protoplanetary disks and detect CO 3-2 line (carbon monoxide) emission from galaxies during the epoch of reionization (Di Francesco et al. 2013).
- Band 2 ($65 - 90$ GHz): represents the final band on ALMA to be completed and development of the Band 2 receivers was announced in 2020 with first light dependent on the performance of pre-production receivers currently being tested. Band 2 aims to study gas in external galaxies allowing for measurement of the cool molecular gas mass and study the properties and evolution of dense gas where star-forming density is rapidly declining (Fuller et al. 2016).
- Band 3 ($84 - 116$ GHz): is used to observe molecular clouds in galactic and extra-galactic regions, image molecules in the cold interstellar medium (ISM) and detect molecular gas in the disks of young stellar objects (YSO). It covers the longest currently active wavelength range and aids in phase calibrations of the other bands.
- Band 4 (125-163 GHz): is used to observe the ISM and aid in understanding the formation of stars and galaxies. In the $125 - 163$ GHz band molecules including carbon sulphide, formaldehyde, deuterium compounds, and carbon chain molecules can be detected. In cool, star-forming regions these substances can be found in abundance.
- Band 5 (163-211 GHz): provides detailed studies of the water content in a wide range of objects such as young and evolved stars, the ISM and regions surrounding black holes. Furthermore, the emission of ionised carbon from objects seen soon after the big-bang has been detected by Band 5. This may enable astronomers to probe the earliest stages of galaxy formation.
- Band 6 (211-275 GHz): allows for the study of a variety of objects including, molecular gas in planetary nebulae, molecules on active comets, the heating processes in red giants and afterglows of GRBs (gamma ray bursts).
- Band 7 (275-373 GHz): provides astronomers with an insight into the gas and dust disks which surround new-born stars, seeing into regions obscured in the visible spectrum

such as star-forming clouds and early galaxies. Band 7 has also enabled measurements of global wind patterns on Mars and has measured the water content of Venus's atmosphere.

- Band 8 (385-500 GHz): enables interferometric imaging of the atomic carbon distribution around a planetary nebula. Many atoms and molecules have radio emission lines, with one of the most attractive being the carbon line at 0.6 mm.
- Band 9 (602-720 GHz): allows astronomers to study molecular clouds at higher temperatures and densities with greater angular resolution. Observation of dust traps surrounding young stars using Band 9 have answered long-standing planetary formations questions. These regions provide a haven for dust particles to grow and become large enough to survive on their own eventually forming comets, planets, and other rocky bodies
- Band 10 (787-950 GHz): the highest frequency band of ALMA can only operate under ideal atmospheric conditions due to low atmospheric transmission. Recently has enabled the detection of complex molecules and jets of heavy water streaming from star forming regions in the Cat's Paw Nebula ('NRAO - ALMA Band 10' 2018).

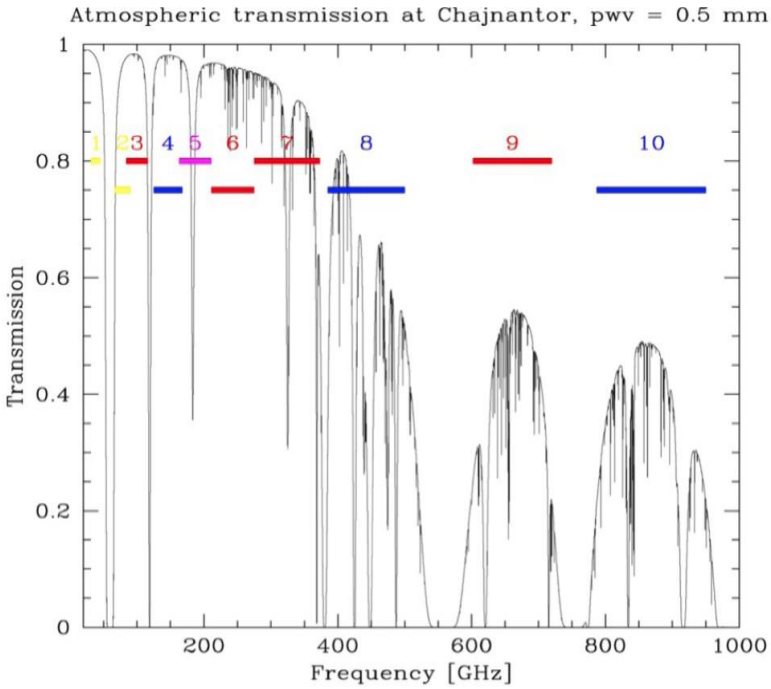

Figure 1-4: Overview of the atmospheric transmission of ALMA's different bands as measured from the Atacama site ('ALMA - ESO Receiver Bands' 2016).

Although the scope of the science performed by ALMA is remarkable, there are many limitations to ground based observations. In Figure 1-4, the atmospheric transmission across ALMA's spectral range is shown. Each of ALMA's bands span "water-windows" and it is clear

that there is substantial attenuation even at this ideal ground based site. These limited windows also mean that abundant atmospheric molecules such as H_2O, O_2 and many other species are blocked from observation (Tak 2012). Aside from attenuating the source signal, the atmosphere and areas surrounding the instrument emit their own thermal signal giving rise to "sky-noise" which can be orders of magnitude greater than the sources signal (Archibald et al. 2002). This limits the effective sensitivity of the instrument. Techniques such as chopping and telescope nodding are used to overcome these problems, but residual effects remain in the measured signal. Furthermore, variations in the atmosphere's refractive index can cause fluctuations in path lengths from the source to the telescope which degrades the instruments signal to noise ratio.

1.1.2 Herschel Space Observatory

The Herschel Space Observatory completed a 3.5-year study of the far-infrared (FIR) from 2009-2013. Herschel was the first and only dedicated space telescope to study celestial objects in the FIR range ($55 - 671\ \mu m$). The mission's prime science objectives focused on understanding the physical and dynamical processes in the ISM, the following objectives were outlined in its mission statement (Pilbratt et al. 2010):

- "*To conduct a wide-area sky survey measuring the dust-obscured star formation activity over cosmic time of galactic and extra-galactic sources*".
- "*Provide detailed physical and chemical studies of the ISM of our own galaxy and beyond*".
- "*Use observational astro-chemistry tools to understand the stellar and interstellar lifecycles and to investigate the processes involved in star formation and stellar evolution, including gas and dust disks around young, main sequence and evolved stars*".
- "*Investigate the atmospheres of solar system objects including minor bodies such as comets and trans-neptunium's objects*"

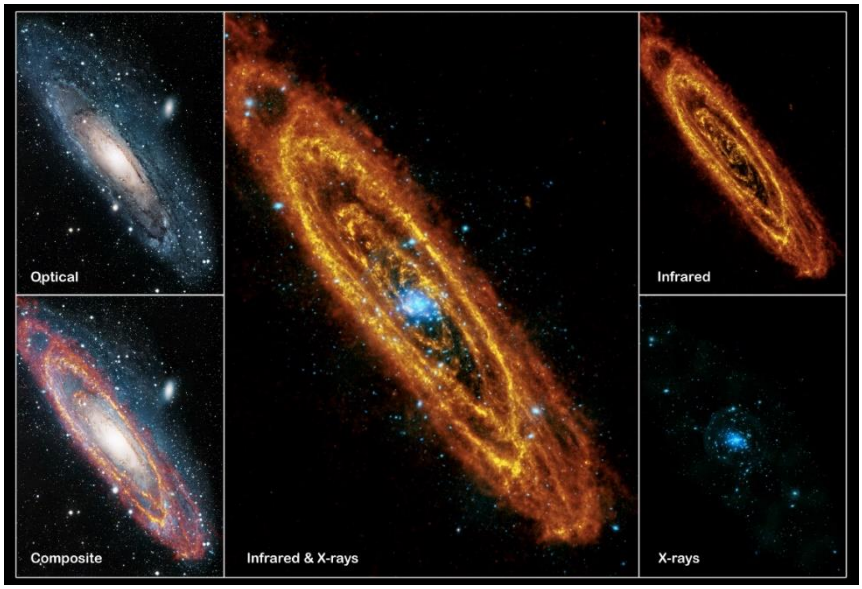

Figure 1-5: Composite image in the FIR (Herschel) and X-ray (XMM-Newton) of the Andromeda Galaxy. ('ESA - Andromeda Galaxy (M31)' 2011).

Set in a classical Cassegrain arrangement, Herschel imaged sources in the sub-millimetre and far-infrared range ($55 - 671$ μm) through its science payload comprised of three instruments: HiFi (Heterodyne Instrument for the Far Infrared), PACS (Photodetector Array Camera and Spectrometer) and SPIRE (Spectral and Photometric Imaging Receiver) (Pilbratt et al. 2010).

1. The HIFI instrument was a very high-resolution spectrometer and observed in seven bands covering $480 - 1910$ GHz. Bands 1 to 5 provided continuous coverage from $480 - 1250$ GHz using SIS mixers. Band 6, split into low and high sub-bands, covered the range $1410 - 1910$ GHz using hot-electron bolometer (HEB) mixers (Pilbratt et al. 2010)
2. PACS consisted of two sub-instruments: an imaging dual-band photometer and integral field line spectrometer. In imaging dual-band photometry mode, PACS imaged a field of view of 1.75×3.5 arcminutes^2 simultaneously in two bands, either $60 - 85$ μm or $85 - 125$ μm and $125 - 210$ μm, with full beam sampling in each band (Pilbratt et al. 2010). In integral field spectroscopy mode, PACS performed spectroscopy between 51 and 220 μm with a field of view of 47×47 arcseconds^2, resolved into 5×5 germanium/gallium photoconductor pixel arrays. In this mode PACS had a resolving power between 1000 and 4000.
3. SPIRE was comprised of a three band imaging photometer and an imaging Fourier transform spectrometer, using arrays of spider-web bolometers with neutron transmutation doped (NTD) germanium temperature sensors as its detectors (Pilbratt et

al. 2010). The spectrometer was operated in continuous scan mode and its spectral resolution could be adjusted in the range between 0.04 and $0.8\ \mathrm{cm}^{-1}$.

The legacy left by Herschel over its short lifetime can be captured by the numerous Herschel related publication (~2500 papers) and the insights made into fundamental processes which occur in the Universe. Herschel-HIFI has uncovered detail about the structure and chemical composition of the ISM, finding that the atomic and molecular phases of interstellar clouds are mixed rather than layered (Tak 2012). Another key finding was that neither H_2O nor O_2 are major carriers of oxygen in the ISM and play only a minor role in the ISM's cooling processes (Tak 2012). In Solar studies, it was found that planetary interaction plays an important role. That was shown by observations of exchange of compounds (such as H_2O) through comets and asteroids with planets and their moons (Tak 2012). Herschel-SPIRE has shown through observations of Arp 220, a nearby ultra-luminous infrared galaxy with two merging nuclei, that the molecular gas is influenced by the mechanical energy from the ongoing merger (Rangwala et al. 2011).

The proposed FIR space observatory SPICA, section 1.4, would have provided the next step in the advancement of FIR astronomy building on the legacy of Herschel. Herschel was fundamentally limited by its poor sensitivity, only objects with powers $> 10^{-18}\ \mathrm{Wm}^{-2}$ could be imaged. This meant Herschel could only resolve a handful of the brightest, closest and most massive young protoplanetary discs (Ferlet et al. 2010). SPICA aimed to overcome this limitation by offering two orders of magnitude increased sensitivity, allowing for a much wider catalogue objects to be imaged. Furthermore, SPICA aimed to offer coverage of frequency ranges beyond those measurable from ground based site such as ALMA. Observing in this domain would provide complementary diagnostic measurements for example of the dust, ice and atomic features of protoplanetary disc.

1.1.3 Wider Applications of Terahertz Imaging

The applications of terahertz radiation are far-reaching, extending beyond just astronomical applications. With great interest in the possibilities this portion of the spectrum offers, applications to many sectors have be found including: Earth-science, medicine, security, manufacturing and communications.

Meteorological studies often rely on complementary observations made in the millimetre wave range. Remote sensing at these frequencies exploit lines of high attenuation i.e. $183\ \mathrm{GHz}$, to

obtain temperature and humidity profiles of the atmosphere (De Maagt 2007). At selected windows, observations of the Earth can be made from orbit even under adverse weather conditions. Particularly interesting is imaging of the sea-ice and ice-clouds, to better understand their composition which is then fed into climate models. Moreover, terahertz observations can aid in climatological models, making important measurement of the concentrations of man-made pollutants such as CFCs (chlorofluorocarbons) which have caused damage to the Ozone layer (De Maagt 2007).

In the medical field there is great interest in the development of terahertz imaging methods because of the non-ionizing nature of the radiation and the unique perspective provided compared to conventional medical imagining techniques i.e. CT (computerized tomography), MRI (magnetic resonance imaging) and ultrasound. The most exciting application is the use of terahertz imaging for cancer detection, especially in the early stages – when cancers are much more treatable greatly increasing patient's survival rate (Cheon 2019). Most solid cancers begin on the surface of soft tissues, a region which is not optimal for conventional imaging methods. Terahertz radiation is sensitive to variations in the cell structure and hydration levels associated with the malignant process (Cheon 2019).

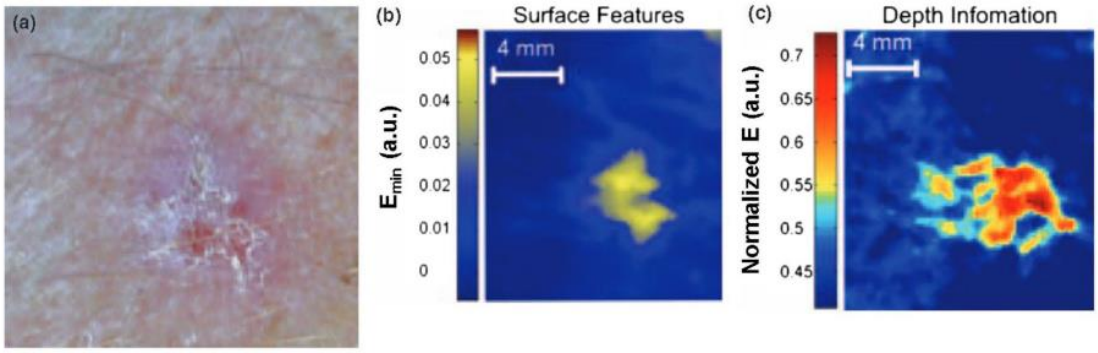

Figure 1-6 a)Image of a cancer lesion on a patients arm, b) Terahertz image of the surface of the lesion, c) Terahertz image of the tumour at 250 μm *(Cheon 2019)*

The use of terahertz imaging in the security and manufacturing sectors has been widely adopted. The technologies are used in airport scanners to make non-invasive inspections of passengers for weapons or illegal substances, seeing through materials which are normally opaque (De Maagt 2007). Terahertz imaging also provides a means of non-destructive testing allowing for the inspection and quality control of manufactured goods (De Maagt 2007). In the communications sector, promising developments have been made at terahertz frequencies. Laboratory experiments have even seen data transfer speeds of up to 100 Gbps over 20 m, and it is envisioned that the terahertz band will enable Tbps transfer speeds in the near future (Akyildiz, Jornet, and Han 2014).

1.2 Terahertz Technologies – Detector Systems

In general, detection systems can be broken into two distinct categories: *coherent* and *incoherent*. To probe the dynamics and composition of the interstellar medium, detectors capable of resolving terahertz emissions and atomic absorption lines are required. Both coherent and incoherent detectors are capable of such observations. However, the application of each detector technology is dependent on the observations being made. Coherent detector systems are favoured when finer spectral resolution is required. For example, to probe the composition of individual dust clouds a frequency resolution of ~ 1 MHz or sub-km/s velocity resolution is required (Walker 2015). For many observations such resolution is not necessary, for example studies of the CMB, dust continuum and external galaxies. In these cases, incoherent detectors are favoured as they are not bound by the quantum mechanical noise limits associated with coherent detector systems (Harris 1990).

Before detailing the two implementations of the detector systems and their associated devices, it is important to consider how environmental and system (electrical and heat) noise levels can effect detector efficiency. Detector systems are used to increase the source's observed flux density to a level where it can be detected and quantified. The unwanted noise produced from optics, detectors and the atmosphere should be minimised. The power received from a source can be much less than the noise power generated from the detector system itself (Walker 2015). Moreover, for ground based experiments there is an added noise power level due to the interaction of cosmic photons with water vapour in the atmosphere which adds to the difficulty of isolating the source signal.

As discussed in section 1.1, ground based terahertz telescopes are located at specialised sites which minimise atmospheric attenuation and sky-noise levels. Unfortunately, this alone is not sufficient since the instrument noise flux stemming from the detector system may still drown out any astronomical signals (Walker 2015). The detector's noise flux, S_v^{sym}, depends on contributions from each element in the system. A signal to noise ratio (SNR) equal to one implies that the rms-noise level is equal to the observed signals flux density S_v^o:

$$S_v^o \approx \Delta S_v^{rms}, \text{for SNR} = 1 \ . \qquad (1.2.1)$$

When expressed in terms of noise temperatures the relationship between rms-noise and system flux noise is given as:

$$\Delta T_v^{rms} = \frac{K_s T_{sym}}{\sqrt{\Delta\tau_{int} B_{pd}}} \qquad (1.2.2)$$

where ΔT_v^{rms} – rms noise temperature of the system (K), T_{sym} – system noise temperature, K_s – sensitivity constant, $\Delta\tau_{int}$ – post detection integration time and B_{pd} – post detection bandwidth related to the frequency resolution (Hz) (Walker 2015). To detect an astronomical source with a temperature of T_v^s, one must integrate over time $\Delta\tau_{int}$ with a prediction bandwidth B_{pd}, until the source temperature is above the rms-noise floor. The greater the system noise temperature T_{sym}, the longer the necessary integration time is to reach the target value of ΔT_v^{rms}:

$$\frac{T_v^s}{\Delta T_v^{rms}} > 1 \ . \qquad (1.2.3)$$

Integration times are limited in practice by gain stability, which restricts $\Delta\tau_{int}$ to 10 – 30 seconds. Instabilities can arise from individual components, interactions between components or atmospheric noise. Methods known as position-switching or frequency-switching are used to normalise these effects (Walker 2015). Observations are made in an *off* position or frequency where no source signal is seen, for the same length of time ($\Delta\tau_{int}$). The *off* measurements are then subtracted from the *on* measurement of the source, and the difference spectrum calibrated by multiplying the receivers output power by a temperature conversion factor or *Cal*. This *Cal* is obtained by having the receiver observe a load at a known temperature. Many scans (*on* and *off*) can be averaged together to meet the total $\Delta\tau_{int}$ requirement.

1.2.1 Coherent Detection

The vast majority of stellar emissions are produced by random atomic processes in celestial bodies and as such these sources are largely incoherent. At terahertz frequencies coherent receivers are used to investigate the composition, evolution and dynamics of astronomical objects such as star-forming regions, molecular clouds, photo-dominated regions around young or bright stars and shock processes in the ISM. Coherent detection relies on relationship

between the incident radiation and an internal synthetic reference signal. The incoming signal's component which is in phase with the monochromatic local oscillator (LO) is selected. This retention of the phase information is what separates the coherent and incoherent detector technologies.

However, as a consequence of retaining the phase information there is a limitation on the sensitivity of coherent detection. This limit is known as the *Quantum Limit* and refers to the phase selection imposed by the LO causing an uncertainty on the number of photons detected. The advantage of coherent detection is that there is greater spectral resolution and the signals from different telescopes can be coherently combined. In theory, coherent detectors are limited by the Heisenberg Uncertainty principle, and can never be as sensitive as incoherent detectors. They cannot measure the incoming energy at a given time to within one photon of energy (Harris 1990).

$$\Delta E \Delta t \geq \frac{\hbar}{2} \Rightarrow \Delta N \Delta \phi \geq \frac{1}{2}, \qquad (1.2.4)$$

where $\Delta N$and $\Delta \phi$ give the number of photons and their phase respectively. Coherent detectors or heterodyne-spectrometers for the terahertz band consist of two distinct parts. The first is the receiver-end, which performs a frequency shift on the incoming radiation. The LO signal effectivity phase stamps photons as they arrive, this is necessary for the frequency shift. The second, detector-end, consists of spectrometers which preform analysis on the shifted signal. These different parts are illustrated in Figure 1-7.

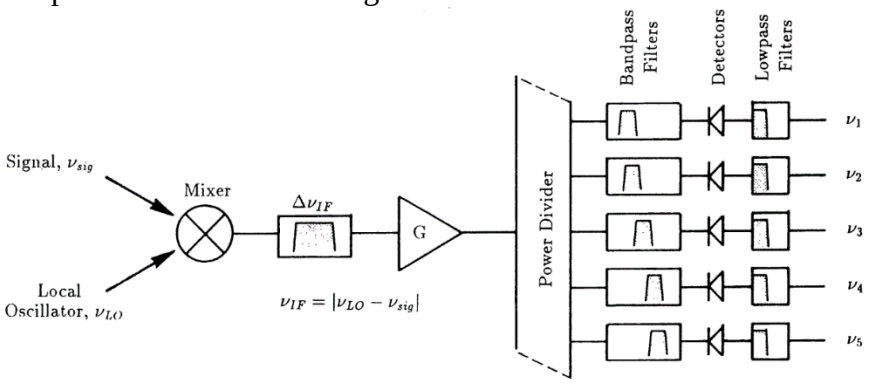

Figure 1-7 Schematic drawing of the layout of a coherent detection system. Receiver-end shows the mixing of the signal and local oscillators sources to produce the intermediate frequency, the detector-end shows the detector/spectrometer arrangement (Harris 1990)

If two currents, of different but near-by frequency, beat in the same non-linear electric circuit a new set of frequencies will be produced by these currents. This is the basic operational principle of a mixer device in the receiver, whose purpose is to translate the frequency of an electromagnetic signal. Frequency mixers are generally thought of a 3-port devices: 2-ports are inputs and the remaining port is an output. An ideal mixer takes two input signals and combines them in such a manner that the output is the sum and difference of the two base sources, or some multiple of their sum or difference. The ports have the following labels associated with them LO (Local Oscillator), RF (Signal Frequency) and IF (Intermediate Frequency) (Walker 2015).

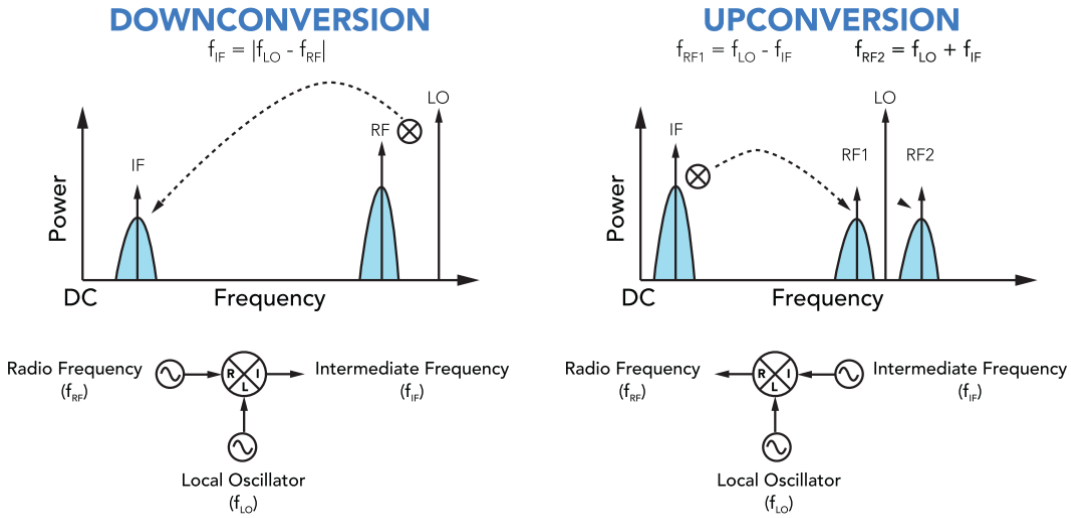

Figure 1-8 Graphical overview of the down/up conversion routines (Marki and Marki 2010)

A heterodyne receiver is optimised for detection of this difference frequency, typically down-converted to a few GHz for a terahertz heterodyne receiver. The receiver-end deals with the terahertz radiation directly from the source and its main components are: the LO which delivers a continuous reference frequency to the mixer, the mixer onto which the SF and LO radiation impinge and the optics which couple incoming radiation to the mixer (Hübers 2008). The detector-end deals with the converted IF signal and its main components are: the IF processor that amplifies the difference signal output by the mixer and the spectrometer/detector components for the detection of the processed IF signal (Hübers 2008). The IF and SF can be interchanged as secondary inputs or output depending on the desired application i.e. *down-conversion* or *up-conversion* (Hübers 2008).

The operation of the mixer is somewhat similar to that of relay device. It is activated by the LO signal which moderates the flow of photons through the receiver. The mixer is biased on the kink of the I-V curve so that the LO's voltage excursions are sufficient to swing the mixing

device between *on* and *off* states. The sharper the kink of the I-V curves the better, as less LO and signal power will be required for the down conversion process, implying the receiver will be more sensitive (Walker 2015). The IF amplifier's input bandwidth defines the spectral window centred on the down converted signal which will appear at the receiver's output. Two such frequency bands may be down-converted, one centred at $f_{USB} = f_{LO} + f_{IF}$ (upper sideband) and another at $f_{LSB} = f_{LO} - f_{IF}$ (lower sideband). Some mixers separate both of these side bands i.e. Dual Side Band (DSB) devices. However, other mixers may only retain information about a Single Side Band (SSB).

1.2.2 Mixers

Mixers for the terahertz band fall into two classes – non-cryogenically or cryogenically cooled. The assignment to one of these classes depends largely on the type of mixing device that is employed – Schottky Diode Mixer (SDM), Superconductor Insulator Superconductor (SIS) or Hot-Electron Bolometer (HEB). SDM is a semiconductor device which can operate at a range of different temperatures and may benefit from cooling but it is not strictly necessary. SIS and HEB exploit phenomena associated with superconductivity and thus are required to be cryogenically cooled to operate. Devices which do not rely on heavy cryogenic systems and may be adequately cooled by passive methods have many advantages over their cryogenic counterparts. Figure 1-9, shows that all of these technologies have uses across the terahertz range, with the noise temperature requirement ultimately determining the required mixer type.

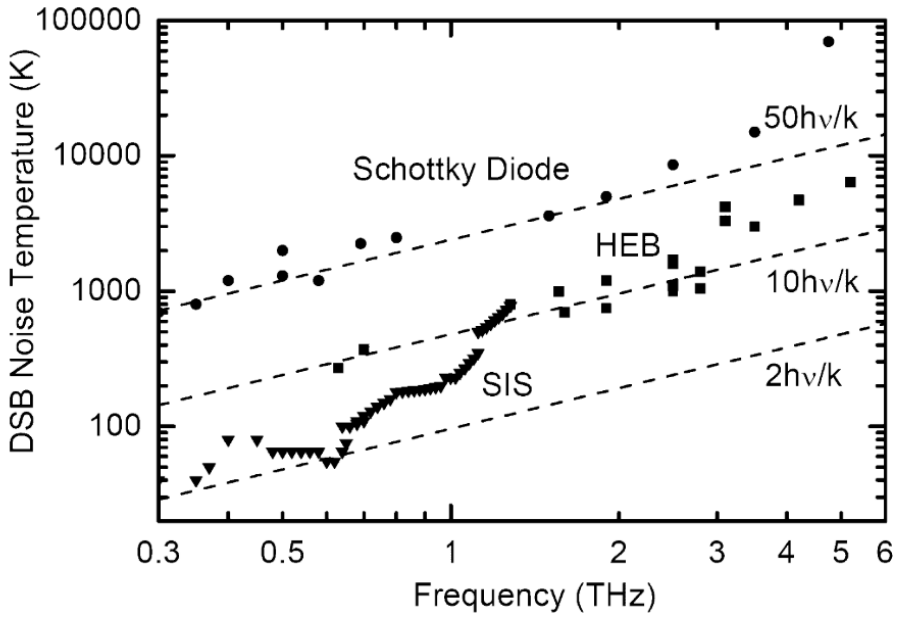

Figure 1-9 Noise temperatures of the different mixer technologies (SDM, HEB and SIS) at their operating frequencies (Hübers 2008)

Superconducting materials rely on the formation of weakly bound electron pairs known as Cooper pairs. Cooper pairs are formed via free electron interaction with the materials crystalline lattice. As electrons pass by positive ions in the lattice an acoustic wake is left behind, due to the attractive force between them. In the acoustic wake a tube of positive ions is left which can attract a second electron. If the first electron moves exactly opposite the second it will be attracted to its acoustic wake. The transfer of acoustic energy between electrons passing through the material's crystalline lattice forms weak bonds. Electrons linked in this manner share the same energy state and are known as Cooper pairs. Their existence leads to zero DC resistivity observed when the material is said to be super conducting i.e. below its critical temperature. The bonds in these Cooper pairs are so weak that an incoming stream of photons or current in excess of a critical current can cause them to break, resulting in the superconducting material returning to normal non-superconducting behaviour.

Schottky Diode Mixers have the highest noise and require the largest amount of LO power (~ 3 mW) but do not require cryogenic cooling. Furthermore, they have the widest IF bandwidth and are quite stable. A potential barrier is formed by bringing together a semiconductor and a small amount of metal wire. The charge neutrality at the interface results in a parabolic curve of the potential and the formation of a depletion region in the semiconductor. The current flow through the diode is due to: thermionic emission over the barrier, tunnelling through the barrier and generation or recombination inside or outside the depletion region. At terahertz frequencies, conduction occurs primarily through thermionic emission. For such cases, the I-V characteristic curve of the Schottky Diode takes on an exponential form. This exponential nature of the I-V curve provides the necessarily sharp non-linearity required for efficient high sensitivity mixing. Upper limits of these devices depend on the junction capacitance and series resistance at the operating bias voltage (Walker 2015).

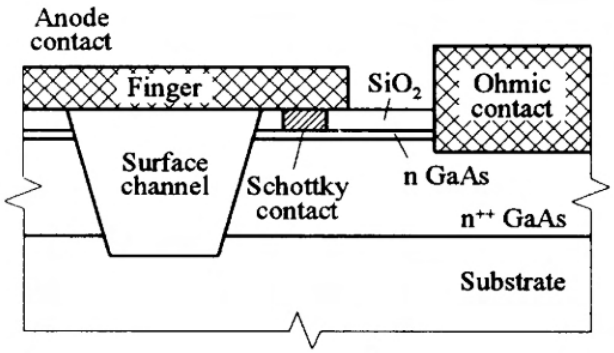

Figure 1-10 Surface channel design for a Schottky diode mixer (Hübers 2008)

Superconductor Insulator Superconductor Mixers provide the lowest noise temperature and can have a relatively wide bandwidth ~10 GHz. They require very small LO power (~ 3 μW) but have an upper frequency limit imposed by the energy gap of the superconductive material typically ~1.4 THz. SIS devices are formed by creating a "superconducting sandwich" composed of two superconducting layers separated by an insulating layer effectively forming a capacitor type shaped device. The insulating layer must have thickness roughly equal to the coherence length of Cooper pairs in the superconducting material (Walker 2015). This keeps the potential for Cooper pairs to form across the insulating layer. As Cooper pairs occupy the same energy level quantum mechanical tunnelling across the insulating layer can occur even with no voltage applied. This device is known as a Josephson junction and tunnelling of Cooper pairs produces a Josephson supercurrent observed on the SIS device I-V curve as a sharp spike. This current maximum value depends on the cross-sectional area of the insulating layer and the Josephson critical current density, which itself depends on the type and thickness of the insulating layer used (Walker 2015).

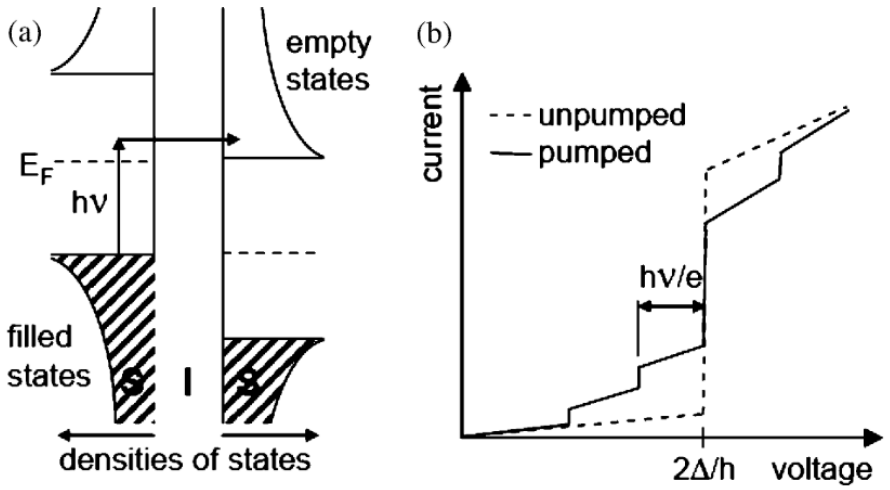

Figure 1-11 a) SIS mixer illustration of the tunnelling process with applied voltage and b) example of the non-linearity of the pumped and un-pumped states (Hübers 2008)

The characteristic I-V curve for an SIS-device appears at zero bias voltage as a vertical spike, if the system is supplied with some +/- bias voltage a steady slope is observed on the I-V curve, see Figure 1-11. This causes a change in potential energy and as a result the Cooper pairs on either side of the insulating layer will no longer share the same energy level causing the associated supercurrent to cease, in effect the device is powered off. Some small leakage is experienced until the bias voltage reaches that of the binding energy of Cooper pairs, this is known as the sub-gap region (Walker 2015). The bias voltage at this point is referred to as the energy gap voltage. For bias voltages which exceed the energy gap voltage, the tenuous bonds

between Cooper pairs can be broken and there is a rush of electrons across the insulator, resulting in a sharp transition in the I-V Curve, at this point the SIS device is powered on. Effectively all Cooper pairs are broken and the device returns to normal operation. This high-level of non-linearity is exploited by the SIS mixer to achieve very high efficiency mixing. The device is biased just below this non-linearity such that any incoming photons will deliver the energy necessary to break the Cooper pairs already under stress from the bias voltage.

1.2.3 Incoherent Detection

Incoherent detectors do not retain any knowledge of the phase information of the incident photon. As discussed in section 1.2, coherent detectors systems are favoured where high spectral resolution is required. However, for many observation including CMB studies and dust continuum measurements this high spectral resolution is not necessary. Incoherent detectors' indifference to phase means that they are not subject to the quantum mechanical noise limits associated with coherent detector systems (Walker 2015). The scheme for the incoherent receivers is much more straight forward. Photons enter the optical system which selects the frequency range to be observed, and the filtered light is then incident on one or more detectors which produce an output signal which is proportional to the incident power. Many incoherent detectors use bolometric type devices to measure incident radiation. Bolometers are thermal detectors that exploit the change in electrical resistance of a material with temperature. Photons incident on an absorbing layer cause a heating effect, which in turn produces a change in the material's resistance. Typically, heavily doped semiconductors materials such as ion-implanted silicon or neutron-transmutation doped germanium are used.

Two emerging superconducting incoherent detector devices which have been identified for use in contemporary terahertz telescope systems:

- Transition Edge Sensors (TES) – Advanced bolometric devices
- Microwave Kinetic Inductance Detectors (MKIDs) – Similar to SIS mixer

In fact, Transition Edge Sensors have been selected as the detection technology for the SAFARI instrument, see section 1.4.1. These devices take advantage of this tenuous bond between Cooper pairs, by DC biasing a superconducting bridge in the transition region between *superconducting* and *non-superconducting*. The slightest influx of power from an incident photon will result in heating and cause a transition between these two states of the

superconducting material. Some of the challenges associated with the development of this technology were to:

- develop a stable biasing method which did not interfere with the state of the device, and
- develop a mechanism to readout when transitions between states had occurred.

The superconducting devices are voltage biased rather than current biased. This choice avoids any potential for Joule heating that can lead to thermal runaway inside the superconducting material. This can occur when bias electrons and the crystal lattice cause a portion of the device to return to normal, which leads to further heating and so on until the whole device is no longer below the required critical temperature to be superconducting. Often TES sensors are used in conjunction with another superconducting device known as SQUID (Superconducting Quantum Interference Device) to readout the transitions, see Figure 1-12. SQUIDs are composed of two identical Josephson junctions in parallel and are employed as very sensitive magnetometers (Walker 2015).

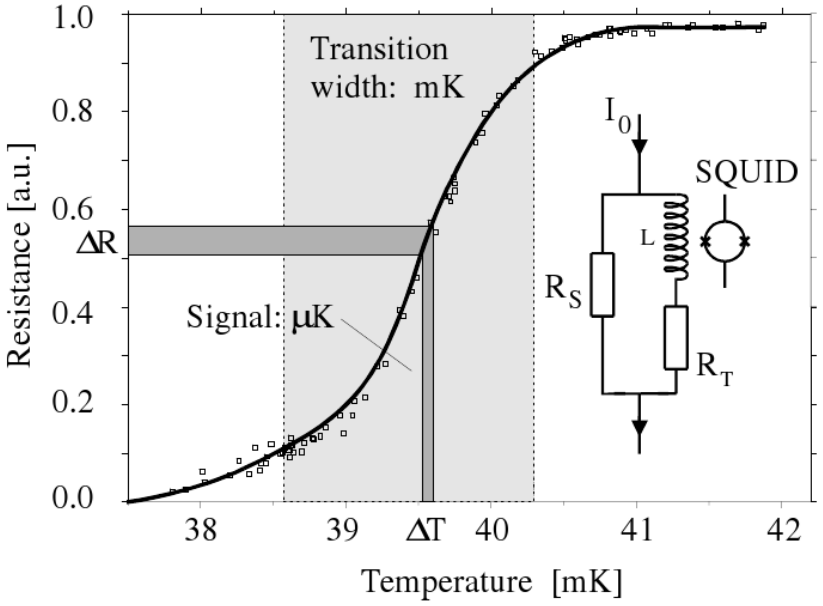

Figure 1-12 Shows the transition curve between the superconducting and non-superconducting phases. Inner circuit diagram details the typical arrangement of the TES and SQUID readout devices (Höhne et al. 1999)

In a typical set-up the TES is voltage biased by driving a current source through a load resistor. A voltage is selected such that the TES is placed in a *self-biased* region where power dissipated in the device is constant with the applied voltage. Furthermore, the TES is operated in series with a coil, which is inductively coupled to the SQUID. The coil produces a magnetic field which is dependent on the bias current to the circuit, as such variations in the photon flux

through the TES device can be measured via the change in magnetic field in the coil via the coupled SQUID.

Microwave Kinetic Inductance Detectors achieve their sensitivity through the breaking of Cooper pairs within a superconducting film. However, the pair-breaking mechanism is exploited differently than in other superconducting devices. Here, it is the variation of the superconducting layer's impedance due to pair-breaking that is used to determine the incident photon flux (Walker 2015). When photons strike the super-cooled material the time varying potential associated with the photons will accelerate the Cooper pair charge carriers in such a way as to reflect or absorb the incoming photons. The acceleration will be opposed by the inertia of the Cooper pairs, causing a phase lag between the incident electric field and the field produced by the Cooper pairs at the superconductors surface.

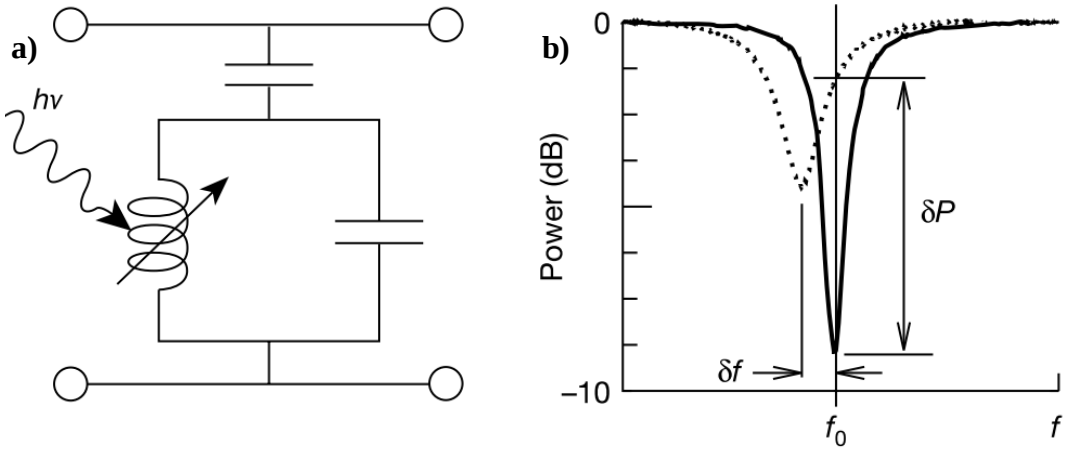

Figure 1-13 a) MKIDs circuit diagram with incident photon causing a change in the kinetic inductance and b)incident photon causes a variation in both inductance and resistance which alters the circuit's resonance point (Day et al. 2003)

Electrical phase lag is the same that would be produced by an inductor which opposes the finite rate of current-change through it. As the phase lag is rooted in the Cooper pairs dynamics, it is referred to as a kinetic inductance. The kinetic inductance, L_K, can be determined by equating the total kinetic energy of the Cooper pairs, KE_C, with the equivalent inductive energy, IE_C

$$\frac{1}{2}(2m_e v^2)(n_{CP} lA) = \frac{1}{2} L_K I^2 \qquad (1.2.5)$$

where v is the average Cooper pair velocity, n_{CP} is the number density of Cooper pairs and I is the superconducting current through the film. Incident photons with energies greater than the binding energy of the Cooper pairs can break them causing a reduction in the number of pairs

available in the material (Walker 2015). This reduces the device's superconductivity and causes increased resistance and inductance. Generally, the increase in inductance is many times greater than it is for resistance. The kinetic inductance can be determined by building a resonance circuit with the superconducting layer placed in parallel with a known capacitance and measuring the circuit's resonance frequency. In Figure 1-13, the variation of inductance when illuminated causes a change in the MKID's resonance frequency and as a result transmission at a fixed frequency. This change in frequency or transmission can be used to determine the incident power.

1.3 Terahertz Technologies – Sources

There now exist several technologies for sources of terahertz radiation to be used as local oscillators, or to emit a freely propagating beam in the terahertz band. Good LO sources must have the following properties:

- LO frequency must be selected such that down conversion can be performed at the signal frequency () i.e. $f_{LO} = f_{RF} \pm f_{IF}$.
- LO power must be sufficient to switch between the *on* and *off* states across the non-linearity of the I-V curve of the mixer device.
- LO power must be stable, such that the Allen-time of the receiver is not impacted by variation in power (Walker 2015).
- LO must be of pure enough tone in frequency and phase such that sufficient tolerance is maintained. Typical tolerance could be less than ~5 times the linewidth to be measured (Walker 2015).

Schottky diode frequency multipliers are commonly used as LO sources in ground and space based millimetre and sub-millimetre instruments. At Maynooth a Rohde & Schwarz VNA (Vector Network Analyser), with millimetre converter heads, allows for measurements of antennas in the W-band ($75 - 110$ GHz ZVA-Z110) and beyond ($500 - 1100$ GHz) via newly purchased converters RPG-ZC750 and RPG-ZC1100. However, due to the nature of frequency multiplied sources, with increasing multiplication factors comes significant power loss. This means that it becomes extremely challenging to push frequency multiplied sources into the "super-THz" range beyond 2.0 THz (Walker 2015). To make the move into higher frequencies while maintaining adequate power levels an alternative source known as a Quantum Cascade Laser (QCL) is commonly used. These devices can reach frequencies of ~ 5 THz, but require

cryogenic cooling to operate (Walker 2015). A QCL provides a coherent narrowband source for the analysis of an Offner re-imaging system, presented in chapter 5, as a potential focal plane solution for the SAFARI instrument.

Because of fundament physical limitations of conventional laser diodes, they cannot coherently emit photons at terahertz frequencies. Quantum Cascade Laser devices overcome these limitations by taking a different approach. Regular semiconductor lasers have electrons recombining with holes to release photons with an emission frequency equal to the bandgap, which is dependent on the composition of the semiconductor material. The QCL is a unipolar device (i.e. only one type of charge carrier is involved as only the conduction band is used) which exploits optical transitions between electronic states created by spatial confinement in semiconductor multi-quantum-wells, via the quantum engineering of electronic wave functions on a nanometre scale (O'Sullivan and Murphy 2012). Typically, 500 – 1500 alternating layers of thickness of just a few atoms are grown of alloy materials.

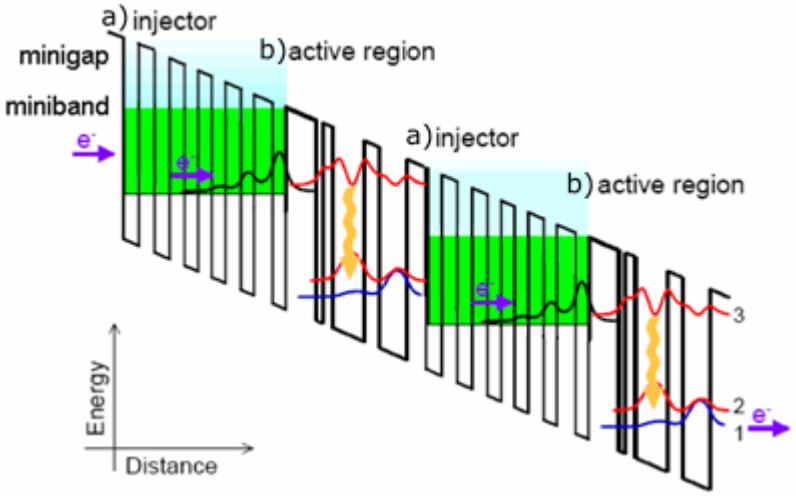

Figure 1-14 Conduction band diagram for two adjacent QCL stages. Each stage has an a) injector region – where electron injection and transitions occur b) active region – where lasing occurs (Mei et al. 2017)

QCLs are generally based on a three-level system, electrons are injected into the upper level of the active region, where laser transition occurs to the middle level followed by a rapid depletion to the lower level. The injector region collects and provides electrons for the upper level of the quantum wells, and a suitable design of layer thicknesses creates a population inversion between the upper and middle levels – this is shown in Figure 1-14. The cascading of super-lattice periods means that the passage of one electron can produce many photons (O'Sullivan and Murphy 2012). The most common QCL designs are based on GaAs or AlGaAs super-lattices. To select the desired frequency and generate a terahertz beam, a periodic series of slots

are etched into the top conducting electrode and the active layer at half wavelength intervals. As terahertz photons propagate through the layers the slots provide a region of constructive interference that guides the photons and forms terahertz beams at each end of the layer (O'Sullivan and Murphy 2012). Development of QCLs is still on going, and significant challenges remain in expanding the frequency regime of these devices, along with increasing their operational temperature.

Frequency Multipliers share similarities with the mixer devices introduced in section 1.2.1, as both rely on a non-linear device and a strong signal. However, unlike mixers, frequency multiplied sources receive only a single signal ($V_{SF} = 0$), leaving the Taylor expansion equation with only a $\cos(\omega_{LO}t)^n$ terms. In a generic multiplier for each value of n it will generate a harmonic signal of frequency $n \times \omega_{LO}$ with an additional multiplicative amplitude factor of $[2^{n-1}]^{-1}$. These frequency multipliers act as harmonic generators with decreasing amounts of power for higher frequency components, dependent on n (Walker 2015).

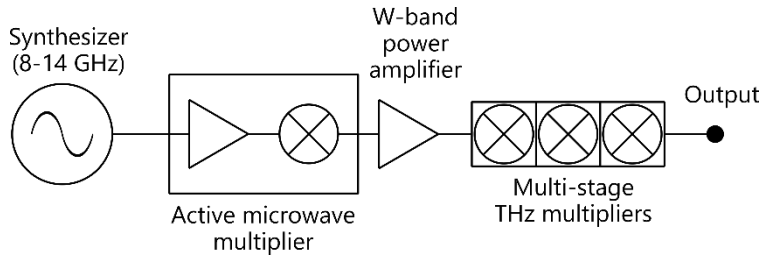

Figure 1-15 Frequency multiplied-based source chain. Here, a synthetic signal (~10 GHz) goes through two stages of multiplication, from X-band to W-band and then from W-band to the desired LO frequency. The W-band signal is amplified to accommodate for losses in the multiplication process (Walker 2015).

For an n^{th}-harmonic multiplier, the highest possible values of power converted P_n occurs when there is only real power in the circuit of the harmonic of interest. Here, the multiplier is said to be 100% efficient. This condition is only met when the device is terminated in a pure reactance for all but the desired frequency. A typical frequency converter chain is shown in Figure 1-15. The chain begins with a computer controlled microwave synthesiser source, capable of producing a continuous wave with power ~ 15 mW and frequencies in the X-band ($8 - 11$ GHz) or Ku-band ($12 - 18$ GHz). This synthetic wave is passed through one or many active multipliers (frequency multiplier and amplifier unit) until a desired frequency is reached, typically W-band frequency. The W-band signal must then pass through a power amplifier, which typically increases the signal power to ~ 100 mW. Finally, the signal is then further frequency multiplied to achieve the desired LO frequency with the multiplication factor given by $n = f_{LO}/f_{W-band}$. To reach f_{LO}, the signal is passed through a chain of multipliers, with

multiplication factors of $\times 2$, $\times 3$ or $\times 4$. The multiplier's efficiency drops sharply with increasing multiplication factor and to counteract this most devices are composed of a chain of doublers or triplers.

1.4 Space Infrared Telescope for Cosmology and Astrophysics (SPICA)

The Infrared Space Observatory, SPICA (Space Infrared Telescope for Cosmology and Astrophysics) was shortlisted as one of three candidate missions for the ESA medium-class mission program M5. In October 2020 SPICA was withdrawn from the M5 mission program due to financial constraints. This ambitious project, along with the technological advancements made, will eventually be restructured into a future far-infrared mission, hopefully succeeding with the strong foundation the SPICA mission consortium has provided. SPICA was collaboration between ESA and the Japanese Aerospace Exploration Agency (JAXA) with a number of international collaborators driving the development of the science instruments.

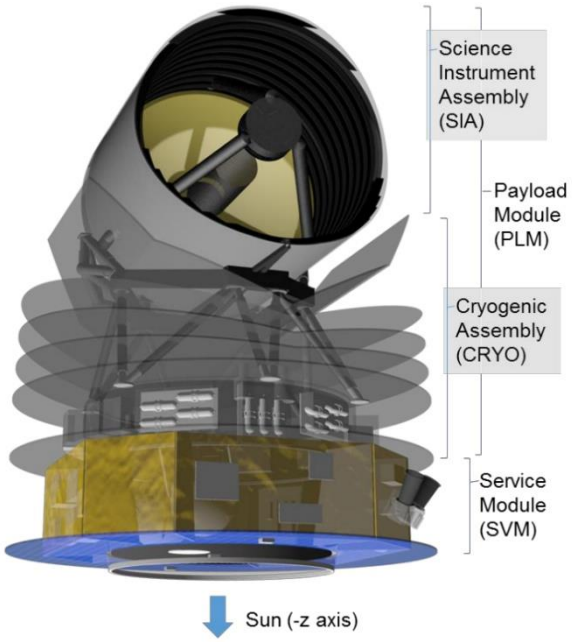

Figure 1-16 SPICA spacecraft arrangement, showing the instrument, cryogenic and service modules (Roelfsema 2018)

In many ways SPICA was the successor to the Herschel Space Observatory, section 1.1.2, offering observations of celestial objects in the mid to far-infrared range. SPICA aimed to expand the work of Herschel, addressing remaining questions around the formative and evolutionary processes of galaxies, stars and planetary systems. Observations in the FIR range provide an insight into their dynamical and chemical states which are obscured to other frequency ranges. The science objectives of the SPICA mission can be separated into three core

packages (1) *birth and evolution of active galactic nuclei*, (2) *star formation history of the universe* and (3) *formation of planetary systems* (Roelfsema 2018).

1.4.1 SPICA Instrument Overview

SPICA had planned a Ritchey-Chrétien arrangement, with payload of two imaging-spectrometer instruments that make up the focal plane assembly: SAFARI (SPICA Far-Infrared Instrument) and SMI (SPICA Mid-Infrared Instrument) (Roelfsema 2018). Together SAFARI and SMI provide continuous spectroscopic coverage over a wavelength range of $17 - 230$ μm. SPICA's telescopic system is composed of two Silicon Carbide (SiC) mirrors, the large cooled primary mirror (2.5 m) and the secondary mirror (0.612 m) which utilizes wavefront correction technology. SAFARI and SMI utilize state-of-the-art detector technologies, which in combination with the large cooled telescope unit provide sensitivity levels which far exceeds Herschel, see Figure 1-17. An ESA study of "a next generation cryogenic infrared telescope" and proven heritage technologies from the Herschel and AKARI missions informed many of these design choices (Roelfsema 2018).

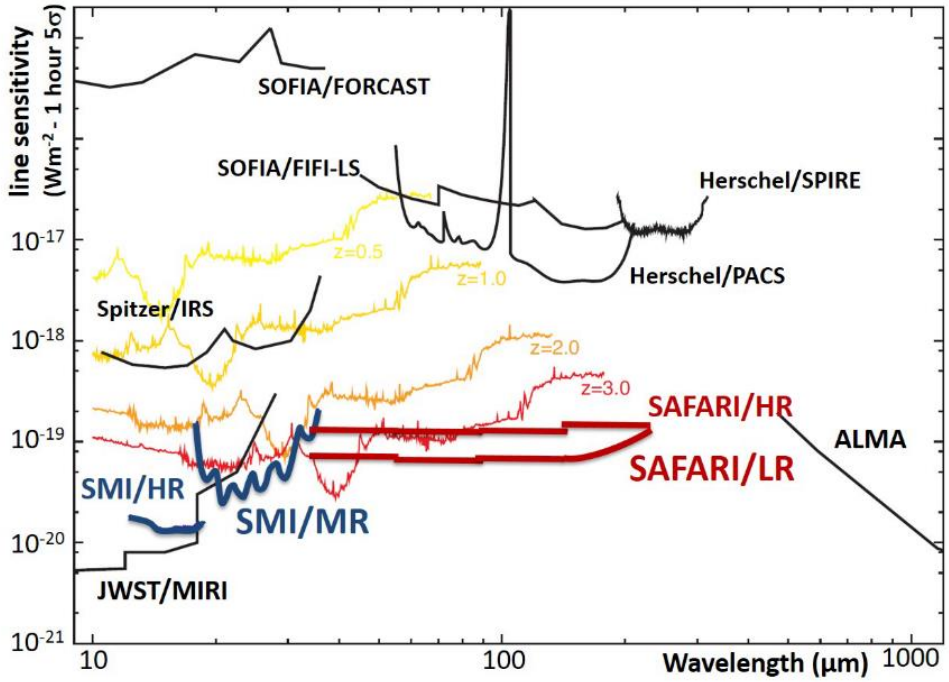

Figure 1-17 SPICA's instruments wavelength coverage and sensitivity compared with past, present and future missions (Roelfsema 2018)

SMI covers the wavelength range of $12 - 36$ μm with four separate channels. These channels are summarised in Figure 1-17 and detailed below with their respective wavelength ranges and resolutions:

- SMI/LR (Low Resolution) – wavelength range of $17 - 36$ μm with resolution of $R = 50 - 120$.
- SMI/MR (Mid Resolution) - wavelength range of $18 - 36$ μm with resolution of $R = 1300 - 2300$.
- SMI/HR (High Resolution) - wavelength range of $12 - 18$ μm with resolution of $R \sim 23000$.
- SMI/CAM – Broadband central wavelength at 34 μm with resolution of $R = 5$.

Two types of detector technologies are utilized by the SMI channels. For the shorter wavelength SMI/HR channels Si:As 1000×1000 photoconductors arrays are used, while for the remaining longer wavelength channels Si:Sb 1000×1000 photoconductors arrays are used. There is a significant drop in quantum efficiency of these detectors in each other bands, thus, both are required to cover SMI's spectral range.

SAFARI covers the wavelength range of $34 - 230$ μm and is optimised to achieve the highest level of sensitivity at moderate resolutions of $R \sim 300$ (limited by the thermal, power, pixel number and mass of space-based telescopes). Additionally, SAFARI can operate in a high resolution mode to study line profiles, which would enable such measurements as the inflow and outflow of gases from active galactic nuclei. This is achieved via the use of a Martin-Puplett interferometer (Audley, de Lange, Jackson, et al. 2018) – allowing for the LR mode to achieve sensitivity values of 5×10^{-20} W/m^2 for a transition edge sensor (TES) array with a NEP of 2×10^{-19} W/$\sqrt{\text{Hz}}$ (Audley, de Lange, Gao, et al. 2018). The intermediate optics of SAFARI includes an Offner relay arrangement (see chapter 5) which, via a 2D beam steering mirror (BSM), is used to switch between calibration sources or SAFARI's two resolution modes.

SAFARI's full spectral range is covered by four separate grating modules, covering the short, medium, long and very-long wavelength regions of the desired spectral range (SW: $34 - 56$ μm, MW: $54 - 89$ μm, LW: $87 - 143$ μm, VLW: $140 - 230$ μm). Each of the grating modules contains a block of super-cooled TES detector arrays coupled to multimode waveguide feeds and reflecting cavities (Audley, de Lange, Gao, et al. 2018). The ultra-sensitive TES detectors are being developed and fabricated at Cambridge, along with ongoing collaboration for the complete pixel design between Cardiff, SRON and Maynooth. The TESs offer 2 orders of magnitude greater sensitivity than bolometers previously used in ground based

observations, an optical efficiency of $> 50\%$ and an NEP of $2 \times 10^{-19}\,\mathrm{W}/\sqrt{\mathrm{Hz}}$ has been demonstrated for single detectors (Audley, de Lange, Gao, et al. 2018).

Each block of TES detector arrays is composed of three detector rows of 294 spectral pixels, each row corresponding to a single spatial pixel on the sky. Together three spatial pixels in a line give 2 arcmin of SAFARI field-of-view, each row samples the 147 elements of the dispersed spectrum. Compared with square arrays, the row layout allows for easier packing and wiring of the detectors due to the increased space available in the spatial direction as shown in Figure 1-18. Here focal ratios are used to define the spectral (F_1) and spatial (F_2) directions. The three spatial rows are used to avoid gaps in spectral coverage due to possible detector failures. Furthermore, with three spatial pixels it can be ensured that there is always a spatial pixel on the sky such that there are no observation time penalties for background subtraction (Audley, de Lange, Gao, et al. 2018).

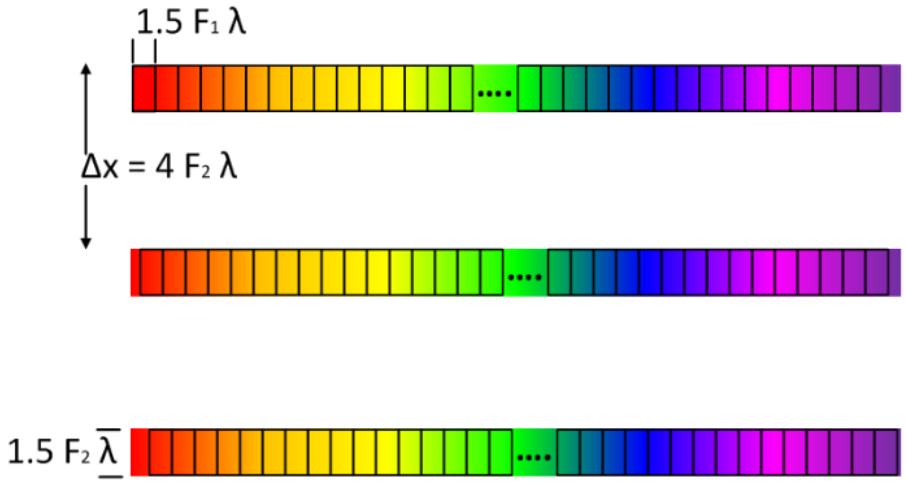

Figure 1-18 SAFARI detector array configuration. Each cell represents a feed aperture, colour coded to show the dispersion direction and each row represents a single spatial pixel on the sky (Audley, de Lange, Gao, et al. 2018).

Adjacent detector rows are offset by 1/3 of a spatial pixel, ensuring that a narrow (unresolved) line which falls on a spectral pixel boundary in one of the spatial pixels will be captured even if it falls on a dead spectral pixel in one of the rows. Pixel spacing of $\Delta x = 4F_2\lambda$ is sufficient to ensure no contamination between on-source and off-source pointings for background subtraction (Audley, de Lange, Gao, et al. 2018). The physical size of the focal plane is dictated by the focal and wavelength, for each grating module there is a slight variation ranging from $7\ \mathrm{mm} \times 239\ \mathrm{mm}$ for the SW band to $9\ \mathrm{mm} \times 251\ \mathrm{mm}$ for the VLW band. The total detector count is limited by the thermal conductance of the readout wiring. For the full instrument there are a total of 3840 detectors and, with multiplexing factor of 160, the detectors could be read

by 24 channels, with an excess readout capacity for up to 10 blind pixels per channel (Audley, de Lange, Gao, et al. 2018). The configuration of the detector arrays combines shorter subarray modules of 3×49 detectors to make up the desired 3×294 detectors in the focal plane for the four bands.

1.5 Thesis Overview

Each of SAFARI's sensitive pixels are composed of a multi-moded feed structure, an absorbing layer and a reflecting cavity. These devices rely on accurate and efficient modelling techniques to ensure optimal performance of the instrument. In the following chapters the necessary mode-matching routines needed to model each section of the pixel are developed and applied in the analysis of SAFARI-type pixels.

Chapter 2: Introduces the core waveguide, scattering, cascading and mode-matching theory used throughout the thesis for ideal cases. Many of these fundamental methods have been reformulated in terms of vector potentials and line-integrals, the consequences of these reformulations are detailed. Finally, the methods are applied to complete waveguide system to obtain their scattering parameters and characterise their far-field pattern.

Chapter 3: Extends the mode-matching techniques detailed in chapter 2 to allow for non-ideal boundary surfaces to be modelled. The effects of non-PEC (Perfect Electrically Conductive) walls on the uniform section and junction section are considered in detail. Furthermore, a simple but powerful model is adapted to allow for the inclusion of a surface roughness on the non-PEC boundary walls. Finally, a method for including an absorber layer as an infinitely thin sheet is detailed and the mechanism using the line-integral form which allows for the modelling of arbitrary absorber shape is detailed.

Chapter 4: Many novel features which have been developed are presented in this chapter. The first steps towards developing a fully parallelised version of the scattering code are presented with promising results in both speed and accuracy. Here a single powerful GPU device and PyOpenCL (Opencl 2009) are used to develop a working prototype of mode matching code with GPU optimisations. A novel idea of constructing a virtual non-reciprocal port to which all structure losses could be mapped to is presented. Using the absorber layer as the lossy element the advantages and limitations of this approach are considered.

Chapter 5: In this chapter much of the work done in modelling components for the SAFARI device is presented. Several different aspects of the overall design are considered, from the focal plane arrangement to the different pixel and feedhorn designs. The mode matching and physical optics tools developed at Maynooth are used to characterise and optimise these different components.

Chapter 2 – Theoretical Framework

For millimetre and sub-millimetre wave applications the ability to accurately design and characterise components is of critical importance. These devices commonly take the form of waveguide structures, which function to guide the incident electromagnetic radiation to some of the sensor technologies introduced earlier or to further optics in an efficient manner (i.e. with minimal loss in power). In this chapter the fundamental theory used to describe the fields within the waveguides, in terms of auxiliary vector potentials, is introduced. Moreover, the building blocks necessary to realise complete waveguide structures are introduced and their effect on the field properties is characterised.

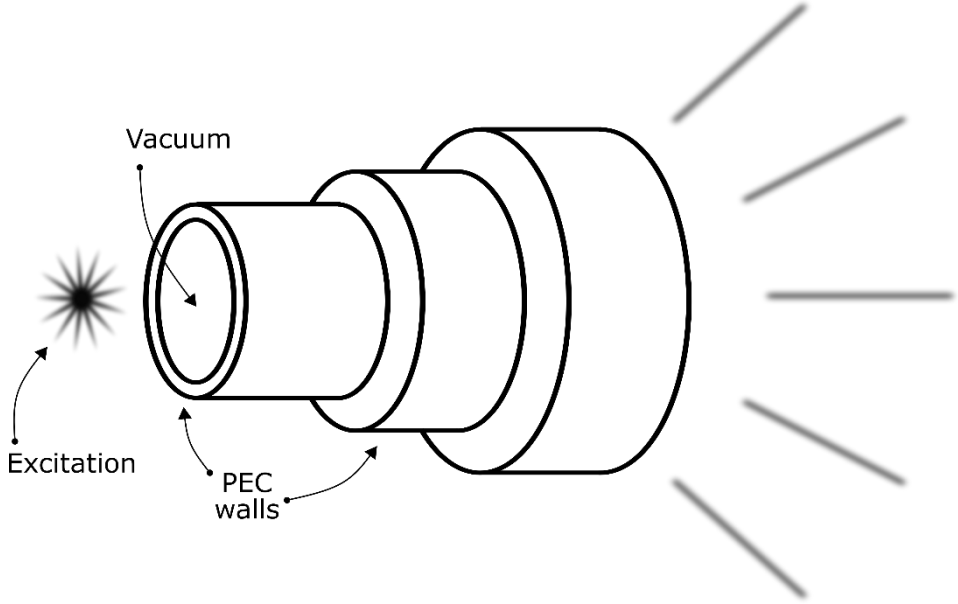

Figure 2-1: Schematic drawing of a guide structure with PEC walls, vacuum medium and a stimulus applied to the throat of the guide producing a radiation field from the exiting aperture.

Above, in Figure 2-1, a schematic drawing of a guide structure is presented. This waveguide is a hollow structure which is filled with an isotropic medium, often taken to be vacuum or free space. The medium is bound by a conducting surface, which is commonly assumed to be ideal or a perfect electric conductor (PEC). For an applied stimulus to the entrance aperture, here taken as the left hand side, the excitation of the fields which may exist within the structure will occur namely transverse electric (TE) and transverse magnetic (TM) fields (C. A. Balanis 2012). These fields can propagate within the bound structure and produce an aperture field at the opposite end of the guide which will radiate out from the exiting aperture of the guide. This field will be highly dependent on the geometry of the structure. It must be accurately modelled to fully understand its radiation characteristics.

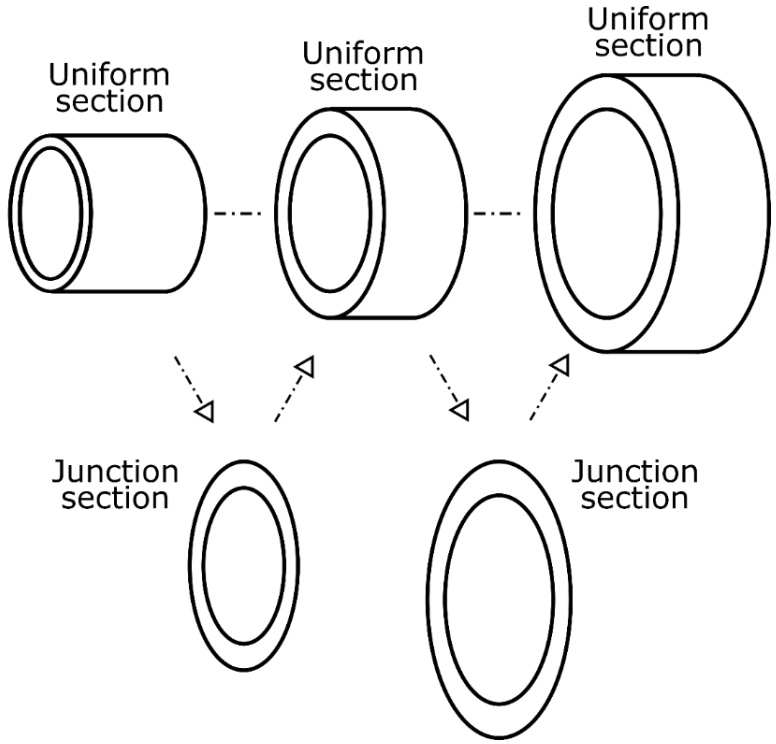

Figure 2-2: Exploded view of the elements which make up the guide section presented earlier. The uniform guide and junction sections represent the core components necessary for modelling waveguide components.

The example shown in Figure 2-1, while very much simplified in terms of the number of distinct steps, is representative of actual millimetre and sub-millimetre components. As illustrated in Figure 2-2, it may be segmented into smaller fundamental components i.e. uniform sections and junction sections. These components are the necessary building blocks needed to represent complete guide structures. The junction sections are used to link the uniform guide sections together to build up the overall shape of the device. Equivalently, the electromagnetic problem can be broken down into a description of propagation in individual uniform sections, in terms of a set of waveguide modes, and a description of scattering of those modes at discontinuities.

To achieve this, Maxwell's equations for each section must be solved subject to strict boundary conditions. These boundary conditions are imposed by the geometry of the structure and the bounding material (C. A. Balanis 2012). Key among those is the requirement that within a PEC section there exists no transverse electric field component along the wall. However, before this can be correctly applied the relevant electromagnetic theory must be first introduced to describe the problem. Much of the electromagnetic theory necessary in the implementation of the modified mode-matching methods in taken from (C. A. Balanis 2012) and is presented in a distilled form in the following sections.

2.1 Auxiliary Vector Potentials

The devices that are to be modelled are mostly hollow and bound by electrically conducting surfaces. Hollow here means being filled with either vacuum or a dielectric medium such as air. As such, those interior regions are free of field sources. In the absence of sources Maxwell's equations for harmonic fields of frequency ω take the following form in SI units:

$$\nabla \cdot \boldsymbol{D} = 0 \qquad (2.1.1) \qquad \nabla \cdot \boldsymbol{B} = 0 \qquad (2.1.2)$$

$$\nabla \times \boldsymbol{E} = -j\omega \boldsymbol{B} \qquad (2.1.3) \qquad \nabla \times \boldsymbol{H} = j\omega \boldsymbol{D} \qquad (2.1.4)$$

$$\boldsymbol{D} = \epsilon \boldsymbol{E} \qquad (2.1.5) \qquad \boldsymbol{B} = \mu \boldsymbol{H} \qquad (2.1.6)$$

At this point it may be natural to proceed by directly solving Maxwell's equations, with appropriate boundary conditions, to find the electric and magnetic fields, which are measurable quantities. This approach is taken by many (Gleeson 2004; Doherty 2012; McCarthy 2014; Kalinauskaitė and Murphy 2018) and is a perfectly valid. In the interest of greater flexibility when dealing with arbitrary geometries, an alternative approach is taken here.

Instead of directly solving Maxwell's equations to obtain the fields, the procedure can be split into two steps. Firstly, the auxiliary electric and magnetic vector potentials are determined. These potentials give an alternative mathematical representation of the problem. Secondly, and only when needed, the electric and magnetic fields are explicitly evaluated from those potentials. The electric and magnetic auxiliary vector potentials are formally introduced now, as in C. A. Balanis (2012), while in the following sections it is demonstrated that this approach offers an advantage when dealing with more complex geometries (such as offset transitions between rectangular and cylindrical waveguides). In some of the steps taken to introduce the auxiliary vector potentials the following common vector calculus identities are required:

$$\nabla \times (\boldsymbol{u}_1 + \boldsymbol{u}_2) = \nabla \times \boldsymbol{u}_1 + \nabla \times \boldsymbol{u}_2 \qquad (2.1.7) \qquad \nabla \cdot \nabla \times \boldsymbol{u}_1 = 0 \qquad (2.1.8)$$

$$\nabla \times \nabla \tilde{u} = 0 \qquad (2.1.9) \qquad \nabla \times \nabla \times \boldsymbol{u}_1 = \nabla(\nabla \cdot \boldsymbol{u}_1) - \nabla^2 \boldsymbol{u}_1 \qquad (2.1.10)$$

2.1.1 Magnetic Vector Potential

In a source free region, the magnetic flux density $\boldsymbol{B}$ is always solenoidal ($\nabla \cdot \boldsymbol{B} = 0$). For an arbitrary vector potential $\boldsymbol{A}$, the magnetic flux density $\boldsymbol{B_A}$ defined as:

$$\boldsymbol{B}_A = \nabla \times \boldsymbol{A} \tag{2.1.11}$$

automatically this satisfies the divergence equation (2.1.2), due to the identity given in (2.1.8). Here subscript $(\,)_A$ denotes fields due to the vector potential $\boldsymbol{A}$. The magnetic field $\boldsymbol{H_A}$ is then given by:

$$\boldsymbol{H}_A = \frac{1}{\mu}\nabla \times \boldsymbol{A} \tag{2.1.12}$$

From Maxwell's curl equation (2.1.3), the electric field is also related to $\boldsymbol{A}$ by:

$$\nabla \times \boldsymbol{E}_A = -j\omega\mu\boldsymbol{H}_A = -j\omega\nabla \times \boldsymbol{A} \tag{2.1.13}$$

$$\nabla \times (\boldsymbol{E}_A + j\omega\boldsymbol{A}) = 0 \tag{2.1.14}$$

Using vector identity (2.1.9) the vector field $(\boldsymbol{E}_A + j\omega\boldsymbol{A})$ can be expressed as the gradient of a scalar function ψ_e such that:

$$\boldsymbol{E}_A + j\omega\boldsymbol{A} = -\nabla\psi_e \tag{2.1.15}$$

$$\boldsymbol{E}_A = -\nabla\psi_e - j\omega\boldsymbol{A} \tag{2.1.16}$$

Expressing both sides of equation (2.1.4) in terms of functions of vector potential $\boldsymbol{A}$ gives:

$$\nabla \times \frac{1}{\mu}\nabla \times \boldsymbol{A} = j\omega\mu\epsilon(-\nabla\psi_{\mathrm{e}} - j\omega\boldsymbol{A}) \tag{2.1.17}$$

$$\frac{1}{\mu}[\nabla(\nabla\cdot\boldsymbol{A})-\nabla^2\boldsymbol{A}]=j\omega\mu\epsilon(-\nabla\psi_{\mathrm{e}}-j\omega\boldsymbol{A}) \qquad (2.1.18)$$

$$\nabla^2\boldsymbol{A}+\beta^2\boldsymbol{A}=\nabla(\nabla\cdot\boldsymbol{A}+j\omega\mu\epsilon\psi_e) \qquad (2.1.19)$$

where $\beta=\omega\sqrt{\mu\epsilon}$.

Using the Lorentz gauge:

$$\nabla\cdot\boldsymbol{A}=-j\omega\mu\epsilon\psi_e \qquad (2.1.20)$$

$$\psi_e=-\frac{1}{j\omega\mu\epsilon}\nabla\cdot\boldsymbol{A} \qquad (2.1.21)$$

equation (2.1.19) can be reduced to a simple wave equation form in a source free region:

$$\nabla^2\boldsymbol{A}+\beta^2\boldsymbol{A}=0, \qquad (2.1.22)$$

and the electric field due to $\boldsymbol{A}$ is:

$$\boldsymbol{E_A}=-j\omega\boldsymbol{A}-j\frac{1}{\omega\mu\epsilon}\boldsymbol{\nabla}(\boldsymbol{\nabla}\cdot\boldsymbol{A}) \qquad (2.1.23)$$

2.1.2 Electric Vector Potential

Alternatively, the electric vector potential $\boldsymbol{F}$ can be used to represent the fields. In a source free region, the electric flux density $\boldsymbol{D}$ is always solenoidal ($\nabla\cdot\boldsymbol{D}=0$). For an arbitrary vector potential $\boldsymbol{F}$, the electric flux density $\boldsymbol{D_F}$ defined as**:**

$$\boldsymbol{D}_F=-\nabla\times\boldsymbol{F} \qquad (2.1.24)$$

which satisfies the divergence equation (2.1.1), due to the identity given in (2.1.8). Here subscript $(\,)_F$ denotes fields due to the vector potential $\boldsymbol{F}$. The electric field $\boldsymbol{E_F}$ is then given by:

$$\boldsymbol{E_F} = -\frac{1}{\epsilon}\nabla \times \boldsymbol{F} \tag{2.1.25}$$

From Maxwell's curl equation (2.1.4), the magnetic field is also related to $\boldsymbol{F}$ by:

$$\nabla \times \boldsymbol{H}_F = j\omega\epsilon \boldsymbol{E}_F = j\omega(-\nabla \times \boldsymbol{F}) \tag{2.1.26}$$

$$\nabla \times (\boldsymbol{H}_F + j\omega \boldsymbol{F}) = 0$$

Using vector identity (2.1.9) the vector field $(\boldsymbol{H}_F + j\omega\boldsymbol{F})$ can be expressed as the gradient of a scalar function ψ_m such that:

$$\boldsymbol{H}_F + j\omega\boldsymbol{F} = -\nabla\psi_m \tag{2.1.27}$$

$$\boldsymbol{H}_F = -\nabla\psi_m - j\omega\boldsymbol{F}$$

Expressing both sides of equation (2.1.3) in terms of functions of vector potential $\boldsymbol{F}$ gives:

$$\nabla \times -\frac{1}{\epsilon}\nabla \times \boldsymbol{F} = j\omega\mu\epsilon(-\nabla\psi_m - j\omega\boldsymbol{F}) \tag{2.1.28}$$

$$\frac{1}{\epsilon}[\nabla^2\boldsymbol{F} - \nabla(\nabla \cdot \boldsymbol{F})] = j\omega\mu\epsilon(-\nabla\psi_m - j\omega\boldsymbol{F}) \tag{2.1.29}$$

$$\nabla^2\boldsymbol{F} + \beta^2\boldsymbol{F} = \nabla(\nabla \cdot \boldsymbol{F} + j\omega\mu\epsilon\psi_m) \tag{2.1.30}$$

Using the Lorentz gauge:

$$\nabla \cdot \boldsymbol{F} = -j\omega\mu\epsilon\psi_m \qquad (2.1.31)$$

$$\psi_m = -\frac{1}{j\omega\mu\epsilon}\nabla \cdot \boldsymbol{F} \qquad (2.1.32)$$

equation (2.1.30) can be reduced to a simple wave equation form in a source free region:

$$\nabla^2\boldsymbol{F} + \beta^2\boldsymbol{F} = 0, \qquad (2.1.33)$$

and the magnetic field due to $\boldsymbol{F}$ is:

$$\boldsymbol{H_F} = -j\omega\boldsymbol{F} - j\frac{1}{\omega\mu\epsilon}\boldsymbol{\nabla}(\boldsymbol{\nabla} \cdot \boldsymbol{F}) \qquad (2.1.34)$$

2.2 Electromagnetic Modes in Uniform Waveguide Sections

Electromagnetic modes are particular field configurations that satisfy Maxwell's equations, subject to appropriate boundary conditions. Mathematically this sets up a boundary value problem (BVP). In general, there exist infinitely many solutions to such BVPs and thus an infinite number of modes. In this section only hollow guides, uniform in cross-section and bound by conducting walls, are considered. Independent modes propagating in such structures can be selected to be either transverse electric (TE) or transverse magnetic (TM) – with electric or magnetic field components, respectively, orthogonal to the direction of propagation. Transverse electromagnetic (TEM) modes are not admitted (C. A. Balanis 2012).

2.2.1 Transverse Electric (TE) Modes

Transverse electric modes are field configurations with electric field orthogonal to a reference direction. Here the reference direction is taken to be the guide axis, which is also the *z*-axis of a Cartesian coordinate system. The mode's reference direction is indicated in its name, where it might be ambiguous. A TE mode propagating in the *z*-direction is given in this notation as TE^z.

Assuming a source free region within the guide boundaries, the fields can be given in terms of the electric vector potential $\boldsymbol{F}$, as shown in section 2.1.2. Cartesian components of the electric field are found by expanding equation (2.1.25):

$$\boldsymbol{E_F} = \hat{\boldsymbol{a}}_x\left[-\frac{1}{\epsilon}\left(\frac{\partial F_z}{\partial y}-\frac{\partial F_y}{\partial z}\right)\right]+\hat{\boldsymbol{a}}_y\left[-\frac{1}{\epsilon}\left(\frac{\partial F_x}{\partial z}-\frac{\partial F_z}{\partial x}\right)\right]+\hat{\boldsymbol{a}}_z\left[-\frac{1}{\epsilon}\left(\frac{\partial F_y}{\partial x}-\frac{\partial F_x}{\partial y}\right)\right] \quad (2.2.1)$$

It is clear that an arbitrary TE^z field configuration (with $E_z = 0$) can be produced if $F_x = F_y = 0$ and $F_z \neq 0$, and therefore a single scalar function $F_z(x, y, z)$ can be used to define fields that are automatically TE^z. From equations (2.1.25) and (2.1.34) the corresponding Cartesian field component are:

$$E_x = -\frac{1}{\epsilon}\frac{\partial F_z}{\partial y} \quad (2.2.2) \qquad H_x = -j\frac{c^2}{\omega}\frac{\partial^2 F_z}{\partial x \partial z} \quad (2.2.3)$$

$$E_y = \frac{1}{\epsilon}\frac{\partial F_z}{\partial x} \quad (2.2.4) \qquad H_y = -j\frac{c^2}{\omega}\frac{\partial^2 F_z}{\partial y \partial z} \quad (2.2.5)$$

$$E_z = 0 \quad (2.2.6) \qquad H_z = -j\frac{c^2}{\omega}\left(\frac{\partial^2 F_z}{\partial z^2}+\beta^2 F_z\right) \quad (2.2.7)$$

since $\boldsymbol{F} = (0,\ 0,\ F_z)$**.** Equation (2.1.33) also reduces to:

$$\nabla^2 F_z + \beta^2 F_z = 0 \quad (2.2.8)$$

2.2.2 Transverse Magnetic (TM) Modes

Likewise, transverse magnetic modes are field configurations with magnetic field orthogonal to a reference direction. With the reference direction aligned with the guide axis (*z*-axis of a Cartesian coordinate system). Again, where necessary the mode's reference direction is indicated in its name. A TM mode propagating in the *z*-direction is given as TM^z.

Assuming a source free region within the guide boundaries, the fields can be given in terms of the magnetic vector potential $\boldsymbol{A}$, as shown in section 2.1.1. Cartesian components of the magnetic field are found by expanding equation (2.1.12):

$$\boldsymbol{H} = \hat{\boldsymbol{a}}_x \left[\frac{1}{\mu}\left(\frac{\partial A_z}{\partial y} - \frac{\partial A_y}{\partial z}\right)\right] + \hat{\boldsymbol{a}}_y \left[\frac{1}{\mu}\left(\frac{\partial A_x}{\partial z} - \frac{\partial A_z}{\partial x}\right)\right] + \hat{\boldsymbol{a}}_z \left[\frac{1}{\mu}\left(\frac{\partial A_y}{\partial x} - \frac{\partial A_x}{\partial y}\right)\right] \quad (2.2.9)$$

It is clear that an arbitrary TM^z field configuration (with $H_z = 0$) can be produced if $A_x = A_y = 0$ and $A_z \neq 0$, and therefore a single scalar function $A_z(x, y, z)$ can be used to define fields that are automatically TM^z. From equations (2.1.12) and (2.1.23) the corresponding Cartesian field component are:

$$H_x = \frac{1}{\mu}\frac{\partial A_z}{\partial y} \quad (2.2.10) \qquad E_x = -j\frac{c^2}{\omega}\frac{\partial^2 A_z}{\partial x \partial z} \quad (2.2.11)$$

$$H_y = -\frac{1}{\mu}\frac{\partial A_z}{\partial x} \quad (2.2.12) \qquad E_y = -j\frac{c^2}{\omega}\frac{\partial^2 A_z}{\partial y \partial z} \quad (2.2.13)$$

$$H_z = 0 \quad (2.2.14) \qquad E_z = -j\frac{c^2}{\omega}\left(\frac{\partial^2 A_z}{\partial z^2} + \beta^2 A_z\right) \quad (2.2.15)$$

since $\boldsymbol{A} = (0,\ 0,\ A_z)$**.** Equation (2.1.22) also reduces to:

$$\nabla^2 A_z + \beta^2 A_z = 0 \quad (2.2.16)$$

2.2.3 Transverse Electric and Magnetic Modes in Infinite Uniform Waveguides with PEC Walls

Solutions to the scalar wave equations, (2.2.8) and (2.2.16)(2.1.16), are found using the separation-of-variables method. Here a scalar potential $Q(x,y,z)$ can be expressed as:

$$Q(x,y,z) = G(x,y)h(z) \tag{2.2.17}$$

The form of $G(x,y)$ and $h(z)$ must be selected carefully to reduce the complexity of the problem and will depend on the boundary conditions. Here the guide is unbounded in the *z*-direction, therefore an appropriate form of $h(z)$ is a combination of travelling waves given by:

$$h(z) = A_1 e^{-j\beta_z z} + A_2 e^{+j\beta_z z}, \tag{2.2.18}$$

where the first and the second term represent forward and backward propagating waves, respectively. The form of $G(x,y)$ is not fixed at this point. Individual solutions for the wave equation for TE modes are therefore sought in the following form:

$$F_z(x,y,z) = -\epsilon F(x,y) e^{\mp j\beta_z^{TE} z}, \tag{2.2.19}$$

while the equivalent form for TM modes is:

$$A_z(x,y,z) = \mp\mu A(x,y) e^{\mp j\beta_z^{TM} z} \tag{2.2.20}$$

The additional terms $-\epsilon$ and $\mp\mu$ make the solutions consistent with the phase convention commonly used in literature. Where alternative signs are given such as $\mp$, the top corresponds to forward traveling waves and the bottom to backward traveling waves.

In equation (2.2.19) the form of $F(x,y)$ depends on the guide cross-section and captures the *x* and *y* dependence of the scalar potential function F_z. Substituting this form of the potential into equation (2.2.8) gives:

$$\frac{\partial^2 F_z}{\partial x^2} + \frac{\partial^2 F_z}{\partial y^2} - \left(\beta_z^{TE}\right)^2 F_z + \beta^2 F_z = 0 \qquad (2.2.21)$$

$$\frac{\partial^2 F_z}{\partial x^2} + \frac{\partial^2 F_z}{\partial y^2} + \beta_c^2 F_z = 0 \qquad (2.2.22)$$

The scalar wave equation can then be written as:

$$\nabla^2 F(x,y) + \left(\beta_c^{TE}\right)^2 F(x,y) = 0 \qquad (2.2.23)$$

where

$$(\beta_c^{TE})^2 = \beta^2 - \left(\beta_z^{TE}\right)^2 \text{ with } \beta_z^{TE} = \sqrt{\beta^2 - (\beta_c^{TE})^2} \qquad (2.2.24)$$

Here β_c^{TE} gives the cutoff wave number, and eigenvalue, of a particular modal field and sets the TE mode's propagation constant β_z^{TE}.

The scalar potential $F(x,y)$ is subject to boundary conditions at the walls. The tangential electric field must be zero at the interface between the guide's inner volume and the PEC wall. $\nabla F(x,y)$ is perpendicular to the transverse electric field, since $\nabla F(x,y) \cdot \boldsymbol{E^t} = \left(\frac{\partial F}{\partial x}, \frac{\partial F}{\partial y}\right) \cdot \left(-\frac{1}{\epsilon}\frac{\partial F_z}{\partial y}, \frac{1}{\epsilon}\frac{\partial F_z}{\partial x}\right) = 0$ due to the functional relationship between F_z and $F(x,y)$ as in equation (2.2.19) and both lie in the same *xy*-plane. Since $E_z = 0$ everywhere for a TE mode, the tangential component of the electric field at the wall is zero if and only if $\nabla F(x,y)$ has no component normal to the wall:

$$\frac{\partial F(x,y)}{\partial \hat{n}} = \nabla F(x,y) \cdot \hat{\boldsymbol{n}} = 0 \qquad (2.2.25)$$

Each mode has an associated admittance given by the ratio of the orthogonal components of the mode's electric and magnetic field, given in equations (2.2.2) – (2.2.7). For TE waveguide modes the admittance is given by:

$$Y^{TE} = \frac{H_y}{E_x} = -\frac{H_x}{E_y} \tag{2.2.26}$$

or in terms of the mode's propagation constant:

$$Y^{TE} = \frac{\beta_z^{TE}}{\mu\omega} = \frac{\beta_z^{TE}}{\mu c\beta} = \sqrt{\frac{\epsilon}{\mu}}\frac{\beta_z^{TE}}{\beta} = \frac{\beta_z^{TE}}{\beta}Y_0 \tag{2.2.27}$$

The mode's transverse and longitudinal (z) field components (equations (2.2.2) – (2.2.7)) can be expressed concisely in terms of the gradient of scalar potential function $F(x, y)$. Here the transverse field components at $z = 0$ are given by:

$$\boldsymbol{E}^{t,TE} = -\frac{1}{\epsilon}\nabla F_z \times \hat{z} = \nabla F(x, y) \times \hat{\boldsymbol{z}} \tag{2.2.28}$$

$$\boldsymbol{H}^{t,TE} = \pm\frac{\beta_z^{TE}c^2}{\omega}\epsilon\nabla F(x, y) = \pm Y^{TE}\nabla F(x, y) \tag{2.2.29}$$

and the only non-zero z-component as:

$$H_z^{TE} = -j\frac{c^2}{\omega}\left(\frac{\partial^2 F_z}{\partial z^2} + \beta^2 F_z\right) = -j\frac{c^2}{\omega}\left(-\left(\beta_z^{TE}\right)^2 + \beta^2\right)F_z = j\frac{\left(\beta_c^{TE}\right)^2}{\omega\mu}F(x, y) \tag{2.2.30}$$

Likewise, the same procedure can be applied to a TM mode, expressed in terms of a scalar potential function $A(x, y)$. The scalar wave equation reduces to:

$$\nabla^2 A(x, y) + \left(\beta_c^{TM}\right)^2 A(x, y) = 0 \tag{2.2.31}$$

where

$$(\beta_c^{TM})^2 = \beta^2 - \left(\beta_z^{TM}\right)^2 \Rightarrow \beta_z^{TM} = \sqrt{\beta^2 - (\beta_c^{TM})^2} \tag{2.2.32}$$

Here β_c^{TM} gives the cutoff wave number, and eigenvalue, of a particular modal field and sets the TM modes propagation constant β_z^{TM}.

The scalar potential $A(x, y)$ is subject to boundary conditions at the walls. The tangential electric field must be zero at the interface between the guide's inner volume and the PEC wall. At the wall E_z is tangential to the wall for a uniform guide and as such must be zero:

$$E_z = -j\frac{c^2}{\omega}\left(\frac{\partial^2 A_z}{\partial z^2} + \beta^2 A_z\right) = -j\frac{c^2}{\omega}(-(\beta_z^{TM})^2 A_z + \beta^2 A_z) \\ = -j\frac{c^2}{\omega}\left(\beta_c^{TM}\right)^2 A_z = 0 \tag{2.2.33}$$

Consequently, for the tangential electric field to disappear on the contour of the guide ∂S it is necessary that:

$$A(x, y) = 0, \text{on } \partial S \tag{2.2.34}$$

This also ensures that the tangential component of the electric field at the wall is zero in the *xy*-plane.

Each modal field has an associated impedance which is given by the ratio of the orthogonal components of the mode's electric and magnetic fields:

$$Z^{TM} = \frac{E_x}{H_y} = -\frac{E_y}{H_x} \tag{2.2.35}$$

or in terms of the mode's propagation constant:

$$Z^{TM} = \frac{\beta_z^{TM}}{\epsilon\omega} = \frac{\beta_z^{TM}}{\epsilon c\beta} = \sqrt{\frac{\mu}{\epsilon}}\frac{\beta_z^{TM}}{\beta} = \frac{\beta_z^{TM}}{\beta} Z_0. \tag{2.2.36}$$

The transverse field components at $z = 0$ are given by:

$$\boldsymbol{E}^{t,TM} = \frac{\beta_z^{TM} c^2}{\omega} \nabla A(x,y) = Z^{TM} \nabla A(x,y) \tag{2.2.37}$$

$$\boldsymbol{H}^{t,TM} = \frac{1}{\mu} \nabla A_z \times \hat{\boldsymbol{z}} = \pm(-\nabla A(x,y) \times \hat{\boldsymbol{z}}) \tag{2.2.38}$$

and the remaining non-zero z-component is:

$$E_z^{TM} = -j\frac{c^2}{\omega}\left(\frac{\partial^2 A_z}{\partial z^2} + \beta^2 A_z\right) = -j\frac{c^2}{\omega}\left(-\left(\beta_z^{TM}\right)^2 + \beta^2\right) A_z = \pm j \frac{\left(\beta_c^{TM}\right)^2}{\omega\epsilon} A(x,y) \tag{2.2.39}$$

2.2.4 Modal Field Expansion

At a particular reference plane along the propagation axis of a waveguide, taken to be $z = 0$, the total electric and magnetic fields (representing a solution of the boundary value problem) are obtained as a linear combination of modal fields:

$$\boldsymbol{E}^t = \boldsymbol{E}_{all}^{t,TE} + \boldsymbol{E}_{all}^{t,TM} \tag{2.2.40}$$

$$\boldsymbol{H}^t = \boldsymbol{H}_{all}^{t,TE} + \boldsymbol{H}_{all}^{t,TM}, \tag{2.2.41}$$

where

$$\boldsymbol{E}_{all}^{t,TE} = \sum_i \left(a_i^{TE,+} \boldsymbol{E}_i^{t,TE,+} + a_i^{TE,-} \boldsymbol{E}_i^{t,TE,-}\right) \tag{2.2.42}$$

$$\boldsymbol{E}_{all}^{t,TM} = \sum_i \left(a_i^{TM,+} \boldsymbol{E}_i^{t,TM,+} + a_i^{TM,-} \boldsymbol{E}_i^{t,TM,-}\right) \tag{2.2.43}$$

$$\boldsymbol{H}_{all}^{t,TE} = \sum_i \left(a_i^{TE,+} \boldsymbol{H}_i^{t,TE,+} + a_i^{TE,-} \boldsymbol{H}_i^{t,TE,-}\right) \tag{2.2.44}$$

$$\boldsymbol{H}_{all}^{t,TM} = \sum_i \left(a_i^{TM,+} \boldsymbol{H}_i^{t,TM,+} + a_i^{TM,-} \boldsymbol{H}_i^{t,TM,-}\right) \tag{2.2.45}$$

As before $(\pm)$ superscripts indicate forward and backward propagating waves respectively and a_n^X is the mode's amplitude. The number of modes is infinite (Olver et al. 2011), but in practice only a finite subset of all modes is required to achieve sufficient accuracy.

Each mode has a cut-off frequency:

$$f_c = \frac{1}{2\pi}\sqrt{\mu\epsilon}\beta_c \qquad (2.2.46)$$

Above this frequency β_z is real. For fixed mode amplitude a change of position along the *z*-axis changes the phase of the modal fields but not their magnitude provided there is no mechanism for loss i.e. uniform hollow PEC guide. The mode is said to be propagating, and its field configuration is consistent with real power flux along the *z*-axis. On the other hand if $f < f_c$, β_z becomes imaginary and the magnitude of modal fields decays exponentially with position. The mode is said to be non-propagating, or evanescent. Evanescent modes carry only imaginary power.

The impact of highly evanescent modes on power propagation is necessarily localised, because of their high rate of decay. As such their contribution to the overall propagating solution becomes asymptotically negligible, once their cut-off frequency is sufficiently greater than the operating frequency. Conventionally, the number of TE and TM modes that are included in the modal expansion is limited to N^{TE} and N^{TM}. This finite subset includes modes effectively contributing to the overall field. Furthermore, the transverse field components can be expressed using the scalar potentials as follows:

$$\boldsymbol{E}^t \cong \sum_i^{N_{TE}} \left(a_i^{TE,+} + a_i^{TE,-}\right) \nabla F_i(x,y) \times \hat{\boldsymbol{z}} + \sum_j^{N_{TM}} \left(a_i^{TM,+} + a_i^{TM,-}\right)\, Z_j^{TM} \nabla A_j(x,y) \qquad (2.2.47)$$

$$\boldsymbol{H}^t \cong \sum_i^{N_{TE}} \left(a_i^{TE,+} - a_i^{TE,-}\right) Y_i^{TE} \nabla F_i(x,y) + \sum_j^{N_{TM}} \left(-a_i^{TM,+} + a_i^{TM,-}\right) \nabla A_j(x,y) \times \hat{\boldsymbol{z}} \qquad (2.2.48)$$

2.2.5 Modal Power Normalisation

For a unit amplitude each mode carries certain complex power. This can be used to apply consistent normalisation to individual modes. The total complex power carried by the mode is obtained from the integral flux of the Poynting vector over the cross-section of the guide:

$$P_m(S) = \int_S \left(\frac{1}{2}\boldsymbol{E}_m \times \boldsymbol{H}_m^*\right) \cdot d\boldsymbol{S}, \tag{2.2.49}$$

where the $\boldsymbol{E}_m$ and $\boldsymbol{H}_m$, are the transverse electric and magnetic fields for the mode.

The complex modal power for a nominally forward propagating TE mode is given by:

$$P_m^{TE}(S) = +\frac{1}{2}\int_S \left((\nabla F_m(x,y) \times \hat{\boldsymbol{z}}) \times (Y_m^{TE} \nabla F_m(x,y))^*\right) \cdot d\boldsymbol{S} \tag{2.2.50}$$

Since the cross-section S is orthogonal to the *z*-axis:

$$P_m^{TE}(S) = +\frac{1}{2} Y_m^{TE^*} \int_S \left(\nabla F_m(x,y)^* \cdot \nabla F_m(x,y)\right) dS = +\frac{1}{2} Y_m^{TE^*} D_{mm}, \tag{2.2.51}$$

where

$$D_{ij} = \langle \nabla F_i | \nabla F_j \rangle = \int_S \left(\nabla F_m(x,y)^* \cdot \nabla F_m(x,y)\right) dS \tag{2.2.52}$$

Similarly, for a forward propagating TM mode, the complex modal power is:

$$P_m^{TM}(S) = +\frac{1}{2}\int_S \left((Z_m^{TM} \nabla A_m(x,y)) \times (\nabla A_m(x,y) \times \hat{\boldsymbol{z}})^*\right) \cdot d\boldsymbol{S} \tag{2.2.53}$$

$$P_m^{TM}(S) = +\frac{1}{2} Z_m^{TM} \int_S \left(\nabla A_m(x,y)^* \cdot \nabla A_m(x,y)\right) dS = +\frac{1}{2} Z_m^{TM}\, C_{mm}, \tag{2.2.54}$$

where

$$C_{ij} = \langle \nabla A_i | \nabla A_j \rangle = \int_S \left(\nabla A_m(x,y)^* \cdot \nabla A_m(x,y) \right) dS \qquad (2.2.55)$$

Here D_{mm} and C_{mm} give the frequency-independent modal power factors for TE and TM modes respectively. These integrals correspond to self-coupling of modes within a uniform waveguide, and their value can be determined analytically for common waveguide cross-sections.

The power carried by a TE or TM mode also depends on the modal admittance or impedance respectively. These quantities are proportional to the mode's propagation constant (equations (2.2.27) and (2.2.36)). Their value is real for propagating modes, imaginary for evanescent modes and zero at the cut-off frequency:

$$Y^{TE} = +\frac{Y_0 \beta_z}{\beta} = \begin{cases} \frac{Y_0}{\beta}\sqrt{\beta^2 - \beta_c^2}\,, \text{for } f > f_c \\ 0\,, \text{for } f_c = f \\ -\frac{jY_0}{\beta}\sqrt{\beta_c^2 - \beta^2}, \text{for } f < f_c \end{cases} \qquad (2.2.56)$$

$$Z^{TM} = +\frac{Z_0 \beta_z}{\beta} = \begin{cases} \frac{Z_0}{\beta}\sqrt{\beta^2 - \beta_c^2}\,, \text{for } f > f_c \\ 0\,, \text{for } f_c = f \\ -\frac{jZ_0}{\beta}\sqrt{\beta_c^2 - \beta^2}, \text{for} f < f_c \end{cases} \qquad (2.2.57)$$

In past implementations of the mode matching method, such as (Kalinauskaitė and Murphy 2018), modes were strictly normalised to unit power magnitude ($+1$ Watt for propagating modes, $+j$ Watt for evanescent TE modes and $-j$ Watt for evanescent TM modes). However, modes cannot strictly be normalised this way at their cut-off frequency. Even close to cut-off numerical implementations can suffer from instability, due to an abrupt step from unit imaginary to real power as the character of the mode changes.

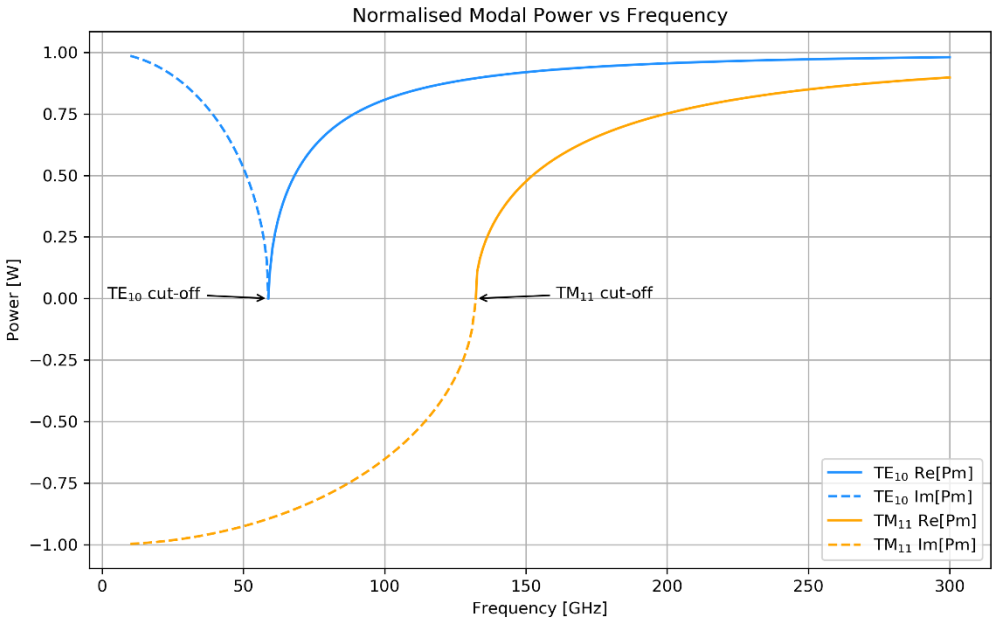

Figure 2-3: Illustration of the new frequency dependent approach to mode normalisation. Below cut-off modes are evanescent carrying imaginary power only, as they pass through their respective cut-off frequencies there is a smooth transition from complex to real power through zero as required. The values shown are for modes in WR10 waveguide section

This can be avoided by normalising the mode to a unit power magnitude asymptotically, far from its cut-off frequency, by passing the magnitude of modal power through zero as the frequency passes through the cut-off, as exemplified in Figure 2-3. The character of modal power, that is whether the value is real or positive imaginary, or negative imaginary, remains unchanged.

In this work modes are normalised to have the following magnitude of power:

$$P^{TE}_{norm\,mag} = \begin{cases} \dfrac{Y^{TE}}{Y_0} \text{ for } f \geq f_c \\ \sqrt{\dfrac{\beta^2}{\beta_c^2}}\dfrac{|Y^{TE}|}{Y_0} \text{ for } f < f_c \end{cases}$$

$$P^{TM}_{norm\,mag} = \begin{cases} \dfrac{Z^{TM}}{Z_0} \text{ for } f \geq f_c \\ \sqrt{\dfrac{\beta^2}{\beta_c^2}}\dfrac{|Z^{TM}|}{Z_0} \text{ for } f < f_c \end{cases}$$

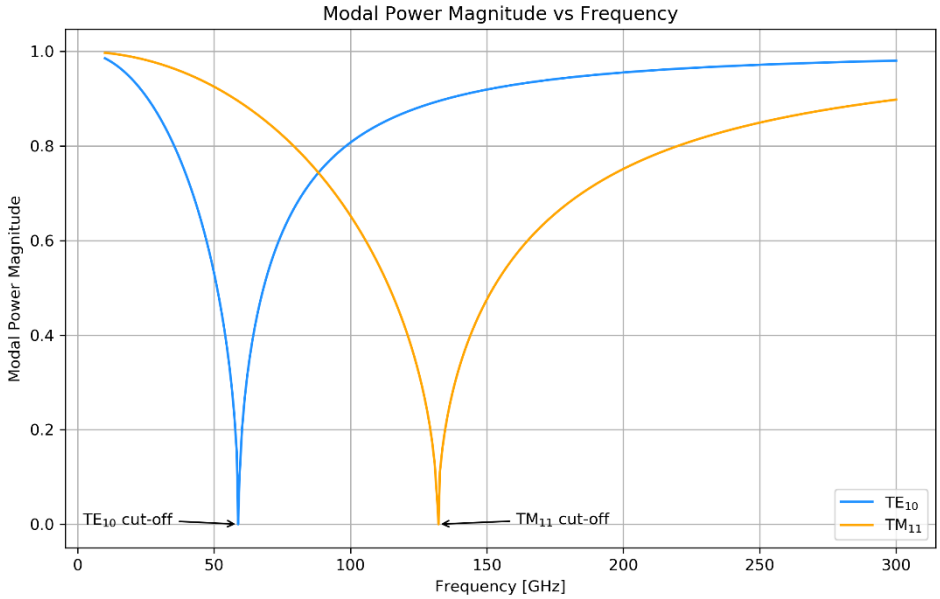

Figure 2-4: Modal power magnitude as a function of frequency. For frequencies far away from cut-off complex modal power tends towards $\pm j$ for evanescent modes and +1 for propagating modes, as shown in Figure 2-3

2.3 Rectangular and Cylindrical Waveguides

In this section the specific boundary conditions posed by uniform rectangular or cylindrical waveguide sections are considered. The expressions for scalar potential functions $F(x, y)$ and $A(x, y)$ that satisfy equations (2.2.23) and (2.2.31), respectively, are derived. As shown, these potentials functions give the modal transverse field components consistent with the guide's cross-section.

2.3.1 Uniform Rectangular Waveguides

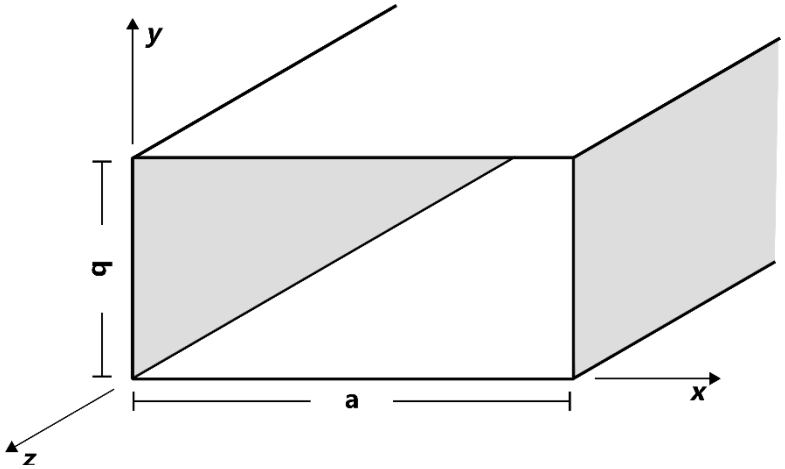

*Figure 2-5: Geometry of the model rectangular waveguide section with dimensions (*a,b*) orientated with respect to the propagation direction z.*

A uniform rectangular guide section is defined by dimensional parameters (a, b) that give the guide's width and height. At a given frequency the number of guide modes propagating will be limited by these dimensions. With set boundaries, the form of the scalar potential $F(x, y)$ and $A(x, y)$ can be found. The general boundary condition requires the tangential electric field to be zero at the walls. Thus, the boundary conditions for the rectangular waveguide are given by:

$$E_x(0 \le x \le a, y = 0 \text{ or } b, z) = 0 \qquad E_z(0 \le x \le a, y = 0 \text{ or } b, z) = 0 \qquad (2.3.1)$$

$$E_y(x = 0 \text{ or } a, 0 \le y \le b, z) = 0 \qquad E_z(x = 0 \text{ or } a, 0 \le y \le b, z) = 0 \qquad (2.3.2)$$

where the limits in equation (2.3.1) provide the boundary conditions for the top and bottom of the guide, while equation (2.3.2) governs the left and right boundaries.

With set (x, y) boundaries, the separation-of-variables method can be completed for the scalar potential function $F_z(x, y, z)$ such that:

$$F_z(x, y, z) = F(x, y)h(z) = f(x)g(y)h(z) \tag{2.3.3}$$

In section 2.2.3, the scalar potential $F_z(x, y, z)$ has a *z*-dependency that takes the form of a traveling waves. As the guide is bound in both *x* and *y* directions the form of the remaining transverse components must take the form of standing waves. Thus, the holding solution in equation (2.3.3) is expressed with a more appropriate set of function equations that describe the standing and traveling wave components.

$$f(x) = C_1 \cos(\beta_x x) + D_1 \sin(\beta_x x) \tag{2.3.4}$$

$$g(y) = C_2 \cos(\beta_y y) + D_2 \sin(\beta_y y) \tag{2.3.5}$$

$$h(z) = A_3 e^{-j\beta_z z} + B_3 e^{j\beta_z z} \tag{2.3.6}$$

The forward traveling scalar potential $F_z(x, y, z)$ can then be substituted into equations (2.2.2) and (2.2.4), and gives the TE mode's electric field components as

$$E_x^+(x, y, z) = -A_3 \frac{\beta_y}{\epsilon} [C_1 \cos(\beta_x x) + D_1 \sin(\beta_x x)][-C_2 \sin(\beta_y y) + D_2 \cos(\beta_y y)] e^{-j\beta_z z} \tag{2.3.7}$$

$$E_y^+(x, y, z) = -A_3 \frac{\beta_x}{\epsilon} [-C_1 \sin(\beta_x x) + D_1 \cos(\beta_x x)][C_2 \cos(\beta_y y) + D_2 \sin(\beta_y y)] e^{-j\beta_z z} \tag{2.3.8}$$

The boundary conditions along the guide walls are given by equations (2.3.1) - (2.3.2). The trivial solutions for these boundary conditions are $D_1 = D_2 = 0$. The non-trivial solutions for the given boundary conditions require that $\sin(\beta_y b) = 0$ and $\sin(\beta_x a) = 0$, with solutions:

$$\beta_x = \frac{m\pi}{a} \text{ and } \beta_y = \frac{n\pi}{b} \text{ for } m, n \in \mathbb{Z}^+ \cup \{0\}, \tag{2.3.9}$$

where β_x and β_y represent the transverse wavenumbers consistent with the boundary conditions. Applying these solutions, the electric field components reduce to:

$$E_x^+ = -A_3 \frac{\beta_y}{\epsilon} [C_1 \cos(\beta_x x)]\left[-C_2 \sin\left(\beta_y y\right)\right] e^{-j\beta_z z} \tag{2.3.10}$$

$$E_y^+ = A_3 \frac{\beta_x}{\epsilon} [-C_1 \sin(\beta_x x)]\left[C_2 \cos\left(\beta_y y\right)\right] e^{-j\beta_z z} \tag{2.3.11}$$

Thus, the scalar potential function, $F_z^+(x, y, z)$, can be expressed in the following form:

$$F_z^+(x, y, z) = A_{mn} \cos(\beta_x x) \cos\left(\beta_y y\right) e^{-j\beta_z z} \tag{2.3.12}$$

where A_{mn} is obtained by expressing the remaining constant values as a single normalisation factor. In a similar manner the magnetic scalar potential function $A_z(x, y, z)$ can be shown to be:

$$A_z^+(x, y, z) = B_{mn} \sin(\beta_x x) \sin\left(\beta_y y\right) e^{-j\beta_z z} \tag{2.3.13}$$

The eigenvalue of the wave equation in both cases is given by:

$$\beta_c^2 = \beta_x^2 + \beta_y^2 = \left(\frac{m\pi}{a}\right)^2 + \left(\frac{n\pi}{b}\right)^2 \tag{2.3.14}$$

Each rectangular waveguide mode is indexed by a pair of integer values m, n shown in equation (2.3.9), such that the transverse electric and magnetic modes are in general expressed as TE_{mn} or TM_{mn}. The indices are subject to some restrictions. For TE modes both mode indices m, n cannot be zero at the same time. For TM modes (in a rectangular guide) m, n must be non-zero. Otherwise, the scalar potential becomes constant and all components given by the electric and magnetic fields vanish. The cutoff frequency can be expressed in terms of the eigenvalues derived as shown below:

$$f_c = \frac{1}{2\pi}\sqrt{\mu\epsilon}\,\beta_c = \frac{1}{2\pi}\sqrt{\mu\epsilon}\,\sqrt{\beta_x^2 + \beta_y^2} \qquad (2.3.15)$$

For TE and TM modes their electric field components, as in equations (2.2.28) - (2.2.29) and (2.2.37) - (2.2.38) respectively, are obtained from the complete form of the scalar potential functions letting $A_{mn} = 1$. The electric field components for TE and TM modes are then given by:

$$\boldsymbol{E}^{t,TE} = \left(-\beta_x \sin(\beta_x x)\cos(\beta_y y)\right)\hat{\boldsymbol{x}} + \left(-\beta_y \cos(\beta_x x)\sin(\beta_y y)\right)\hat{\boldsymbol{y}} \qquad (2.3.16)$$

$$\boldsymbol{E}^{t,TM} = \left(\beta_x \cos(\beta_x x)\sin(\beta_y y)\right)\hat{\boldsymbol{x}} + \left(\beta_y \sin(\beta_x x)\cos(\beta_y y)\right)\hat{\boldsymbol{y}} \qquad (2.3.17)$$

Furthermore, the modal powers of TE and TM modes can be derived analytically from their resulting fields. The modal power, given in equations (2.2.51) and (2.2.54) corresponds to self-coupling modes within uniform waveguides. The modal power magnitude expression for the rectangular TE modes (D_{ij}) is:

$$D_{ij} = \left(\beta_{c,i}^{TE}\right)^2 \delta_{ij} \int_0^a \int_0^b \cos^2(\beta_{x,i}x)\cos^2(\beta_{y,i}y)\,dydx \qquad (2.3.18)$$

$$= \left(\beta_{c,i}^{TE}\right)^2 \delta_{ij} \left(\frac{a}{2} + \frac{\sin(2\beta_{x,i}a)}{4\beta_{x,i}}\right)\left(\frac{b}{2} + \frac{\sin(2\beta_{y,i}b)}{4\beta_{y,i}}\right) \qquad (2.3.19)$$

$$= \left(\left(\frac{m_i\pi}{a}\right)^2 + \left(\frac{n_i\pi}{b}\right)^2\right)\left(\frac{ab}{4}\right)(1+\delta_{m_i,0})(1+\delta_{n_i,0})\delta_{ij} \qquad (2.3.20)$$

and for TM (C_{ij}) modes:

$$C_{ij} = \left(\beta_{c,i}^{TM}\right)^2 \delta_{ij} \int_0^a \int_0^b \sin^2(\beta_{x,i}x)\sin^2(\beta_{y,i}y)\,dydx \qquad (2.3.21)$$

$$= \left(\left(\frac{m_i\pi}{a}\right)^2 + \left(\frac{n_i\pi}{b}\right)^2\right)\left(\frac{ab}{4}\right)\delta_{ij} \qquad (2.3.22)$$

A selection of modal fields that exist in a rectangular waveguide section are presented in Figure 2-6. The field distribution of the fundamental TE_{10} mode (fundamental mode) is shown along with a few higher order modes which are either TE or TM.

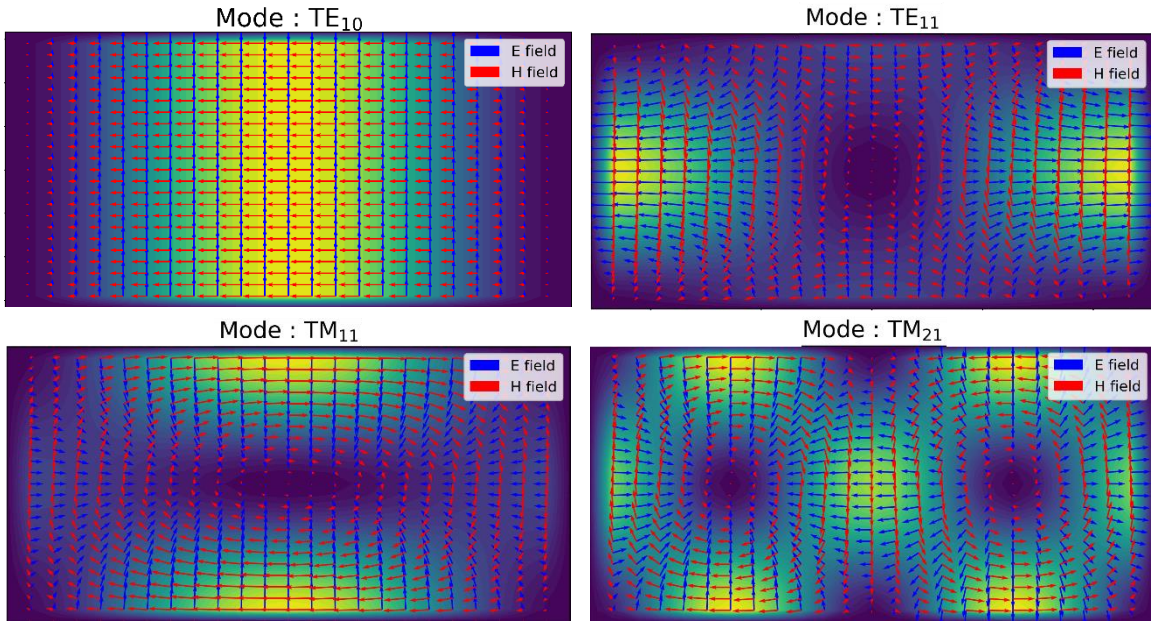

Figure 2-6: Shows an example of the modal fields which are supported in the uniform rectangular guide section.

2.3.2 Uniform Cylindrical Waveguides

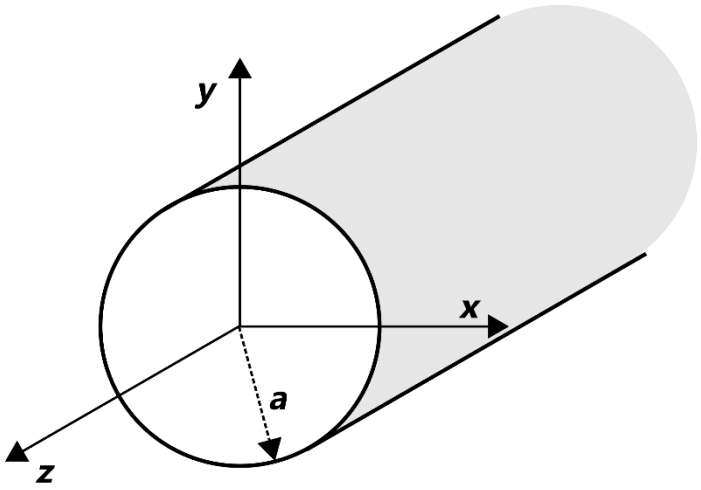

Figure 2-7 Details the geometry of the cylindrical waveguide section of radius (a) orientated with respect to the propagation direction z

In this section the same procedure as in section 2.3.1 is followed to describe the modal fields within cylindrical waveguide sections. However, because of the symmetry of the problem's geometry it is convenient to change coordinate systems from Cartesian to cylindrical coordinates. The cylindrical guide's cross-section, shown in Figure 2-7, is described by a single dimensional parameter (a) that gives the guide's radius. The boundary conditions require that the tangential electric field be zero at the guide walls:

$$E_\phi(\rho = a, \phi, z) = 0 \qquad (2.3.23)$$

Moreover, the fields must be finite within the guide and have a minimum periodicity in ϕ of 2π.

In the cylindrical case the scalar potential function $F_z(x, y, z)$ becomes $F_z(\rho, \phi, z)$, the separation-of-variables method can be completed for the scalar potential function $F_z(\rho, \phi, z)$ such that:

$$F_z(\rho, \phi, z) = f(\rho)g(\phi)h(z) \qquad (2.3.24)$$

The scalar potential is sought with a z-dependence given by equation (2.2.19). As the guide is bound in the radial directions the form of the radial terms represent standing waves given by

the first and second kind of the Bessel function, while the cosine and sine terms represent periodic waves which naturally have the periodicty required in ϕ (C. A. Balanis 2012). Thus, the holding solution in equation (2.3.24) can be expressed with a more appropriate set of functions that describe the standing and traveling wave components.

$$f(\rho) = A_1 J_m(\beta_\rho \rho) + B_1 Y_m(\beta_\rho \rho) \tag{2.3.25}$$

$$g(\phi) = C_2 \cos(m\phi) + D_2 \sin(m\phi) \tag{2.3.26}$$

$$h(z) = A_3 e^{-j\beta_z z} + B_3 e^{j\beta_z z} \tag{2.3.27}$$

From properties of the Bessel function constant B_1 must be equal to zero since $Y_m(\rho = 0) = \infty$, and the field must remain finite within the guide:

$$f(\rho) = A_1 J_m(\beta_\rho \rho) \tag{2.3.28}$$

$$g(\phi) = C_2 \cos(m\phi) + D_2 \sin(m\phi) \tag{2.3.29}$$

$$h(z) = A_3 e^{-j\beta_z z} + B_3 e^{j\beta_z z} \tag{2.3.30}$$

The forward traveling scalar potential $F_z(\rho, \phi, z)$ can then be substituted into equation (2.2.28), and gives the TE mode's electric field components as:

$$\nabla F_z(\rho, \phi, z) = \frac{\partial F_z}{\partial \rho}\hat{\boldsymbol{\rho}} + \frac{1}{\rho}\frac{\partial F_z}{\partial \phi}\hat{\boldsymbol{\phi}} + \frac{\partial F_z}{\partial z}\hat{\mathbf{z}} \tag{2.3.31}$$

$$E_\phi^+(\rho = a, \phi, z) = \beta_\rho \frac{A_{mn}}{\epsilon} J'_m(\beta_\rho a)\,[C_2 \cos(m\phi) + D_2 \sin(m\phi)] e^{-j\beta_z z} \tag{2.3.32}$$

The required boundary condition, $E_\phi(\rho = a, \phi, z) = 0$, is only satified provided $J'_m(\beta_\rho a) = 0$ which can only occur for:

$$\beta_\rho = \frac{\chi'_{mn}}{a} \tag{2.3.33}$$

where χ'_{mn} is the n^{th} root ($n = 1,2, ...$) of the derivative of the Bessel function J'_m of the first kind and of order m ($m = 0,1,2, ...$). The scalar potential function can be expressed in the form of two orthogonal solutions given by:

$$F_z^+(\rho, \phi, z) = A_{mn} J_m(\beta_\rho \rho) \begin{pmatrix} \cos(m\phi) \\ \sin(m\phi) \end{pmatrix} e^{-j\beta_z z} \tag{2.3.34}$$

Applying the same treatment to the transverse magnetic field, a similar expression for $A_z^+(\rho, \phi, z)$ is obtained, again in the form of two orthogonal solutions:

$$A_z^+(\rho, \phi, z) = B_{mn} J_m(\beta_\rho \rho) \begin{pmatrix} \cos(m\phi) \\ \sin(m\phi) \end{pmatrix} e^{-j\beta_z z} \tag{2.3.35}$$

where $\beta_\rho = \frac{\chi_{mn}}{a}$ where χ_{mn} is the n^{th} root ($n = 1,2, ...$) of the Bessel function J_m of the first kind and of order m ($m = 0,1,2, ...$). The two orthogonal solutions also define the modes polarisation direction, either cosine or sine i.e. $\text{TE}_{11\text{c}}$ or $\text{TE}_{11\text{s}}$.

The general equation for the cutoff frequency for either the transverse electric or magnetic modes is given as:

$$\beta_c = \beta_\rho \Rightarrow f_c = \frac{\beta_\rho}{2\pi\sqrt{\mu\epsilon}} \tag{2.3.36}$$

Furthermore, the modal powers factors of TE and TM modes can be derived analytically from their resulting fields. The modal power, given in equations (2.2.51) and (2.2.54) correspond to self-coupling modes within uniform waveguides. Below the modal power magnitude factors for the cylindrical TE modes (D_{ij}) are:

$$D_{ij} = \left(\beta_{c,i}^{TE}\right)^2 \delta_{ij} \int_S (F_i)^2 dS \tag{2.3.37}$$

$$D_{ij} = \left(\beta_{c,i}^{TE}\right)^2 \delta_{ij} \int_0^a \int_0^{2\pi} J_{m_i}^2(\beta_{\rho,i}\rho) \begin{pmatrix} \sin(m\phi)^2 \\ \cos(m\phi)^2 \end{pmatrix} \rho d\rho d\phi \tag{2.3.38}$$

$$= \left(\beta_{c,i}^{TE}\right)^2 \delta_{ij} \pi \left(1 + \delta_{mi,0}\right) \int_0^a \rho\, J_{m_i}^2(\beta_{\rho,i}\rho) d\rho \tag{2.3.39}$$

$$= \left(\beta_{c,i}^{TE}\right)^2 \delta_{ij} \pi \left(1 + \delta_{mi,0}\right) \int_0^1 at\, J_{m_i}^2(\chi'_{mn}t) a dt \tag{2.3.40}$$

To reduce the integral involving the Bessel function, to standard form it is necessary to consider the integral identity along with the Bessel recurrence relations (F. W. Olver et al. 2017):

$$\int_a^b x J_m^2(cx) dx = \frac{x^2}{2} \left[J_m^2(cx) - J_{m-1}(cx) J_{m+1}(cx)\right]_b^a \tag{2.3.41}$$

$$\frac{2mJ_m(x)}{x} = J_{m-1}(x) + J_{m+1}(x) \tag{2.3.42}$$

$$2J'_m(x) = J_{m-1}(x) - J_{m+1}(x) \tag{2.3.43}$$

Applying the integral identity and the appropriate recurrence relations an analytic solution may be obtained in standard form as:

$$D_{ij} = \left(\frac{\chi'_{m,n}}{a}\right)^2 \delta_{ij} \pi \left(1 + \delta_{mi,0}\right) a^2 \left[\frac{1}{2\chi'^2_{m,n}} \left(\chi'^2_{m,n} - m^2\right) J_{m_i}^2(\chi'_{mn})\right] \tag{2.3.44}$$

$$= \frac{\delta_{ij} \pi \left(1 + \delta_{mi,0}\right)}{2} \left(\chi'^2_{m,n} - m^2\right) J_{m_i}^2(\chi'_{mn}) \tag{2.3.45}$$

The modal power magnitude factors for TM modes (C_{ij}) are:

$$C_{ij} = \left(\beta_{c,i}^{TM}\right)^2 \delta_{ij} \int_S (A_i)^2 dS \tag{2.3.46}$$

$$= \left(\beta_{c,i}^{TM}\right)^2 \delta_{ij} \int_0^a \int_0^{2\pi} J_{m_i}^2(\beta_{\rho,i}\rho) \begin{pmatrix} \sin(m\phi)^2 \\ \cos(m\phi)^2 \end{pmatrix} \rho d\rho d\phi \tag{2.3.47}$$

$$= \frac{\delta_{ij}\pi\left(1+\delta_{mi,0}\right)\chi_{mn}^2}{2} J_{m_i}^2(\chi'_{mn}) \tag{2.3.48}$$

Cylindrical modes are indexed by integer values m and n and a polarisation index which selects either cosine or sine modulation in ϕ (denoted by c or s respectively). In most cases there exist two valid orthogonal solutions for each set of m, n indices as shown in equations (2.3.34) and (2.3.35). For $m = 0$, only one non-trivial solution exists, the cosine solution for both TE and TM modes. An example of the modal fields which can exist in cylindrical waveguides is shown in Figure 2-8.

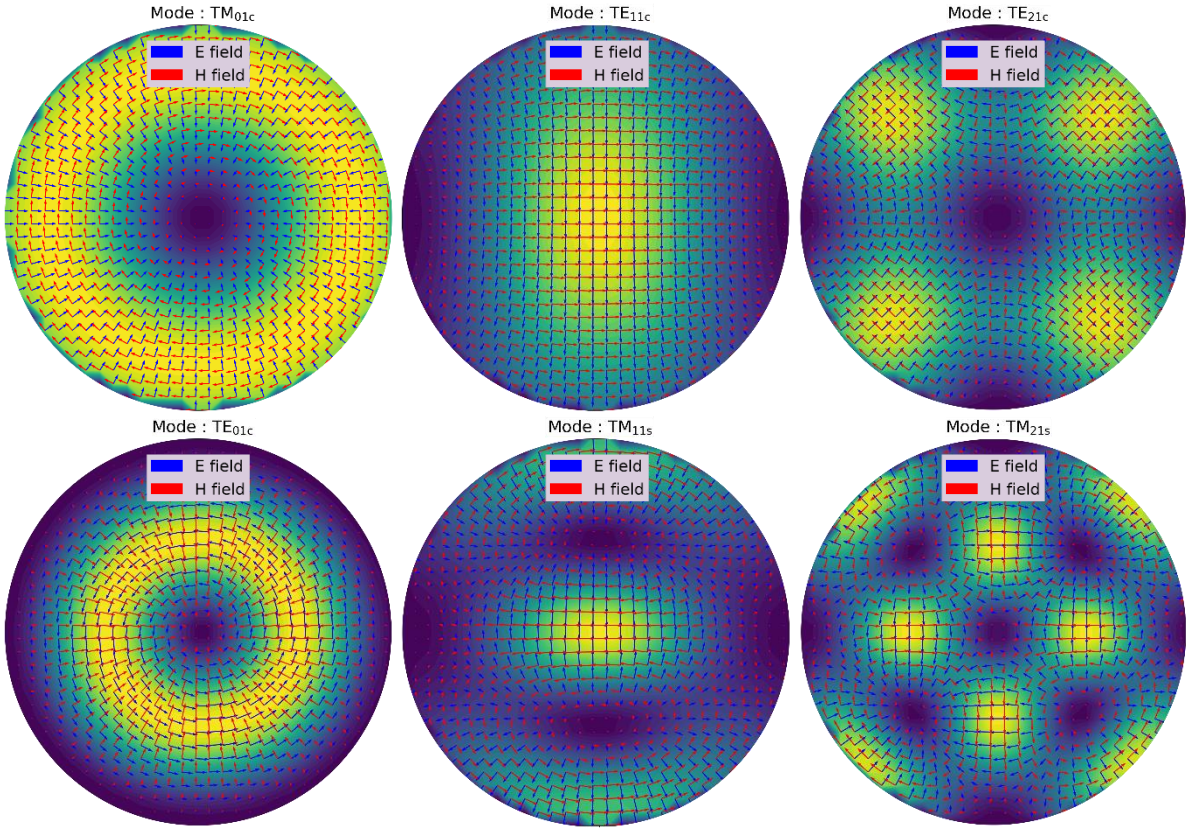

Figure 2-8: Shows an example of the modal fields which are supported in the uniform cylindrical guide section.

The relationship between the modal electric field and its potential is different for TE and TM modes, their polarisation indices must be opposite for the electric field to be aligned in the same direction. Coupling between TE and TM modes is much more likely to occur if their fields point in the same direction. In Figure 2-9, the TE_{11c} and TM_{11s} have their electric field in the same direction so there is a potential for coupling (this is not the case for TE_{11c} and TM_{11c}).

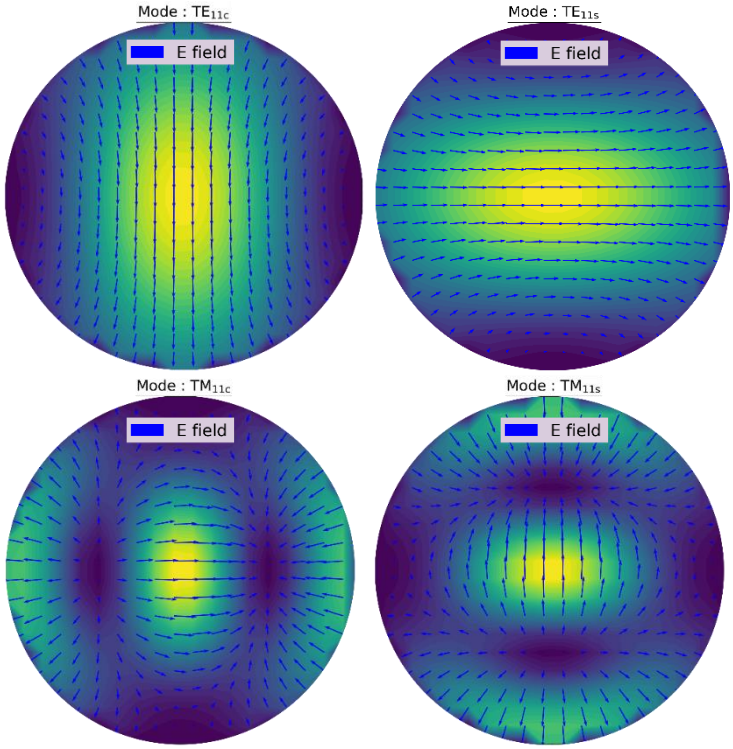

Figure 2-9 Shows the cylindrical waveguide modes, for counter-polarised modes, with E-field lines present only

2.3.3 Scattering Operators

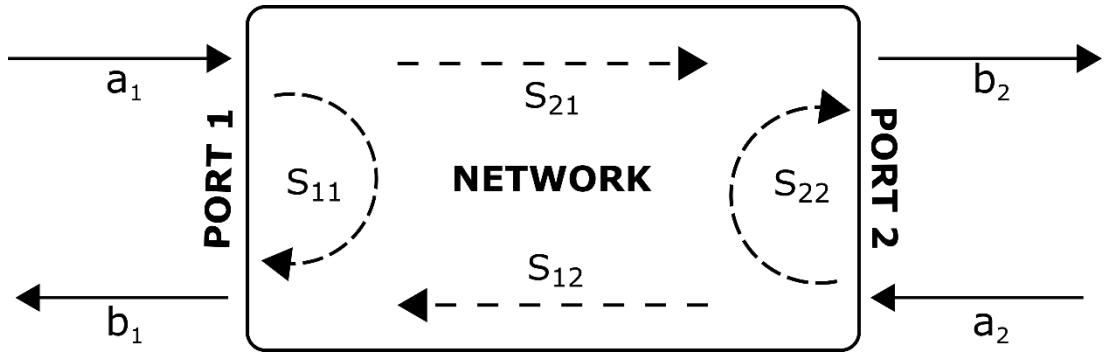

Figure 2-10 A schematic overview of the network arrangement of a two-port device. At each port there exist incoming and outgoing amplitudes "a" *and* "b" *respectively. The relationship between these amplitudes is governed by the reflection and transmission through the network as represented by the s-parameters.*

Each guide section can be represented by its own scattering matrix $\boldsymbol{S}$, this matrix describes the power coupling between guide modes at the different ports which compose the network (Olver et al. 2011). In Figure 2-10, this network section has only two ports and is said to be a two-port network. The scattering matrix is a matrix of size $m \times m$ where m is the number of ports in the network. The elements that compose the scattering matrix are known as scattering parameters or s-parameters, which describe the mode coupling at particular ports. Here these ports are defined arbitrarily at planes within a length of a guide section. Conventionally ports would be at the beginning and end of a network where there is a transition i.e. to a VNA head or free-space. The $\boldsymbol{S}_{11}$ and $\boldsymbol{S}_{22}$ s-parameters describe the power reflected from port 1 and 2 respectively for a given excitation at the port. In contrast, $\boldsymbol{S}_{12}$ and $\boldsymbol{S}_{21}$ give the power transmitted between ports. For some stimulus applied to the network, the transfer of power is described by:

$$\begin{bmatrix} \boldsymbol{b}_1 \\ \boldsymbol{b}_2 \end{bmatrix} = [\boldsymbol{S}] \begin{bmatrix} \boldsymbol{a}_1 \\ \boldsymbol{a}_2 \end{bmatrix} = \begin{bmatrix} \boldsymbol{S}_{11} & \boldsymbol{S}_{12} \\ \boldsymbol{S}_{21} & \boldsymbol{S}_{22} \end{bmatrix} \begin{bmatrix} \boldsymbol{a}_1 \\ \boldsymbol{a}_2 \end{bmatrix} \qquad (2.3.49)$$

Above, the terms $\boldsymbol{a}_1$ and $\boldsymbol{a}_2$ are column vectors which give the input mode amplitudes at port 1 and 2 respectively while the column vectors $\boldsymbol{b}_1$ and $\boldsymbol{b}_2$ give the outgoing mode amplitudes that are obtained by solving equation (2.3.49).

Fields in a uniform PEC guide section are described by a set of propagating and evanescent modes (TE and TM). As the guide is uniform throughout and the walls are idealised, there is

no back-scattering or reflection from this guide. Thus, the scattering parameters which describe the power reflected from the network's ports must be zero i.e. $\boldsymbol{S}_{11} = \boldsymbol{S}_{22} = \boldsymbol{0}$. Since the guide is uniform the modes present may only couple bijectively to themselves. As such, the transmission scattering parameters $\boldsymbol{S}_{12}$ and $\boldsymbol{S}_{21}$ must be purely diagonal matrices. Consequently, since there is no mechanism for loss i.e. zero reflection of power, once the mode is fully propagating there will be lossless transmission of power in that mode. Each mode has a phase delay introduced by its respective propagation constant β_i. The transmission scattering parameters are described by:

$$[\boldsymbol{S}_{21}] = [\boldsymbol{S}_{12}] = [\boldsymbol{V}] = [\delta_{mn} e^{-\beta_m l}] \qquad (2.3.50)$$

Where represents δ_{mn} the diagonal modes self-coupled power. In Figure 2-11, the simulated scattering parameters for an example waveguide section are shown. There is no reflection component shown as a null result is obtained from both CST and S-TNG simulation and full transmission is achieved once the mode is propagating i.e. $f > f_c$.

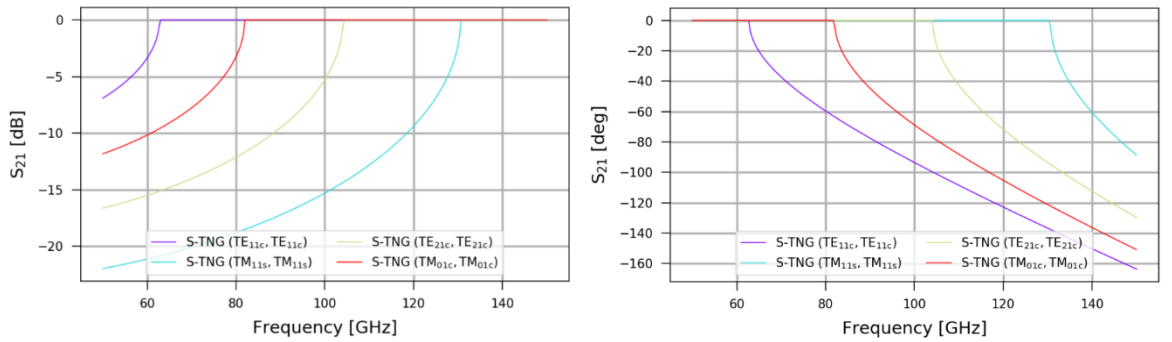

Figure 2-11 : Scattering parameters for a uniform cylindrical guide section of radius 1.4 mm. Zero reflection is obtained from simulation results of this section and full transmission is observed once the mode begins fully propagating.

2.4 Mode Matching in PEC guides

Mode matching methods are required at step discontinuities (junctions) between waveguide sections, to ensure that the overall propagation is modelled correctly (Olver et al. 2011). The mode matching technique matches the total transverse fields, carried by individual modes, on both sides of a junction. The transverse fields must be matched at this interface such that the conservation of complex power for incident modes is maintained (Figlia and Gentili 2002). The coupling between modes is highly dependent on the symmetry at the discontinuity, for concentric guides section coupling will occur between modes of same azimuthal orders only.

If symmetry is broken this behaviour is not guaranteed. Junction configurations where one guide is fully retained in the others cross-section are only discussed.

In such a junction, the two guides will be referred to as '*Left*' and '*Right*' or *L* and *R* at $z = 0$. The order of the guides, with cross-sections S_L & S_R is such that $S_L \subset \mathrm{S_R}$. The common cross section of the two guides is $\Omega = \mathrm{S_L} \cap S_R$ and the region defined by $\Sigma = (S_L \cup S_R) - \Omega$ represents an overlap between S_R and a PEC material bounding S_L. Here, since guide *L* and *R* are ordered "small" to "large", $S_L = \Omega$. The general boundary conditions required for transverse fields at the PEC junction are:

$$\boldsymbol{E}_L = \boldsymbol{E}_R, \text{on } \Omega \qquad (2.4.1)$$

$$\boldsymbol{H}_L = \boldsymbol{H}_R, \text{on } \Omega \qquad (2.4.2)$$

$$\boldsymbol{E}_L = \boldsymbol{E}_R = 0, \text{on } \Sigma \qquad (2.4.3)$$

The electric and magnetic fields on both sides of the interface must be equal (continuous). By definition the electric field in the left and right guide must be zero over Σ.

From section 2.2.4, the complete set of functions which span any transverse electric or magnetic fields are the set of corresponding modal TE and TM fields, shown in equations and (2.2.47) and (2.2.48). In guide *R*, the complete set of functions required to span the electric field are given by $(\nabla F_i^{\mathrm{R}} \times \hat{\boldsymbol{z}}, Z_j^{TM} \nabla A_j^R)$. Here the super-script "*R*" refers to the cross-section of guide *R* while the terms i, j denote the modes index of the TE and TM modes respectively. The electric field in guide *L* is spanned by the same function set, as the fields must match on Ω. Likewise, the complete set of functions which span any transverse magnetic field is the set of modal TE and TM magnetic fields, given in guide *L* as $(Y_i^{TE} \nabla F_i^{\mathrm{L}}, \nabla A_j^L \times \hat{\boldsymbol{z}})$.

A scalar product $\left(P = \int_S \boldsymbol{A}^{t^*} \cdot \boldsymbol{B}^t \, dS\right)$ can be defined for the transverse fields. In PEC junctions, the potentials can be made real valued so the conjugation is not strictly necessary. For continuous fields at the interface, the scalar product with the appropriate base functions can be determined. Furthermore, in each case the mapping of modal power across the junction through mode coupling paths (TE − TE, TE − TM, TM − TE and TM − TM) are considered.

2.4.1 Electric Field and Magnetic Field Projections

The boundary conditions imposed by the PEC junction require that both the electric and magnetic fields be continuous across the intersection of the two guide sections Ω, while the electric field disappears on Σ (i.e. $\boldsymbol{E}_L = \boldsymbol{E}_R$ and $\boldsymbol{H}_L = \boldsymbol{H}_R$ over Ω). By determining the scalar products for the corresponding set of functions which span both the electric ($\nabla F_i^{\mathrm{R}} \times \hat{\boldsymbol{z}}, Z_j^{TM} \nabla A_j^R$) and magnetic fields ($Y_i^{TE} \nabla F_i^{\mathrm{L}}, \nabla A_j^L \times \hat{\boldsymbol{z}}$), and enforcing the boundary conditions, the projections appropriate for electric and magnetic fields can be expressed as shown:

Base	**Electric Field Projections**	
TE	$\int_{S_L} (\nabla F_i^R \times \hat{\boldsymbol{z}}) \left(\boldsymbol{E}^t{}_{all}^{TE,L} + \boldsymbol{E}^t{}_{all}^{TM,L} \right) dS = \int_{S_L} (\nabla F_i^R \times \hat{\boldsymbol{z}}) \left(\boldsymbol{E}^t{}_{all}^{TE,R} + \boldsymbol{E}^t{}_{all}^{TM,R} \right) dS$	*(2.4.4)*
TM	$\int_{S_L} (\nabla A_j^R) \left(\boldsymbol{E}^t{}_{all}^{TE,L} + \boldsymbol{E}^t{}_{all}^{TM,L} \right) dS = \int_{S_L} (\nabla A_j^R) \left(\boldsymbol{E}^t{}_{all}^{TE,R} + \boldsymbol{E}^t{}_{all}^{TM,R} \right) dS$	*(2.4.5)*
Base	**Magnetic Field Projections**	
TE	$\int_{S_L} (\nabla F_i^L) \left(\boldsymbol{H}^t{}_{all}^{TE,L} + \boldsymbol{H}^t{}_{all}^{TM,L} \right) dS = \int_{S_L} (\nabla F_i^L) \left(\boldsymbol{H}^t{}_{all}^{TE,R} + \boldsymbol{H}^t{}_{all}^{TM,R} \right) dS$	*(2.4.6)*
TM	$\int_{S_L} (\nabla \mathrm{A}_j^{\mathrm{L}} \times \hat{\boldsymbol{z}}) \left(\boldsymbol{H}^t{}_{all}^{TE,L} + \boldsymbol{H}^t{}_{all}^{TM,L} \right) dS = \int_{S_L} (\nabla \mathrm{A}_j^{\mathrm{L}} \times \hat{\boldsymbol{z}}) \left(\boldsymbol{H}^t{}_{all}^{TE,R} + \boldsymbol{H}^t{}_{all}^{TM,R} \right) dS$	*(2.4.7)*

As the cross-section of guide *R* is composed of the intersection and overlap region of the two guides (i.e. $\Sigma = (S_L \cup S_R) - \Omega$) and since the electric field is necessarily zero on Σ, it is correct to consider only the cross-section of guide *L* when performing the projection. These integrals can be expanded using the relationships between the transverse modal fields and vector potentials introduced in section 2.2.3 and shown in equations (2.2.47) and (2.2.48). Once expanded, the field matching problem is expressed in terms of a set of integrals involving

individual modal electric and magnetic potentials. For example, by expanding the TE base function for the electric field projection, shown in equation (2.4.4), the following constraints are obtained for modal amplitudes; for each TE base function ($\nabla F_i^{\mathrm{R}} \times \hat{\boldsymbol{z}}$) is indexed by "$i$":

$$\begin{aligned}
&\sum_j^{N_{TE}} \left(a_j^{L,TE,+} + a_j^{L,TE,-}\right) \int_{S_L} \left(\nabla F_i^{\mathrm{R}} \times \hat{\boldsymbol{z}}\right)\left(\nabla F_j^{\mathrm{L}} \times \hat{\boldsymbol{z}}\right) dS \\
&\qquad + \sum_j^{N_{TM}} \left(a_j^{L,TM,+} + a_j^{L,TM,-}\right) Z_j^{L,TM} \int_{S_L} \left(\nabla F_i^{\mathrm{R}} \times \hat{\boldsymbol{z}}\right)\left(\nabla A_j^{L}\right) dS \\
&\qquad = \sum_j^{N_{TE}} \left(a_j^{R,TE,+} + a_j^{R,TE,-}\right) \int_{S_R} \left(\nabla F_i^{\mathrm{R}} \times \hat{\boldsymbol{z}}\right)\left(\nabla F_j^{\mathrm{R}} \times \hat{\boldsymbol{z}}\right) dS \\
&\qquad + \sum_j^{N_{TM}} \left(a_j^{R,TM,+} + a_j^{R,TM,-}\right) Z_j^{R,TM} \int_{S_L} \left(\nabla F_i^{\mathrm{R}} \times \hat{\boldsymbol{z}}\right)\left(\nabla A_j^{R}\right) dS
\end{aligned} \tag{2.4.8}$$

In all of these constraints a series of common integrals appear, and reoccur in other scattering problems considered in the following chapters. By evaluating these common integrals, the scattering problem for the PEC junction is converted to a system of algebraic equations:

Type	Integrals	Modes Involved	
B	$B_{ij}^{kl}(S) = \int_S \nabla A_i^k \cdot \left(\nabla F_j^l \times \hat{\boldsymbol{z}}\right) dS$ $-B_{ji}^{lk}(S) = \int_S \nabla F_i^k \cdot \left(\nabla A_j^l \times \hat{\boldsymbol{z}}\right) dS$	**Mixes TE & TM modes**	*(2.4.9)*
C	$C_{ij}^{kl}(S) = \int_S \nabla A_i^k \cdot \nabla A_j^l dS$	**Only TM**	*(2.4.10)*
D	$D_{ij}^{kl}(S) = \int_S \nabla F_i^k \cdot \nabla F_j^l dS$	**Only TE**	*(2.4.11)*

where indices k, l indicate the guide, while i, j index the modes in their respective guides.

The modal field amplitudes can also be reduced to a more concise form, using:

$$\boldsymbol{e}_{TE/TM}^{g} = \left[a_i^{x,TE/TM,+} + a_i^{x,TE/TM,-}\right], \text{for } g = L \; or \; R \qquad (2.4.12)$$

$$\boldsymbol{h}_{TE/TM}^{g} = \left[a_i^{x,TE/TM,+} - a_i^{x,TE/TM,-}\right], \text{for } g = L \; or \; R \qquad (2.4.13)$$

Using this more concise notation for the integrals and the corresponding amplitudes, the electric field projections shown in equations (2.4.4) and (2.4.5) can be reduced to the following form:

Base	Electric Field Projections	
TE	$\boldsymbol{e}_{TE}^{L}\boldsymbol{D}^{RL}(S_L) + \boldsymbol{e}_{TM}^{L}\boldsymbol{Z}^{L,TM}\boldsymbol{B}^{LR}(S_L) = \boldsymbol{e}_{TE}^{R}\boldsymbol{D}^{RR}(S_R) + \boldsymbol{e}_{TM}^{R}\boldsymbol{Z}^{R,TM}\boldsymbol{B}^{RR}(S_R)$	*(2.4.14)*
TM	$\boldsymbol{e}_{TE}^{L}\boldsymbol{B}^{RL}(S_L) + \boldsymbol{e}_{TM}^{L}\boldsymbol{Z}^{L,TM}\boldsymbol{C}^{RL}(S_L) = \boldsymbol{e}_{TE}^{R}\boldsymbol{B}^{RR}(S_R) + \boldsymbol{e}_{TM}^{R}\boldsymbol{Z}^{R,TM}\boldsymbol{C}^{RR}(S_R)$	*(2.4.15)*

The projections can be expressed in matrix form, which fully captures the electric field boundary constraint, as shown:

$$\begin{bmatrix} \boldsymbol{D}_L^{RL} & (\boldsymbol{B}_L^{LR})^T\boldsymbol{Z}^L \\ \boldsymbol{B}_L^{RL} & \boldsymbol{C}_L^{RL}\boldsymbol{Z}^L \end{bmatrix}\begin{bmatrix} \boldsymbol{e}_{TE}^{L} \\ \boldsymbol{e}_{TM}^{L} \end{bmatrix} = \begin{bmatrix} \boldsymbol{D}_R^{RR} & (\boldsymbol{B}_R^{RR})^T\boldsymbol{Z}^R \\ \boldsymbol{B}_R^{RR} & \boldsymbol{C}_R^{RR}\boldsymbol{Z}^R \end{bmatrix}\begin{bmatrix} \boldsymbol{e}_{TE}^{R} \\ \boldsymbol{e}_{TM}^{R} \end{bmatrix} \qquad (2.4.16)$$

Likewise, the same procedure and notation can be applied to the magnetic field projections to obtain the following:

Base	Magnetic Field Projections	
TE	$\boldsymbol{h}_{TE}^{L}\boldsymbol{Y}^{L,TE}\boldsymbol{D}^{LL}(S_L) + \boldsymbol{h}_{TM}^{L}\boldsymbol{B}^{LL}(S_L) = \boldsymbol{h}_{TE}^{R}\boldsymbol{Y}^{R,TE}\boldsymbol{D}^{LR}(S_L) + \boldsymbol{h}_{TM}^{R}\boldsymbol{B}^{RL}(S_L)$	*(2.4.17)*
TM	$-\boldsymbol{h}_{TE}^{L}\boldsymbol{Y}^{L,TE}\boldsymbol{B}^{LL}(S_L) + \boldsymbol{h}_{TM}^{L}\boldsymbol{C}^{LL}(S_L) = -\boldsymbol{h}_{TE}^{R}\boldsymbol{Y}^{R,TE}\boldsymbol{B}^{LR}(S_L) + \boldsymbol{h}_{TM}^{R}\boldsymbol{C}^{LR}(S_L)$	*(2.4.18)*

In matrix form, this gives the constraint:

$$\begin{bmatrix} \boldsymbol{D}_L^{LL}\boldsymbol{Y}^L & (\boldsymbol{B}_L^{LL})^T \\ \boldsymbol{B}_L^{LL}\boldsymbol{Y}^L & \boldsymbol{C}_L^{LL} \end{bmatrix} \begin{bmatrix} \boldsymbol{h}_{TE}^L \\ \boldsymbol{h}_{TM}^L \end{bmatrix} = \begin{bmatrix} \boldsymbol{D}_R^{LR}\boldsymbol{Y}^R & (\boldsymbol{B}_L^{RL})^T \\ \boldsymbol{B}_L^{LR}\boldsymbol{Y}^R & \boldsymbol{C}_R^{LR} \end{bmatrix} \begin{bmatrix} \boldsymbol{h}_{TE}^R \\ \boldsymbol{h}_{TM}^R \end{bmatrix} \quad (2.4.19)$$

Here the terms $\boldsymbol{Z}$ and $\boldsymbol{Y}$ in equations (2.4.16) and (2.4.19) are diagonal matrices composed of the modal impedances and admittances, respectively.

The matrix equations (2.4.16) and (2.4.19), can be solved to find the overall scattering matrix of the PEC junction. In the more compact form the matrix equations that describe the projections take the following form:

$$\boldsymbol{P}_L\boldsymbol{e}^L = \boldsymbol{Q}_R\boldsymbol{e}^R \quad (2.4.20)$$

$$\boldsymbol{Q}_L\boldsymbol{h}^L = \boldsymbol{P}_R\boldsymbol{h}^R \quad (2.4.21)$$

where $\boldsymbol{P}_L$ and $\boldsymbol{P}_R$ represent the power coupled between modes across the discontinuity, while $\boldsymbol{Q}_L$ and $\boldsymbol{Q}_R$ represent the "self-coupled" power of modes on the left and right hand side of the discontinuity respectively.

To determine the scattering parameters for this system it is assumed that there is only excitation through a single port at a time. For example, by considering an excitation through guide *L* only the $\boldsymbol{S}_{LL}$ and $\boldsymbol{S}_{RL}$ can be determined. With no excitation through guide *R* the TE and TM modal fields amplitudes can be reduced as shown:

$$\boldsymbol{e}_{TE}^{\prime R} = [a^{R,TE,+}] = \boldsymbol{h}_{TE}^{\prime R} \;\therefore\; \boldsymbol{P}_L\boldsymbol{e}^L = \boldsymbol{Q}_R\boldsymbol{e}^{\prime R} \quad (2.4.22)$$

$$\boldsymbol{e}_{TM}^{\prime R} = [a^{R,TM,+}] = \boldsymbol{h}_{TM}^{\prime R} \;\therefore\; \boldsymbol{Q}_L\boldsymbol{h}^L = \boldsymbol{P}_R\boldsymbol{e}^{\prime R} \quad (2.4.23)$$

Using the pseudo-inverse of $\boldsymbol{Q}_R$, a best fit expression for $\boldsymbol{e}^{\prime R} = \boldsymbol{Q}_R^{+}\boldsymbol{P}_L\boldsymbol{e}^L$ is obtained. The pseudo-inverse $\boldsymbol{Q}_R^{+}$ is the $n \times m$ matrix which inverts $\boldsymbol{Q}_R$ from column to row space and satisfies the Moore-Penrose conditions (Strang 2013). . Substituting this new expression into

the second matrix equation given in equation (2.4.23), the scattering parameter $\boldsymbol{S}_{LL}$ can be obtained:

$$\boldsymbol{Q}_L\boldsymbol{h}^L = \boldsymbol{P}_R\boldsymbol{Q}_R^+\boldsymbol{P}_L\boldsymbol{e}^L \;\Rightarrow \boldsymbol{h}^L = \boldsymbol{Q}_L^+\boldsymbol{P}_R\boldsymbol{Q}_R^+\boldsymbol{P}_L\boldsymbol{e}^L \tag{2.4.24}$$

$$\boldsymbol{a}^{L,+} - \boldsymbol{a}^{L,-} = \boldsymbol{Q}_L^+\boldsymbol{P}_R\boldsymbol{Q}_R^+\boldsymbol{P}_L(\boldsymbol{a}^{L,+} + \boldsymbol{a}^{L,-}) \tag{2.4.25}$$

$$(\boldsymbol{I} - \boldsymbol{Q}_L^+\boldsymbol{P}_R\boldsymbol{Q}_R^+\boldsymbol{P}_L)\boldsymbol{a}^{L,+} = (\boldsymbol{I} + \boldsymbol{Q}_L^+\boldsymbol{P}_R\boldsymbol{Q}_R^+\boldsymbol{P}_L)\boldsymbol{a}^{L,-} \tag{2.4.26}$$

$$\boldsymbol{S}_{LL} = (\boldsymbol{I} + \boldsymbol{Q}_L^+\boldsymbol{P}_R\boldsymbol{Q}_R^+\boldsymbol{P}_L)^{-1}(\boldsymbol{I} - \boldsymbol{Q}_L^+\boldsymbol{P}_R\boldsymbol{Q}_R^+\boldsymbol{P}_L) \tag{2.4.27}$$

From equation (2.4.22) the scattering parameter $\boldsymbol{S}_{RL}$ can be determined by taking similar approach and using the previously derived form of the $\boldsymbol{S}_{LL}$ scattering parameter as:

$$\boldsymbol{Q}_R^+\boldsymbol{P}_L(\boldsymbol{a}^{L,+} + \boldsymbol{a}^{L,-}) = \boldsymbol{a}^{R,+} \;\Rightarrow \boldsymbol{a}^{R,+} = \boldsymbol{Q}_R^+\boldsymbol{P}_L(\boldsymbol{I} + \boldsymbol{S}_{LL})\boldsymbol{a}^{L,+} \tag{2.4.28}$$

$$\boldsymbol{S}_{RL} = \boldsymbol{Q}_R^+\boldsymbol{P}_L(\boldsymbol{I} + \boldsymbol{S}_{LL}) \tag{2.4.29}$$

The remaining scattering parameters for the junction formulation can be determined by repeating this procedure, assuming excitation only through the opposite guide *R*. The resulting scattering parameters for the PEC junction are as follows:

$$\boldsymbol{S}_{LL} = (\boldsymbol{I} + \boldsymbol{Q}_L^+\boldsymbol{P}_R\boldsymbol{Q}_R^+\boldsymbol{P}_L)^{-1}(\boldsymbol{I} - \boldsymbol{Q}_L^+\boldsymbol{P}_R\boldsymbol{Q}_R^+\boldsymbol{P}_L) \tag{2.4.30}$$

$$\boldsymbol{S}_{RL} = \boldsymbol{Q}_R^+\boldsymbol{P}_L(\boldsymbol{I} + \boldsymbol{S}_{LL}) \tag{2.4.31}$$

$$\boldsymbol{S}_{RR} = (\boldsymbol{Q}_R^+\boldsymbol{P}_L\boldsymbol{Q}_L^+\boldsymbol{P}_R + \boldsymbol{I})^{-1}(\boldsymbol{Q}_R^+\boldsymbol{P}_L\boldsymbol{Q}_L^+\boldsymbol{P}_R - \boldsymbol{I}) \tag{2.4.32}$$

$$\boldsymbol{S}_{LR} = \boldsymbol{Q}_L^+\boldsymbol{P}_R(\boldsymbol{I} - \boldsymbol{S}_{RR}) \tag{2.4.33}$$

2.4.2 Line Integral Form of Common Integrals

The common integrals present in the previous section, equations (2.4.9) - (2.4.11), are defined as surface integrals. By reformulating these in terms of line integrals a more readily numerically integrable form of the mode coupling equations is achieved. This form allows for increased efficiency when numerical methods are required i.e. for scenario were no analytic solutions to coupling integrals can be found. Type-B integrals, which mix TE and TM modes, were defined as:

$$B_{ij}^{kl}(S) = \int_S \nabla A_i^k \cdot \left(\nabla F_j^l \times \hat{\boldsymbol{z}}\right) dS \qquad (2.4.34)$$

where k, l identify the guide (L or R), i indexes TM modes in guide k and j indexes TE modes in guide L. Using symmetries of the scalar triple product this can be expressed as:

$$B_{ij}^{kl}(S) = \int_S \nabla A_i^k \times \nabla F_j^l \cdot \hat{\boldsymbol{z}} dS = \int_S \nabla A_i^k \times \nabla F_j^l \cdot d\boldsymbol{S} \qquad (2.4.35)$$

By applying the general vector calculus relations $\nabla \times \nabla\psi = 0$ and $\nabla \times (\phi \boldsymbol{u}) = \phi \nabla \times \boldsymbol{u} + \nabla\phi \times \boldsymbol{u}$, with $\boldsymbol{u} = \nabla F_j^l$ and $\phi = A_i^k$, it is shown that:

$$\nabla \times \left(A_i^k \nabla F_j^l\right) = A_i^k \nabla \times \nabla F_j^l + \nabla A_i^k \times \nabla F_j^l = \nabla A_i^k \times \nabla F_j^l \qquad (2.4.36)$$

Or alternatively, with $\boldsymbol{u} = \nabla A_i^k$ and $\phi = F_j^l$:

$$\nabla \times \left(F_j^l \nabla A_i^k\right) = F_j^l \nabla \times \nabla A_i^k + \nabla F_j^l \times \nabla A_i^k = \nabla F_j^l \times \nabla A_i^k \qquad (2.4.37)$$

$$\therefore \nabla A_i^k \times \nabla F_j^l = \nabla \times \left(A_i^k \nabla F_j^l\right) = -\nabla \times \left(F_j^l \nabla A_i^k\right)$$

The expression for the Type-B integral becomes:

$$B_{ij}^{kl}(S) = \int_S \nabla A_i^k \times \nabla F_j^l \cdot d\boldsymbol{S} = \int_S \nabla \times \left(A_i^k \nabla F_j^l\right) \cdot d\boldsymbol{S} = -\int_S \nabla \times \left(F_j^l \nabla A_i^k\right) \cdot d\boldsymbol{S} \quad (2.4.38)$$

Finally, by applying Stokes' Theorem as in Figlia and Gentili (2002) the integral can be reduced to line integral form as:

$$B_{ij}^{kl}(S) = \int_{\partial S} \left(A_i^k \nabla F_j^l\right) d\boldsymbol{l} = -\int_{\partial S} \left(F_j^l \nabla A_i^k\right) d\boldsymbol{l} \quad (2.4.39)$$

From the boundary conditions given in section 2.2.3, the potential $A_i^k = 0$ on the edge of guide S_k, therefore $B_{ij}^{kl}(S_k) = 0$. In the case for $k = L$ and $l = R$, this corresponds to the well-known property of a junctions – TM modes from the smaller guide do not couple to TE modes in the larger guide. This result can be used to simplify some of the elements in the power coupling matrices $\boldsymbol{P}_L$ and $\boldsymbol{P}_R$ in section 2.4.1.

A similar procedure is applied to the Type-C and D integrals to obtained their line-integral form. For example, the Type-D, which couples the TE modes across the discontinuity, is reduced:

$$D_{ij}^{kl}(S) = \int_S \nabla F_i^k \cdot \nabla F_j^l dS \quad (2.4.40)$$

By applying Green's first theorem the integral is expressed in terms of both a line and surface integral:

$$D_{ij}^{kl}(S) = \int_S \nabla F_i^k \cdot \nabla F_j^l dS = \int_{\partial S} F_i^k \nabla F_j^l \cdot \hat{\boldsymbol{n}} dl - \int_S F_i^k \nabla \cdot \nabla F_j^l dS \quad (2.4.41)$$

$$D_{ij}^{kl}(S) = \int_S \nabla F_i^k \cdot \nabla F_j^l dS = \int_{\partial S} F_j^l \nabla F_i^k \cdot \hat{\boldsymbol{n}} dl - \int_S F_j^l \nabla \cdot \nabla F_i^k dS \quad (2.4.42)$$

By applying the Laplacian operator in both equations, the following expressions are obtained:

$$D_{ij}^{kl}(S) = \int_{\partial S} F_i^k \nabla F_j^l \cdot \hat{\boldsymbol{n}} dl - \left(\beta_{c,j}^{l,TE}\right)^2 \int_S F_i^k F_j^l dS \qquad (2.4.43)$$

$$D_{ij}^{kl}(S) = \int_{\partial S} F_j^l \nabla F_i^k \cdot \hat{\boldsymbol{n}} dl - \left(\beta_{c,i}^{k,TE}\right)^2 \int_S F_j^l F_i^k dS \qquad (2.4.44)$$

where $\beta_{c,j}^{l,TE}$ describes the cutoff wave number for the mode. At this point three distinct cases can be considered:

(i) $k = l$ gives that the cross-section of the guides is the same, this reduces the problem to that of the uniform guide case. Here the boundary condition will require that $\nabla F_j^l \cdot \hat{\boldsymbol{n}} = 0$ as derived in section 2.2.3.

$$D_{ij}^{kk}(S) = \left(\beta_{c,j}^{k,TE}\right)^2 \int_S F_i^k F_j^k dS \qquad (2.4.45)$$

(ii) $k \neq l$ gives that the cross-sections of the guides are not the same (i.e. R and L respectively) and here it is assumed that modes are not the same i.e. have different cutoff wavenumbers. By obtaining the difference of equations (2.4.43) and (2.4.44) and again applying the boundary condition, the Type-D integral can be expressed in line integral form:

$$D_{ij}^{RL}(S_L) = \frac{\left(\beta_{c,i}^{L,TE}\right)^2 \int_{dS} F_j^L \nabla F_i^R \cdot \hat{\boldsymbol{n}} dl}{\left(\beta_{c,j}^{L,TE}\right)^2 - \left(\beta_{c,i}^{R,TE}\right)^2} \qquad (2.4.46)$$

(iii) $k \neq l$ gives that the cross-sections of the guide are not the same and here it is assumed that modes have the same cutoff wavenumbers.

$$D_{ij}^{RL}(S_L) = \left(\beta_{c,j}^{L,TE}\right)^2 \int_S F_i^R F_j^L dS \qquad (2.4.47)$$

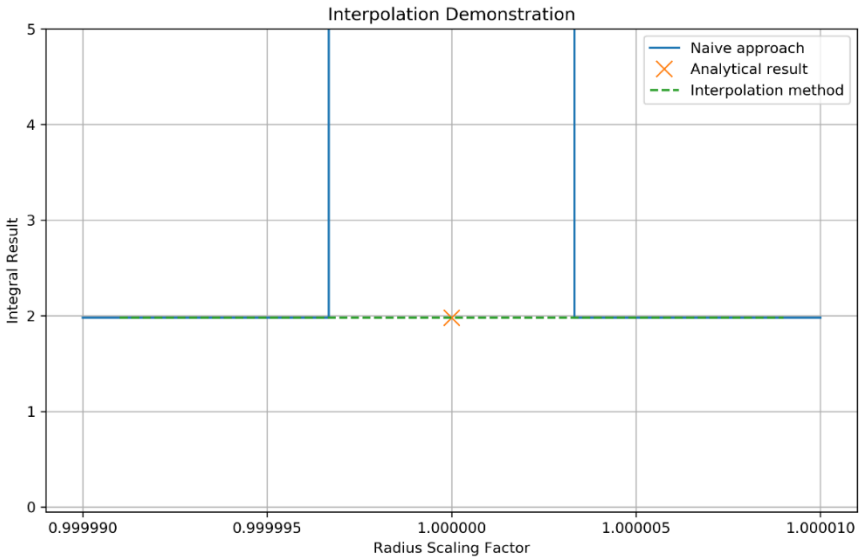

Figure 2-12 Demonstrates the interpolation method used to avoid the singularity.

It is clear that equation (2.2.46) will have a singularity, where $\beta_{c,j}^{L,TE} = \beta_{c,i}^{R,TE}$, as shown in Figure 2-12. However, it is not strictly necessary to use equation (2.4.47) for numerical evaluation. Instead, by slightly altering the radius of one of the guides, and thus its corresponding modes wavenumber, the singularity can be avoided i.e. $\left(\beta_{c,j}^{L,TE}\right)^2 - \left(\beta_{c,i}^{R,TE} \times (1+\epsilon)\right)^2 \neq 0$. For a set of $\epsilon = [-\epsilon, +\epsilon]$, for $\epsilon \to 0$ the integral results can be determined close to both sides of the singularity. Through interpolation methods an excellent approximation of the result for $D_{ij}^{RL}(S_L)$ can be obtained. From Figure 2-12, it can be shown that there is excellent agreement between the interpolated and analytic result.

The procedure for obtaining the expression for the Type-C integrals is almost identical to the Type-D case, only the boundary condition will differ. For completeness the Type-C coupling equations are presented:

$$(i)\ C_{ij}^{kk}(S) = \left(\beta_{c,j}^{k,TM}\right)^2 \int_S A_i^k A_j^k dS \qquad (2.4.48)$$

$$(ii)\ C_{ij}^{RL}(S_L) = \frac{\left(\beta_{c,i}^{R,TM}\right)^2 \int_{dS} A_i^R \nabla A_j^L \cdot \hat{\boldsymbol{n}} dl}{\left(\beta_{c,i}^{R,TM}\right)^2 - \left(\beta_{c,j}^{L,TM}\right)^2} \qquad (2.4.49)$$

$$(iii)\ C_{ij}^{RL}(S_L) = \left(\beta_{c,j}^{L,TM}\right)^2 \int_S A_i^R A_j^L dS \qquad (2.4.50)$$

For several classes of junction geometries, the coupling integrals (B, C and D) can be determined analytically. Where analytic solutions are available they are used in preference to the numerical form and are shown in Appendix A.1.

2.4.3 Testing and Verification of the PEC Junctions

To verify the essential correctness of the implementation and to ascertain its numerical accuracy, the mode-matching approach is benchmarked against an industry standard software package for computational electromagnetics. CST Microwave Studio, a finite element solver, is used to produce reference estimates of the scattering parameters for identical systems. Even where applicable symmetries are applied to the CST models, the modes used in these simulations can be identified by their waveguide order and cutoff frequencies allowing for direct comparison. Modes in CST are identified by numerically solving the relevant boundary value problem, and as such occasional phase mismatches are present due to the different phase conventions used ($\pm 180°$). However, this does not indicate a lack of equivalency. The following test cases are considered for the verification of the PEC mode-matching method (SCATTER-TNG), the frequency range for each test case was selected to allow many modes to propagate in the test structures.

- Junction of two cylindrical waveguides of radius $1.4\ \text{mm}$ and $1.7\ \text{mm}$ with lengths $1\ \text{mm}$, over a frequency range of $f = 50 - 150\ \text{GHz}$ (144 modes considered: 16 radial and 5 azimuthal orders).
    - With no offset (concentric case) and
    - With a $0.2\ \text{mm}$ offset in the *x*-direction of the second guide
- Junction of two rectangular waveguides a WR10 section ($2.54\ \text{mm} \times 1.27\ \text{mm}$) and rectangular waveguide ($3.2\ \text{mm} \times 2.0\ \text{mm}$) with lengths $1\ \text{mm}$, over a frequency range of $f = 30 - 250\ \text{GHz}$ (112 modes considered: 8 Cartesian orders).
    - With no offset (concentric case)
    - With a $0.2\ \text{mm}$ offset in the *x*-direction of the second guide
- Junction of a WR10 and a cylindrical $r = 1.7\ \text{mm}$ guides with lengths $1\ \text{mm}$, over $f = 50 - 150\ \text{GHz}$ (with 112 modes and 120 modes 8 radial/8 azimuthal orders considered)
    - With no offset (concentric case)
    - With a $0.25\ \text{mm}$ offset in the x-direction of the second guide

The number of channels allowed for mode coupling is highly dependent on the level of symmetry between the two guides involved in the mode-matching integrals. For concentric cases modes are restricted to coupling to modes with the same azimuthal order and provided they have the correct polarisation. However, when offsets are introduced the axes of symmetry can be reduced or completely lost opening further channels to mode coupling. For cases were

modes do not couple to one another the integral for these cases can be ignored in favour of the analytic result of zero. In terms of simulation times, with geometry, frequency sampling and the number of mode being accurately modelled taken as equivalent, simulation times for CST can be significantly longer. The verifying datasets produced below for simple coupling sections took 1 hour to be generated using S-TNG and upwards of 5 hours to for CST. It should be noted that this implementation of S-TNG was prototyped in Python and one would expect much reduced simulation times for compiled code such as C.

2.4.3.1 Cylindrical to cylindrical junction:

In the concentric case comparisons with the equivalent CST models shows excellent agreement. Here, in both reflection and transmission (S_{11} and S_{21}) there is agreement between the two models even down to a level of below -80 dB. Furthermore, the correct channels for mode coupling are present. In this test case it can be seen that there is coupling of modes to the same mode and also between different mode types provided they have the correct polarisation.

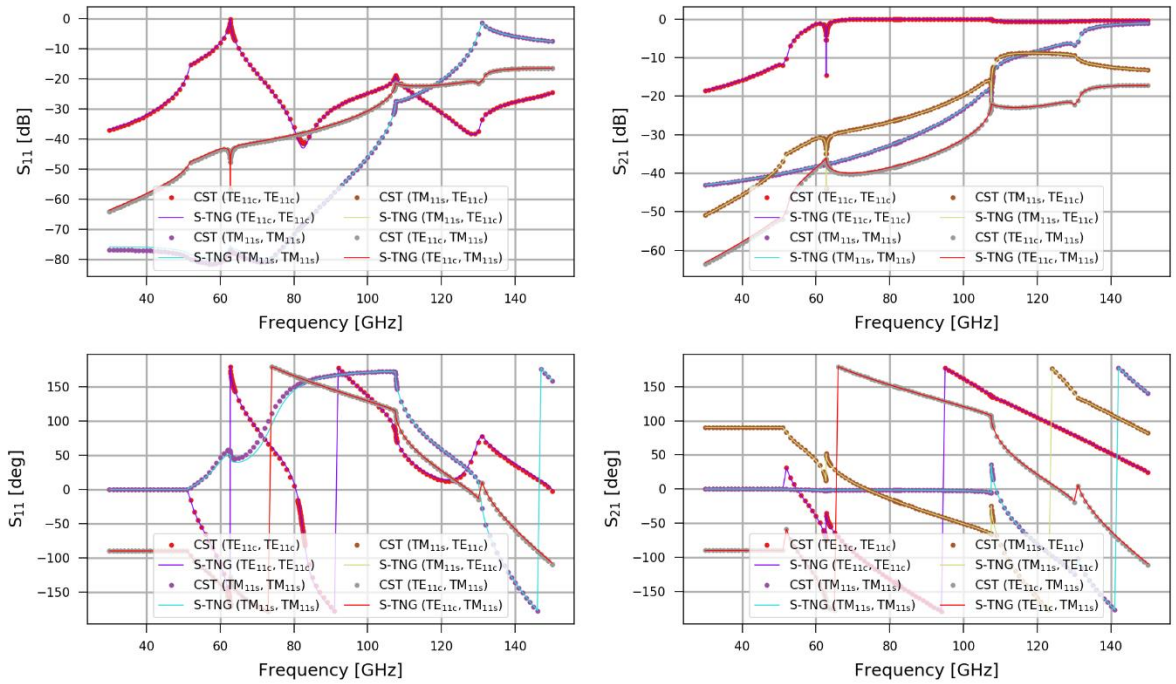

Figure 2-13: Concentric PEC cylindrical junction $1.4\ mm - 1.7\ mm$ *with,144 modes 16 radial orders and 5 azimuthal orders considered. Reflection (*S_{11}*) and Transmission (*S_{21}*) scattering parameters shown for both CST and SCATTER-TNG. The legend notation of the following figures denotes the coupling between modes i.e. coupling between (Mode A, Mode B)*

In the non-centric case, the requirement that modes must only couple to modes with the same azimuthal order is no longer in place. This offset case introduces scattering among many different azimuthal orders, see Figure 2-14. As such the number of azimuthal and radial order modes needed to accurately model non-concentric cases is larger than that of the completely concentric case. However, the level of agreement between the CST and SCATTER-TNG models is equivalent to the concentric case.

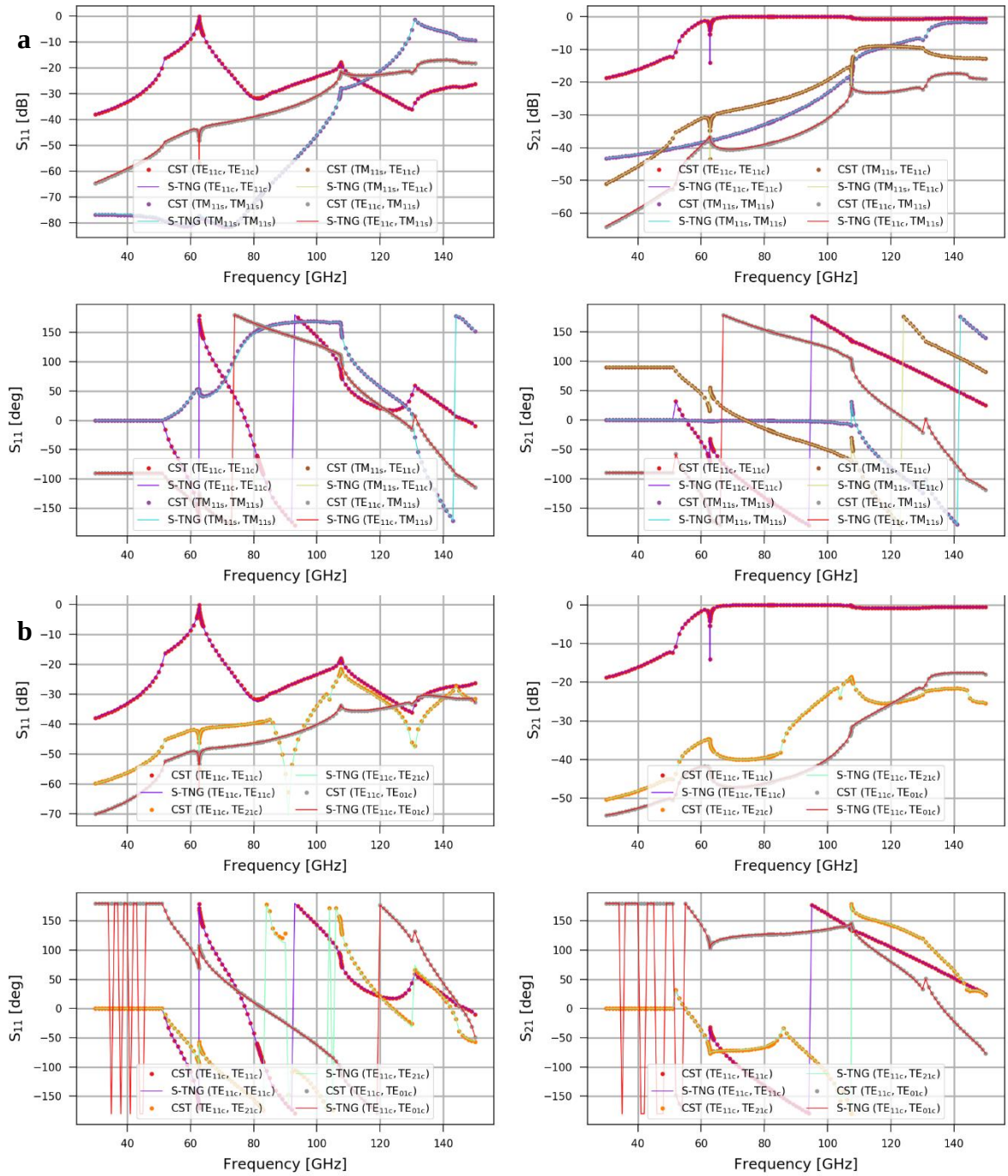

Figure 2-14: (a) Offset (Δx = 0.2 mm) PEC cylindrical junction 1.4 mm − 1.7 mm with,144 modes 16 radial orders and 5 azimuthal orders considered. (b)Shows the extra channels of mode coupling which exist due to the offset present

Again, there is excellent agreement between the two models even down a level of below -80 dB and that the expected channels for mode coupling are present. It can be shown that those extra channels introduced by the offset also have excellent agreement.

2.4.3.2 *Rectangular to rectangular junctions:*

In Figure 2-15 and Figure 2-16, for both the concentric and offset comparisons with the equivalent CST models effectively perfect agreement is observed. Here, in both reflection and transmission (S_{11} and S_{21}) there is agreement between the two models even down a level of below -80 dB. Furthermore, the correct channels for mode coupling are present. In the CST results, below -80 dB, noise can be observed in phase and magnitude due to the finite accuracy of the numerical solver which may be also limited by the CST simulation settings selected.

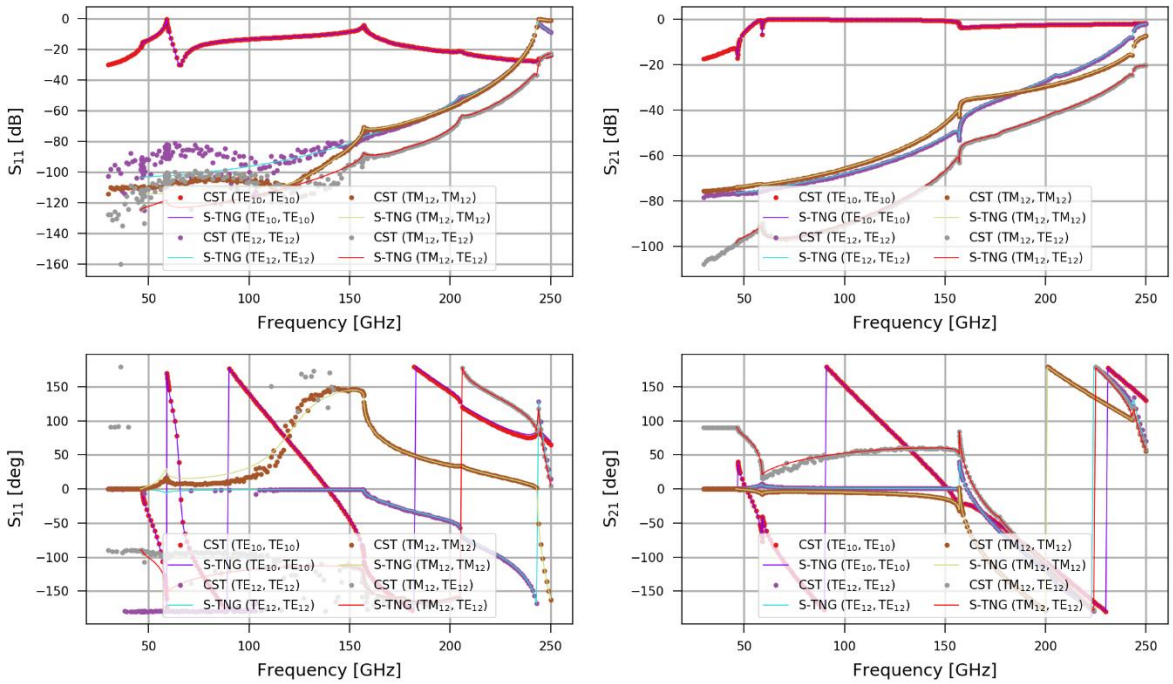

Figure 2-15: Concentric PEC rectangular junction with 112 modes 8 Cartesian orders considered. Reflection (S_{11}) and Transmission (S_{21}) scattering parameters shown for both CST and SCATTER-TNG

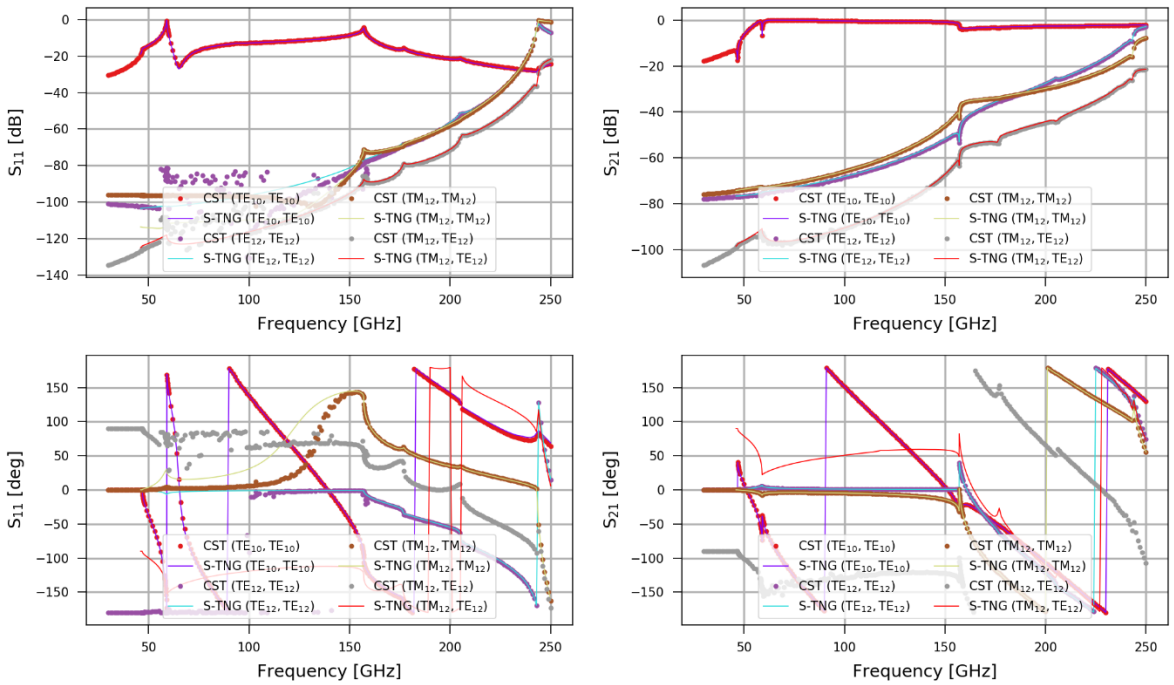

Figure 2-16: Offset (dx 0.2) PEC rectangular junction with 112 modes 8 Cartesian orders considered. Reflection (S_{11}) and Transmission (S_{21}) scattering parameters shown for both CST and SCATTER-TNG

2.4.3.3 Rectangular to Circular Junction

An important transition between rectangular and circular geometries can now be effectively treated numerically using the contour mode matching approach presented in section 2.4.2. This type of transition often appears in the throat region of feedhorns where there is a necessary region which morphs from rectangular to circular cross-section i.e. a cylindrical waveguide fed by a WR10 connected to a VNA source.

As before, CST is used as an independent benchmark in the test cases. To ensure the correct polarisation directions are used, CST waveguide ports must have their polarisations fixed. Without this, modes will have the correct orthogonality in their respective and similar guides but not necessarily when geometries are mixed. In CST's port definition the polarisation is locked at 0 degrees and 90 degrees for the rectangular and circular guides respectively. This ensures the same convention as that used in SCATTER-TNG is employed. In Figure 2-17 and Figure 2-18, excellent agreement for both offset and non-offset case is observed. As the geometry is mixed a large number of modes is required to accurately model this scenario.

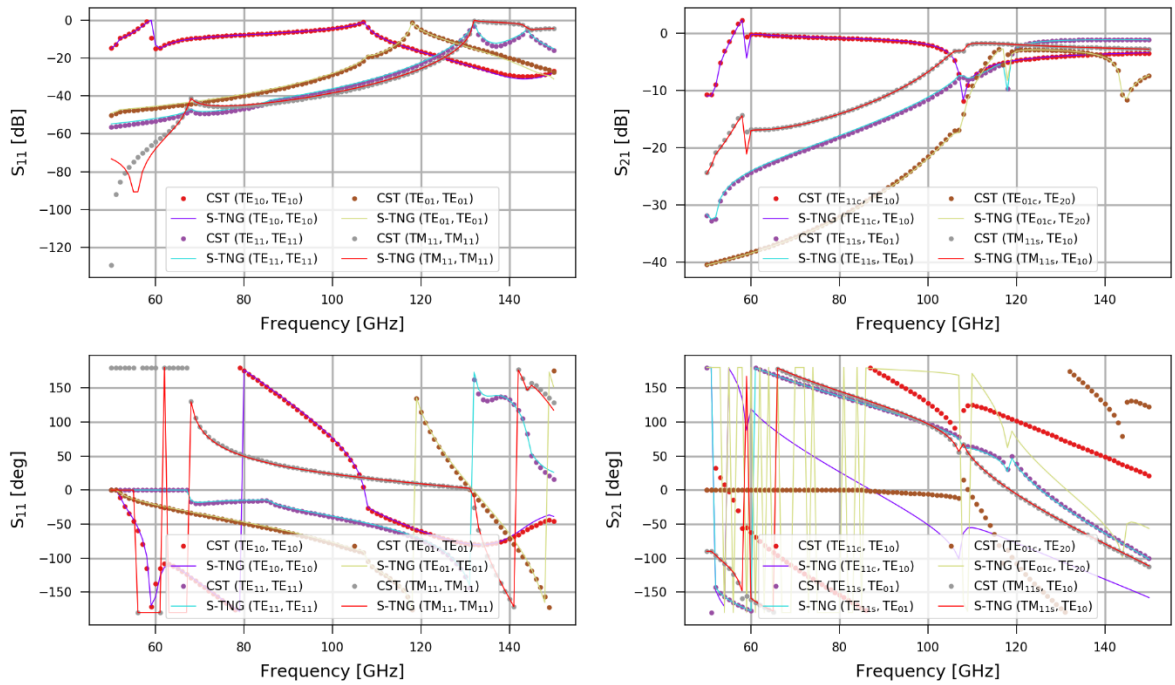

Figure 2-17: PEC concentric junction mixed geometry junction WR10 (112 Modes 8 Cartesian orders) to Circular (144 Modes 16 radial orders and 5 azimuthal orders).. Reflection (S_{11}) and Transmission (S_{21}) scattering parameters shown for both CST and SCATTER-TNG

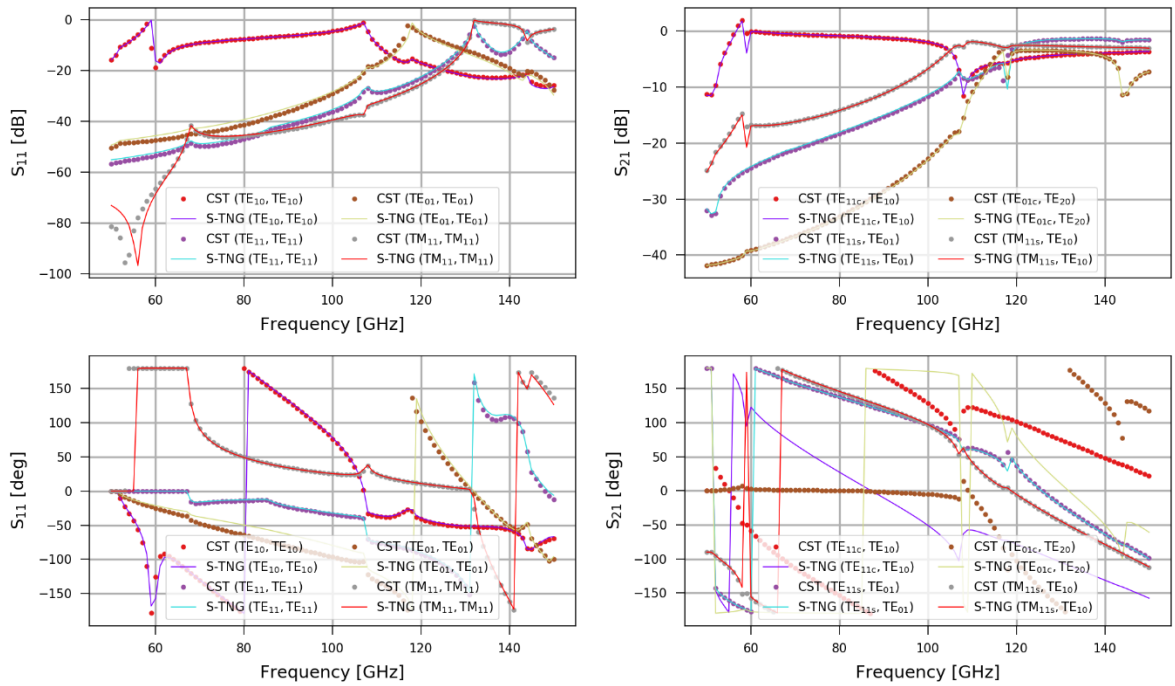

Figure 2-18 PEC offset junction mixed geometry junction WR10 (112 Modes 8 Cartesian orders) to Circular (144 Modes 16 radial orders and 5 azimuthal orders). Reflection (S_{11}) and Transmission (S_{21}) scattering parameters shown for both CST and SCATTER-TNG

2.5 Cascading of Scattering Matrices

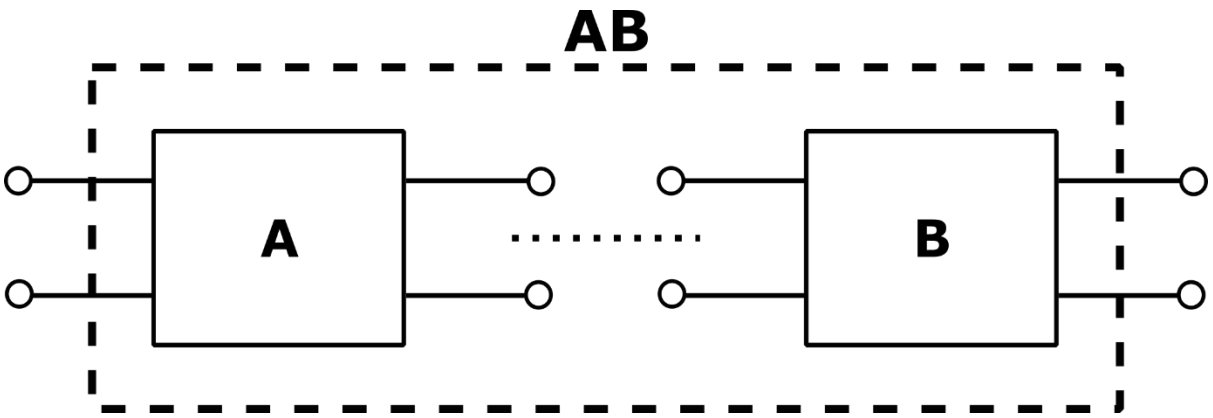

Figure 2-19: Representation of a two port network AB composed of the enclosed two port networks A and B. The enclosed networks are cascaded together such that new network correctly accounts for reflection and transmission of the constituent networks.

Cascading methods are used to construct more complex structures from the basic building blocks that were introduced in sections 2.3 and 2.4. Cascading combines the scattering matrices of two distinct networks, such as a uniform network element and junction network, to form the overall scattering matrix of the composite system. By repeating this process, the scattering matrix for a complete waveguide structure can be constructed. These individual networks will usually have only two ports but the method can be extended to allow for cascading between $m{:}\,n$ port, should it be necessary. The cascading technique can be introduced by considering two N-port networks A and B, both of which can be represented by their own scattering matrices which take the form:

$$\boldsymbol{b}^{A} = [\boldsymbol{S}^{A}]\boldsymbol{a}^{A} \tag{2.5.1}$$

$$\boldsymbol{b}^{\boldsymbol{B}} = [\boldsymbol{S}^{B}]\boldsymbol{a}^{B} \tag{2.5.2}$$

Where $\boldsymbol{a}^{X} = [a_i^X]$ represents the amplitudes of the incident modes, $\boldsymbol{b}^{X} = [b_i^X]$ represents the amplitudes of the outgoing modes and X gives the network element of interest. Ports in the two constituent networks that are connected to each other will vanish in the resulting network, while the remaining will become its external ports. The number of modes considered in each network is given by N_X. These modes can be separated into *remaining* (in the external ports; denoted by **R**) and *vanishing* (those in the vanishing internal ports of the complete network; denoted by **V**). This puts further constraints on the amplitudes of the incident and outgoing modes, which

are reordered to put all remaining modes first. The scattering matrix for each network can be correspondingly refactored using the same notation as shown:

$$\boldsymbol{a}^{X} = \begin{bmatrix} \boldsymbol{a}^{X,R} \\ \boldsymbol{a}^{X,V} \end{bmatrix} \tag{2.5.3}$$

$$\boldsymbol{b}^{X} = \begin{bmatrix} \boldsymbol{b}^{X,R} \\ \boldsymbol{b}^{X,V} \end{bmatrix} \tag{2.5.4}$$

$$\begin{bmatrix} \boldsymbol{b}^{X,R} \\ \boldsymbol{b}^{X,V} \end{bmatrix} = \begin{bmatrix} \boldsymbol{S}^{X}_{R,R} & \boldsymbol{S}^{X}_{R,V} \\ \boldsymbol{S}^{X}_{V,R} & \boldsymbol{S}^{X}_{V,V} \end{bmatrix} \begin{bmatrix} \boldsymbol{a}^{X,R} \\ \boldsymbol{a}^{X,V} \end{bmatrix} \tag{2.5.5}$$

The vanishing modes of network A are connected one-to-one to the same modes in network B, while the remaining modes of the network do not mix.

$$N_{A,R} = N_A - N_{A,V} \tag{2.5.6}$$

$$N_{B,R} = N_B - N_{B,V} \tag{2.5.7}$$

$$N_{A,V} = N_{B,V} = N_V \tag{2.5.8}$$

$$\therefore \boldsymbol{a}^{B,V} = \boldsymbol{b}^{A,V} \text{and } \boldsymbol{a}^{A,V} = \boldsymbol{b}^{B,V} \tag{2.5.9}$$

To obtain the scattering matrix for the combined network the amplitudes of the remaining outgoing modes $\begin{bmatrix} \boldsymbol{b}^{A,R} \\ \boldsymbol{b}^{B,R} \end{bmatrix}$ must be expressed wholly in terms of the amplitudes of the remaining input modes $\begin{bmatrix} \boldsymbol{a}^{A,R} \\ \boldsymbol{a}^{B,R} \end{bmatrix}$. The overall scattering matrix of the combined network S^{AB} links the input and output modes as follows:

$$\begin{bmatrix} \boldsymbol{b}^{A,R} \\ \boldsymbol{b}^{B,R} \end{bmatrix} = \boldsymbol{S}^{AB} \begin{bmatrix} \boldsymbol{a}^{A,R} \\ \boldsymbol{a}^{B,R} \end{bmatrix} \tag{2.5.10}$$

and can be shown to be:

$$S^{AB} = \begin{bmatrix} S^A_{R,R} + S^A_{R,V}\left(I - S^B_{V,V}S^A_{V,V}\right)^{-1}S^B_{V,V}S^A_{V,R} & S^A_{R,V}\left(I - S^B_{V,V}S^A_{V,V}\right)^{-1}S^B_{V,R} \\ S^B_{R,V}\left(I - S^A_{V,V}S^B_{V,V}\right)^{-1}S^A_{V,R} & S^B_{R,R} + S^B_{R,V}\left(I - S^A_{V,V}S^B_{V,V}\right)^{-1}S^A_{V,V}S^B_{V,R} \end{bmatrix} \quad (2.5.11)$$

The complete derivation of the cascading procedure is given in Appendix A.2.

Some common situations where the cascading procedure is required are as follows:

- Joining of a uniform segment with a junction segment and repeating this process allows for complete horn geometries to be constructed.
- Joining of a uniform network with a network representing a short allows a cavity section to be modelled.

2.5.1 Example: cascading a 2-port network with a 2-port network

The second port of the network A is connected to the first port of network B. The number of modes in port 1 (remaining) and 2 (vanishing) are respectively $N_{A,1} = N_{A,R}$ and $N_{A,2} = N_{A,V} = N_V$. In network B the number of modes in port 1 (vanishing) is $N_{B,1} = N_{A,2} = N_V$ while the remaining port 2 modes are $N_{B,2} = N_{B,R}$. All remaining modes of network A are in port 1 while all remaining modes of network B are in port 2. The scattering matrix for the cascaded network has the form:

$$\boldsymbol{S}^{AB} = \begin{bmatrix} \boldsymbol{S}^{AB}_{11} & \boldsymbol{S}^{AB}_{12} \\ \boldsymbol{S}^{AB}_{21} & \boldsymbol{S}^{AB}_{22} \end{bmatrix} \quad (2.5.12)$$

$$\begin{aligned} \boldsymbol{S}^{AB}_{11} &= \boldsymbol{S}^{A}_{11} + \boldsymbol{S}^{A}_{12}(\boldsymbol{I} - \boldsymbol{S}^{B}_{11}\boldsymbol{S}^{A}_{22})^{-1}\boldsymbol{S}^{B}_{11}\boldsymbol{S}^{A}_{21} \\ \boldsymbol{S}^{AB}_{12} &= \boldsymbol{S}^{A}_{12}(\boldsymbol{I} - \boldsymbol{S}^{B}_{11}\boldsymbol{S}^{A}_{22})^{-1}\boldsymbol{S}^{B}_{12} \\ \boldsymbol{S}^{AB}_{21} &= \boldsymbol{S}^{B}_{21}(\boldsymbol{I} - \boldsymbol{S}^{A}_{22}\boldsymbol{S}^{B}_{11})^{-1}\boldsymbol{S}^{A}_{21} \\ \boldsymbol{S}^{AB}_{22} &= \boldsymbol{S}^{B}_{22} + \boldsymbol{S}^{B}_{21}(\boldsymbol{I} - \boldsymbol{S}^{A}_{22}\boldsymbol{S}^{B}_{11})^{-1}\boldsymbol{S}^{A}_{22}\boldsymbol{S}^{B}_{12} \end{aligned} \quad (2.5.13)$$

2.5.2 Example: cascading a 2-port network with a 1-port network

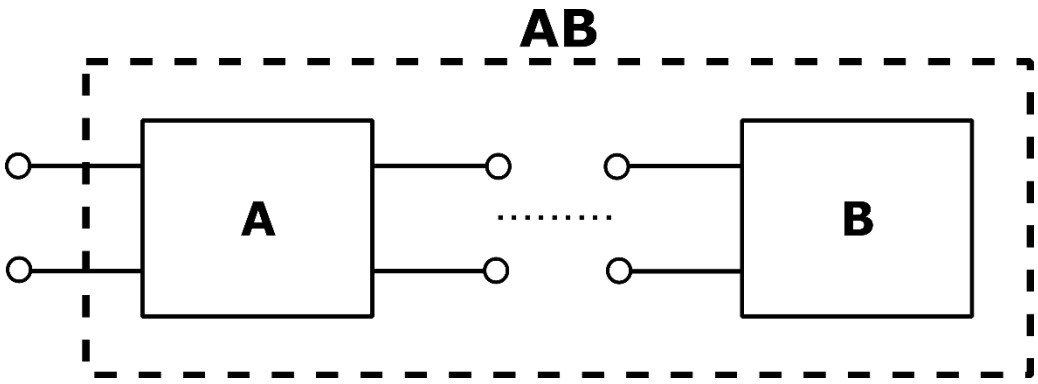

Figure 2-20 : Representation of a 1 port network AB composed of the enclosed networks A (2-port) and B (1-port).

The second port of A is connected to the only port of B. The number of modes in network A's port 1 (remaining) and port 2 (vanishing) are given respectively as $N_{A,1} = N_{A,R}$ and $N_{A,2} = N_{A,V} = N_V$. In network B's only port (vanishing) has its mode number given by $N_{B,1} = N_{A,2} = N_V$, and $N_{B,R} = 0$. In this case $\boldsymbol{S}_{R,V}^{B}$, has zero rows, $\boldsymbol{S}_{R,R}^{B}$ has no elements and $\boldsymbol{S}_{V,R}^{B}$ has zero columns. This means that the overall scattering matrix for the cascaded system reduces to a single scattering parameter as all modes are in one port:

$$\boldsymbol{S}^{AB} = [\boldsymbol{S}_{R,R}^{A} + \boldsymbol{S}_{R,V}^{A}\left(\boldsymbol{I} - \boldsymbol{S}_{V,V}^{B}\boldsymbol{S}_{V,V}^{A}\right)^{-1}\boldsymbol{S}_{V,V}^{B}\boldsymbol{S}_{V,R}^{A}] \tag{2.5.14}$$

$$\boldsymbol{S}_{11}^{AB} = \boldsymbol{S}_{11}^{A} + \boldsymbol{S}_{12}^{A}(\boldsymbol{I} - \boldsymbol{S}_{11}^{B}\boldsymbol{S}_{22}^{A})^{-1}\boldsymbol{S}_{11}^{B}\boldsymbol{S}_{21}^{A} \tag{2.5.15}$$

2.5.3 Single Port Networks

There are some fundamental networks which have yet to be discussed up to this point. Following on from the example of cascading a 2-port network with a 1-port network presented in section 2.5.2, there are two single port networks that can be introduced. These are the Short and Match networks. The short network or backshort can be cascaded with a waveguide section to form a cavity structure, such that there is reflection from the back-end of the guide. Here, perfect reflection is expected from a PEC backshort and as such its only scattering parameter has the following form:

$$\boldsymbol{S}_{11}^{backshort} = -\boldsymbol{I}, \tag{2.5.16}$$

Conversely, the match network can also be cascaded with a waveguide section to provide an idealised termination point for the guide i.e. there will be no reflection from the match-network. Here, perfect absorption is expected from the match and its only scattering parameter has the following form:

$$\boldsymbol{S}_{11}^{match} = [\mathbf{0}] \tag{2.5.17}$$

2.6 Far-Field Propagation

For a complete description of the waveguide structures, a thorough analysis of their radiation characteristics is required. While there exist many different types of antenna structures, in this thesis only aperture antenna type designs are considered. Aperture antennas are described by their definite aperture, usually a few wavelengths in cross-section, and have electric and magnetic fields present at the aperture when excited. The process for determining the radiation patterns of these structures can separated into two operations.

- **Internal propagation –** this deals with determining the fields present at the aperture of the antenna.
- **External propagation** – this deals with predicting the far-field radiation pattern, and near field if required, based on the aperture field of the waveguide.

The following sections will discuss the underlying theory and the methods used in SCATTER-TNG to evaluate radiated fields. Furthermore, an SVD routine developed by (McCarthy 2014) to aid in the computation and interpretation of these radiation patterns is introduced.

2.6.1 Internal Propagation – Aperture Fields

The correct prediction of the radiation field depends significantly on the accurate description of the antenna's aperture field. Effectively, the aperture field becomes the source for the radiation field in the far-field (Olver et al. 2011). The field equivalence principle states that a radiating field $\boldsymbol{E}, \boldsymbol{H}$ at $z > 0$ caused by some source at $z < 0$ may also be obtained by introducing an imaginary conducting surface at $z = 0$, which has an electric current density $\boldsymbol{J_s}$ and magnetic current density $\boldsymbol{J_m}$ given by:

$$\boldsymbol{J_s} = \hat{\boldsymbol{n}} \times \boldsymbol{H_a} - \text{ surface current} \tag{2.6.1}$$

$$\boldsymbol{J_m} = -\hat{\boldsymbol{n}} \times \boldsymbol{E_a} - \text{magnetic surface current} \qquad (2.6.2)$$

Here, this imaginary surface represents the aperture of the antenna where $\boldsymbol{E_a}$ and $\boldsymbol{H_a}$ describe the tangential electric and magnetic fields at this new surface defined as the aperture plane. These $\boldsymbol{E_a}$ and $\boldsymbol{H_a}$ fields are obtained by solving the waveguide structure's internal problem.

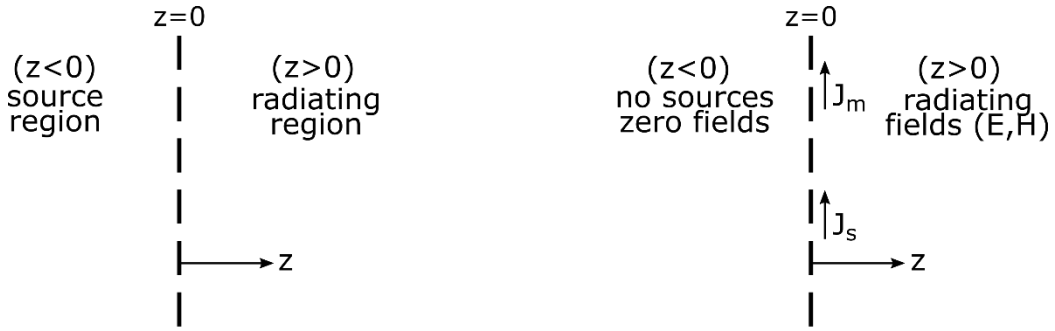

Figure 2-21: Demonstration of the Field Equivalence Principle applied to a plane aperture.

The modal fields described earlier in section 2.2.3 can be exploited to the determine the required electric and magnetic fields at the aperture. The aperture fields of pure waveguide modes in uniform sections have already been given in section 2.3. However, to assemble the final guide's full aperture field requires considering all of its modes, and each of their individual contributions with correct amplitude and phase. The respective electric and magnetic tangential aperture fields can be obtained from following equations:

$$\boldsymbol{E_a} = \sum_{\boldsymbol{i}}^{\boldsymbol{N}} A_i \cdot \boldsymbol{E_i} \qquad (2.6.3)$$

$$\boldsymbol{H_a} = \sum_{\boldsymbol{i}}^{\boldsymbol{N}} A_i \cdot \boldsymbol{H_i} \qquad (2.6.4)$$

where N gives the mode number being considered, A_i gives the relative amplitude of the mode and $\boldsymbol{E_i}$ or $\boldsymbol{H_i}$ gives the modal electric or magnetic field. The relative amplitudes of the propagating modes are required to obtain the exiting aperture field. Conveniently, the scattering parameters, introduced in section 2.3.3, describe how the modal amplitudes are transformed

between the input and output ports of the radiating structure. Using the $\boldsymbol{S}_{21}$ scattering parameter, an expression for the modal amplitudes at the exit aperture is obtained:

$$\boldsymbol{b}_2 = \boldsymbol{S}_{21} \cdot \boldsymbol{a}_1 \qquad (2.6.5)$$

where the column vector $\boldsymbol{a}_1$ gives the incident mode amplitudes that provide the excitation to port 1. Equation (2.6.5) ensures that the correct outgoing amplitudes, $\boldsymbol{b}_2$, for each modal field are obtained.

2.6.2 External Propagation – Radiation Fields

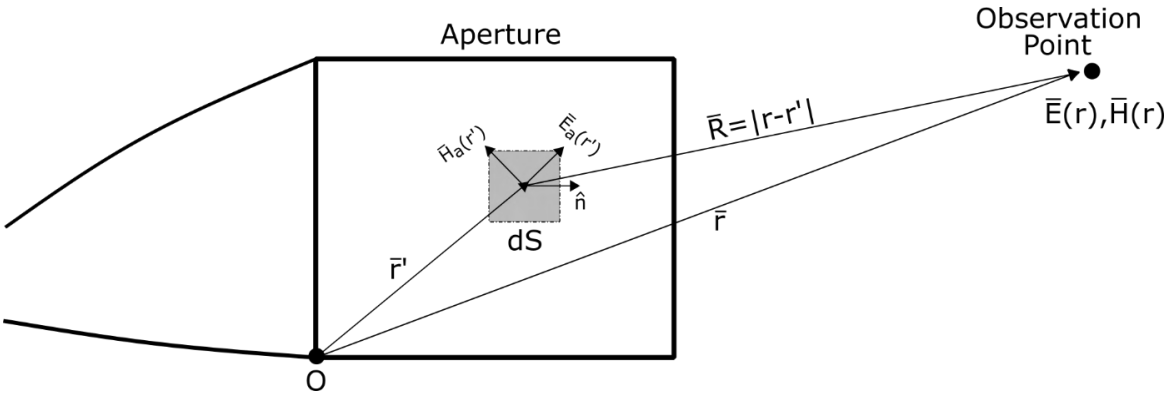

Figure 2-22: Shows the layout of the aperture field and its projection to a point in the far-field.

The aperture is aligned such that its surface normal $\hat{\boldsymbol{n}}$ is in the $+z$-direction, and aperture field is orientated in the *xy*-plane as in Figure 2-22. The solution to the inhomogeneous vector potential wave equation describes how the radiation field propagates due to a current density at some source position (C. A. Balanis 2012). In the *z*-direction this vector potential wave equation takes a familiar form:

$$\nabla^2 A_z + \beta^2 A_z = -\mu J_z \qquad (2.6.6)$$

where A_z is the z-component of the vector potentials, and J_z is the *z*-component of the current density present. The solution to this equation is given by:

$$A_z = \frac{\mu}{4\pi} \iiint_V J_z \frac{e^{-j\beta r}}{r} dv' \qquad (2.6.7)$$

For the generalised form of the wave equation, the remaining *x* and *y*-components must be considered. The source itself need not be located at the origin of the system and is defined by the primed coordinates (x', y', z') in the vector potential solution as given by:

$$\boldsymbol{A_s}(x,y,z) = \frac{\mu}{4\pi}\iiint_V \boldsymbol{J_s}(x',y',z')\frac{e^{-j\boldsymbol{\beta}\cdot\boldsymbol{R}}}{R}dv' \tag{2.6.8}$$

Equation (2.6.8) represents the vector potential field due to the electric current density. In a similar manner, the vector potential which exists as a result of solely magnetic current density is:

$$\boldsymbol{A_m}(x,y,z) = \frac{\epsilon}{4\pi}\iiint_V \boldsymbol{J_m}(x',y',z')\frac{e^{-j\boldsymbol{\beta}\cdot\boldsymbol{R}}}{R}dv' \tag{2.6.9}$$

Here, the length *R* gives the distance from any point at the source to the observation point and is expressed in the following manner from (C. Balanis 2016). If the source is assumed to be a thin dipole (i.e. $x' = y' = 0$), positioned along the *z*-axis then *R* becomes:

$$R = |\boldsymbol{R}| = |\boldsymbol{r} - \boldsymbol{r'}| = \sqrt{(x-x')^2 + (y-y')^2 + (z-z')^2} \tag{2.6.10}$$

$$R = \sqrt{x^2 + y^2 + (z-z')^2} = \sqrt{x^2 + y^2 + z^2 + (-2zz' - z'^2)} \tag{2.6.11}$$

$$R = \sqrt{r^2 + (-2rz'\cos\theta - z'^2)} \approx r - z'\cos\psi + \frac{1}{r}\left(\frac{z'^2}{2}\sin\psi\right) + \cdots \tag{2.6.12}$$

where

$$\begin{aligned} r^2 &= x^2 + y^2 + z^2 \\ z &= r\cos\psi \end{aligned} \tag{2.6.13}$$

here ψ represents the angle between $\boldsymbol{r}$ and $\boldsymbol{r'}$.

Using the binomial expansion, the radial component is approximated by the first two terms of the expansion. The remaining higher order terms of the binomial expansion tend to zero as the far-field zone ($\beta r \gg 1$) is approached, simplifying the radiation equations significantly. The radial distance component in the far-field $\boldsymbol{R}$, from any point (x', y', z') on the aperture plane to the observation point (x, y, z) can be assumed to be parallel to the radial distance $\boldsymbol{r}$ from the origin to the same observation point. Here, amplitude variations with depend on $R \approx r$, while phase variations are given by $R \approx r - r' \cos\psi$.

The aperture plane and the observation screen may be arbitrarily curved, however, it is common to assume that they are both flat. Effectively the volume integrals defined for the vector potentials can be reduced to surface integrals (Orfanidis 2008). Thus, the vector potentials from both current density sources on the aperture plane can be defined in the as:

$$\boldsymbol{A_s}(\boldsymbol{r}) = \mu \frac{e^{-j\beta r}}{4\pi r} \iint_A \boldsymbol{J_s}(\boldsymbol{r'}) e^{-j\boldsymbol{k}\cdot\boldsymbol{r'}}\, dx'dy' \qquad (2.6.14)$$

$$\boldsymbol{A_m}(\boldsymbol{r}) = \epsilon \frac{e^{-j\beta r}}{4\pi r} \iint_A \boldsymbol{J_m}(\boldsymbol{r'}) e^{-j\boldsymbol{k}\cdot\boldsymbol{r'}}\, dx'dy' \qquad (2.6.15)$$

For a flat aperture in the *xy*-plane, $\boldsymbol{k}\cdot\boldsymbol{r'}$ is expanded as:

$$\boldsymbol{k}\cdot\boldsymbol{r'} = k_x x' + k_y y' = k\cos\phi\sin\theta\, x' + k\sin\phi\sin\theta\, y' \qquad (2.6.16)$$

A common approximation made at this point is to assume the aperture fields are of type TEM. This assumes that these fields approximately satisfy the Huygens source definition i.e. assumes an orthogonal relationship between the electric and magnetic components ($E_{ax} = \eta_0 H_{ay}$) and ($E_{ay} = -\eta_0 H_{ax}$). By assuming the axial electric and magnetic fields approach zero at the guide aperture the aperture fields can be taken approximately as Huygens sources.

The integrals given in equations (2.6.14) and (2.6.15), which describes the radiation vectors, can be redefined in terms of the aperture fields present on the aperture plane. In these integrals the electric and magnetic field components can be separated from one another, simplifying the problem:

$$\boldsymbol{A_s}(\theta,\phi) = \mu\frac{e^{-j\beta r}}{4\pi r}\big(\hat{\boldsymbol{z}} \times \boldsymbol{g}(\theta,\phi)\big) = \mu\frac{e^{-j\beta r}}{4\pi r}\hat{\boldsymbol{z}} \times \iint_A \boldsymbol{H_a}(\boldsymbol{r'})e^{-j\boldsymbol{k}\cdot\boldsymbol{r'}}\,dx'dy' \qquad (2.6.17)$$

$$\boldsymbol{A_m}(\theta,\phi) = \epsilon\frac{e^{-j\beta r}}{4\pi r}\big(-\hat{\boldsymbol{z}} \times \boldsymbol{f}(\theta,\phi)\big) = \epsilon\frac{e^{-j\beta r}}{4\pi r} - \hat{\boldsymbol{z}} \times \iint_A \boldsymbol{E_a}(\boldsymbol{r'})e^{-j\boldsymbol{k}\cdot\boldsymbol{r'}}\,dx'dy' \qquad (2.6.18)$$

where $\boldsymbol{H_a} = \hat{x}H_{ax} + \hat{y}H_{ay}$ and $\boldsymbol{E_a} = \hat{x}E_{ax} + \hat{y}E_{ay}$. Likewise, the two expression for $\boldsymbol{f}, \boldsymbol{g}$ can be resolved into their separate components. The radiated E-field, in spherical coordinates, is given by:

$$E_\theta = jk\frac{e^{-jkr}}{4\pi r}\big[(f_x\cos\phi + f_y\sin\phi) + \eta\cos\theta\,(g_x\cos\phi - g_y\sin\phi)\big] \qquad (2.6.19)$$

$$E_\phi = jk\frac{e^{-jkr}}{4\pi r}\big[\cos\theta\,\big(f_y\cos\phi - f_x\sin\phi\big) - \eta(g_x\cos\phi + g_y\sin\phi)\big] \qquad (2.6.20)$$

Applying Huygens principle simplifies the radiated E-field given in equations (2.6.19) and (2.6.20) to:

$$E_\theta = jk\frac{e^{-jkr}}{4\pi r}\big[(1+\cos\theta)(f_x\cos\phi + f_y\sin\phi)\big] \qquad (2.6.21)$$

$$E_\phi = jk\frac{e^{-jkr}}{4\pi r}\big[(1+\cos\theta)\big(f_y\cos\phi - f_x\sin\phi\big)\big] \qquad (2.6.22)$$

where the $(1+\cos\theta)$ term is known as the obliquity factor.

For aperture antennas it is common practice to present the polarised co-polar and cross-polar fields. Using Ludwig's third definition, these can be readily obtained from the spherical coordinates of the radiated E-field (Olver et al. 2011). The co-polar and cross-polar fields are expressed in terms of spherical coordinates as:

$$E_{co} = E_\theta \sin\phi + E_\phi \cos\phi \tag{2.6.23}$$

$$E_{xp} = E_\theta \cos\phi - E_\phi \sin\phi \tag{2.6.24}$$

This definition assumes the aperture's electric field is directed along the *y*-axis. The co-polar component represents the field aligned with the preferred direction and the cross-polar component represents its orthogonal pair, counter to the preferred direction.

2.6.3 Far-Field Representation - Rectangular and Circular Apertures

In sections 2.3.1 and 2.3.2, the expressions for the electric and magnetic modal fields are presented for rectangular and cylindrical geometries. The radiated far-field from these waveguide sections can be obtained by taking the Fourier transform of the field component of interest. Thus, the far-field radiation pattern for a rectangular aperture is given in Cartesian coordinates as:

Electric Fields

$$f_x(\theta_0, \phi_0) \cong \int_S E_{ax}(x, y) \exp(jk(x \sin\theta_0 \cos\phi_0 + y \sin\theta_0 \sin\phi_0))\ dS \tag{2.6.25}$$

$$f_y(\theta_0, \phi_0) \cong \int_S E_{ay}(x, y) \exp(jk(x \sin\theta_0 \cos\phi_0 + y \sin\theta_0 \sin\phi_0))\ dS \tag{2.6.26}$$

Magnetic Fields

$$g_x(\theta_0, \phi_0) \cong \int_S H_{ax}(x, y) \exp(jk(x \sin\theta_0 \cos\phi_0 + y \sin\theta_0 \sin\phi_0))\ dS \tag{2.6.27}$$

$$g_y(\theta_0, \phi_0) \cong \int_S H_{ay}(x, y) \exp(jk(x \sin\theta_0 \cos\phi_0 + y \sin\theta_0 \sin\phi_0))\ dS \tag{2.6.28}$$

In a similar manner, the far-field radiation pattern from a cylindrical aperture is obtained. For convenience the Fourier transform is performed in cylindrical coordinates, which gives:

Electric Fields

$$f_x(\theta_0, \phi_0) \cong \int_0^{\rho} \int_0^{2\pi} E_{ax}(\rho, \phi_a) \exp\big(jk(\rho \sin\theta_0 \cos(\phi_0 - \phi_a))\big)\, \rho d\rho d\phi_a \qquad (2.6.29)$$

$$f_y(\theta_0, \phi_0) \cong \int_0^{\rho} \int_0^{2\pi} E_{ay}(\rho, \phi_a) \exp\big(jk(\rho \sin\theta_0 \cos(\phi_0 - \phi_a))\big)\, \rho d\rho d\phi_a \qquad (2.6.30)$$

Magnetic Fields

$$g_x(\theta_0, \phi_0) \cong \int_0^{\rho} \int_0^{2\pi} H_{ax}(\rho, \phi_a) \exp\big(jk(\rho \sin\theta_0 \cos(\phi_0 - \phi_a))\big)\, \rho d\rho d\phi_a \qquad (2.6.31)$$

$$g_y(\theta_0, \phi_0) \cong \int_0^{\rho} \int_0^{2\pi} H_{ax}(\rho, \phi_a) \exp\big(jk(\rho \sin\theta_0 \cos(\phi_0 - \phi_a))\big)\, \rho d\rho d\phi_a \qquad (2.6.32)$$

2.6.4 Singular Value Decomposition Applied to Far-Field Propagation

An antenna's far-field radiation pattern is dependent on its aperture field. For single moded horns the aperture field is composed of a single mode, some single mode horns may use contributions from higher order modes to improve the performance i.e. shaped horns, but ultimately only one mode is present in the aperture. While in multimoded horns, the aperture field is composed of the contributions from many partially coherent modes which propagate in the structure. As such, the resulting radiation patterns behaviour can be challenging to understand.

A singular value decomposition (SVD) approach, as detailed in McCarthy (2014), allows for the modeset required for field reconstruction to be reduced to a subset of effective contributing modes or 'singular' modes, without any loss in accuracy. These form a new basis set to

represent the system, meaning they are orthogonal and independent of one-another. Singular modes may be neither TE or TM modes, but can be a combination of both i.e. the hybrid HE_{11} would be a valid singular mode of a corrugated type horn. By performing SVD the valid mode combinations and their contributions are determined. Allowing for a greater knowledge of the devices behaviour for the singular modes present. SVD can also be implemented to achieve significant performance improvements in the analysis of multi-mode structures. For an arbitrary field excitation at the aperture, the known singular modes obtained from SVD allow the excitation to be reduced to mode amplitudes which propagate in the structure. This can lead to reduced simulation time for repeated arbitrary field excitations.

For $\boldsymbol{S}$ an $m \times n$ matrix, which represents a scattering parameter (normally S_{21} is considered). The SVD of this matrix is given by:

$$\boldsymbol{S} = \boldsymbol{U} \cdot \boldsymbol{\Sigma} \cdot \boldsymbol{V}^{+} \qquad (2.6.33)$$

Here each of these elements have the following meaning:

- $\boldsymbol{U}$ is an $m \times m$ unitary matrix, the columns of $\boldsymbol{U}$ are known as the left singular vectors $\boldsymbol{u_i}$.
- $\boldsymbol{\Sigma}$ is an $m \times n$ diagonal matrix, where the diagonal elements are the singular values of $\boldsymbol{S}$. These are indexed by $\sigma_i = \Sigma_{ii}$ arranged in order of decreasing value, of these singular values only β elements are non-zero and this gives the length of singular values which needs to be considered
- $\boldsymbol{V}^{+}$ is an $n \times n$ unitary matrix, where the $+$ indicates the pseudoinverse or conjugate transpose such that $\boldsymbol{V}^{+} \cdot \boldsymbol{V} = \boldsymbol{I_n}$. The columns of V are known as the right singular vectors $\boldsymbol{v_i}$.

It can be shown that the left singular vectors are the eigenvectors of $\boldsymbol{S} \cdot \boldsymbol{S}^{+}$, and likewise the right singular vectors are the eigenvectors of $\boldsymbol{S}^{+} \cdot \boldsymbol{S}$. The singular values are given by the non-zero roots of the eigenvalues from these expressions. Vectors $\boldsymbol{U}$ and $\boldsymbol{V}$ are said to be unitary meaning their columns form a set of orthonormal vectors, which can be taken as a basis set to represent $\boldsymbol{S}$.

$$\boldsymbol{S} = \boldsymbol{U} \cdot \boldsymbol{\Sigma} \cdot \boldsymbol{V}^{+} \tag{2.6.34}$$

$$\boldsymbol{S} \cdot \boldsymbol{V} = \boldsymbol{U} \cdot \boldsymbol{\Sigma} \cdot \boldsymbol{V}^{+} \cdot \boldsymbol{V} = \boldsymbol{U} \cdot \boldsymbol{\Sigma} \tag{2.6.35}$$

$$\boldsymbol{S}^{+} \cdot \boldsymbol{S} \cdot \boldsymbol{V} = \boldsymbol{V} \cdot \boldsymbol{\Sigma}^{+} \cdot \boldsymbol{U}^{+} \cdot \boldsymbol{U} \cdot \boldsymbol{\Sigma} \cdot \boldsymbol{V}^{+} \cdot \boldsymbol{V} = \boldsymbol{V} \cdot \boldsymbol{\Sigma}^{+} \cdot \boldsymbol{\Sigma} \tag{2.6.36}$$

Singular modes are obtained from the basis sets contained within the columns of the two unitary vectors. The aperture fields of the horn for an arbitrary excitation can be reconstructed using them as a basis set instead of all individual waveguide modes. Singular value theory gives the following relation: $\boldsymbol{S} \cdot \boldsymbol{v_i} = \sigma_i \boldsymbol{u_i}$. It is clear from this that the right eigenvectors can be used as a basis to represent the input modes and the left eigenvectors can represent the output modes, once they are scaled by their corresponding singular value. Assuming correctly normalised mode coefficients $\boldsymbol{A}$, the input field can be expressed as:

$$\mathbf{K}_{in} = \sum_{i} A_i \boldsymbol{v_i} = \boldsymbol{V} \cdot \boldsymbol{A} \tag{2.6.37}$$

$$\mathbf{K}_{in}^{+} \cdot \mathbf{K}_{in} = \boldsymbol{A}^{+} \cdot \boldsymbol{V}^{+} \cdot \boldsymbol{V} \cdot \boldsymbol{A} = \sum_{i} |A_i|^2 \tag{2.6.38}$$

This gives the total power in the input field. The output field is obtained by applying the scattering parameter being considered. This transforms the singular vector at the input field to the output as the scattering matrix operates on the input modes.

$$\mathbf{K}_{out} = \sum_{i} A_i \boldsymbol{S} \cdot \boldsymbol{v_i} = \boldsymbol{S} \cdot \boldsymbol{V} \cdot \boldsymbol{A} = \boldsymbol{U} \cdot \boldsymbol{\Sigma} \cdot \boldsymbol{V}^{+} \cdot \boldsymbol{V} \cdot \boldsymbol{A} = \boldsymbol{U} \cdot \boldsymbol{B} \tag{2.6.39}$$

$$\boldsymbol{B} = \boldsymbol{\Sigma} \cdot \boldsymbol{A} \Rightarrow B_i = \sigma_i A_i \tag{2.6.40}$$

$$\mathbf{K}_{out}^{+} \cdot \mathbf{K}_{out} = \boldsymbol{A}^{+} \cdot \boldsymbol{\Sigma}^{+} \cdot \boldsymbol{U}^{+} \cdot \boldsymbol{U} \cdot \boldsymbol{\Sigma} \cdot \boldsymbol{A} = \sum_{i} |\sigma_i|^2 |A_i|^2 = \sum_{i} \alpha_i |A_i|^2 \qquad (2.6.41)$$

The output field can be then expressed as in equation (2.6.41). Here $\boldsymbol{B}$ represents the effective output mode coefficients which are related to the effective input mode coefficients through the singular values of $\boldsymbol{S}$. Using this method, the effective modes which contribute meaningfully to propagation of power can be isolated, as can their contribution to the far-field of the system.

2.7 Design and Implementation of Pure and Multimode Horns

The choice of feed horn is very much dependent on the application of the instrument. Whether for communications or measurement, the application of the device places requirements on the type of feed to be used. For example, the size, bandwidth, efficiency and co/cross-polar levels are all factors which must be considered when choosing the feed structure. A short summary of each type of feed modelled in this thesis is given.

2.7.1 Pure-Mode Horns

Pure-Mode type horns, as the name suggests, have aperture fields composed of a single waveguide mode only and as such single mode dependent radiation patterns. Compared to other devices, the geometry of the structure does not influence the radiation field as significantly. The radiation pattern is highly dependent on the transverse components of the aperture field. Common structures that may produce single moded horns are conical and pyramidal geometries.

Pure-Mode horns can be split into two groups based on the ratio of the aperture size and the desired wavelength of operation. These groups are (i) small aperture horns $\sim 1.5\ \lambda$ (ii) medium aperture horns $\sim 6\ \lambda$.

- For small aperture pure mode horns, the relationship between the geometry of the device and the structures radiation pattern are more strongly dependent on one another. As such, the precise geometry of the horn must be known in order to accurately model the structure. This is due to the currents outside the structure further contributing to the observed field pattern. These types of horns are employed for use in small diameter front fed reflector antennas where there a limits on mass and volume of the detector system.

- Medium aperture pure mode horns are not suitable for high performance feeds since their radiation patterns often have relatively high cross-polar levels. These types of structures are more commonly employed as separate antenna elements rather than feeds. Pyramidal type horns are commonly used as standard gain horns since they can be manufactured accurately and are well understood.

2.7.1.1 Conical Pure-Mode Horns

In conical pure-mode horns the TE_{11} mode exists as the fundamental singular mode which dominates the aperture field. In general, these types of structures make for poor feed horns as they have poor radiation pattern symmetry and high cross-polar levels. High cross-polar levels are not desirable and limit the applicability of these structures in high performance feed devices. The cross-polar levels here are a function of the aperture diameter. By reducing the aperture diameter, the cross-polar fields may be also reduced or cancelled resulting in a better performing horn in terms of lower cross-polar levels; typically this occurs for $D \approx 1.15\,\lambda$. The co-polar pattern is a function of the phase centre s-factor $\left(s = \frac{a^2}{2\lambda L}\right)$ for increasing phase factor values wider beam patterns are observed along with increased asymmetry between the E and H fields.

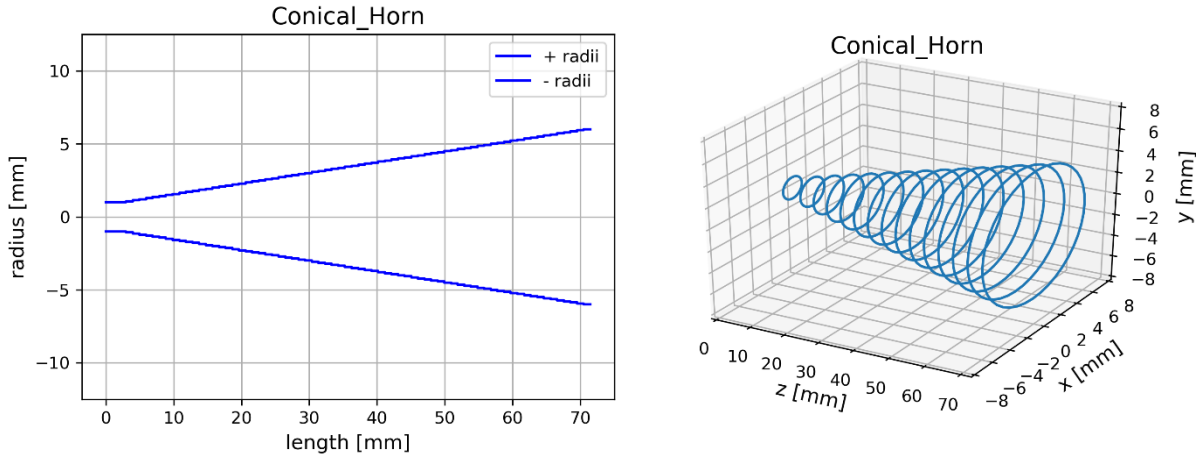

Figure 2-23: Shows the profile of the conical structure and a 3D visualisation of the feed.

Broader beams and bandwidth leads to reduced gain and poor aperture efficiency. When designing conical feed horns there is a delicate balancing act to obtain acceptable cross-polar levels, desired bandwidth and minimum losses at the aperture field. These factors greatly influence the design of the horn. The pure-mode conical horn illustrated in Figure 2-23 taken from Olver, Clarricoats, et al. (2011), has an aperture diameter of 4λ and a semi-flare angle of 5°, it was designed for operation at 100 GHz. As observed in Olver, Clarricoats, et al. (2011)

and discussed earlier, this structure is expected to have quite high cross-polar levels and have poor symmetry between the E and H-plane co-polar patterns. From the simulation of this horn

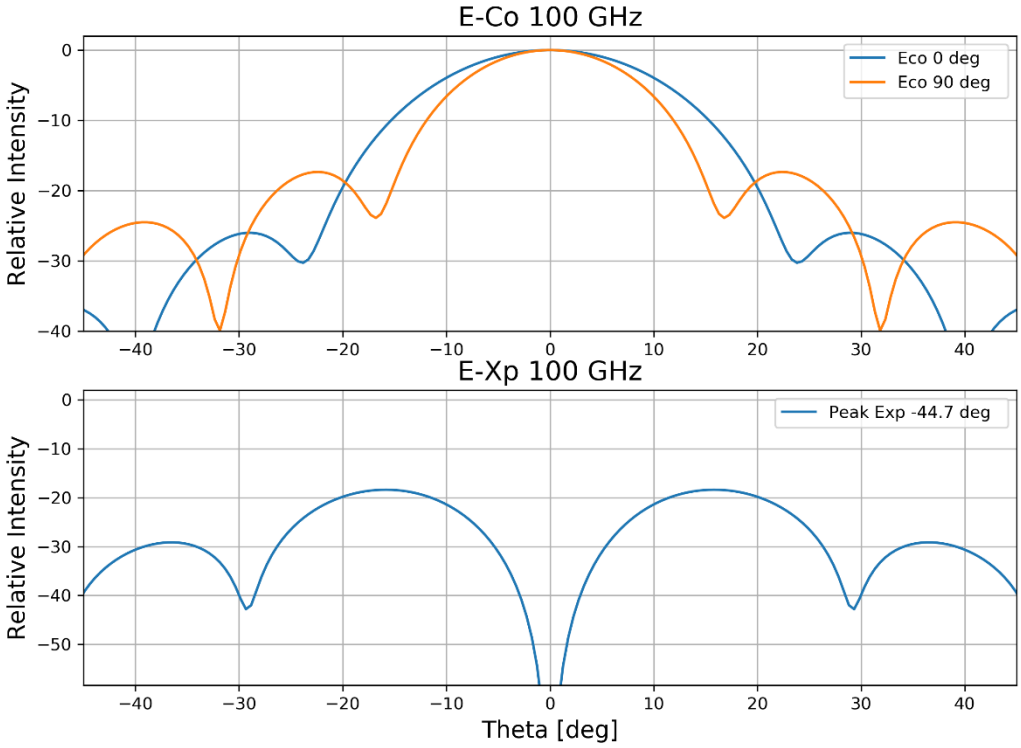

Figure 2-24: Plot of the co-polar and cross-polar fields for the conical case; it is observed that there is poor symmetry in the co-polar field cuts and quite high peak cross-polar levels.

performed, shown in Figure 2-24, peak cross-polar levels of ~ -18 dB and high asymmetry between the co-polar cuts are observed. Such radiation patterns are typical of pure mode conical devices.

2.7.1.2 Pyramidal Pure-Mode Horns

In Pyramidal Pure-Mode horns the TE_{10} is the fundamental mode which dominates the aperture field of horn. These structures have either a rectangular or square aperture and can be thought of as being composed of two sectoral horns. One which will determine the E-field "E-field Horn" and another which will determine the H-field "H-field Horn". The phase factors or s-factors which influence the overall design of the horn for the E-field and H-field horns are given by

$$s_H = \frac{A^2}{8\lambda R_H}, s_E = \frac{B^2}{8\lambda R_E} \tag{2.7.1}$$

Where A and B represent the width and height dimensions of the guide, while R_H and R_E give the wall length from the centre of the E-field and H-field horns throat to the aperture. As before in the conical case, the cross-polar levels are linked to the aperture dimensions. For increasing aperture size, a greatly reduced cross-polar component is observed below acceptable levels ~ -40 dB. The range of application for pyramidal horns is limited by the asymmetry of the co-polar patterns. As they are essentially found from the two different sectoral horns which compose the pyramidal structure they do not interact in the same manner as in the conical case. A pure-mode pyramidal horn shown in Figure 2-25, again taken from (Olver et al. 2011) has a square aperture of width 5λ and a semi-flare angle of $12°$. It was also designed for operation at 100 GHz. The structure is fed by a WR10 waveguide.

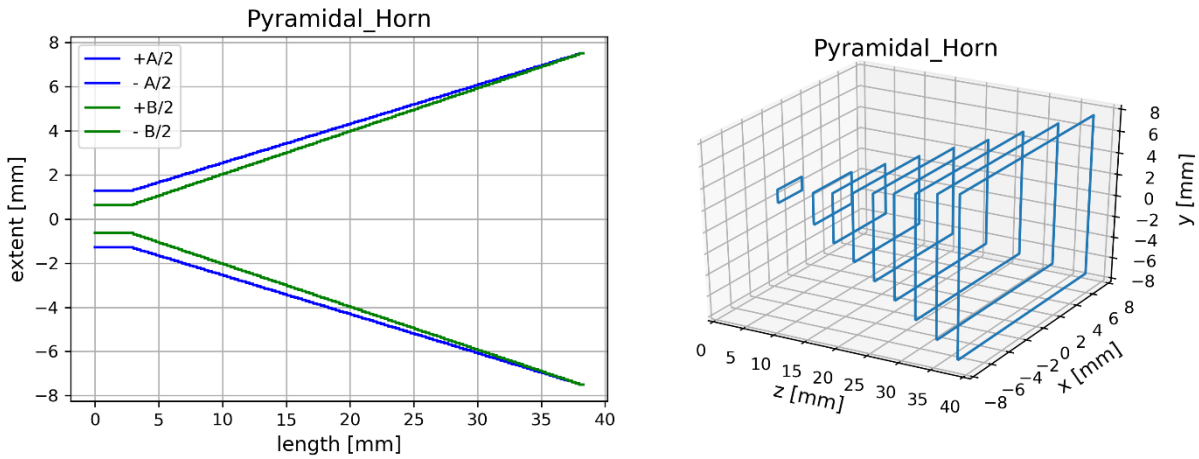

Figure 2-25: Shows the profile of the pyramidal structure and a 3D visualisation of the feed.

For this structure, using (Olver et al. 2011) as a benchmark, peak cross-polar levels of the order of -40 dB with respect to the co-polar values are expected with co-polar cuts that have poor symmetry. As observed in Figure 2-26, simulation gives the expected low cross-polar levels and asymmetric co-polar radiation pattern.

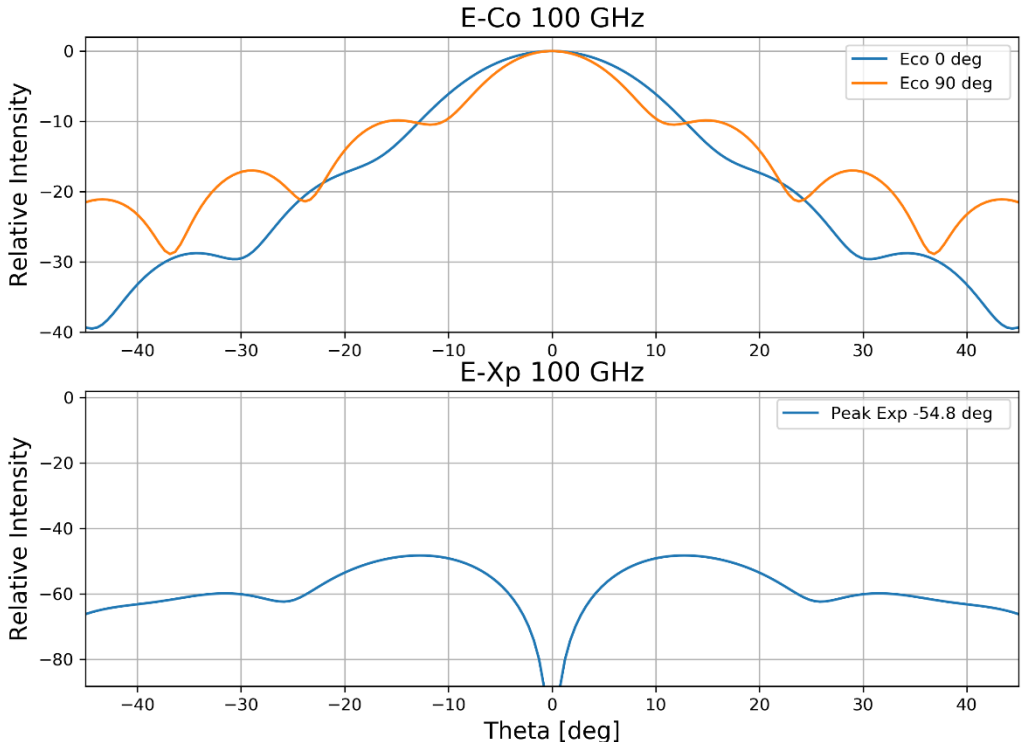

Figure 2-26: Plot of the co-polar and cross-polar fields for the pyramidal case; it is observed that there is poor symmetry in the co-polar field cuts and reduced peak cross-polar levels compared to the conical case.

2.7.2 Hybrid-mode and Multimode Horns

There is an important distinction to be made when one considers multi-moded horns; a true multi-moded horn is defined as having many modes propagating end-to-end in the structure. As such, the aperture field will be made of a combination of the modal fields present in the aperture. In contrast, single-moded waveguide's aperture field is only composed of the fundamental mode for that structure. Single-moded horns can however take advantage of higher order modes to improve their performance but are not considered true multi-moded horns but rather hybrid-mode horns by definition. The number of non-negligible singular values obtained from the SVD procedure will indicate whether the structure is multimoded ($s > 1$) or single-moded ($s = 1$). An example of a multimoded structure is presented in the last section of this chapter.

As a natural progression from pure-mode horns, the hybrid-mode horns are discussed. The aperture field of hybrid-mode horns is no longer purely composed of the fundamental waveguide mode. Instead, there will be a combination of desired modes which make up the aperture field which have been selected to enhance the radiation pattern of the fundamental mode. There is a difficulty in designing these structures such that the desired modes are generated and are propagated efficiently through the device. Commonly, these devices are split

into two classes (i) shaped pattern horns and (ii) tracking horns. Only shaped pattern horns are considered here (Olver et al. 2011).

In shaped pattern horns, higher-order modes are added with the correct phase and amplitude to the fundamental mode to improve the horn's radiation and efficiency performance. In the design process, certain modes are selected in the aperture of the horn so that the desired radiation pattern can be achieved. To excite these new modes suitable geometric additions must be made to the smooth walled horns already introduced in the last section. Here, higher order modes can be excited via the introduction of a sharp discontinuity or by introducing a dielectric section, effectively modes can be made to propagate by changing the geometry or the medium. The discontinuity is typically followed by a phasing section to phase the modes in the correct ratio.

The transitions selected to excite particular waveguide modes are highly frequency dependent i.e. beyond an upper frequency limit undesired modes may begin to propagate as their cut-off frequencies are exceeded. As such, the operational bandwidth of shaped horns is typically limited i.e. structures are limited to operate in particular wavelength ranges. Shaped pattern horns are typically designed to improve certain performance factors of the horn:

- to reduce the cross-polar levels and improve co-polar pattern symmetry
- to alter the basic shape of a Gaussian co-polar pattern; this can make illumination of the reflector more uniform with a change in angle, increasing the overall efficiency, or
- to specifically match the focal region fields of reflector antennas.

The shaped pattern or spline horn design shown in Figure 2-27 was developed as one focal plane solution for the proposed COrE (Cosmic Origins Explorer) project (Bouchet et al. 2010). This is a single band device with an operating range between 85 – 115 GHz. This design is optimised for low return loss and high co-polar symmetry and Gaussicity. In Figure 2-27 the COrE horn structure is shown. By applying this shaped pattern to the horn's geometry much improved radiation performance versus conventional conical structures can be achieved. Simulated radiation patterns for this horn can be seen in Figure 2-28.

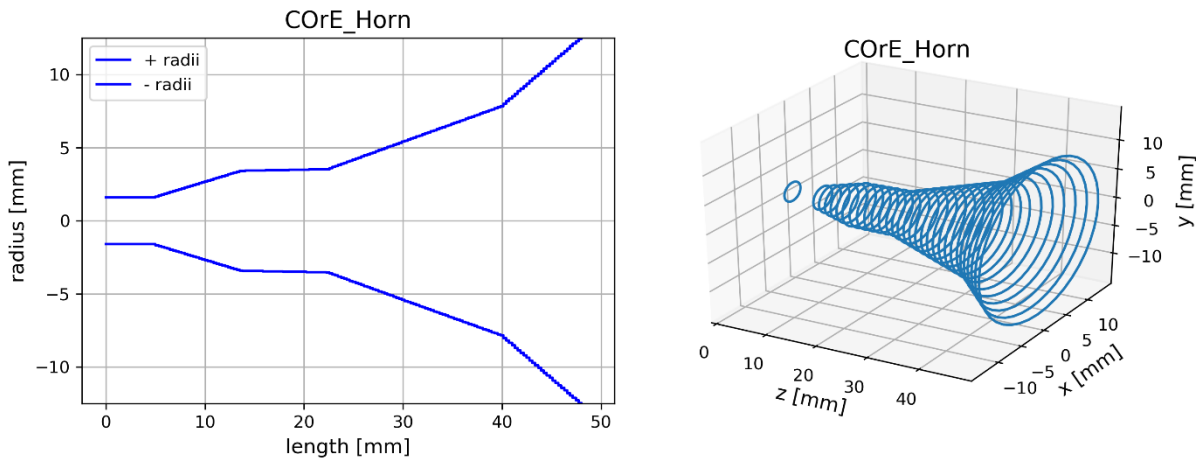

Figure 2-27: Shows the profile of the COrE feed and a 3D visualisation of the feed.

Here cross-polar levels are below -40 dB and there is excellent symmetry observed in the co-polar components. This is achieved by the excitation of higher-order modes in the shaped structure which has been optimised to combine modes with the fundamental TE_{11} mode in the correct manner. A similar approach is used in corrugated structures, however, shaped horns have the advantage of being easier to manufacture compared to corrugated horns (Granet, Bolton, and Moorey 2004).

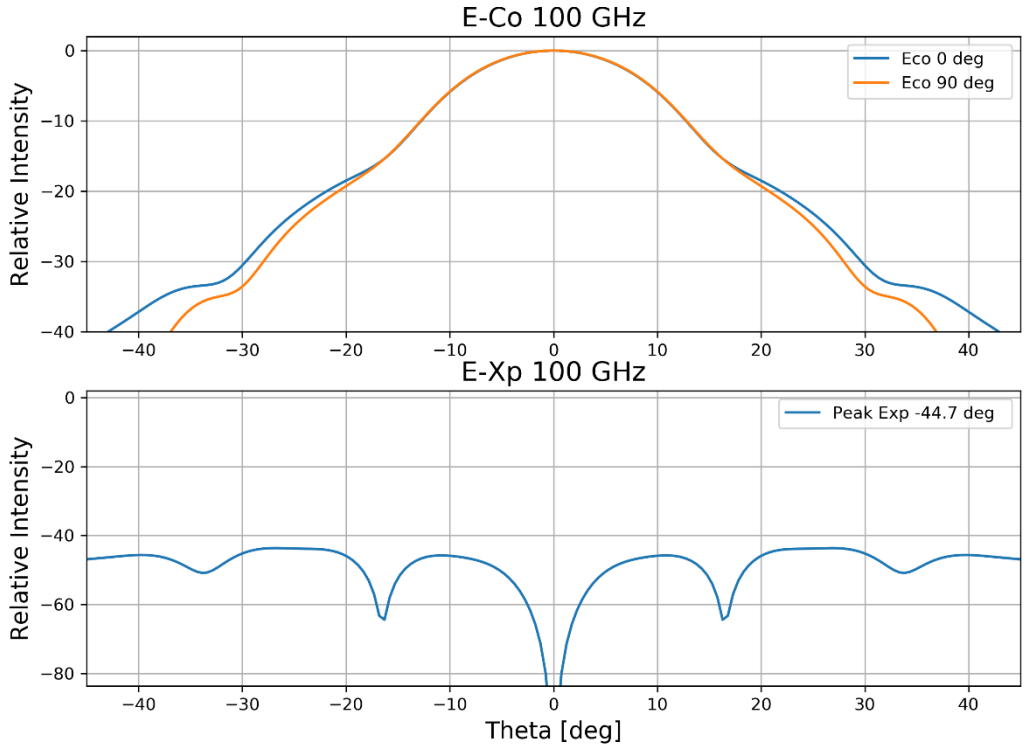

Figure 2-28: Plot of the co-polar and cross-polar fields for the COrE horn; it is observed that there is excellent symmetry in the co-polar field cuts and low peak cross-polar levels.

2.7.3 Corrugated Horns

Corrugated horns have become the favoured feed antenna for use in reflector antennas for a wide range of applications including commutations and remote sensing where high performance is required. These feeds have superior performance compared to their smooth walled counterparts. In their radiation patterns, high co-polar symmetry is observed along with exceptionally low cross-polar levels. High-performance operation is dependent on the internal structure of the horn, which alters the field pattern. Here the field is changed such to provide the desirable axial beam symmetry, low-side-lobes and low cross-polarisation, over a certain bandwidth.

These criteria can only be met when the horn produces an aperture electric field which has almost no curvature. Some slight non-linearity is required to cancel all cross-polar components. The linear fields required cannot be produced by a guide which supports TE or TM modes only since these inherently have some curvature associated with their field patterns. Only hybrid modes, a combination of TE and TM modes, can produce the desired linear field.

In the design of corrugated horn structures, one typically begins with a list of desired specifications and during the developmental stages the design is analysis and altered to obtain the ideal radiation properties and input impedance of the device. Typically, there are four main parts to consider when designing a corrugated horn (Olver et al. 2011).

- **Aperture Diameter –** An appropriate aperture diameter must be selected to give the desired co-polar beam width. However, there is an inherent trade of between aperture diameter and flare angle which must be considered.
- **Flare Angle and Horn Profile –** Are selected to satisfy the horns length and co-polar requirement obtained from the horns specifications. As the flare angle is increased, the influence of the spherical phase cap becomes dominant and the dependence on the aperture diameter is lost. There are advantages and disadvantages to wide-flare angle horns and profiled horns.
- **Corrugation Geometry –** The geometry of the corrugation must be chosen to give the minimal cross-polarisation levels at the desired central frequency. For a large aperture this requires the corrugations to be $\sim\frac{1}{4}\lambda$ in depth, if there are a large number of corrugations per wavelength. For shorter wavelengths, the optimal depth increases as it also does if there are fewer corrugations per wavelength. If slots are less than this

quarter wavelength value, inductive reactance can be generated and the EH_{11} mode can be excited. This is a surface wave mode and has a concentration of power near the boundary walls and causes high levels of cross-polarisation (Abbas-Azimi, Mazlumi, and Behnia 2009).

- **Throat Region –** The throat of the horn should be designed to give a good impedance match to the smooth walled input selection, allowing for efficient transfer of power between the horn and throat sections. Typically a TE_{11} mode is matched with a hybrid HE_{11} mode in the corrugated section. To achieve this, the corrugation depth can be tapered from the first few slots $\sim\frac{1}{2}\lambda$ down to the operational depth within the corrugated device. This gradual increase in slot depth can avoid the excitation of the EH_{11} mode (Abbas-Azimi, Mazlumi, and Behnia 2009).

The feed horns designed for the QUBIC (Q & U Bolometric Interferometer for Cosmology) mission are an example of corrugated structures (Scully et al. 2016). These are dual-band devices with an operational range of 120 – 240 GHz (single-moded $120 - 170$ GHz, multi-moded $200 - 240$ GHz). At the higher frequency range the QUBIC horn becomes multimoded as higher order modes reach their cut-off frequencies and begin to propagate. The geometry of a QUBIC type horn is given in Figure 2-29.

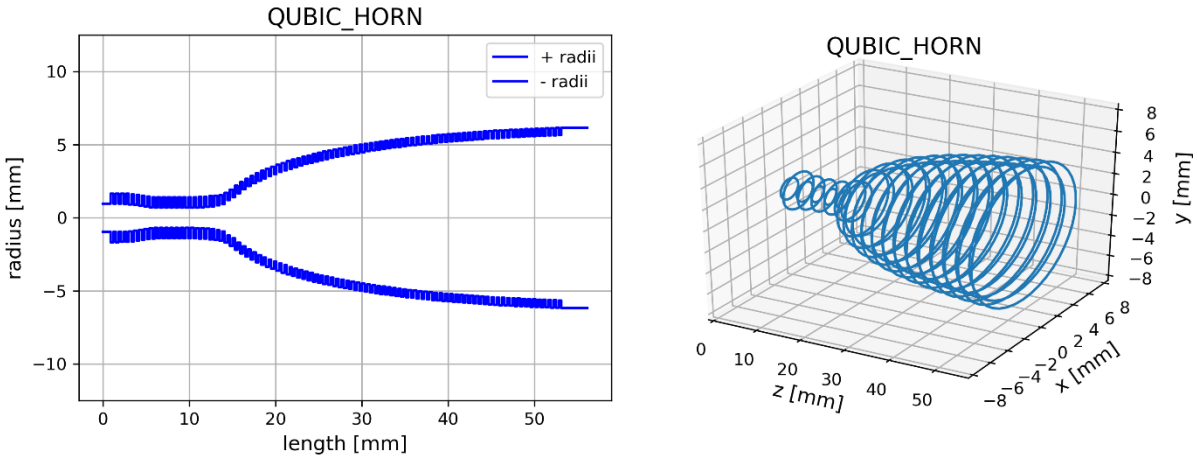

Figure 2-29: Shows the profile of the QUBIC feed and a 3D visualisation of the feed.

The single moded far-field pattern for the frequency range ($120 - 170$ GHz) is shown in Figure 2-30, and is consistent with the predictions made earlier. The cross-polar levels are at –40 dB and there is excellent symmetry in the co-polar field cuts due to the formation of the hybrid HE_{11} mode as desired.

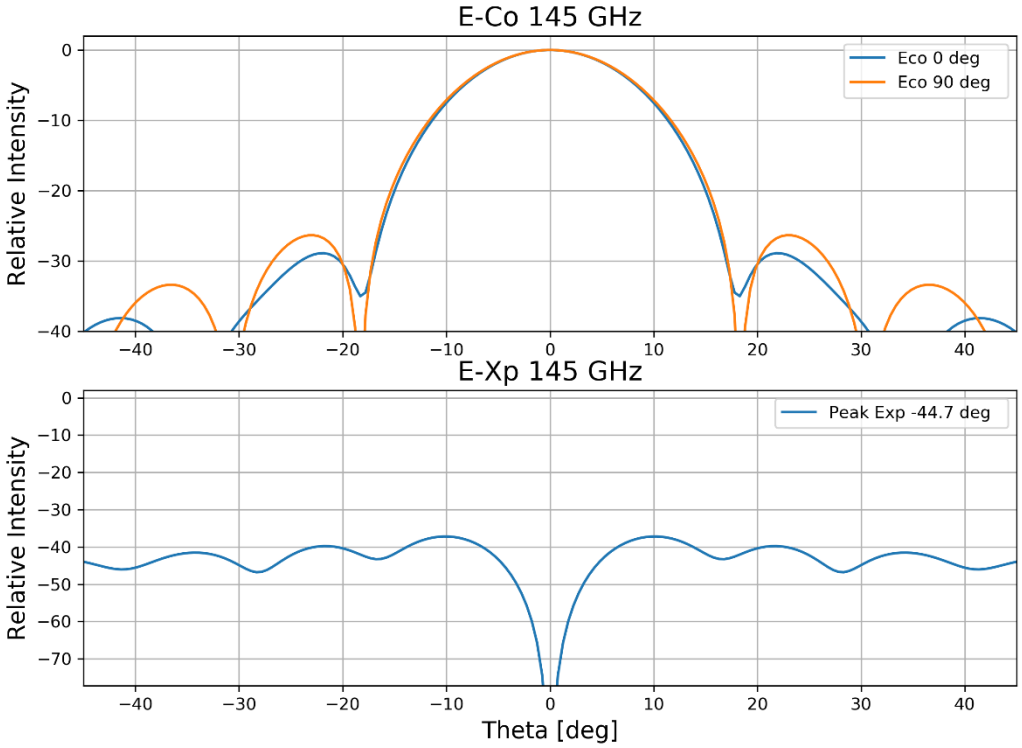

Figure 2-30: Plot of the co-polar and cross-polar fields for the QUBIC horn; it is observed that there is excellent symmetry in the co-polar field cuts and quite low peak cross-polar levels.

In general, for the multi-moded corrugated structures, the cross-polar levels tend to increase with the inclusion of higher order modes. The co-polar patterns shape is highly dependent on the relative phasing of the modes that exist in the guide, which is controlled by the horn's profile (A. D. Olver et al. 2011). Again, this must be tailored to specific design criteria for the application of the multimoded structure.

Although the QUBIC horn has a multimoded range it is designed such that much of the co-polar symmetry from the single moded case is retained and the cross-polar levels remain quite low. As shown in Figure 2-31, there is good symmetry in the co-polar cuts above -15 dB and the cross-polar levels have increased but remain below -20 dB. However, the QUBIC horn cannot be considered an example of a truly multimoded horn. The characteristic of true multimoded horns are that its co-polar field becomes flat and symmetry between the cuts is lost. In chapter 6, the SAFARI type horn provides an example of a truly multimoded waveguide.

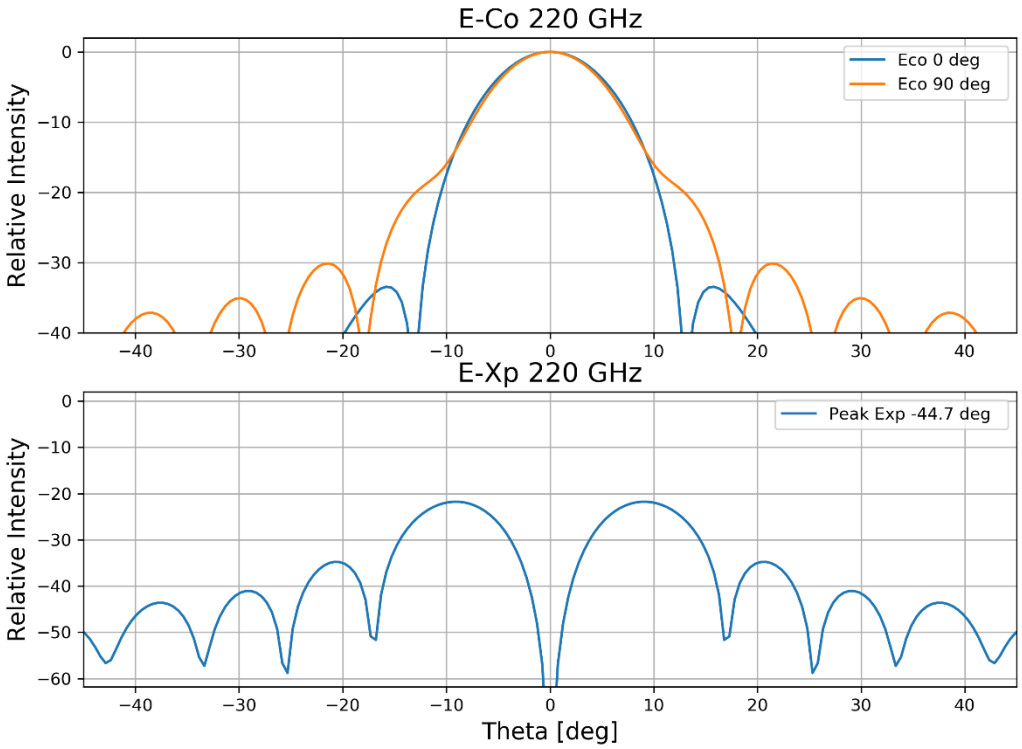

Figure 2-31: Plot of the Co-polar and Cross-polar fields for the QUBIC horn multimode case; it is observed that there is good symmetry in the co-polar field cuts and acceptable peak cross-polar levels.

2.8 Summary

This chapter introduces the new theoretical framework upon which S-TNG is built. The key components being the reformulation of the mode matching methods in terms of auxiliary potential functions, a completely new mechanism for mode normalisation and the derivation of the line integral form of the common mode coupling integrals (i.e. the common B, C and D types shown in section 2.4.2). The accuracy of this new formulation is demonstrated throughout this chapter with direct comparison to industry standard software CST Microwave Studio. Combined with the cascading methods, shown in section 2.5, the ability to model complete waveguide structures is achieved. Finally, for completeness the methods necessary for examining the radiation characteristics of horn antenna's (aperture field calculations, Fourier transforms and singular value decomposition) are discussed, implemented, and demonstrated in sections 2.6 and 2.7.

Chapter 3 – Extension of Mode-Matching Methods

As waveguide technologies continue to be developed for use in millimetre and sub-millimetre applications, the need for their accurate and efficient characterisation remains. Many of these new devices rely on exploiting multi-moded operation and operate in higher frequency bands. However, a more comprehensive approach is required to correctly predict the behaviour of these structures than presented in chapter 2. In particular, the assumption of ideal surfaces (i.e. perfect electrically conducting boundaries) may no longer be entirely valid. At higher frequencies the surface impedance $Z_s(\omega)$, due the finite wall conductivity of the waveguide, approaches non-negligible levels. Furthermore, in multi-moded structures the necessary higher order modes will have their fields distributed away from the centre of the guide. Thus, there is potential for power dissipation from the higher order modes through the non-PEC walls, and the PEC assumption may no longer be appropriate.

To overcome this, the mode-matching methods are extended to consider finite wall conductivity along the boundary. Here the boundary is assumed to be a good conductor, but with non-zero surface impedance. These surfaces are referred to as "lossy" throughout this chapter. The extension to the mode-matching method is based on work presented in J Shafii and Vernon (2002) and Wade and Macphie (1990), where the physical foundations of a modal description of the operation of such lossy guides and junctions were first discussed. When non-zero surface impedance is assumed due to the physical surface parameters, such as finite wall conductivity, the boundary conditions considered previously change. Most importantly the tangential electric field is no longer zero along the boundary as illustrated in Figure 3-1.

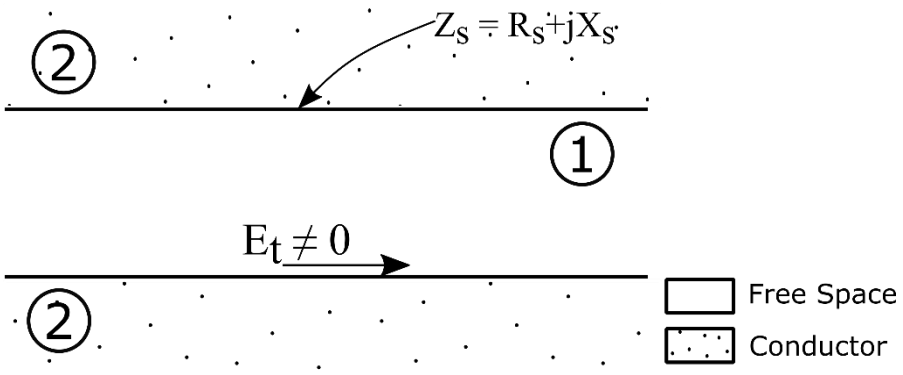

Figure 3-1: Shows the necessary non-zero tangential electric field along the interface between free-space and boundary wall of finite conductivity.

This has consequences for both the uniform guide and junction sections, which will be covered in the following sections.

In line with the lossy waveguide sections introduced in this chapter, a method to model an absorber layer using the mode-matching methods is presented in section 3.3. The method developed by (Doherty 2012) is re-considered, where the absorber layer is treated as an infinitely thin layer with sheet resistance R_s. Moreover, the absorber layer can now have any arbitrary shape via application of the contour-integral approach presented in chapter 2. This will allow for characterisation and optimisation of cavity or waveguide coupled absorber sections.

As the device's operational frequency increases, the waveguide dimensions are reduced correspondingly. As such, high frequency components require novel manufacturing methods to be realised. Manufacturing techniques such as direct etching or wire erosion are employed for singular THz waveguide and platelet stacking techniques are used for waveguide arrays (Chattopadhyay et al. 2018). Surface imperfections or associated surface roughnesses are an unavoidable result of fabrication and can have a dramatic effect on the surface impedance at sub-millimetre wavelengths. The Gradient Model as presented in G Gold and Helmreich (2017) is adapted to the mode-matching method to model surface imperfections. For a given roughness associated with the wall material, its contribution to the effective surface impedance can be determined and included in the model.

3.1 Ohmic Losses in Guide Walls

To correctly model multi-moded and high frequency waveguide components, a rigorous treatment of the boundary walls is required. As presented in J Shafii and Vernon (2002), by including large yet finite conductivity in the description of the mode-matching method the effects of lossy surface can be accurately modelled. In this section the procedure for including ohmic losses in waveguide walls is presented. Furthermore, the necessary modifications to the uniform PEC guide section are given using the notation introduced in chapter 2.

Along the guide wall, at the interface between an isotropic non-conducting medium and a perfect conducting surface (denote media 1 and 2 respectively)the boundary conditions from (Jackson 1998) are:

$$\hat{\boldsymbol{n}} \cdot \boldsymbol{D_1} = q_{es} \tag{3.1.1}$$

$$\hat{\boldsymbol{n}} \times \boldsymbol{H_1} = \boldsymbol{J}_s \tag{3.1.2}$$

$$\hat{\boldsymbol{n}} \times (\boldsymbol{E_1} - \boldsymbol{E_2}) = 0 \tag{3.1.3}$$

$$\hat{\boldsymbol{n}} \cdot (\boldsymbol{B_1} - \boldsymbol{B_2}) = 0 \tag{3.1.4}$$

with a unit normal ($\hat{\boldsymbol{n}}$) directed outward from the conducting surface and q_{es} surface charge density. Only the normal electric and tangential magnetic fields can exist just outside the PEC surface and fields drop to zero within the conductor.

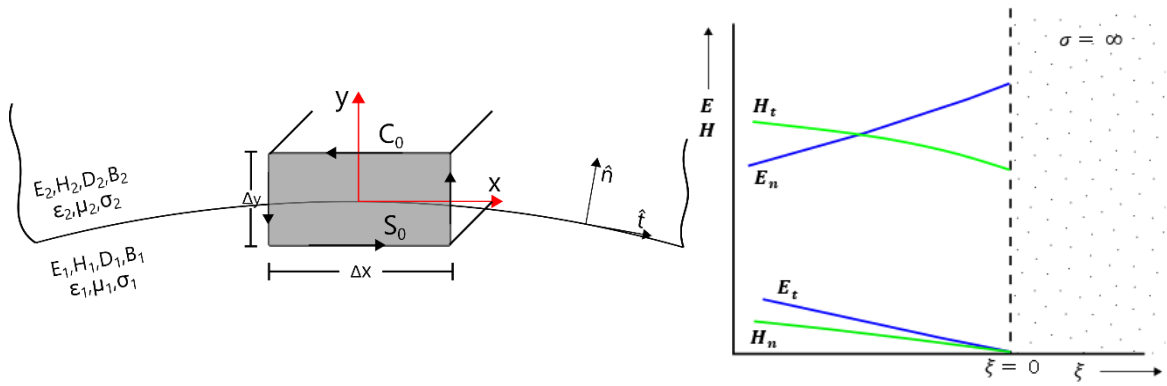

Figure 3-2 Arrangement along the interface between the conducting and propagation media, with a description of the fields near the surface of a perfect conductor (Jackson 1998) (subscripts n and t refer to the normal and tangential fields respectively).

Fields in the vicinity of conducting surfaces with large yet finite conductively must behave approximately as those at a PEC interface. For thin skin depths ($\delta \approx \sqrt{\frac{2}{\omega \mu_c \sigma}}$), the boundary conditions given in (3.1.1) and (3.1.2) remain approximately true, however, care must be taken to correctly examine the processes in this thin transitional region. From Ohms law ($\boldsymbol{J} = \sigma \boldsymbol{E}$), for finite conductivity there cannot be a surface layer of current as implied by equation (3.1.2). Instead this becomes:

$$\hat{\boldsymbol{n}} \times (\boldsymbol{H_1} - \boldsymbol{H}_2) = 0 \qquad (3.1.5)$$

Assuming just outside the conductor there exists a normal electric field $\boldsymbol{E}_n$ and tangential magnetic field $\boldsymbol{H}_t$, as for the PEC case. If $\boldsymbol{H}_t$ exists outside the conductor then from equation (3.1.5), this implies the same $\boldsymbol{H}_t$ exists inside the surface. Ignoring current displacement in the conductor, Maxwell's curl equations become:

$$\boldsymbol{E}_2 \cong \frac{1}{\sigma} \nabla \times \boldsymbol{H}_2 \qquad (3.1.6)$$

$$\boldsymbol{H}_2 \cong -\frac{i}{\mu_c \omega} \nabla \times \boldsymbol{E}_2 \qquad (3.1.7)$$

where harmonic variation $e^{-i\omega t}$ is assumed. The gradient operator is simplified, to $\nabla \cong -\hat{\boldsymbol{n}} \frac{\partial}{\partial \xi}$, with ξ being the normal coordinate into the conductor. Other derivative directions operating on the fields are neglected, and the curl equations become:

$$\boldsymbol{E}_2 \cong -\frac{1}{\sigma} \hat{\boldsymbol{n}} \times \frac{\partial \boldsymbol{H}_2}{\partial \xi} \qquad (3.1.8)$$

$$\boldsymbol{H}_2 \cong \frac{i}{\mu_c \omega} \hat{\boldsymbol{n}} \times \frac{\partial \boldsymbol{E}_2}{\partial \xi} \qquad (3.1.9)$$

where μ_c gives the permeability of the conductor. Combined these give:

$$\frac{\partial^2}{\partial \xi^2}(\hat{\boldsymbol{n}} \times \boldsymbol{H}_2) + \frac{2i}{\delta^2}(\hat{\boldsymbol{n}} \times \boldsymbol{H}_2) = 0 \tag{3.1.10}$$

$$\hat{\boldsymbol{n}} \cdot \boldsymbol{H}_2 = 0 \tag{3.1.11}$$

where δ gives the skin depth of the material. The solution for the magnetic field in the conductor is:

$$\boldsymbol{H}_2 = \boldsymbol{H}_t e^{-\frac{\xi}{\delta}(1-i)} \tag{3.1.12}$$

From $\hat{\boldsymbol{n}} \cdot \boldsymbol{H}_2 = 0$, the field must be parallel to the surface. Finally, the electric field in the conductor is approximately given as:

$$\boldsymbol{E}_2 \approx \sqrt{\frac{\mu_c \omega}{2\sigma}}(1-i)(\hat{\boldsymbol{n}} \times \boldsymbol{H}_2) \tag{3.1.13}$$

These solutions for the fields within the conductor exhibit a rapid exponential decay as observations are made further into the conductor. Fields in the conductor are parallel to the surface and propagate normal to it, with magnitudes that depend only on the tangential magnetic field on the surface. From equation (3.1.3), there exists a small tangential electric field on the surface given by:

$$\boldsymbol{E}_{1t} \approx \sqrt{\frac{\mu_2 \omega}{2\sigma_2}}(1-i)(\hat{\boldsymbol{n}} \times \boldsymbol{H}_2) \text{ where } \xi = 0 \text{ then } \boldsymbol{H}_2 = \boldsymbol{H}_t \tag{3.1.14}$$

where $\hat{\boldsymbol{n}}$ is the unit vector normal to the contour of the waveguide interior, and $\hat{\boldsymbol{t}}$ is the unit vector tangential to the contour, both being orthogonal to the propagation direction $\hat{\boldsymbol{z}}$:

$$\hat{\boldsymbol{n}} \times \hat{\boldsymbol{t}} = \hat{\boldsymbol{z}}, \quad \hat{\boldsymbol{t}} \times \hat{\boldsymbol{z}} = \hat{\boldsymbol{n}}, \quad \hat{\boldsymbol{n}} \times \hat{\boldsymbol{z}} = \hat{\boldsymbol{t}}. \tag{3.1.15}$$

Without solving the complete problem, it is clear from the derivation of the tangential electric field component at the boundary that this additional boundary condition accounts for the ohmic loss dissipation of the overall field. This in effect is the result of a perturbation from the PEC boundary conditions. In this section purely DC treatment on the conductivity is considered which are unlikely to hold true for THz or far-infrared frequencies (Kirley et al. 2015).

3.1.1 Ohmic Losses in Uniform Guide Sections

In a uniform guide section, the transverse and axial fields can be determined by exploiting the relationship between the electric and magnetic fields and unit vector identities given in equation (3.1.15). The guide's surface normal ($\hat{\boldsymbol{n}}_s$) is opposite to the contour normal, such that $\hat{\boldsymbol{n}}_s = -\hat{\boldsymbol{n}}$. Hence, the z-component of the magnetic field is always tangential to the surface of the guide. As such, it is linked to the component of the electric field parallel to $\hat{\boldsymbol{t}}$. This relationship between the axial magnetic field and the tangential electric field is shown:

Axial Magnetic Field

$$\boldsymbol{E}_t = Z_s(\omega)\hat{\boldsymbol{n}}_s \times \boldsymbol{H} \tag{3.1.16}$$

$$\boldsymbol{E}_t = Z_s(\omega)(-\hat{\boldsymbol{n}}) \times (\hat{\boldsymbol{z}}\boldsymbol{H})\hat{\boldsymbol{z}} = Z_s(\omega)(-\hat{\boldsymbol{n}}) \times H^z\hat{\boldsymbol{z}} \tag{3.1.17}$$

$$\boldsymbol{E}_t = Z_s(\omega)H^z\hat{\boldsymbol{t}} = E^t\hat{\boldsymbol{t}} \tag{3.1.18}$$

$$H^z = \frac{E^t}{Z_s(\omega)} \tag{3.1.19}$$

Since $\hat{\boldsymbol{t}}$ is orthogonal to $\hat{\boldsymbol{z}}$, only $\boldsymbol{E}_t$ must be considered.

In a similar manner, the component of the magnetic field parallel to $\hat{\boldsymbol{t}}$ is linked to the z-component of the electric field, as shown:

$$\boldsymbol{E}_t = Z_s(\omega)\hat{\boldsymbol{n}}_s \times \boldsymbol{H} \tag{3.1.20}$$

$$\boldsymbol{E}_t = Z_s(\omega)(-\hat{\boldsymbol{n}}) \times ((\hat{\boldsymbol{t}}\boldsymbol{H})\hat{\boldsymbol{t}}) \tag{3.1.21}$$

$$\boldsymbol{E}_t = Z_s(\omega)(\hat{\boldsymbol{t}}\boldsymbol{H})\hat{\boldsymbol{t}} \times \hat{\boldsymbol{n}} = -Z_s(\omega)(\hat{\boldsymbol{t}}\boldsymbol{H})\hat{\boldsymbol{z}} = E^z\hat{\boldsymbol{z}} \tag{3.1.22}$$

$$E^z = -Z_s(\omega)(\hat{\boldsymbol{t}}\boldsymbol{H}) \tag{3.1.23}$$

As for the PEC junction, the complete set of functions that span any transverse electric field is the set of modal (TE and TM) electric fields in the guide ($\nabla F_i \times \hat{\boldsymbol{z}}, Z_j^{TM}\nabla A_j$). For the transverse magnetic field, the appropriate base function set is the set of modal (TE and TM) magnetic fields in guide ($Y_i^{TE}\nabla F_i, \nabla A_j \times \hat{\boldsymbol{z}}$). Similarly, the complete set of functions that span any axial electric field is the set of modal electric fields in the guide (A_j) as defined. For the axial magnetic field, the appropriate base function set is the modal magnetic fields in the guide (F_i). For the axial fields the inner product can be defined as:

$$\langle A, B\rangle = \int_S \boldsymbol{A}^{z*} \times \boldsymbol{B}^z dS, \tag{3.1.24}$$

where $*$ indicates a complex conjugate, as the associated impedance for the lossy uniform section can take on complex values, it is necessary to include this.

In general, the curl form of Maxwell's equations will be used for the derivation of the lossy waveguide solutions. For clarity, only the set-up and main results of the derivation are shown.

$$(\nabla \times \boldsymbol{H})^z = +j\omega\epsilon\boldsymbol{E}^z \Rightarrow \nabla(\boldsymbol{H}^t \times \hat{\boldsymbol{z}}) = +j\omega\epsilon E^z \tag{3.1.25}$$

$$(\nabla \times \boldsymbol{E})^z = -j\omega\mu\boldsymbol{H}^z \Rightarrow \nabla(\boldsymbol{E}^t \times \hat{\boldsymbol{z}}) = -j\omega\mu H^z \tag{3.1.26}$$

$$(\nabla \times \boldsymbol{H})^t = +j\omega\epsilon \boldsymbol{E}^t \Rightarrow \left(\nabla_t H^z \times \frac{\partial \boldsymbol{H}^t}{\partial z}\right) \times \hat{\boldsymbol{z}} = +j\omega\epsilon \boldsymbol{E}^t \qquad (3.1.27)$$

$$(\nabla \times \boldsymbol{E})^t = -j\omega\mu \boldsymbol{H}^t \Rightarrow \left(\nabla_t E^z \times \frac{\partial \boldsymbol{E}^t}{\partial z}\right) \times \hat{\boldsymbol{z}} = -j\omega\mu \boldsymbol{H}^t \qquad (3.1.28)$$

The axial electric and magnetic field projects are obtained by taking the inner product of the axial Maxwell curl equations with their corresponding base functions:

Axial Electric Field Projection

$$\int_S (A_l)^* \nabla(\boldsymbol{H}^t \times \hat{\boldsymbol{z}})\, dS = \int_S (A_l)^* \nabla(j\omega\epsilon E^z)\, dS \qquad (3.1.29)$$

Axial Magnetic Field Projection

$$\int_S (F_k)^* \nabla(\boldsymbol{E}^t \times \hat{\boldsymbol{z}})\, dS = \int_S (F_k)^* \nabla(-j\omega\mu H^z)\, dS \qquad (3.1.30)$$

Moreover, the transverse field projections are now obtained from the inner product of the transverse Maxwell curl equations and their corresponding base functions:

Transverse Electric Field Projection

TE $$\int_S (F_k \times \hat{\boldsymbol{z}})^* \left(\left(\nabla H^z - \frac{\partial \boldsymbol{H}^t}{\partial z}\right) \times \hat{\boldsymbol{z}}\right) dS = \int_S (F_k \times \hat{\boldsymbol{z}})^* (j\omega\epsilon \boldsymbol{E}^t)\, dS \qquad (3.1.31)$$

TM $$\int_S \left(Z_j^{TM} \nabla A_j\right)^* \left(\left(\nabla H^z - \frac{\partial \boldsymbol{H}^t}{\partial z}\right) \times \hat{\boldsymbol{z}}\right) dS = \int_S \left(Z_j^{TM} \nabla A_j\right)^* (j\omega\epsilon \boldsymbol{E}^t)\, dS \qquad (3.1.32)$$

Transverse Magnetic Field Projection

$$\text{TE} \quad \int_S (Y_k^{TE}\nabla F_k)^* \left(\left(\nabla E^z - \frac{\partial \boldsymbol{E}^t}{\partial z}\right) \times \hat{\boldsymbol{z}}\right) dS = \int_S (Y_k^{TE}\nabla F_k)^* (-j\omega\mu \boldsymbol{H}^t)\, dS \tag{3.1.33}$$

$$\text{TM} \quad \int_S (\nabla A_j \times \hat{\boldsymbol{z}})^* \left(\left(\nabla E^z - \frac{\partial \boldsymbol{E}^t}{\partial z}\right) \times \hat{\boldsymbol{z}}\right) dS = \int_S (\nabla A_j \times \hat{\boldsymbol{z}})^* (-j\omega\mu \boldsymbol{H}^t)\, dS \tag{3.1.34}$$

The projections are performed in a similar manner as in the PEC junction derivation shown in chapter 2 allowing for the field relationships to be expressed algebraically. The modal field expansions of $H^z, E^z, \boldsymbol{E}^t$ and $\boldsymbol{H}^t$ are expressed in chapter 2 section (2.2.2) – (2.2.4).

An important point to note is that because of the new boundary condition, the PEC waveguide basis is not ideal since the PEC basis modes require $E_t = 0$. A strong assumption is made, as in J Shafii and Vernon (2002), that these modes remain appropriate. The guide wall is considered to be a good conductor and as such the mode should not be strongly perturbed. In fact, even if $E_t \neq 0$, the magnetic field component will not be strongly perturbed.

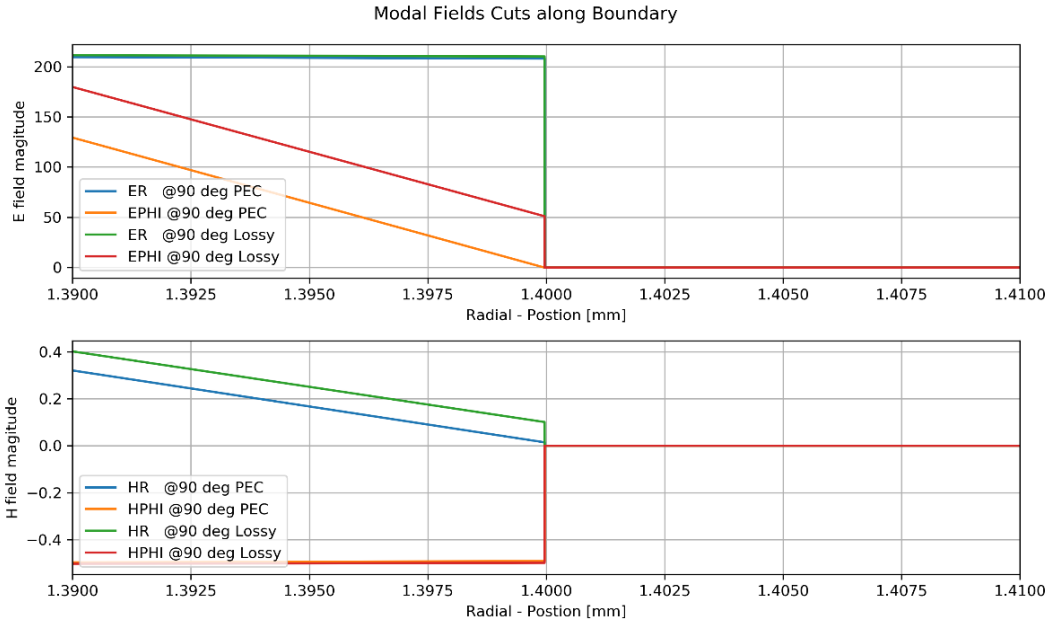

Figure 3-3 Plot of the electric and magnetic field components along the boundary for PEC and Lossy ($\sigma = 5.8 \times 10^4\ S/m$) walls generated from CST. Here 'R' and 'PHI' correspond to the transverse and normal components respectively.

In the derivation, for integrals along the edge involving E_t, the magnetic field expression is used to avoid explicit evaluation of the electric field along the boundary. This allows for the modes to be treated as effectively unchanged. By inspecting the fields along the wall from CST these assumptions can be investigated. From Figure 3-3, it can be seen that at the boundary there is significant increase in the electric field magnitude away from $E_t = 0$ when non-PEC walls are considered. Comparatively, the magnitude of the magnetic field varies by just a small amount.

Performing these projections leads to a set of differential equations which describe the mode amplitude for the modes present in the uniform lossy guide. The full system of equations when solved is given as:

$$\frac{d\boldsymbol{a}}{dz} = \begin{bmatrix} \boldsymbol{\beta_z} & \boldsymbol{0} \\ \boldsymbol{0} & \boldsymbol{\beta_z} \end{bmatrix}^{+} \begin{bmatrix} -i\boldsymbol{\beta_z^2} + \boldsymbol{X} + \boldsymbol{Y} & \boldsymbol{X} - \boldsymbol{Y} \\ -\boldsymbol{X} + \boldsymbol{Y} & i\boldsymbol{\beta_z^2} - \boldsymbol{X} - \boldsymbol{Y} \end{bmatrix} \boldsymbol{a} = \boldsymbol{W}\boldsymbol{a} \tag{3.1.35}$$

where

$$\boldsymbol{a}^{+} = \begin{bmatrix} \boldsymbol{a}^{TE,+} \\ \boldsymbol{a}^{TM,+} \end{bmatrix} \text{ and } \boldsymbol{a}^{-} = \begin{bmatrix} \boldsymbol{a}^{TE,-} \\ \boldsymbol{a}^{TM,-} \end{bmatrix} \text{ give } \boldsymbol{a} = \begin{bmatrix} \boldsymbol{a}^{TE,+} \\ \boldsymbol{a}^{TM,+} \\ \boldsymbol{a}^{TE,-} \\ \boldsymbol{a}^{TM,-} \end{bmatrix} \tag{3.1.36}$$

$$\boldsymbol{\beta_z} = \begin{bmatrix} \boldsymbol{\beta_z^{TE}} & \boldsymbol{0} \\ \boldsymbol{0} & \boldsymbol{\beta_z^{TM}} \end{bmatrix} = \begin{bmatrix} \beta_{z,1}^{TE} & 0 & 0 & 0 & 0 & 0 \\ 0 & \ddots & 0 & 0 & \ddots & 0 \\ 0 & 0 & \beta_{z,N_{TE}}^{TE} & 0 & 0 & 0 \\ 0 & 0 & 0 & \beta_{z,1}^{TM} & 0 & 0 \\ 0 & \ddots & 0 & 0 & \ddots & 0 \\ 0 & 0 & 0 & 0 & 0 & \beta_{z,N_{TM}}^{TM} \end{bmatrix} \tag{3.1.37}$$

with the $\boldsymbol{X}$ and $\boldsymbol{Y}$ matrices given by:

$$\boldsymbol{X} = \frac{1}{2} Z_s(\omega) \beta_z^{+} \begin{bmatrix} \boldsymbol{H} & \boldsymbol{0} \\ \boldsymbol{0} & \boldsymbol{0} \end{bmatrix} \tag{3.1.38}$$

$$\boldsymbol{Y} = \frac{1}{2} Z_s(\omega) \beta_z^{+} \begin{bmatrix} \boldsymbol{K} & \boldsymbol{L} \\ \boldsymbol{M} & \boldsymbol{N} \end{bmatrix} \tag{3.1.39}$$

The integrals elements of $\boldsymbol{X}$ and $\boldsymbol{Y}$ are given by:

$$H_{ij} = -\frac{Z_s(\omega)\left(\beta_{c,i}^{TE}\right)^2\left(\beta_{c,j}^{TE}\right)^2}{\omega\mu D_{ii}} \int_{\delta S} F_i F_j dl \tag{3.1.40}$$

$$K_{ij} = -\frac{Z_s(\omega)\beta Y_i^{TE} Y_j^{TE}}{Y_0 D_{ii}} \int_{\delta S} (\hat{t}\nabla F_i)(\hat{t}\nabla F_j) dl \tag{3.1.41}$$

$$L_{ij} = -\frac{Z_s(\omega)\beta Y_i^{TE}}{Y_0 D_{ii}} \int_{\delta S} (\hat{t}\nabla F_i)(\hat{n}\nabla A_j) dl \tag{3.1.42}$$

$$M_{ij} = -\frac{Z_s(\omega)\beta Y_j^{TE}}{Z_0 C_{ii}} \int_{\delta S} (\hat{n}\nabla A_i)(\hat{t}\nabla F_j) dl \tag{3.1.43}$$

$$N_{ij} = -\frac{Z_s(\omega)\beta}{Z_0 C_{ii}} \int_{\delta S} (\hat{n}\nabla A_i)(\hat{n}\nabla A_j) dl \tag{3.1.44}$$

If the $\boldsymbol{X}$ and $\boldsymbol{Y}$ matrices are zero, then it is apparent that the solution of equation (3.1.35) returns to that of a PEC guide:

$$\frac{d\boldsymbol{a}}{dz} = \begin{bmatrix} \boldsymbol{\beta_z} & \mathbf{0} \\ \mathbf{0} & \boldsymbol{\beta_z} \end{bmatrix}^+ \begin{bmatrix} -i\boldsymbol{\beta_z^2} & \mathbf{0} \\ 0 & i\boldsymbol{\beta_z^2} \end{bmatrix} \boldsymbol{a} = \begin{bmatrix} -i\boldsymbol{\beta_z}\boldsymbol{\beta_z^2} & \mathbf{0} \\ \mathbf{0} & i\boldsymbol{\beta_z}\boldsymbol{\beta_{z_z}^2} \end{bmatrix}^+ \boldsymbol{a} \tag{3.1.45}$$

The coupled mode equations have solutions that can also be expressed using the transmission matrix for guide of given length i.e. $\left(\boldsymbol{a}(z) = \boldsymbol{T}(z)\boldsymbol{a}(0)\right)$. Here the complex amplitude vector at a given location can be expressed in terms of the transmission matrix over a given length and the input mode amplitudes. The expression for the coupled mode equations is given as:

$$\frac{d}{dz}\boldsymbol{a}(z) = \boldsymbol{W}\boldsymbol{a}(z), \text{where } \boldsymbol{a}(z) = \begin{bmatrix} a_1(z) \\ \vdots \\ a_n(z) \end{bmatrix} \text{and } \boldsymbol{W} = [n \times n] \tag{3.1.46}$$

The familiar eigenvalue equation gives:

$$\boldsymbol{W}\boldsymbol{x_i} = \lambda_i \boldsymbol{x_i} \tag{3.1.47}$$

where λ_i and $\boldsymbol{x_i}$ give the i[th] eigenvalues and eigenvectors of the matrix $\boldsymbol{W}$. If the corresponding eigenvectors of $\boldsymbol{W}$ form column entries of a matrix $\boldsymbol{Q}$. Then $\boldsymbol{W}$ can be diagonalised, such that the diagonal elements of $\boldsymbol{\Lambda}$ are the eigenvalues of $\boldsymbol{W}$:

$$\boldsymbol{\Lambda} = \boldsymbol{Q^{-1}W Q} = \begin{bmatrix} \lambda_1 & \cdots & 0 \\ \vdots & \ddots & \vdots \\ 0 & \cdots & \lambda_n \end{bmatrix} \tag{3.1.48}$$

For the PEC case the matrix $\boldsymbol{W}$ is already diagonal and as such:

$$\boldsymbol{\Lambda} = \boldsymbol{W} = \begin{bmatrix} \lambda_1 & \cdots & 0 \\ \vdots & \ddots & \vdots \\ 0 & \cdots & \lambda_n \end{bmatrix} \tag{3.1.49}$$

For a single matrix entry, it can be shown that the solution takes the form of a first order ordinary differential equation and for the first amplitude component has the simple exponential solution:

$$\frac{d}{dz}a_1(z) = w_{1,1}\, a_1 \tag{3.1.50}$$

$$\text{Soln: } a_n(z) = e^{\lambda_n z} c_n x_n$$

$$= e^{\lambda_n z} a_n(0), \text{where } a_n(0) \text{ solves the initial value problem}$$

$$\therefore \frac{d}{dz}a_1(z) = \lambda_1 e^{\lambda_1 t}x_1 = \boldsymbol{W}e^{\lambda_1 z}x_1 \tag{3.1.51}$$

$$\lambda_1 x_1 = \boldsymbol{W}x_1$$

Thus, the solution to the full differential equation is:

$$\boldsymbol{a}(z) = e^{\lambda_1 z}c_1 x_1 + \cdots + e^{\lambda_n z}c_n x_n \tag{3.1.52}$$

And for $z = 0$:

$$\boldsymbol{a}(0) = c_1 x_1 + \cdots + c_n x_n = \begin{bmatrix} | & & | \\ x_1 & \dots & x_n \\ | & & | \end{bmatrix}\begin{bmatrix} c_1 \\ \vdots \\ c_n \end{bmatrix} = \boldsymbol{Q}\boldsymbol{c} \tag{3.1.53}$$

Complete solutions for $\boldsymbol{a}(z)$ can be found by extending this form shown for a single amplitude:

$$\boldsymbol{a}(z) = \boldsymbol{Q}\exp(\boldsymbol{\Lambda}\mathrm{z})\mathbf{c} \tag{3.1.54}$$

where $\boldsymbol{c}$ represents the constants $c = \boldsymbol{Q}^{-1}\boldsymbol{a}(0)$ such that $\boldsymbol{a}(z) = \boldsymbol{Q}\exp(\boldsymbol{\Lambda}\mathrm{z})\,\boldsymbol{Q}^{-1}\boldsymbol{a}(0)$ as shown in (Strang 2013). Therefore, the transmission matrix must take the following form:

$$\boldsymbol{T}(\boldsymbol{z}) = \boldsymbol{Q}\exp(\boldsymbol{\Lambda}\mathrm{z})\boldsymbol{Q}^{-1} \tag{3.1.55}$$

For the non-PEC case the matrix $\boldsymbol{W}$ may not be diagonal and as such the first entry of the differential equation has the form:

$$\frac{d}{dz}a_1(z) = w_{1,1}a_1 + \cdots + w_{1,n}a_n \tag{3.1.56}$$

In this case there is evidence that as $\boldsymbol{W}$ is no longer guaranteed to be diagonal, the modal amplitudes may mix. The off-diagonal elements of $\boldsymbol{W}$ will be non-zero for valid mode

combinations in the integrals (3.1.40) – (3.1.44). In the PEC result there was strictly no mixing of the modal amplitudes.

Assuming that the first port of the system is located at $z = 0$ and the second port is located at some distance $z = l$, the corresponding section transmission matrix is $\boldsymbol{T}(l)$. Using the notation for modal amplitudes defined in chapter 2, the system is described by the transmission matrix:

$$\begin{bmatrix} \boldsymbol{b}_2 \\ \boldsymbol{a}_2 \end{bmatrix} = \begin{bmatrix} \boldsymbol{a}_l^+ \\ \boldsymbol{a}_l^- \end{bmatrix} = \boldsymbol{T}(l) \begin{bmatrix} \boldsymbol{a}_0^+ \\ \boldsymbol{a}_0^- \end{bmatrix} = \boldsymbol{T}(l) \begin{bmatrix} \boldsymbol{a}_1 \\ \boldsymbol{b}_1 \end{bmatrix} \tag{3.1.57}$$

$$\begin{bmatrix} \boldsymbol{b}_2 \\ \boldsymbol{a}_2 \end{bmatrix} = \begin{bmatrix} \boldsymbol{T}_{11} & \boldsymbol{T}_{12} \\ \boldsymbol{T}_{21} & \boldsymbol{T}_{22} \end{bmatrix} \begin{bmatrix} \boldsymbol{a}_1 \\ \boldsymbol{b}_1 \end{bmatrix} \tag{3.1.58}$$

Or by the scattering matrix:

$$\begin{bmatrix} \boldsymbol{b}_1 \\ \boldsymbol{b}_2 \end{bmatrix} = \begin{bmatrix} \boldsymbol{S}_{11} & \boldsymbol{S}_{12} \\ \boldsymbol{S}_{21} & \boldsymbol{S}_{22} \end{bmatrix} \begin{bmatrix} \boldsymbol{a}_1 \\ \boldsymbol{a}_2 \end{bmatrix} \tag{3.1.59}$$

where

$$\boldsymbol{S} = \begin{bmatrix} \boldsymbol{S}_{11} & \boldsymbol{S}_{12} \\ \boldsymbol{S}_{21} & \boldsymbol{S}_{22} \end{bmatrix} = \begin{bmatrix} \boldsymbol{T}_{22}^{-1}\boldsymbol{T}_{21} & \boldsymbol{T}_{22}^{-1} \\ \boldsymbol{T}_{11} - \boldsymbol{T}_{12}\boldsymbol{T}_{22}^{-1}\boldsymbol{T}_{21} & \boldsymbol{T}_{12}\boldsymbol{T}_{22}^{-1} \end{bmatrix} \tag{3.1.60}$$

For a section of finite length, the transformation can only be performed if $\boldsymbol{T}_{22}$ can be inverted, as shown the inversion of this term is fundamental to obtaining the scattering parameters. The transfer parameter $\boldsymbol{T}_{22}$ describes the attenuation in the guide, as the length of the section grows so too does the attenuation. Thus, determining $\boldsymbol{T}_{22}^{-1}$ becomes increasingly problematic due to the finite accuracy of the numerical implementation. The approach taken to overcome this limitation is to operate on shorter sections of the lossy guide. Complete sections can be halved as many times as required to ensure accurate computation of their scattering matrices, and then cascaded with itself the same number of times to obtain the scattering matrices of the section of full length.

3.1.2 Mode Coupling in Uniform lossy Sections

The coupling mechanism in uniform PEC guide section requires modes to couple bijectively to themselves only. This process is observed due to the diagonal nature of the matrix $\boldsymbol{W}$ in the coupled mode equation for PEC guides. However, in uniform lossy guide sections this is no longer the case. The additional boundary condition along the guide wall gives rise to off-diagonal entries in $\boldsymbol{W}$, given by integrals (3.1.40) – (3.1.44), which sees coupling between some modes.

In over-moded uniform lossy sections, the effect of interfering currents at the bounding wall due to multiple modes present must be considered. The relative phases of these guide modes can have a strong effect on the power dissipated in waveguide. In general, it is not always correct to consider the individual losses (J Shafii and Vernon 2002). Thus, it can be taken that the power dissipated by modes at the guide walls must be taken together. As a consequence, the correct prediction involves a coupling of the modes within the uniform lossy section. As shown in (J Shafii and Vernon 2002), this method has been verified against other models detailed in both (Collins 1991) and (Jackson 1998).

PEC	**Lossy**
$\mathrm{TE_{mn}} \leftrightarrow \mathrm{TE_{xy}}$ for $\mathrm{TE_{mn}} = \mathrm{TE_{xy}}$ $\mathrm{TM_{mn}} \leftrightarrow \mathrm{TM_{xy}}$ for $\mathrm{TM_{mn}} = \mathrm{TM_{xy}}$	$\mathrm{TE_{mn}} \leftrightarrow \mathrm{TE_{xy}}$ for $\mathrm{m} = \mathrm{x}$ $\mathrm{TM_{mn}} \leftrightarrow \mathrm{TM_{xy}}$ for $\mathrm{m} = \mathrm{x}$ $\mathrm{TE_{mn}} \leftrightarrow \mathrm{TM_{xy}}$ for $\mathrm{m} = \mathrm{x} \neq 0$

(3.1.61)

The valid mode combinations are given by the non-zero solutions to the integrals (3.1.40) – (3.1.44), which have solutions similar to those for the PEC junctions coupling integrals. That is, coupling between the modes is dependent on the azimuthal orders in cylindrical structures and transverse orders of rectangular structures. The resulting mode coupling mechanisms are highlighted in Figure 3-4.

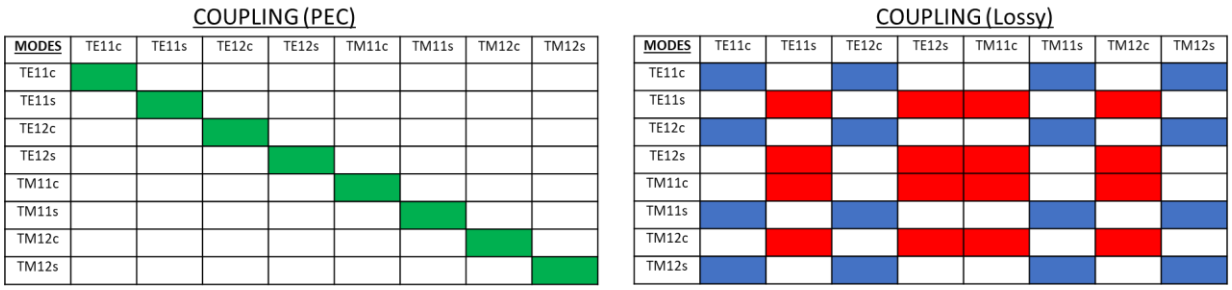

Figure 3-4: Shows the coupling mechanisms for: a) PEC walled uniform guide; self-coupling of waveguide modes is observed b) Lossy walled uniform guide; coupling of modes of similar azimuthal orders is observed (here only like colours will couple to each other).

3.1.3 Testing and Verification of the Uniform Lossy Guide

As for the PEC junction, CST Microwave Studio is used to independently verify the lossy section results for cylindrical and rectangular guide cross-sections. The results presented here are for very low wall conductivity. This is done to exaggerate the effect of the surface impedance, such that a significant deviation from the PEC result is observed. The following test cases are considered for the verification of the uniform lossy guide method:

- A uniform cylindrical guide section of radius $1.4\,\text{mm}$, length $1.0\,\text{mm}$ and wall conductivity of $\sigma = 5.4 \times 10^4\ \text{S/m}$ (56 modes considered: 8 radial and 4 azimuthal orders).
- A uniform rectangular guide section with dimensions of a WR10 guide ($a = 2.54\,\text{mm}, b = 1.27\,\text{mm}$) and wall conductivity of $\sigma = 5.4 \times 10^4\ \text{S/m}$ (112 modes considered: 8 Cartesian orders).

Identical systems are modelled in both CST and the developed mode matching software (SCATTER-TNG or S-TNG) over a frequency range of $30 - 300\,\text{GHz}$ and for a select set of modes the reflection (S_{11}) and transmission (S_{21}) results are compared.

In Figure 3-5, the scattering coefficients for the uniform cylindrical test case are shown and excellent agreement is observed between the results from S-TNG and CST. Additional observation can be made with regard to the cross-coupling of orthogonal modes i.e. ($TE_{11c} \rightarrow TM_{11s}$) in lossy guides as discussed in section 3.1.2. This is in contrast to a PEC guide, where modes strictly do not couple to others.

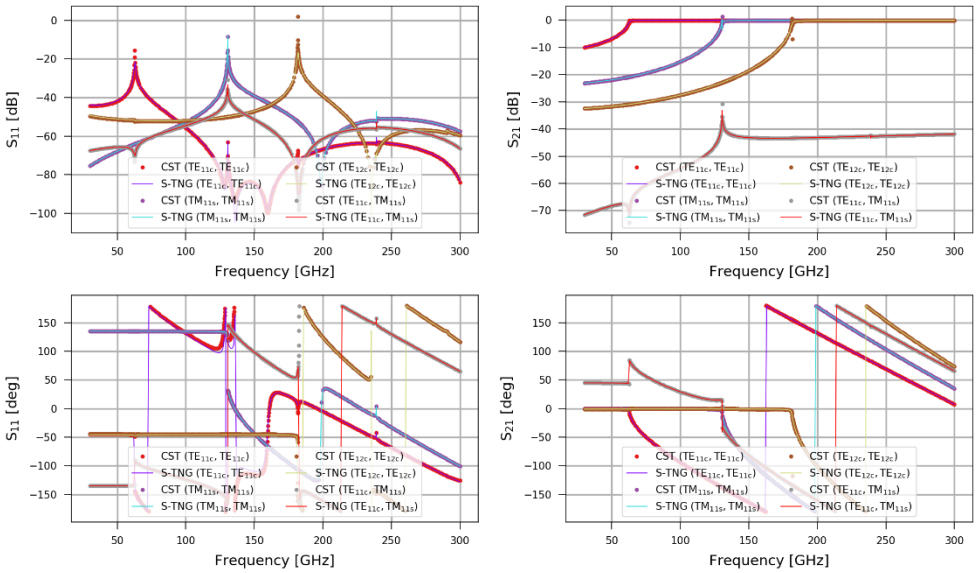

Figure 3-5: Shows the magnitude and phase of the reflection/transmission scattering parameters for a number of mode combinations in a cylindrical lossy uniform guide section. The results are in excellent agreement with the results from an identical simulation performed in CST.

In Figure 3-5, there exists non-zero components of reflection in the lossy guide and a reduction to the overall transmission in each mode, due to the non-zero surface impedance. The results obtained are contrasted with the PEC case in Table 3-1.

We consider a uniform rectangular guide section with dimensions of a WR10 guide ($a = 2.54\ \text{mm}, b = 1.27\ \text{mm}$) and wall conductivity of $\sigma = 5.4 \times 10^4\ \text{S/m}$. Over a frequency range of $30 - 300$ GHz, the result is compared to an identical system modelled in CST and the results for both simulations are shown in Figure 3-6. The results obtained are in line with those obtained for the circular test case and are summarized in the Table 3-1.

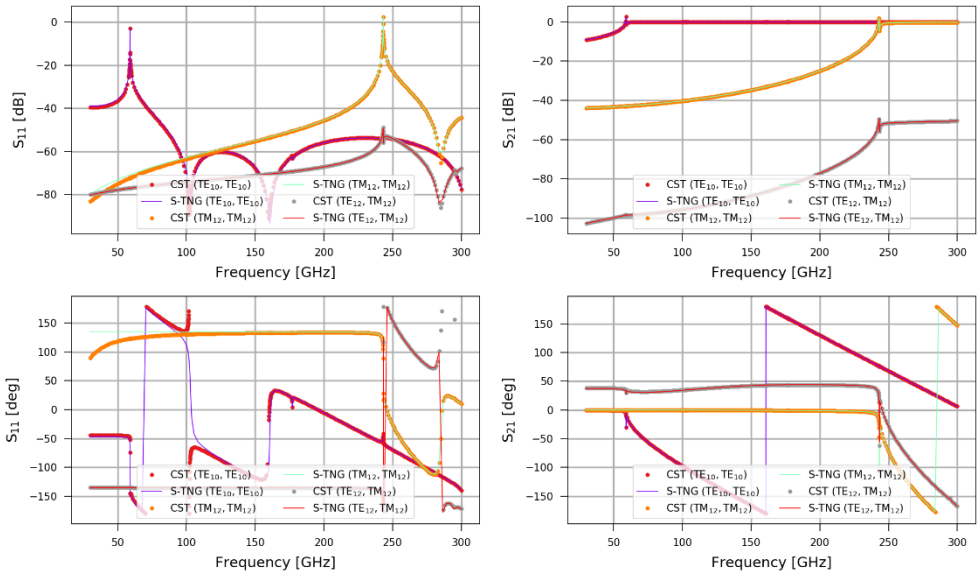

Figure 3-6: Shows the magnitude and phase of the reflection/transmission scattering parameters for a number of mode combinations in a rectangular lossy uniform guide section. The results are in perfect agreement with the results from an identical simulation performed in CST.

Table 3-1 Summarises the expected scattering results for the uniform guide sections, contrasting the results from the PEC and Lossy guide sections for cylindrical and rectangular geometries.

		PEC		NON-PEC	
		Circular Case			
Mode 1	Mode 2	$\lvert S_{11}\rvert$	$\lvert S_{12}\rvert$	$\lvert S_{11}\rvert$	$\lvert S_{12}\rvert$
TE_{11c}	TE_{11c}	0	1	> 0	$0 < \lvert S_{12}\rvert < 1 - \lvert S_{11}\rvert$
TM_{11s}	TM_{11s}	0	1	> 0	$0 < \lvert S_{12}\rvert < 1 - \lvert S_{11}\rvert$
TE_{11c}	TM_{11s}	0	0	> 0	$0 < \lvert S_{12}\rvert < 1 - \lvert S_{11}\rvert$

3.2 Ohmic Losses at Waveguide Discontinuities

The mode matching methods introduced in chapter 2 to account for step discontinuities must also be adapted to consider ohmic losses on the junction boundary walls. In the PEC junction the transverse electric field was zero on the overlap region Σ, which is defined by the intersection of the left guide's metallic wall and the right guide as shown in Figure 3-7. However, when finite wall conductivity is considered this is no longer the case. The overlap region will have non-zero surface impedance, which must be considered. As discussed in section 3.1, there is an electric field component produced on the overlapping region Σ, linked to the surface current density and the tangential component of the magnetic field as in equation (3.1.14). In a similar manner to the uniform lossy guide section the changed boundary conditions will introduce another channel for mode attenuation as power is dissipated over the lossy region. Such representation of the junction element will be from now referred to as *lossy junction*.

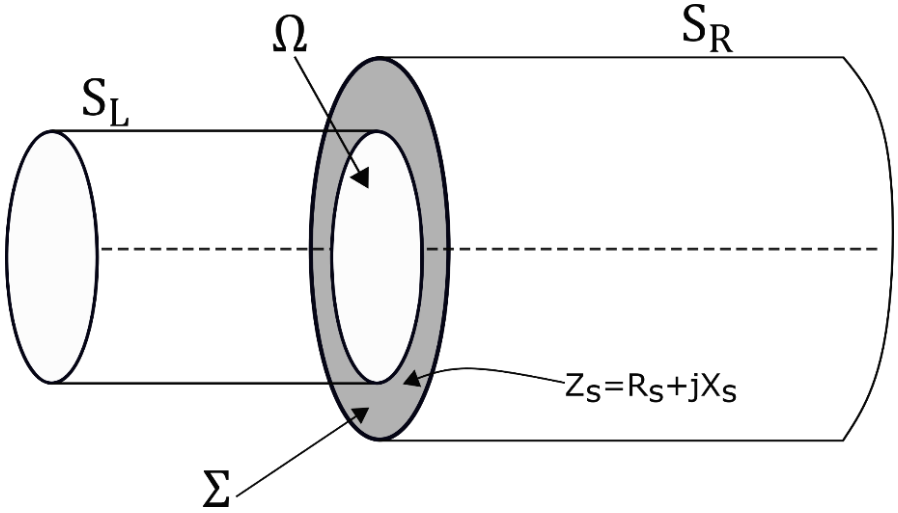

Figure 3-7 Schematic drawing of the junction between two uniform guide sections in which the small is fully enclosed by the large guide. The regions of interest at the junction plane are indicated; Ω is the intersection region and Σ is the overlap region of the guides, which has finite wall conductivity.

For a junction between two guides, as seen in Figure 3-7, the notation previously introduced for a PEC junction is used, the two guides will be referred to as '*Left*' and '*Right*' or L and R at $z = 0$. The order of the guides, with cross sections S_L & S_R is such that $S_L \subset \mathrm{S_R}$. The common cross section of the two guides is $\Omega = \mathrm{S_L} \cap S_R$ and the region defined by $\Sigma = (S_L \cup S_R) - \Omega$ represents an overlap between S_R and a conducting material bounding S_L. Here, since guide L and R are ordered "small" to "large", $\Omega = S_L$. As in the PEC case, electric and magnetic fields on both sides of the interface must be equal:

$$\boldsymbol{E}_L = \boldsymbol{E}_R, \text{on } \Omega \tag{3.2.1}$$

$$\boldsymbol{H}_L = \boldsymbol{H}_R, \text{on } \Omega \tag{3.2.2}$$

Through redefinition of the boundary walls, the electric field in the right guide must be non-zero on the boundary and thus the electric field on the overlap region is given as:

$$\boldsymbol{E}_R \cong Z_w \hat{\boldsymbol{z}} \times \boldsymbol{H}_R, \text{on } \Sigma \tag{3.2.3}$$

where Z_w gives the surface impedance of the overlap region. The complete set of functions which span any transverse electric or magnetic fields are the set of corresponding modal TE or TM fields which are again taken to be those of the PEC waveguide modes. In guide *R*, the complete set of functions required to span the electric field are those given by $(\nabla F_i^{\mathrm{R}} \times \hat{\boldsymbol{z}}, Z_j^{TM} \nabla A_j^R)$. The electric field in guide *L* is also spanned by the same function set, as the fields must match on Ω. Likewise, the complete set of functions which span the transverse magnetic field being matched is the set of modal TE and TM magnetic fields given in guide *L* as $(Y_i^{TE} \nabla F_i^{\mathrm{L}}, \nabla A_j^L \times \hat{\boldsymbol{z}})$.

A scalar product $\left(P = \int_S \boldsymbol{A}^{t^*} \cdot \boldsymbol{B}^t \, dS\right)$ can be defined for the transverse fields, where $*$ indicates a complex conjugate. For the lossy junction case the modal fields are no longer always real valued so the conjugation must be explicitly retained. The procedure for the lossy junction network follows that of the PEC case, apart from the inclusion of the non-zero electric field on the overlap.

3.2.1 Electric field and Magnetic Field Projections

The lossy junction sections boundary conditions require continuous fields at the intersection of the guides and a non-zero component on the overlap region as detailed in equations (2.4.1) - (2.4.3). By determining the scalar products for corresponding set of functions which span both the electric $(\nabla F_i^{\mathrm{R}} \times \hat{\boldsymbol{z}}, Z_j^{TM} \nabla A_j^R)$ and magnetic fields $(Y_i^{TE} \nabla F_i^{\mathrm{L}}, \nabla A_j^L \times \hat{\boldsymbol{z}})$ the boundary conditions can be expressed as:

Base	Electric Field Projections	
TE	$\int_{S_R} (\nabla F_i^R \times \hat{\boldsymbol{z}})^* \left(\boldsymbol{E}^{t^R}_{all}\right) dS = \int_{S_R} (\nabla F_i^R \times \hat{\boldsymbol{z}})^* \left(\boldsymbol{E}^{t^R}_{all}\right) dS$	*(3.2.4)*
	$\int_{S_L} (\nabla F_i^R \times \hat{\boldsymbol{z}})^* \left(\boldsymbol{E}^{t^L}_{all}\right) dS + Z_s^* \int_{\Sigma} (\nabla F_i^R \times \hat{\boldsymbol{z}}) \left(\hat{\boldsymbol{z}} \times \boldsymbol{H}^{t^R}_{all}\right) dS = \int_{S_R} (\nabla F_i^R \times \hat{\boldsymbol{z}})^* \left(\boldsymbol{E}^{t^R}_{all}\right) dS$	
TM	$\int_{S_R} \left(Z_j^{TM} \nabla A_j^R\right)^* \left(\boldsymbol{E}^{t^R}_{all}\right) dS = \int_{S_R} \left(Z_j^{TM} \nabla A_j^R\right)^* \left(\boldsymbol{E}^{t^R}_{all}\right) dS$	*(3.2.5)*
	$Z_j^{TM^*} \int_{S_L} \nabla A_j^{R^*} \left(\boldsymbol{E}^{t^L}_{all}\right) dS + Z_j^{TM^*} Z_s^* \int_{\Sigma} \left(\nabla A_j^R\right)^* \left(\hat{z} \times \boldsymbol{H}^{t^R}_{all}\right) dS = Z_j^{TM^*} \int_{S_R} \left(\nabla A_j^R\right)^* \left(\boldsymbol{E}^{t^R}_{all}\right) dS$	
Base	**Magnetic Field Projections**	
TE	$\int_{S_L} (Y_i^{TE} \nabla F_i^L)^* \left(\boldsymbol{H}^{t^{TE,L}}_{all} + \boldsymbol{H}^{t^{TM,L}}_{all}\right) dS = \int_{S_L} (Y_i^{TE} \nabla F_i^L)^* \left(\boldsymbol{H}^{t^{TE,R}}_{all} + \boldsymbol{H}^{t^{TM,R}}_{all}\right) dS$	*(3.2.6)*
TM	$\int_{S_L} \left(\nabla A_j^{\mathrm{L}} \times \hat{\boldsymbol{z}}\right)^* \left(\boldsymbol{H}^{t^{TE,L}}_{all} + \boldsymbol{H}^{t^{TM,L}}_{all}\right) dS = \int_{S_L} \left(\nabla A_j^{\mathrm{L}} \times \hat{\boldsymbol{z}}\right)^* \left(\boldsymbol{H}^{t^{TE,R}}_{all} + \boldsymbol{H}^{t^{TM,R}}_{all}\right) dS$	*(3.2.7)*

At this point it can be observed that the magnetic field projections are identical to those already obtained in the PEC case with the addition of the strict conjugation to the potential base. The constraints for the magnetic field scalar products, as derived in chapter 2, are:

$$\begin{bmatrix} \boldsymbol{Y}^{L*} \boldsymbol{D}_L^{LL} \boldsymbol{Y}^L & \boldsymbol{0} \\ \boldsymbol{0} & \boldsymbol{C}_L^{LL} \end{bmatrix} \begin{bmatrix} \boldsymbol{h}_{TE}^L \\ \boldsymbol{h}_{TM}^L \end{bmatrix} = \begin{bmatrix} \boldsymbol{Y}^{L*} \boldsymbol{D}_R^{LR} \boldsymbol{Y}^R & \boldsymbol{Y}^{L*} (\boldsymbol{B}_L^{RL})^T \\ \boldsymbol{0} & \boldsymbol{C}_R^{LR} \end{bmatrix} \begin{bmatrix} \boldsymbol{h}_{TE}^R \\ \boldsymbol{h}_{TM}^R \end{bmatrix} \quad (3.2.8)$$

It is clear from the boundary conditions and equation (2.4.4) and (3.2.5) that the modulation to the PEC solution appear in the electric field projection only. In fact, by rearranging these expressions the extra term due to the surface impedance can be isolated where the same process as in chapter 2 is applied to obtain the matrices in terms of the common integrals:

$$\begin{bmatrix} \boldsymbol{D}_L^{RL} & (\boldsymbol{B}_L^{LR})^T \boldsymbol{Z}^L \\ (\boldsymbol{Z}^R)^* \boldsymbol{B}_L^{RL} & (\boldsymbol{Z}^R)^* \boldsymbol{C}_L^{RL} (\boldsymbol{Z}^L) \end{bmatrix} \begin{bmatrix} \boldsymbol{e}_{TE}^L \\ \boldsymbol{e}_{TM}^L \end{bmatrix} - Z_w \begin{bmatrix} \boldsymbol{D}_\Sigma^{RR} \boldsymbol{Y}^R & (\boldsymbol{B}_\Sigma^{RR})^T \\ (\boldsymbol{Z}^R)^* \boldsymbol{B}_\Sigma^{RR} \boldsymbol{Y}^R & (\boldsymbol{Z}^R)^* \boldsymbol{C}_\Sigma^{RR} \end{bmatrix} \begin{bmatrix} \boldsymbol{h}_{TE}^R \\ \boldsymbol{h}_{TM}^R \end{bmatrix}$$

$$= \begin{bmatrix} \boldsymbol{D}_R^{RR} & (\boldsymbol{B}_{\mathrm{R}}^{LR})^T \boldsymbol{Z}^R \\ (\boldsymbol{Z}^R)^* \boldsymbol{B}_R^{RR} & (\boldsymbol{Z}^R)^* \boldsymbol{C}_{\mathrm{R}}^{RR} \boldsymbol{Z}^R \end{bmatrix} \begin{bmatrix} \boldsymbol{e}_{TE}^R \\ \boldsymbol{e}_{TM}^R \end{bmatrix} \tag{3.2.9}$$

$$\begin{bmatrix} \boldsymbol{D}_L^{RL} & \boldsymbol{0} \\ (\boldsymbol{Z}^R)^* \boldsymbol{B}_L^{RL} & (\boldsymbol{Z}^R)^* \boldsymbol{C}_L^{RL} (\boldsymbol{Z}^L) \end{bmatrix} \begin{bmatrix} \boldsymbol{e}_{TE}^L \\ \boldsymbol{e}_{TM}^L \end{bmatrix} = \begin{bmatrix} \boldsymbol{D}_R^{RR} & \boldsymbol{0} \\ \boldsymbol{0} & (\boldsymbol{Z}^R)^* \boldsymbol{C}_{\mathrm{R}}^{RR} \boldsymbol{Z}^R \end{bmatrix} \begin{bmatrix} \boldsymbol{e}_{TE}^R \\ \boldsymbol{e}_{TM}^R \end{bmatrix}$$

$$+ Z_w \begin{bmatrix} \boldsymbol{D}_\Sigma^{RR} \boldsymbol{Y}^R & (\boldsymbol{B}_\Sigma^{RR})^T \\ (\boldsymbol{Z}^R)^* \boldsymbol{B}_\Sigma^{RR} \boldsymbol{Y}^R & (\boldsymbol{Z}^R)^* \boldsymbol{C}_\Sigma^{RR} \end{bmatrix} \begin{bmatrix} \boldsymbol{h}_{TE}^R \\ \boldsymbol{h}_{TM}^R \end{bmatrix} \tag{3.2.10}$$

The highlighted term in (3.2.10) represents the effect of non-zero surface impedance on the overlap region between the guides. Using the notation introduced in chapter 2 the constraints on the modal amplitudes are expressed as:

$$\boldsymbol{P}_L \boldsymbol{e}^L = \boldsymbol{Q}_R \boldsymbol{e}^R + Z_w \boldsymbol{W} \boldsymbol{h}^R \tag{3.2.11}$$

$$\boldsymbol{Q}_L \boldsymbol{h}^L = \boldsymbol{P}_R^+ \boldsymbol{h}^R \tag{3.2.12}$$

where $\boldsymbol{W}$ represents the self-coupling of modes on the overlap region Σ arising from the modified boundary condition. The scattering parameters can be obtained via the same process as for the PEC case, by assuming the ports are alternately excited and determine the respective parameters for the excited ports one at a time. The expressions for the scattering parameters are given by:

$$\boldsymbol{S}_{LL} = (\boldsymbol{I} + \boldsymbol{Q}_L^{+}\boldsymbol{P}_R^{+}(\boldsymbol{Q}_R + Z_w\boldsymbol{W})^{+}\boldsymbol{P}_L)^{-1}(\boldsymbol{I} - \boldsymbol{Q}_L^{+}\boldsymbol{P}_R^{+}(\boldsymbol{Q}_R + Z_w\boldsymbol{W})^{+}\boldsymbol{P}_L) \quad (3.2.13)$$

$$\boldsymbol{S}_{RL} = (\boldsymbol{Q}_R + Z_w\boldsymbol{W})^{+}\boldsymbol{P}_L(\boldsymbol{I} + \boldsymbol{S}_{LL}) \quad (3.2.14)$$

$$\boldsymbol{S}_{RR} = (\boldsymbol{Q}_R^{+}\boldsymbol{P}_L\boldsymbol{Q}_L^{+}\boldsymbol{P}_R^{+} + Z_w\boldsymbol{Q}_R^{+}\boldsymbol{W} + \boldsymbol{I})^{-1}(\boldsymbol{Q}_R^{+}\boldsymbol{P}_L\boldsymbol{Q}_L^{+}\boldsymbol{P}_R^{+} + Z_w\boldsymbol{Q}_R^{+}\boldsymbol{W} - \boldsymbol{I}) \quad (3.2.15)$$

$$\boldsymbol{S}_{LR} = \boldsymbol{Q}_L^{+}\boldsymbol{P}_R^{+}(\boldsymbol{I} - \boldsymbol{S}_{RR}) \quad (3.2.16)$$

3.2.2 Testing and Verification of the Lossy Junction

As before, CST Microwave Studio is used to produce reference estimates of the scattering parameters of identical systems. Only concentric systems are presented as examples in this section. The accuracy of the lossy junction model for offset geometries is similar to the PEC case. Again, very low wall conductivity is used to exaggerate the effect of the surface impedance, so that a significant deviation from the PEC case is observed. The following test cases are considered for the verification of the lossy junction method.

- The junction between two cylindrical waveguide sections: the first of radius 1.4 mm and the second of radius 1.7 mm, both with length 1 mm and wall conductivity of $\sigma = 5.4 \times 10^4$ S/m (72 modes considered: 8 radial and 5 azimuthal orders).
- The junction between two rectangular waveguide sections: a WR10 section (2.54 mm × 1.27 mm) and a larger section (3.2 mm × 2.0 mm) both with lengths of 1 mm and wall conductivity of $\sigma = 5.4 \times 10^4$ S/m (112 modes considered: 8 Cartesian orders).

Identical systems are modelled in both CST and the developed software S-TNG over a frequency range of $30 - 300$ GHz and for a select set of modes the results the reflection (S_{11}) and transmission (S_{21}) results are compared. For the cylindrical and rectangular junctions there is excellent agreement between the two simulations, as seen in Figure 3-8 and Figure 3-9.

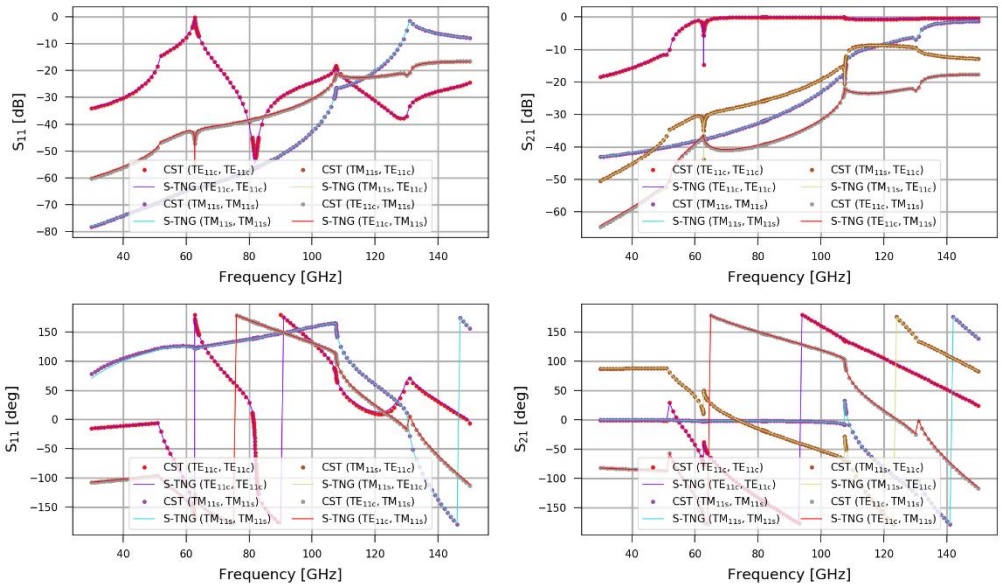

Figure 3-8: Concentric Lossy cylindrical junction $1.4\ mm - 1.7\ mm$ *(*$\sigma = 5.4 \times 10^4\ S/m$*) with,8 radial orders and 5 azimuthal orders considered. Reflection (*S_{11}*) and Transmission (*S_{21}*) scattering parameters shown for both CST and S-TNG*

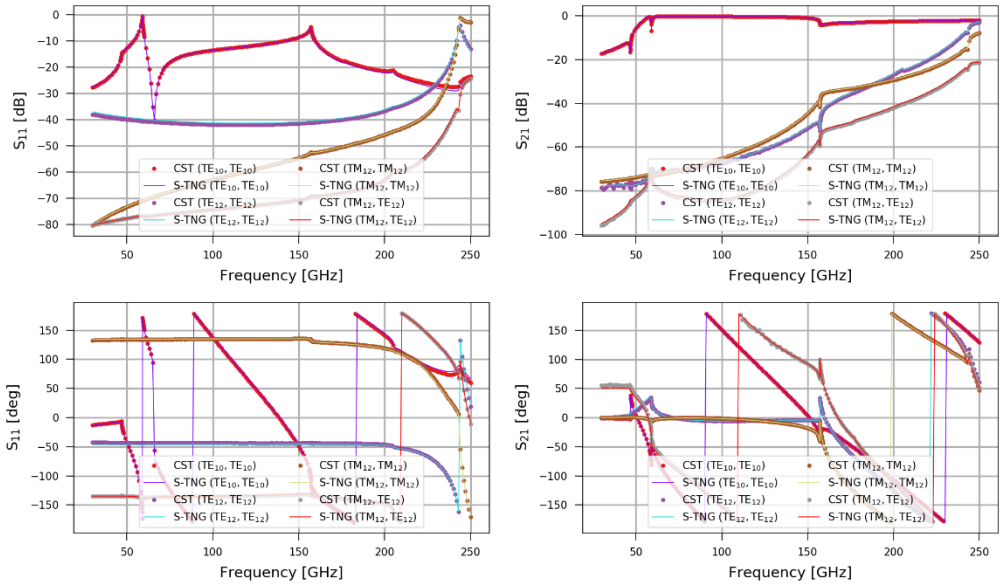

Figure 3-9: Concentric Lossy rectangular junction ($\sigma = 5.4 \times 10^4\ S/m$*) with 112 modes considered. Reflection (*S_{11}*) and Transmission (*S_{21}*) scattering parameters shown for both CST and S-TNG*

The cylindrical lossy test case represents the same geometry as used for PEC cylindrical junction test case in chapter 2 (two cylindrical waveguides of radius 1.4 mm and 1.7 mm with lengths 1 mm, over a frequency range of $f = 50 - 150$ GHz). By inspecting the transmission and reflection coefficients of the fundamental mode in both of these test cases the effects of lossy surface can be observed Figure 3-10. There is slight variation in the reflection coefficient and a much more pronounced effect on the transmission coefficient with much greater attenuation observed in the lossy cases. However, this result is quite exaggerated as due to the poor wall conductivity of $\sigma = 5.4 \times 10^4$ S/m used.

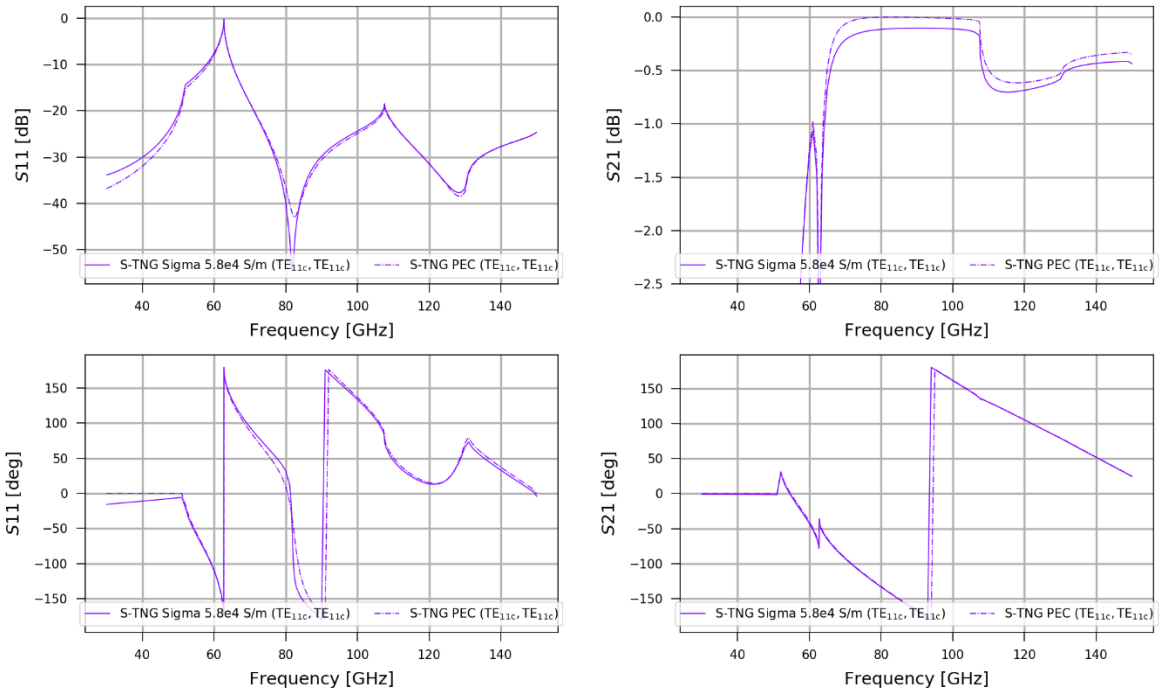

Figure 3-10 Fundamental mode s-parameters shown for concentric cylindrical junction $1.4\ mm - 1.7\ mm$ *for walls* $\sigma = 5.4 \times 10^4\ S/m$ *and PEC.*

3.3 Absorber Layer as an Infinitely Thin Ohmic Sheet

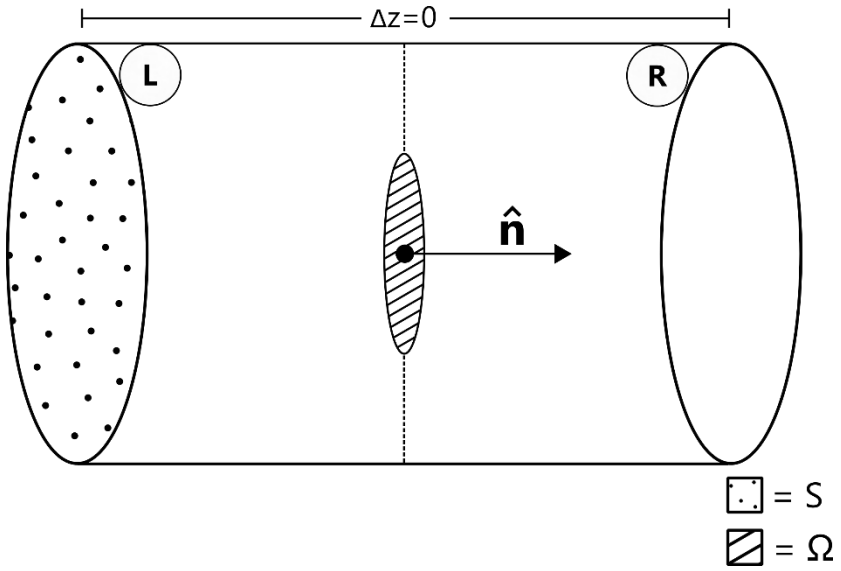

Figure 3-11: Schematic drawing of the infinitely thin absorber section, where the zero lengths are stretched for clarity. The absorber layer (Ω) is placed within a cross-section (S) orientated such that its surface normal is in the direction of propagation.

As discussed in chapter 1, waveguides are commonly used to guide electromagnetic radiation to the detector elements of GHz/THz instruments. Depending on the application these detectors may be either coherent or incoherent. In this section the mode matching analysis techniques are extended to model a class of bolometers detectors (Walker 2015), which are treated as absorbers.

A block of absorber material of finite thickness t partially fills the guide cross-section S. To accurately model this system, it would be necessary to define two new modesets; one new basis modeset within the absorber material Ω and another set of co-axial modes. These co-axial modes would exist in the overlapping region between the absorber's edge and the boundary walls over a length t equal to the thickness of the absorber (Doherty 2012). The set of boundary conditions at the interface of these mode sets would be quite challenging to solve. Instead, to effectively capture these absorber elements the following assumptions are made; the absorber resides completely within the guide's cross-section S, the absorber's shape is described by the contour on Ω and the absorber material is assumed to have negligible thickness, i.e. absorber is considered as a two dimensional resistive sheet, as illustrated in Figure 3-11.

By considering these simplifications, the boundary conditions become much more manageable; requiring that the electric field remain continuous across the absorber layer, while there is a jump in the magnetic field. This is due to the induced surface currents on the resistive sheet

(Bracken 2015). Finally, as the co-axial modes exist over a null space only i.e. with thickness $t = 0$, their influence may be neglected. Using the same definitions of the spaces within the guide as in section 3.2, the boundary conditions for the transverse field are given as:

$$\boldsymbol{E}_L = \boldsymbol{E}_R, \text{on S} \tag{3.3.1}$$

$$\boldsymbol{H}_L = \boldsymbol{H}_R, \text{on } \Sigma \tag{3.3.2}$$

$$\boldsymbol{H}_L = \boldsymbol{H}_R - \boldsymbol{K} \times \hat{\boldsymbol{k}}, \text{on } \Omega. \tag{3.3.3}$$

where $\boldsymbol{K} = \frac{\boldsymbol{E_L}}{R_S} = \frac{\boldsymbol{E_R}}{R_S}$, $\hat{\boldsymbol{k}}$ defines the direction of propagation and R_S is the absorber's sheet resistance with units of ohms per square ($\Omega/\blacksquare$).

Sheet resistance is a measure of the resistance of a two dimensional section where the material's thickness is negligible. As such induced current only occur in the plane of the sheet. The bulk resistance of a material is given by a materials resistivity ρ (Ωm) where $R = \frac{\rho L}{A}$. For the area of the absorber layer composed of width W and thickness t then the resistance becomes:

$$R = \frac{\rho L}{Wt} = \frac{\rho}{t}\frac{L}{W} = \mathrm{R_S}\frac{\mathrm{L}}{W} \tag{3.3.4}$$

where sheet resistance is given as $R_s = \frac{\rho}{t}$. The unit ($\Omega/\blacksquare$) is used if $L = W$ then a square with $R_S = 30\ \Omega/\blacksquare$ has resitance of $R = 30\ \Omega$ regardless of the size of the square.

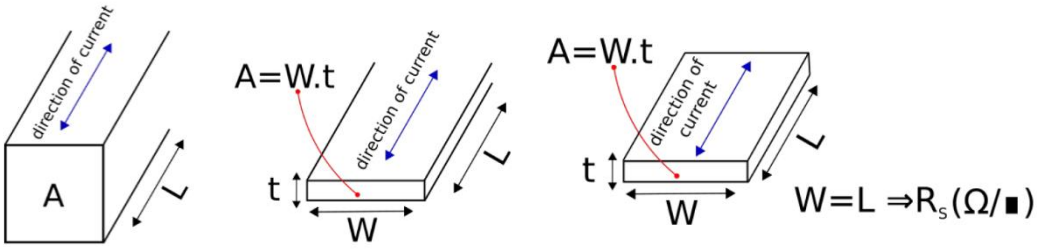

Figure 3-12: Illustration of conventional resistance and sheet resistance.

Although the cross-section remains constant it is convenient to keep track of the L and R regions, as shown in Figure 3-11. The complete set of functions which span any transverse electric or magnetic fields are the set of corresponding modal TE or TM fields which are the

same as those presented in chapter 2. As discussed in chapter 2, this implementation of the mode matching method relies on the use of contour integrals over the surface integrals typically used. This reformulation provides a more readily numerical integrable form of the coupling equations and allows for arbitrary geometry shapes to be efficiently considered in the coupling integrals (Figlia and Gentili 2002).

3.3.1 Electric field and Magnetic Field Projections

The absorber layer section's boundary conditions require continuous fields across the guide with a jump in magnetic field across the absorber layer as detailed in equations (3.3.1) - (3.3.3). By determining the scalar products for corresponding set of functions which span both the electric ($\nabla F_i^{\mathrm{R}} \times \hat{\boldsymbol{z}}, Z_j^{TM} \nabla A_j^R$) and magnetic fields ($Y_i^{TE} \nabla F_i^{\mathrm{L}}, \nabla A_j^L \times \hat{\boldsymbol{z}}$) the boundary conditions can be expressed as:

Base	**Electric Field Projections**	
TE	$\int_S (\nabla F_i^R \times \hat{\boldsymbol{z}})^* \left(\boldsymbol{E}^t{}_{all}^{TE,L} + \boldsymbol{E}^t{}_{all}^{TM,L} \right) dS = \int_S (\nabla F_i^R \times \hat{\boldsymbol{z}})^* \left(\boldsymbol{E}^t{}_{all}^{TE,R} + \boldsymbol{E}^t{}_{all}^{TM,R} \right) dS$	*(3.3.5)*
TM	$\int_S \left(Z_j^{TM} \nabla A_j^R \right)^* \left(\boldsymbol{E}^t{}_{all}^{TE,L} + \boldsymbol{E}^t{}_{all}^{TM,L} \right) dS = \int_S \left(Z_j^{TM} \nabla A_j^R \right)^* \left(\boldsymbol{E}^t{}_{all}^{TE,R} + \boldsymbol{E}^t{}_{all}^{TM,R} \right) dS$	*(3.3.6)*

From the boundary conditions it is clear that the electric field component is unperturbed across the absorber layer. As such, the resulting constraints are identical to those of an ideal junction where the two guide sections have the same cross-section:

$$\begin{bmatrix} \boldsymbol{D}_{(S)} & \boldsymbol{0} \\ \boldsymbol{0} & (\boldsymbol{Z})^* C_{(S)} (\boldsymbol{Z}) \end{bmatrix} \begin{bmatrix} \boldsymbol{e}_{TE}^L \\ \boldsymbol{e}_{TM}^L \end{bmatrix} = \begin{bmatrix} \boldsymbol{D}_{(S)} & \boldsymbol{0} \\ \boldsymbol{0} & (\boldsymbol{Z})^* \boldsymbol{C}_{(S)} (\boldsymbol{Z}) \end{bmatrix} \begin{bmatrix} \boldsymbol{e}_{TE}^R \\ \boldsymbol{e}_{TM}^R \end{bmatrix} \qquad (3.3.7)$$

Base	Magnetic Field Projections	
TE	$\int_S (Y_i^{TE}\nabla F_i^L)^*\left(\boldsymbol{H}^{t}{}_{all}^{TE,L} + \boldsymbol{H}^{t}{}_{all}^{TM,L}\right)dS$ $= \int_\Sigma (Y_i^{TE}\nabla F_i^L)^*\left(\boldsymbol{H}^{t}{}_{all}^{TE,R} + \boldsymbol{H}^{t}{}_{all}^{TM,R}\right)dS$ $+ \int_\Omega (Y_i^{TE}\nabla F_i^L)^*\left(\boldsymbol{H}^{t}{}_{all}^{TE,R} + \boldsymbol{H}^{t}{}_{all}^{TM,R}\right)dS$ $- \frac{1}{R_S}\int_\Omega (Y_i^{TE}\nabla F_i^L)^*\left(\boldsymbol{E}^{t}{}_{all}^{TE,R} + \boldsymbol{E}^{t}{}_{all}^{TM,R}\right)dS$	*(3.3.8)*
TM	$\int_S \left(\nabla A_j^{\mathrm{L}} \times \hat{\boldsymbol{z}}\right)^*\left(\boldsymbol{H}^{t}{}_{all}^{TE,L} + \boldsymbol{H}^{t}{}_{all}^{TM,L}\right)dS$ $= \int_\Sigma \left(\nabla A_j^{\mathrm{L}} \times \hat{\boldsymbol{z}}\right)^*\left(\boldsymbol{H}^{t}{}_{all}^{TE,R} + \boldsymbol{H}^{t}{}_{all}^{TM,R}\right)dS$ $+ \int_\Omega \left(\nabla A_j^{\mathrm{L}} \times \hat{\boldsymbol{z}}\right)^*\left(\boldsymbol{H}^{t}{}_{all}^{TE,R} + \boldsymbol{H}^{t}{}_{all}^{TM,R}\right)dS$ $- \frac{1}{R_S}\int_\Omega \left(\nabla A_j^{\mathrm{L}} \times \hat{\boldsymbol{z}}\right)^*\left(\boldsymbol{E}^{t}{}_{all}^{TE,R} + \boldsymbol{E}^{t}{}_{all}^{TM,R}\right)dS$	*(3.3.9)*

The magnetic field over the absorber is perturbed through the material as given in equation (3.3.3). As such, the magnetic field projection the term scaled by R_s represents the drop in the magnetic field due to the induced surface currents on the absorber layer:

$$\begin{bmatrix} \boldsymbol{Y}^*\boldsymbol{D}_{(S)}\boldsymbol{Y} & \boldsymbol{0} \\ \boldsymbol{0} & \boldsymbol{C}_{(S)} \end{bmatrix}\begin{bmatrix} \boldsymbol{h}_{TE}^L \\ \boldsymbol{h}_{TM}^L \end{bmatrix} = \begin{bmatrix} \boldsymbol{Y}^*\boldsymbol{D}_{(S)}\boldsymbol{Y} & \boldsymbol{0} \\ \boldsymbol{0} & \boldsymbol{C}_{(S)} \end{bmatrix}\begin{bmatrix} \boldsymbol{h}_{TE}^R \\ \boldsymbol{h}_{TM}^R \end{bmatrix} + \frac{1}{Rs}\begin{bmatrix} \boldsymbol{Y}^*\boldsymbol{D}_{(\Omega)}\boldsymbol{Y} & \boldsymbol{Y}^*\left(\boldsymbol{B}_{(\Omega)}\right)^T \\ \boldsymbol{B}_{(\Omega)}\boldsymbol{Y} & \boldsymbol{C}_{(\Omega)} \end{bmatrix}\begin{bmatrix} \boldsymbol{e}_{TE}^R \\ \boldsymbol{e}_{TM}^R \end{bmatrix} \quad (3.3.10)$$

Applying the same reduced form of notation as in the PEC derivation, the above matrix equations are simplified to an equivalent form given by

$$\boldsymbol{Q_E e^L = Q_E e^R} \tag{3.3.11}$$

$$\boldsymbol{Q_H h^L = Q_H h^R + A_b e^R} \tag{3.3.12}$$

Each of the ports can be excited independently and applying the same procedure as in the PEC and lossy junction the scattering parameters of the absorber network are determined as:

$$\boldsymbol{S_{LL} = (I + Q_H^+ Q_H Q_E^+ Q_E + Q_H^+ A_b Q_E^+ Q_E)^{-1}(I - Q_H^+ Q_H Q_E^+ Q_E - Q_H^+ A_b Q_E^+ Q_E)} \tag{3.3.13}$$

$$\boldsymbol{S_{RL} = Q_E^+ Q_E (I + S_{LL})} \tag{3.3.14}$$

$$\boldsymbol{S_{RR} = (Q_E^+ Q_E Q_H^+ Q_H + Q_E^+ Q_E Q_H^+ A_b + I)^{-1}(Q_E^+ Q_E Q_H^+ Q_H - Q_E^+ Q_E Q_H^+ A_b - I)} \tag{3.3.15}$$

$$\boldsymbol{S_{LR} = Q_E^+ Q_E (S_{RR} + I)} \tag{3.3.16}$$

Clearly, there must be full symmetry between the reflection and transmission scattering parameters for both waveguide ports. For a matrix $\boldsymbol{A}$ with linearly independent columns $\boldsymbol{A^+ = (A^* A)^{-1} A^*}$, here the pseudoinverse gives a left inverse such that $\boldsymbol{A^+ A = I}$. This allows equations (3.3.13)- (3.3.16) to be simplified to the fully symmetric form:

$$\boldsymbol{S_{LL} = (2I + Q_H^+ A_b)^{-1}(-Q_H^+ A_b)} \tag{3.3.17}$$

$$\boldsymbol{S_{RL} = (I + S_{LL})} \tag{3.3.18}$$

$$\boldsymbol{S_{RR} = (2I + Q_H^+ A_b)^{-1}(-Q_H^+ A_b)} \tag{3.3.19}$$

$$\boldsymbol{S_{LR} = (S_{RR} + I)} \tag{3.3.20}$$

3.3.2 Testing and Verification of the Infinitely Thin Absorber Model

As before, CST Microwave Studio is used to independently verify the mode-matching implementation of the absorber layer section for selected test cases. The test cases involved a range of waveguide and absorber geometry combinations as shown in Table 3-2. There is particular interest in mixed geometries (i.e. circular absorber in a rectangular guide section) and arbitrary absorber shapes as these examples are easier to model accurately in the line-integral formulation. For all test cases the absorber layers are placed mid-way in a section of length $l = 1$ mm with a sheet resistance value of $R_S = 377\ \Omega/\blacksquare$.

Table 3-2 Summary of the verification test cases for the infinitely thin absorber section

Test No.	Code	Description
1	CC-1	Fully filling concentric circular absorber in a cylindrical guide
2	CC-2	Partially filling concentric circular absorber in a cylindrical guide
3	CR-1	Partially filling concentric rectangular absorber in a rectangular guide
4	AC-1	Annulus absorber in a cylindrical guide
5	AR-1	Annulus absorber in a rectangular guide
6	CJc-1	Partially filling concentric circular absorber in a cavity section

Test No. 1 CC-1:

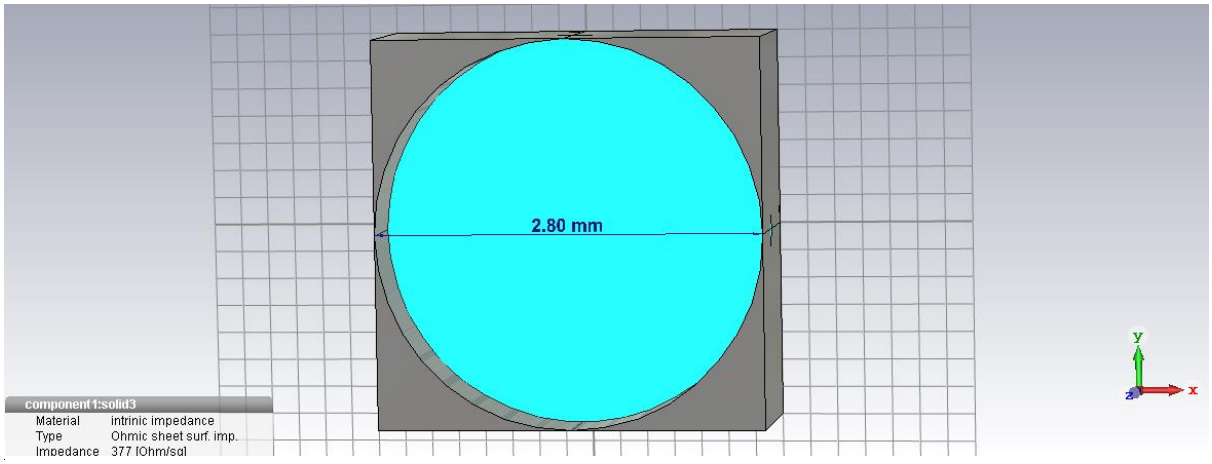

Figure 3-13: Illustration of the system being modelled taken from CST: Cylindrical waveguide and fully filling absorber section.

Test case CC-1 is shown in Figure 3-13, for the selected set of modes there is excellent agreement in both the reflection and transmission results generated by S-TNG and CST as shown in Figure 3-15. In this case, the S-TNG simulation considered 112 modes, 16 radial and 4 azimuthal orders.

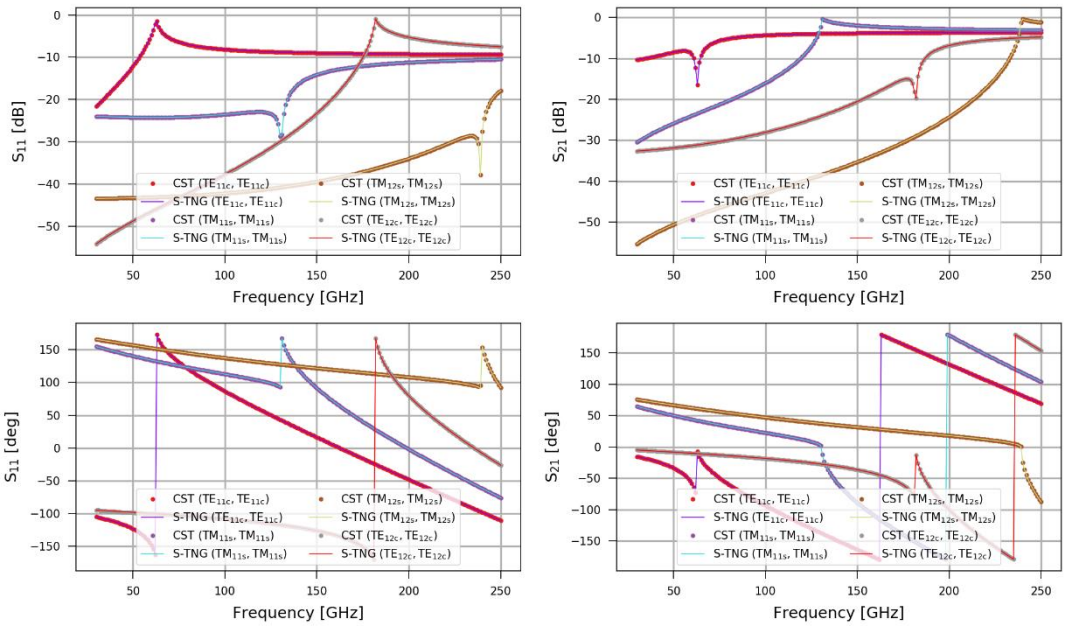

Figure 3-15: Cylindrical waveguide and fully filling absorber section with 112 modes considered, 16 radial and 4 azimuthal orders. Reflection (S_{11}) and Transmission (S_{21}) scattering parameters shown for both CST and S-TNG

CC-1 gives the simplest geometrical arrangement i.e. axial symmetry and no mixing of modes due to the absorber being fully filling ($\Sigma = \Omega$), Since no mixing occurs the number of modes can be drastically reduced in the S-TNG simulation while maintaining excellent agreement with the CST results as shown in Figure 3-14 for the same set of modes. Here, 12 modes are considered, 4 radial and 2 azimuthal orders

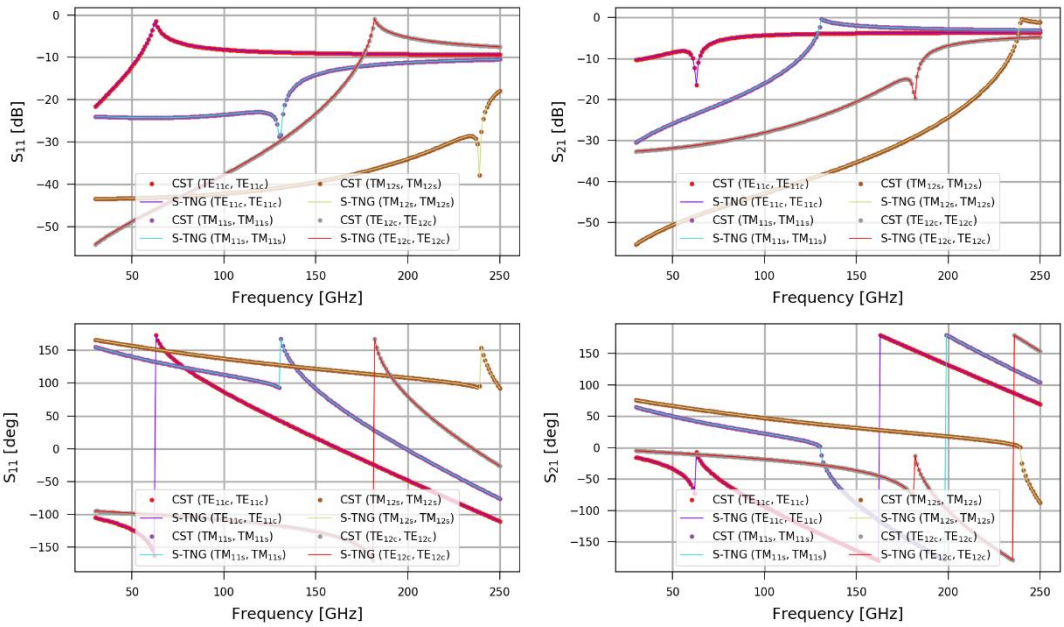

Figure 3-14: Cylindrical waveguide and fully filling absorber section with reduced number of modes present 12 modes are considered, 4 radial and 2 azimuthal orders. Reflection (S_{11}) and Transmission (S_{21}) scattering parameters shown for both CST and S-TNG

Test No. 2 CC-2:

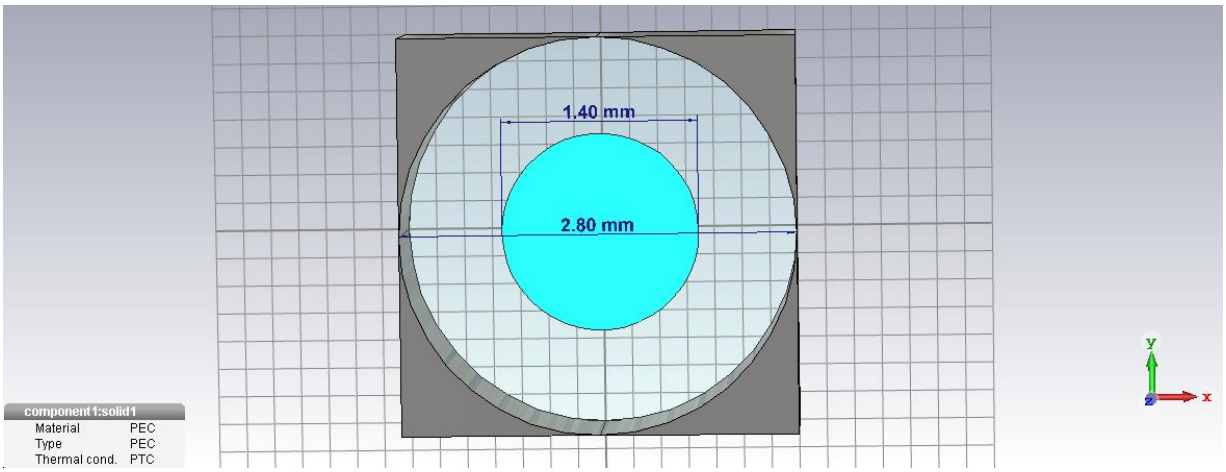

Figure 3-16: Illustration of the system being modelled taken from CST: Cylindrical waveguide and half filling absorber section.

Test case CC-2 is shown in Figure 3-16, for the selected set of modes there is excellent agreement in both the reflection and transmission results generated by S-TNG and CST as shown in Figure 3-17.

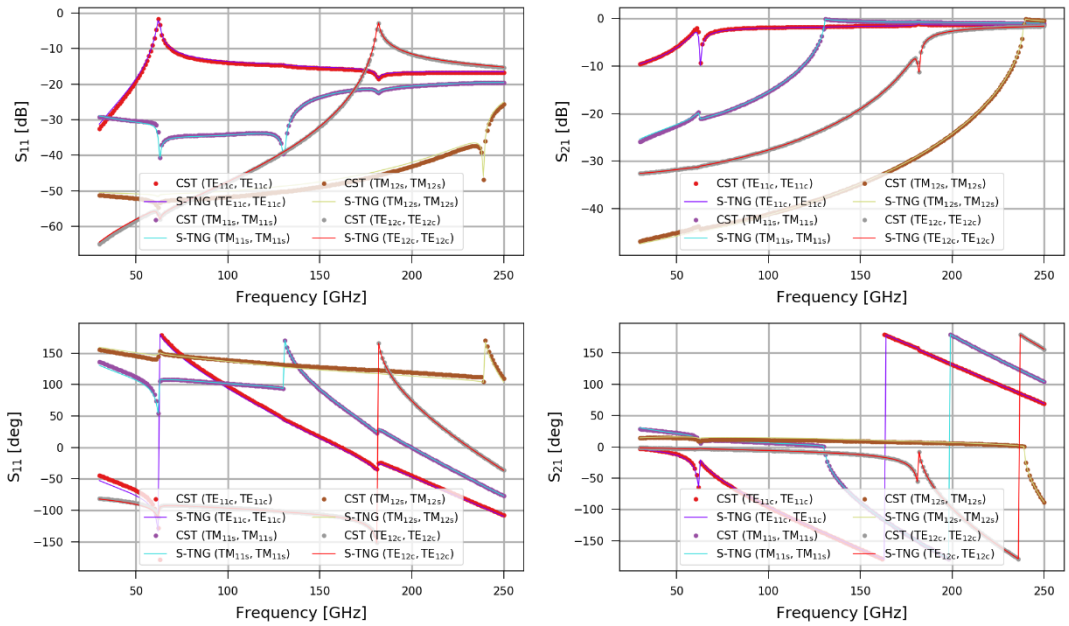

Figure 3-17: Cylindrical waveguide and half filling absorber section with 112 modes considered, 16 radial and 4 azimuthal orders. Reflection (S_{11}) and Transmission (S_{21}) scattering parameters shown for both CST and S-TNG

For test case CC-2:

- To achieve this level of agreement with CST 112 modes are considered, 16 radial and 4 azimuthal orders.

- This increase in mode-number compared to test case CC-1 is required to accurately model CC-2.
- Although axial symmetry remains, mixing of modes occurs due to the partially filling absorber layer.
- In Figure 3-18, when fewer modes are considered, the accuracy of the S-TNG simulation drops and deviation from the CST result is observed. Here, 12 modes are considered, 4 radial and 2 azimuthal orders.

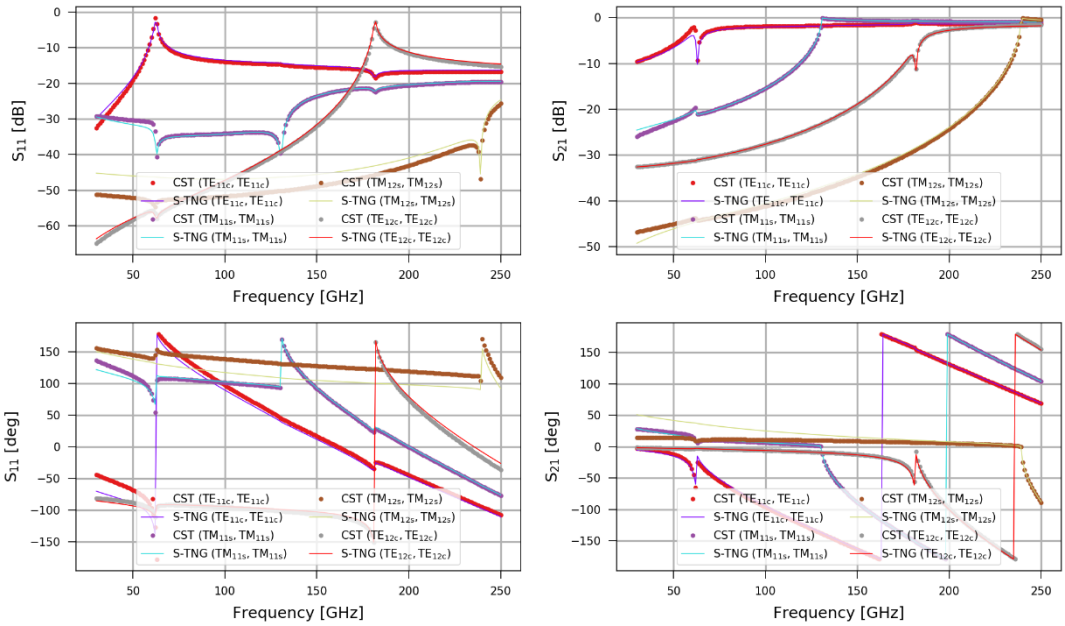

Figure 3-18: Cylindrical waveguide and half filling absorber section with reduced number of modes present 12 modes are considered, 4 radial and 2 azimuthal orders; it is apparent that there is a loss in agreement between the CST and S-TNG results compared to the previous result. Reflection (S_{11}) and Transmission (S_{21}) scattering parameters shown for both CST and S-TNG.

Test No.3 CR-1

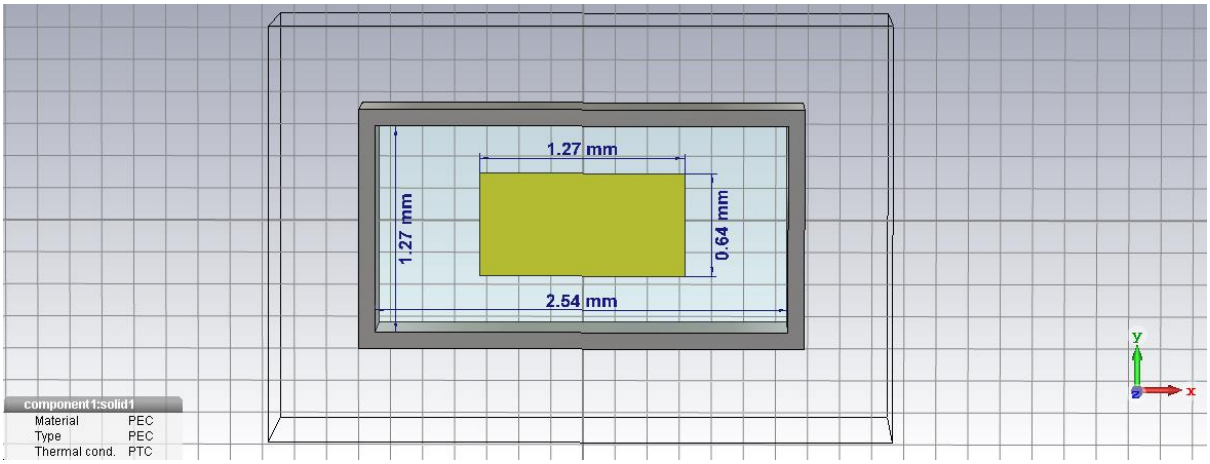

Figure 3-19: Illustration of the system being modelled taken from CST: Rectangular waveguide section with half filling absorber.

Test case CR-1 is shown in Figure 3-19, for the selected set of modes there is excellent agreement in both the reflection and transmission results generated by S-TNG and CST as shown in Figure 3-20.

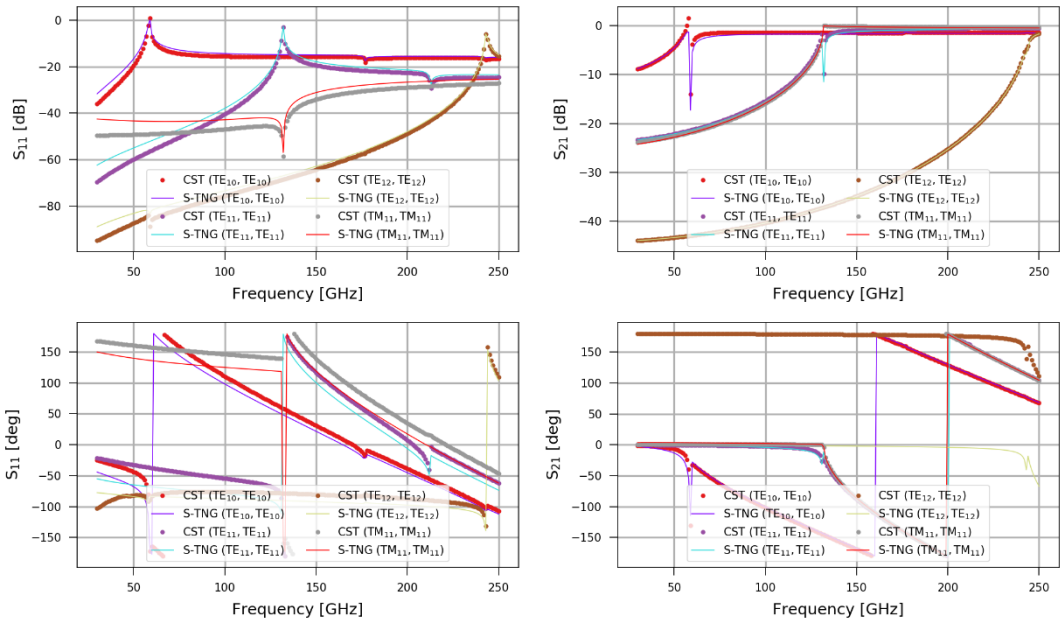

Figure 3-20: : Rectangular waveguide and half filling absorber section with 8 Cartesian orders considered. Reflection (S_{11}) and Transmission (S_{21}) scattering parameters shown for both CST and S-TNG

For test case CR-1:

- As in CC-2, because the absorber section is only partially filling there is a potential for mode mixing.
- A greater number of modes are required to accurately represent the system. For fewer modes considered the disagreement between CST and S-TNG would grow.

- In this case the S-TNG simulation considered 112 modes, corresponding to 8 Cartesian orders.

Test No.4 AC-1

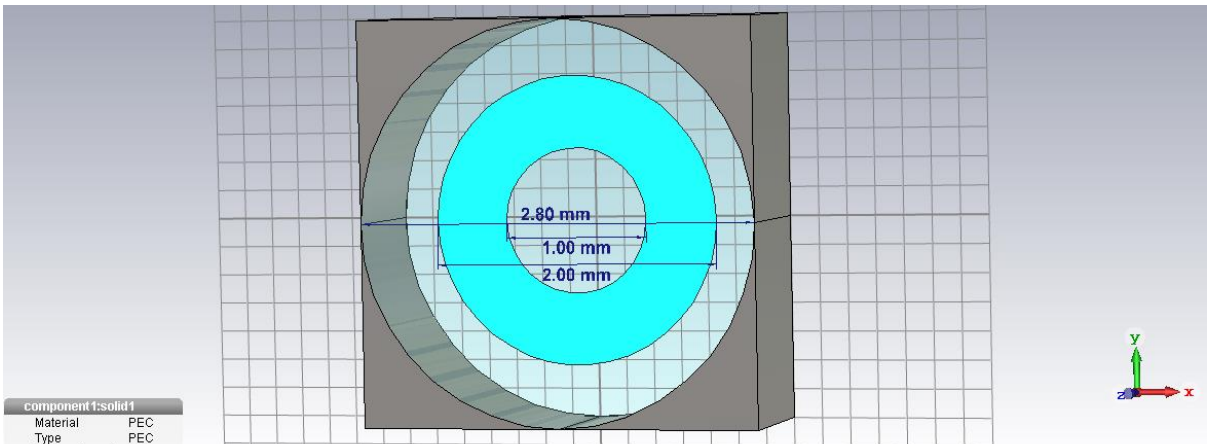

Figure 3-21: Illustration of the system being modelled taken from CST: Cylindrical waveguide and annulus absorber section.

Test case AC-1 is shown in Figure 3-21, for the selected set of modes there is excellent agreement in both the reflection and transmission results generated by S-TNG and CST as shown in Figure 3-22.

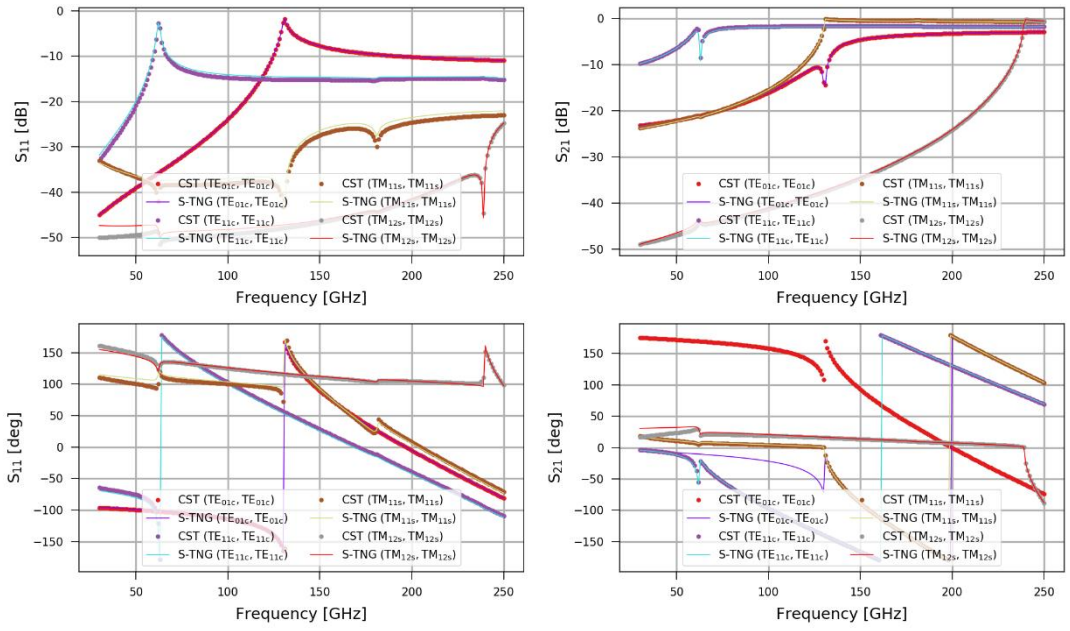

Figure 3-22: Cylindrical waveguide and an annulus absorber section with 112 modes considered, 16 radial and 4 azimuthal orders. Reflection (S_{11}) and Transmission (S_{21}) scattering parameters shown for both CST and S-TNG

For test case AC-1:

- For this test case axial symmetry is maintained even with the unusual shape of the absorber see Figure 3-22.

- There is some slight deviation from the CST results, as before by increasing the number of modes this disagreement can be reduced.

- In this case, the S-TNG simulation considered 112 modes, 16 radial and 4 azimuthal orders.
- Although this absorber geometry has no physical importance, it is interesting to see how well the code can adapt and model unusual absorber geometries and still produce an acceptably accurate result.

Test No.5 AR-1

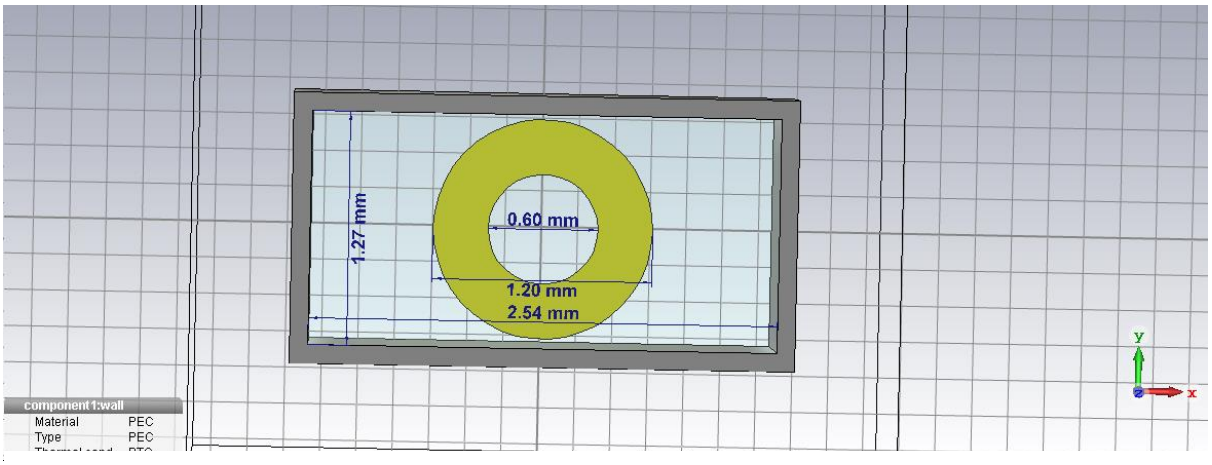

Figure 3-23: Illustration of the system being modelled taken from CST: Rectangular waveguide section with an annulus absorber.

Test case AR-1 is shown in Figure 3-23, for the selected set of modes there is excellent agreement in both the reflection and transmission results generated by S-TNG and CST as shown in Figure 3-24.

For test case AR-1:

- For this test case axial symmetry is maintained even with the unusual shape of the absorber see Figure 3-24.

- There is some slight deviation from the CST results, as before by increasing the number of modes this disagreement can be reduced.

- In this case the S-TNG simulation considered 112 modes, corresponding to 8 Cartesian orders.

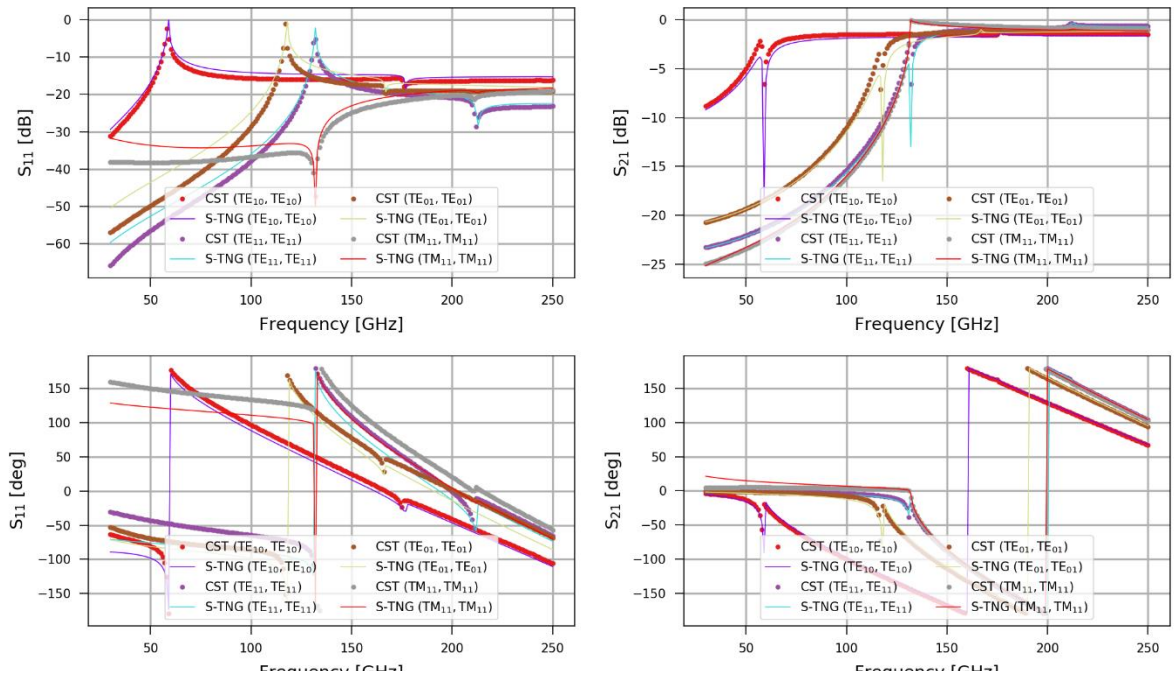

Figure 3-24: Rectangular waveguide and an annulus absorber section with 8 Cartesian orders considered. Reflection (S_{11}) and Transmission (S_{21}) scattering parameters shown for both CST and S-TNG

Test No.6 CJc-1

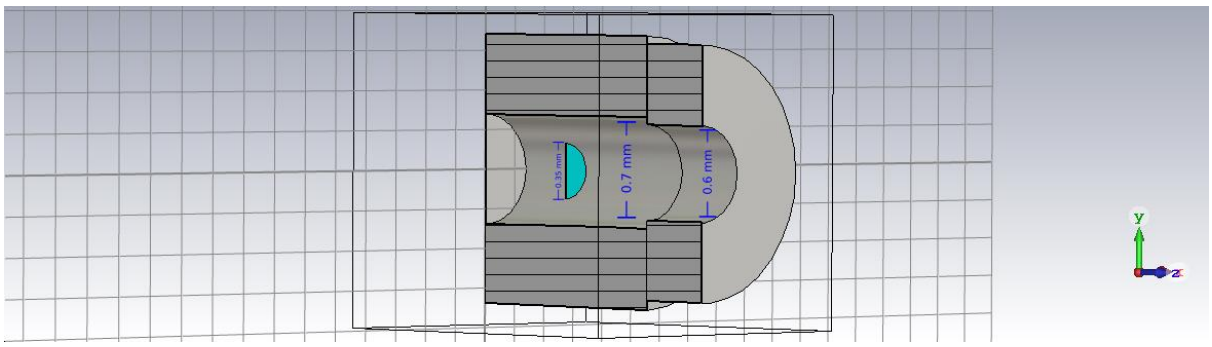

Figure 3-25: Illustration of the system being modelled taken from CST: Cylindrical uniform guide feeding the cavity section.

This example focuses on a much more complicated system with reduced geometry size and an increased frequency range considered. The geometry of the system is shown in Figure 3-25, the smaller uniform guide feeding the cavity has a diameter of 1.2 mm and is of length 1 mm.

The cavity section is formed by cascading the backshort network introduced in chapter 2. While the cavity has a diameter slightly larger than that of the feeding guide, 1.4 mm and has length 3 mm. The absorber section is partially filling the cavity and has an impedance equal to the intrinsic impedance of the free space 377 Ω/■. Again, simulations are performed in both CST and S-TNG allowing for a direct comparison. As shown in Figure 3-26, for propagating modes the agreement between the two sets of results is excellent and as before would improve for a larger number of modes present in the S-TNG simultation. For this test case the S-TNG simulation considered only 8 modes per azimuthal order and 5 azimuthal orders were considered.

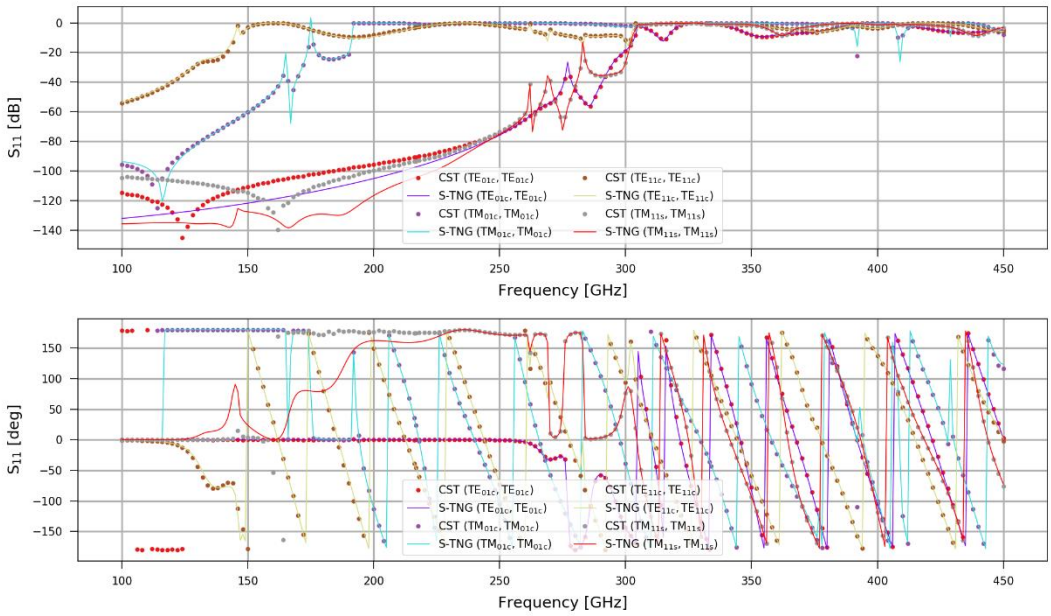

Figure 3-26: Cylindrical cavity with a half filling absorber section Reflection (S_{11}) scattering parameter shown for both CST and S-TNG

3.4 Flat Backshort with Ohmic Losses

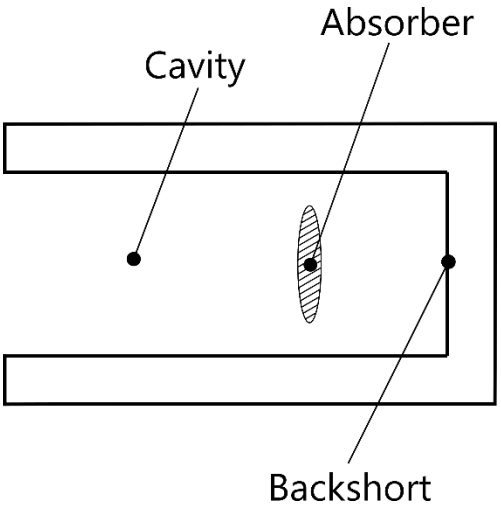

Figure 3-27: Illustration of a cavity coupled absorber section with backshort indicated. The backshort provides a termination point where incident modes are reflected, depending on the wall material these modes may lose power upon reflection.

In chapter 2 the concept of the PEC backshort was introduced which could be cascaded with a typical waveguide section to form a perfectly reflecting cavity structure. This arrangement is similar to the case were an absorber layer completely fills the cross-section (S) of the waveguide. As discussed in section 3.1, where the wall material is assumed to be a good conductor there exists a surface impedance ($Z_s(\omega)$). The general boundary conditions for transverse fields required $\boldsymbol{E}_t = Z_s(\omega)\hat{\boldsymbol{n}}_s \times \boldsymbol{H}$ on S. As the surface normal is in the opposite direction of propagation $\hat{\boldsymbol{n}} = -\hat{\boldsymbol{z}}$, the general boundary condition required for transverse fields at the lossy backshort is:

$$\boldsymbol{E}_t = Z_s(\omega)\boldsymbol{H} \times \hat{\boldsymbol{z}} \text{ on } S \tag{3.4.1}$$

Applying the same procedure as before the complete set of functions which span any transverse electric or magnetic fields are the set of corresponding modal TE or TM fields which are the same as those presented in section 3.2. A scalar product for the transverse fields can be defined, which fully captures the electric field boundary constraint, as:

$$\begin{bmatrix} \boldsymbol{D} & \boldsymbol{0} \\ \boldsymbol{0} & Z^{TM}\boldsymbol{C} \end{bmatrix} \begin{bmatrix} \boldsymbol{e}_{TE} \\ \boldsymbol{e}_{TM} \end{bmatrix} = \begin{bmatrix} Z_s Y^{TE}\boldsymbol{D}_{(S)} & \boldsymbol{0} \\ \boldsymbol{0} & Z_s\boldsymbol{C} \end{bmatrix} \begin{bmatrix} \boldsymbol{h}_{TE} \\ \boldsymbol{h}_{TM} \end{bmatrix} \tag{3.4.2}$$

From equation (3.4.2), the scattering parameters for the TE and TM modes can be solved by expanding the matrices into the following linear equations:

$$\boldsymbol{De}_{TE} = Z_s Y^{TE} \boldsymbol{Dh}_{TE} \Rightarrow \boldsymbol{D}(\boldsymbol{a}^{TE,+} + \boldsymbol{a}^{TE,-}) = Z_s Y^{TE} \boldsymbol{D}(\boldsymbol{a}^{TE,+} - \boldsymbol{a}^{TE,-}) \quad (3.4.3)$$

$$S_{\boldsymbol{ij}}^{TE} = \frac{Z_s Y^{TE} - 1}{Z_s Y^{TE} + 1} \delta_{ij} \quad (3.4.4$$

$$Z^{TM} \boldsymbol{Ce}_{TM} = Z_s \boldsymbol{Ch}_{TM} \Rightarrow Z^{TM} \boldsymbol{C}(\boldsymbol{a}^{TM,+} + \boldsymbol{a}^{TM,-}) = Z_s \boldsymbol{C}(\boldsymbol{a}^{TM,+} - \boldsymbol{a}^{TM,-}) \quad (3.4.5)$$

$$S_{\boldsymbol{ij}}^{TM} = \frac{Z_s - Z^{TM}}{Z_s + Z^{TM}} \delta_{ij} \quad (3.4.6$$

The flat backshort reflects modes according to their own impedance mismatch with the wall with no scattering between modes. The resulting $\boldsymbol{S}_{11}$ is a diagonal matrix, with TE and TM elements shown populating the diagonal entries. It is clear that for a PEC wall ($Z_s = 0$) the scattering matrix becomes $[\boldsymbol{S}_{11}^{backshort}] = [-\boldsymbol{I}]$ as required.

3.5 Physical Surface Roughness Model

The quality of the boundary wall's surface is an important factor to consider when characterising waveguide devices for millimetre and sub-millimetre wave applications. Sub-wavelength surface imperfections or roughness that can arise from the manufacturing process may have a significant impact on the devices performance. At some level, surface imperfections are an unavoidable consequence of the fabrication process. However, the ability to model and analyse these effects is critical for the efficient development of new technologies, especially higher frequency devices where new manufacturing techniques are being refined.

In this section an extension to the mode-matching method to also include a surface roughness model is discussed. The Gradient Model, as presented in (Gold and Helmreich 2017), provides a simple but powerful model of surface roughness at GHz-THz frequencies. The same approach is employed in CST's *Lossy Metal* material, which allows for the inclusion of roughness along the boundary walls of guide sections. By including the gradient model in the mode-matching simulation, the effects of loss due to the boundary walls can be more thoroughly characterised.

The effective surface impedance along the wall will be a result of both the wall's finite bulk conductivity and its surface roughness.

3.5.1 Surface Roughness Gradient Model

The gradient model uses observable roughness parameters and electromagnetic theory to describe surface roughness. A macroscopic view is taken to describe the interaction between the propagating electromagnetic field and the material's surface. It is assumed that the electromagnetic field interacts with the average surface profile of the material (Gold and Helmreich 2017). This is given in terms of the rms-roughness parameter, often included in the technical documents which accompany machined components. This model does not consider the microscopic profile of the surface, as other physical or statistical models such as the snowball model (Huray et al. 2007) do, which relies on many parameters. The gradient model's simplicity means that it is readily implemented, and as macroscopic imperfections are considered valid roughness values will have a non-negligible effect on the surface impedance.

The profile of most machined surfaces has an irregular or random pattern which can be approximated by a normal distribution. This profile of the distribution of heights, is described by a single statistical parameter the rms-roughness (R_q). The rms-roughness gives the standard deviation of the measured distribution of the height profile of the surface. Furthermore, this parameter gives the width of the probability density function $\big(PDF(x)\big)$. The probability density function describes the probability of finding a point on the surface with height x. Finally, integrating the PDF gives the cumulative distribution function $\big(CDF(x)\big)$ which will describe the contact percentage with the material at some distance x from the surface i.e. the amount of the material in contact at that point. The relationship between these statistical parameters is summarised by:

$$R_q = \sqrt{\frac{1}{L}\int_0^L h(x)^2 dx} \tag{3.5.1}$$

$$PDF(x) = \frac{1}{R_q\sqrt{2\pi}} e^{-\frac{x^2}{2R_q^2}} \tag{3.5.2}$$

$$CDF(x) = \int_{-\infty}^{x} PDF(u)du \tag{3.5.3}$$

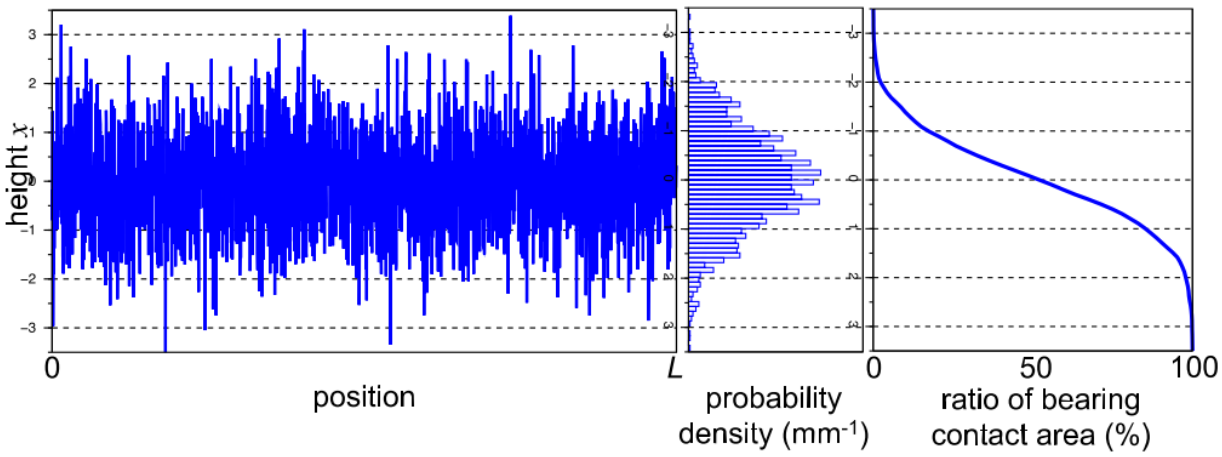

Figure 3-28 Provides a summary of the statistical parameters required to model the surface roughness; a) rms-roughness obtained from the surface profile b) probability density of finding a point at a certain height c) cumulative distribution function give contact percentage with the bulk material (Gold and Helmreich 2017).

Figure 3-28 provides a graphical summary of the key statistical parameters required by the gradient model.

The conditions under which electromagnetic waves can propagate along rough surfaces are considered. For this model to work some restrictions must be made:

- Wavelength must be greater than the conductor dimensions ($\lambda \gg w, t - \text{width, thickness}$)
- Conductor dimensions must be greater than the skin depth ($w, t \gg \delta$)
- Skin depth must be less than or equal to the rms-roughness ($\delta \leq R_q$)
- Finally, R_q must be much less than the structure's dimensions $\left(R_q \ll w, t\right)$, as the electromagnetic field will interact with the average surface profile of the material arising from its roughness.

The appropriate macroscopic surface parameter to describe this is a location dependent conductivity $\sigma(x)$. The profile of the location dependent conductivity follows that of the CDF and is scaled by the bulk conductivity σ_{DC} of the material:

$$\sigma(x) = \sigma_{DC} \cdot CDF(x) \tag{3.5.4}$$

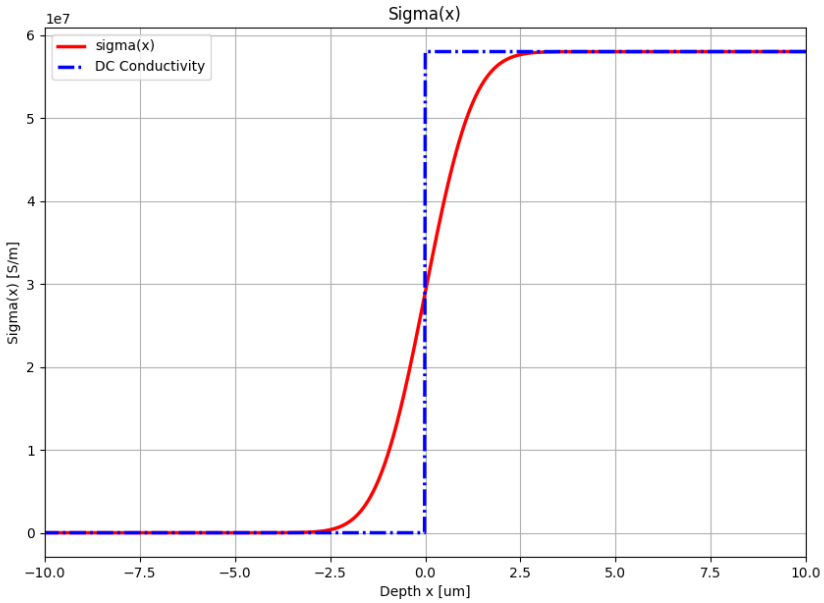

Figure 3-29: Contrasts the conductivity profile of the rough surface ($\sigma_{DC} \cdot CDF(x)$) with the DC-conductivity step of a smooth conductive material.

In Figure 3-29, the DC and location dependent conductivity profiles are seen. For the DC conductivity profile an abrupt step from zero to the bulk conductivity is observed, while the location dependent conductivity profile follows the $CDF(x)$ with bulk conductivity reached well inside the material.

The skin depth of a material can be derived by solving the Helmholtz equation for a smooth material with finite wall conductivity. The solution to this form of the Helmholtz equation describes an exponential decrease in magnetic field and current density, in the material, for increasing depth:

$$\Delta \boldsymbol{B} + k^2 \boldsymbol{B} = 0 \tag{3.5.5}$$

where k is the wavenumber and $k^2 = \frac{\omega}{c_0}\epsilon_r\mu_r - k\omega\mu_0\mu_r\sigma$.

The problem can be reduced to a single dimension, by assuming translational invariance parallel to the conductor's boundary, i.e. the change in a transmission line's surface profile is assumed to be much larger than the penetration depth into the conductor:

$$\frac{\partial^2 B_{||}}{\partial x^2} - j\omega\mu_0\sigma B_{||} = 0 \tag{3.5.6}$$

Here, the x-axis is taken as pointing upright into the material, leading to a differential equation for the magnetic field parallel to the surface given as:

$$B_{||}(x) = B_{||}(0)e^{-(1+j)\frac{x}{\delta}}, \text{with } \delta = \sqrt{\frac{2}{\omega\mu_0\sigma}}. \tag{3.5.7}$$

This solution for the smooth case gives important information about the nature of the result at the upper and lower bounds of the model.

The one-dimensional form of the Helmholtz equation where a location dependent conductivity is considered takes the form:

$$\frac{\partial^2 B_{||}}{\partial x^2} - j\omega\mu_0\sigma B_{||} - \frac{\partial}{\partial x} ln(\sigma) \cdot \frac{\partial B_{||}}{\partial x} = 0 \tag{3.5.8}$$

here the highlighted term is related to the location dependent conductivity. This is a Riccati type differential equation and, in general, can only be solved numerically. The x-direction is chosen to be perpendicular to the metal surface, which is then located in the yz-plane. If the z-direction corresponds to the propagation direction, the remaining component of the magnetic field is B_y. In this case, the current density in the z-direction, J_z, can be calculated as shown:

$$(\nabla \times \boldsymbol{B})_z = \frac{\partial B_y}{\partial x} - \frac{\partial B_x}{\partial y} = \mu_0 J_z \tag{3.5.9}$$

$$J_z = \frac{1}{\mu_0}\frac{\partial B_y}{\partial x} \tag{3.5.10}$$

In Figure 3-30, the magnetic field is shown for the conventional and the location dependent form of the Helmholtz equation for a set of frequencies $[1, 10, 100]$ GHz. In the smooth case, there is an abrupt transition from the field outside the conductor to within. While in the rough case there is a gradual transition from outside to inside the conductor, here $R_q = 1$ µm. This behaviour is consistent with the conductivity profiles shown in Figure 3-29. Clearly, the roughness impacts the magnetic fields away from the plane surface. Furthermore, well inside and away from the conductor the smooth and rough fields begin to match up as expected.

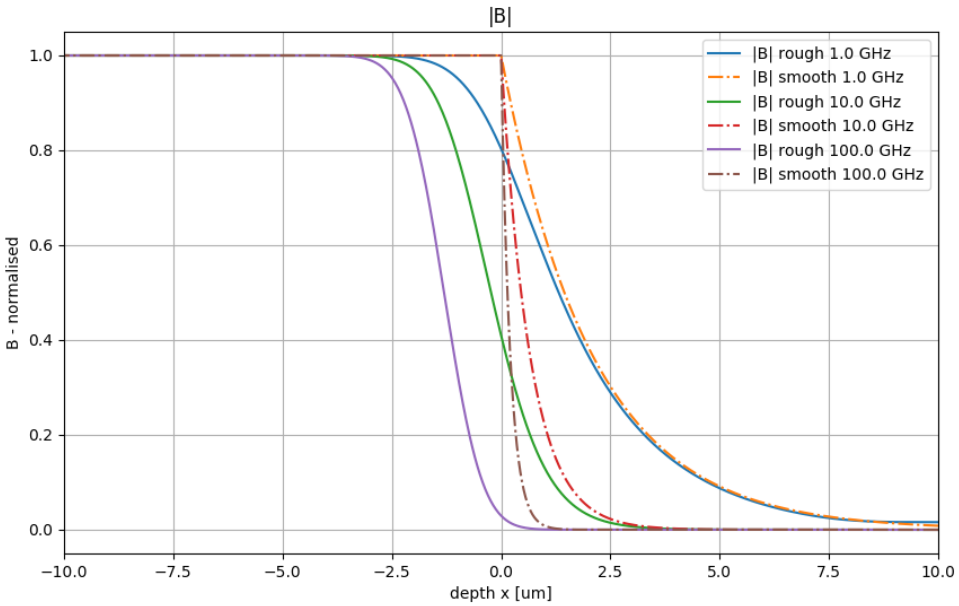

Figure 3-30: Comparison of the magnetic field strengths at $[1, 10, 100]$ GHz inside and outside the conductor for smooth and rough surfaces with equal DC-conductivity. There is a clear effect on the magnetic field strength for the rough surface as the conductor is approached.

Two methods for determining the surface impedance of the rough material are presented in (Gold and Helmreich 2017). One method depends on a single complex frequency component and the other on two real effective material parameters associated with the rough fields. Using the definition of surface impedance, the ratio of the rough fields is determined from Faraday's and Ampere's Laws to obtain $Z_{\blacksquare,rough}$, the rough surface impedance.

Faraday's Law gives:
$$(\nabla \times E)_y = -\frac{\partial E_z}{\partial x} = -j\omega B_y \Rightarrow E_z = \int_{\sigma>0} B_y dx \qquad (3.5.11)$$

Ampere's Law gives:
$$(\nabla \times E)_y = -\frac{\partial E_z}{\partial x} = -j\omega B_y \Rightarrow E_z = \int_{\sigma>0} B_y dx \qquad (3.5.12)$$

$$Z_{\blacksquare,rough} = -\mu_0 \frac{E_z}{B_y} = -j\omega \frac{\int_{\sigma>0} B_y dx}{\int_{\sigma>0} J_z dx} \qquad (3.5.13)$$

The region of integration is only valid for the extent where the conductor is present i.e. $\sigma > 0$.

3.5.2 Verification of Implementation and Analysis of Rough Surface Impedance

To verify the correctness of this implementation of the gradient model CST is used as a benchmark. For test cases with varying degrees of roughness $R_q = [0.5, 1.0, 5.0]$ μm the surface impedance values generated from S-TNG and CST are plotted against one another for a fixed conductivity of $5.8 \times 10^7 \mathrm{S/m}$.

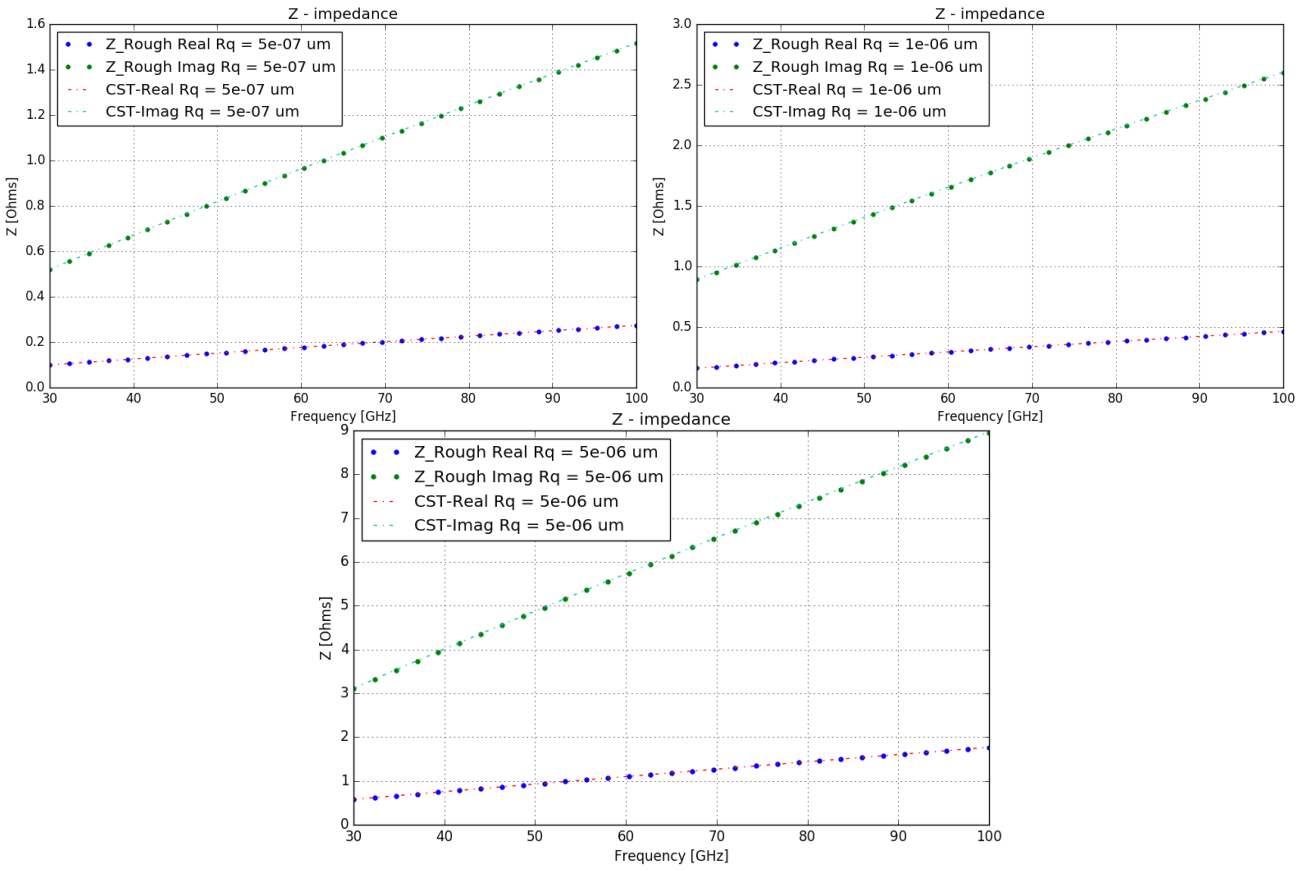

Figure 3-31: Shows the excellent agreement between the CST implementation and the mode-matching implementation for bulk conductivity of $5.8 \times 10^7\ S/m$. *For a)* $R_q = 0.5\ \mu m$ *b)* $R_q = 1\ \mu m$ *and c)* $R_q = 5\ \mu m$

In Figure 3-31, perfect agreement is observed between the two implementations for all roughness value considered.

In sections 3.1.3 and 3.2.2, an exaggerated conductivity value of $\sigma = 5.8 \times 10^4$ S/m was used to observe significant deviation from the PEC case. However, it is clearly not correct to assume this value when modelling physical systems. Typically materials with conductivity values of the order of $\sim 10^7$ S/m are used in waveguide structures. Here, the variation of surface impedance at 100 GHz for a material with excellent conductivity ($\sigma = 5.8 \times 10^7$S/m) and varying roughness $R_q = [0.25 - 25]$ µm is investigated.

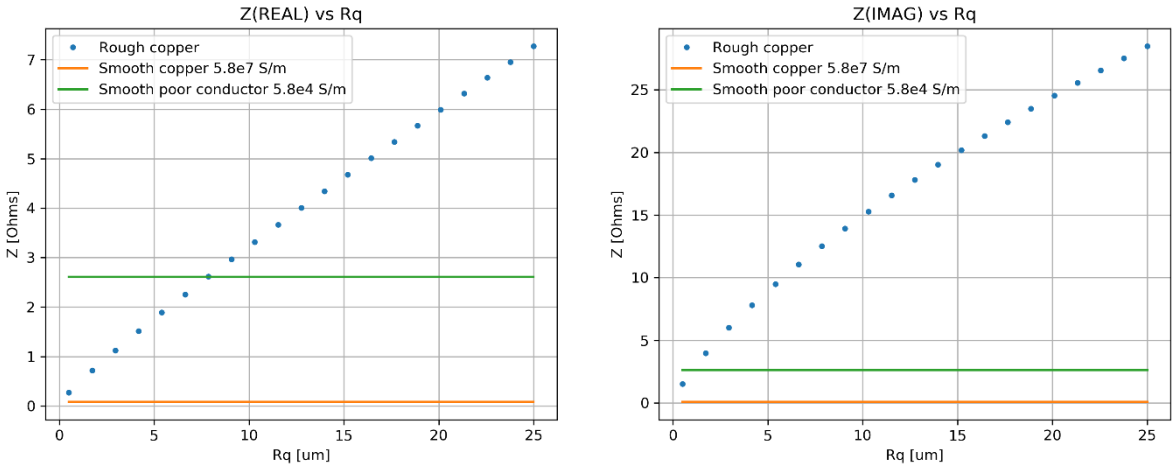

Figure 3-32: Illustrates the variation of surface impedance with increasing surface roughness at 100 GHz plotted with the smooth copper result. The poor conductivity value $\sigma = 5.8 \times 10^4$ S/m used in earlier simulations is also plotted to show how roughness can impact the material's surface impedance.

In Figure 3-32, the rough surface impedance values are compared with smooth copper ($\sigma = 5.8 \times 10^7$S/m) and the poor conductor ($\sigma = 5.8 \times 10^4$S/m) used in earlier test cases. For a roughness of ≈ 7 µm the real impedance for the rough copper material and smooth poor conductor have comparable magnitude, while the imaginary component matches at ≈ 1 µm.

Although the real and imaginary terms grow at different rates, losses consistent with those observed in earlier test cases are obtained by taking the magnitude of the surface impedance. Here, for a roughness of 3 µm the magnitude of the rough surface impedance would be consistent with that of the poor conductor. This is close to 0.1% of the wavelength at 100 GHz, which corresponds to quite an extreme level of roughness (one would hope to have roughness at W-band be closer to 0.1 µm). However, at higher frequency measurements, where the wavelength is in the sub-millimetre range, this level of roughness may be more realistic.

Likewise, by considering how impedance grows with frequency the same trend is observed for the smooth lossy material.

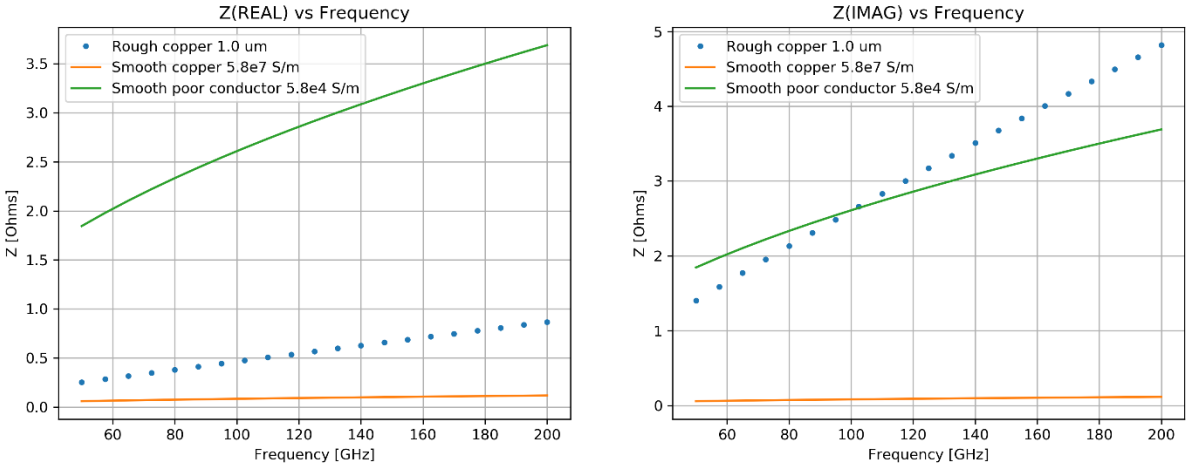

Figure 3-33: Illustrates the variation in surface impedance with frequency for copper with $R_q = 1.0\ \mu m$, smooth cooper and the poor conductor value $\sigma = 5.8 \times 10^4\ S/m$.

In Figure 3-33, a plot of surface impedance against frequency is shown where the three materials introduced earlier are considered. The roughness value selected, 1.0 µm, gives impedance close to the initial starting impedance of the smooth poor conductor case.

The cylindrical junction test presented in section (3.2.2) is revisited with rough lossy walls considered. As observed in Figure 3-34, there is excellent agreement between the two cases. However, the rough surface approach offers a description of the waveguide which is more in line with a real world system.

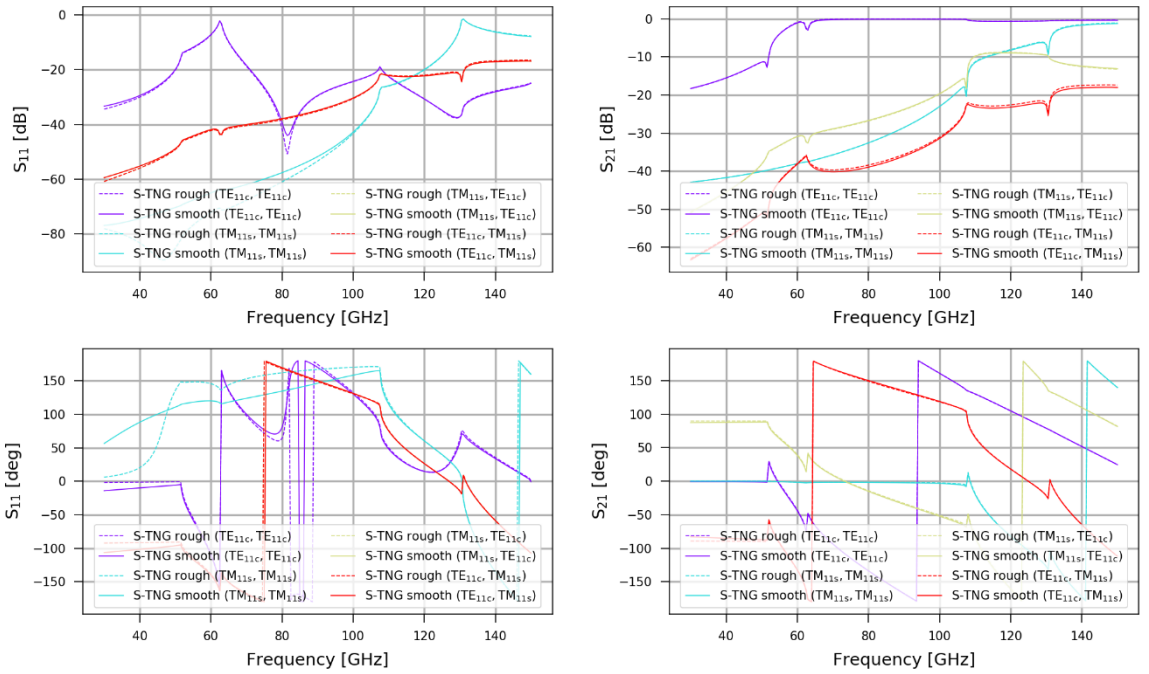

Figure 3-34 Show a comparison between the levels of loss for a copper material with $R_q = 1.0\ \mu m$ and the poor conductor material considered in earlier test cases.

3.6 Experimental Work

For completeness, it was envisioned that the newly developed mode-matching analysis methods would be applied to simple experimental arrangements that could be performed using the Department of Experimental Physics VNA (Vector Network Analyser) laboratory. These measurements would provide experimental verification of the techniques presented in this chapter. The structures to be analysed were a lossy uniform guide section and a cavity coupled absorber device, as shown in Figure 3-35. These systems represent systems which can now be modelled through advancements in the mode-matching software i.e. lossy surfaces and an absorbing surface.

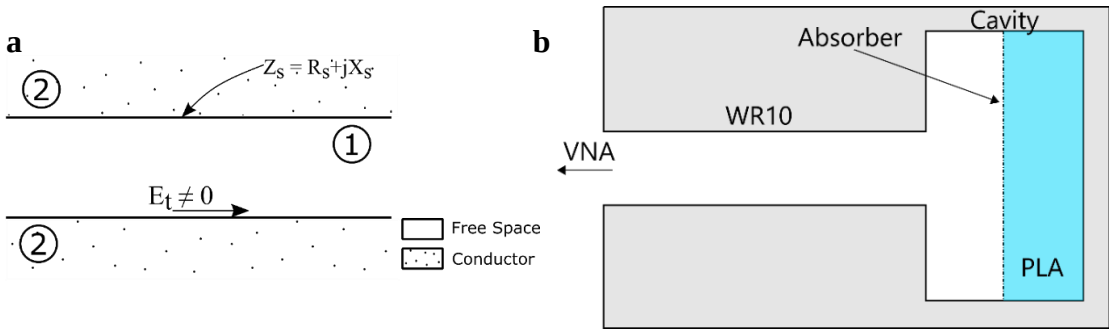

Figure 3-35 a) Shows the lossy uniform guide section complete with the necessary electric field constraints b) Shows the cavity coupled absorber section with the PLA substrate and suspended absorber layer.

A significant amount of preparation was required to facilitate both of these measurements. In the case of the uniform lossy guide section, components had to be machined and a custom Through Reflection Line (TRL) calibration kit for the VNA was designed and fabricated in house. Performing the TRL calibration would allow for the lossy line to be isolated and more accurately measured. In the case of the cavity coupled absorber section, the plan was to suspend the absorber layer (resistive carbon ink) within the guide on 3D printed layer. This meant that the absorber layer sheet resistance and the 3D printed material dielectric properties had to be well characterised before any modelling of the system could be completed.

At this time the results from these experimental test cases are not of sufficient quality to present in this thesis. Ultimately this is due to a number of factors: time constraints due to the VNA laboratory not being accessible for an extended period of time (due to Covid-19 emergency), quality of the machined components necessary for TRL calibration and control of the absorber layer surfaces. However, much of the groundwork has been done so perhaps these measurements may be revisited at another time.

3.7 Summary

This chapter focuses on the advancements made in the modelling capabilities of mode matching methods. The most important of which is the more rigorous treatment of the boundary walls which is necessary for the accurate analysis of high frequency and multimoded waveguides. In the description of the mode-matching method the effects of non-zero surface impedance along the boundary can be accurately modelled by including a large but finite wall conductivity. Furthermore, the non-PEC treatment of the boundary was extended to allow for surface roughness to be included via the simple but power Gradient Model. As in Chapter 2 verifying test cases are presented throughout this chapter to validate the correctness of this lossy walled approach. Finally, the infinitely this absorber layer model developed by (Doherty 2012) was revisited. Using the newly implemented contour integral form of the mode-matching methods it was shown how arbitrary absorber shapes could be trivially modelled.

Chapter 4 – New Tools for Pixel Modelling

The development of additional techniques for the analysis of millimetre and sub-millimetre wave technologies is discussed in this chapter. These features are developed with efficiency, accuracy and simplicity in mind, to provide a new set of tools to solve specific problems encountered by the mode matching software. One potential bottleneck for the analysis of waveguide structures is the use of numerical techniques to evaluate the coupling integrals. Often there may be a situation where no analytic solutions are available (e.g. offset cylindrical junction sections). For more complex geometries or systems, where a large number of modes are considered, the problem becomes increasingly computationally intensive.

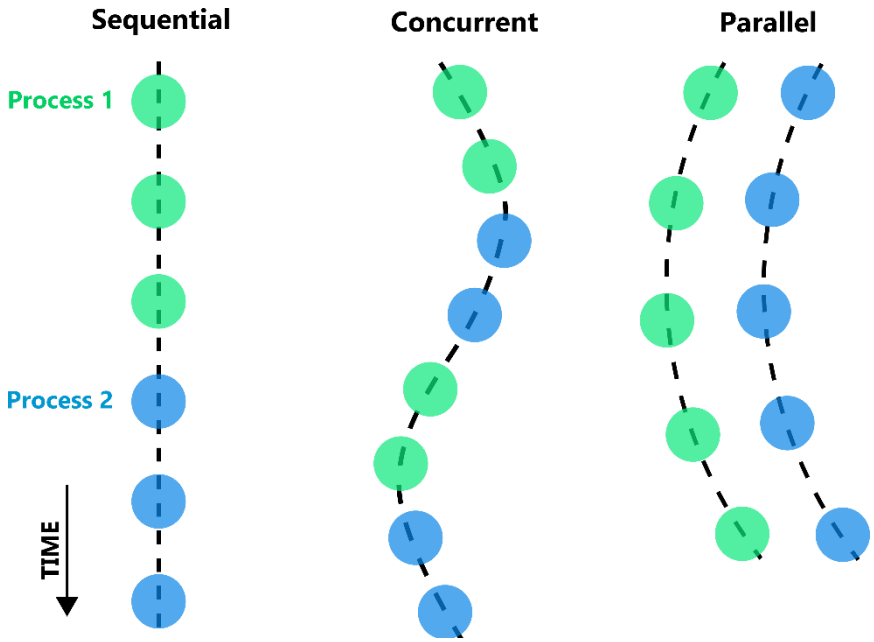

Figure 4-1: Sequential, Concurrent and Parallel execution of processes (https://medium.com/platformer-blog/node-js-concurrency-with-async-await-and-promises-b4c4ae8f4510)

By using hardware acceleration methods, such as GPU (Graphical Processing Unit) computing, these numerical constraints can be alleviated. The implementation of the mode matching methods detailed in the previous chapters have relied on sequential programming techniques, as shown in Figure 4-1, this means tasks are scheduled in order and take place one after another. By considering parallelising the tasks using the added power of the GPU, independent tasks can be separated and performed at the same time, as shown in Figure 4-1. This can radically improve the performance of the software. In this chapter the initial steps are taken towards the development of a fully parallelised implementation of the mode matching techniques presented so far. This section will introduce the necessary tools, software and parallel thinking required to develop efficient implementations of the mode matching methods.

Another novel tool developed in this chapter is the virtual non-reciprocal waveguide port. In Chapter 3, the concept of lossy elements was introduced, including in particular the absorber network segment. It is often difficult to determine the total power dissipated by such a lossy element for a given excitation. Here, rather than determining the overall loss with and without the absorber present, i.e. using the return loss method, the information can be obtained from augmenting the scattering matrix for the system. The conventional 2-port scattering matrix description of the absorber layer is extended to include a virtual port. This virtual port is mapped to the lossy element, enabling the real power dissipated by the lossy element to be accounted for through outgoing virtual modes under the condition of non-reciprocity. In this chapter a practical method for power monitoring of lossy elements using this technique is presented in detail.

Finally, an alternative treatment of the interface between waveguide aperture and free-space is considered. So far this transition has been largely ignored and zero reflection at the aperture was assumed. However, to fully model compact open ended waveguide devices (OEGs), such as waveguide probes, the correct scattering of modes at the interface must be determined. In an attempt to more accurately account for the free-space transition a method to match guide modes to a large but finite set of free-space modes (composed of fan of radiating plane-waves) was proposed. Ultimately, the mode matching method was not suited to this implementation due to the necessarily high density of free-space modes.

4.1 Development of a Parallelised Routine for Mode-Matching Methods

A significant drawback to the sequential numerical technique is the time taken to evaluate the integrals presented in Chapters 2 and 3 where the structure is complex or over-moded. In this section, the set of tools and routines required to solve the numerical coupling integral in parallel are developed. The main goal is to improve the simulation times with no loss in accuracy. Hardware devices such as GPUs (graphical processing units) are well suited to these computationally intensive tasks due to their underlying architecture. One restriction made is that any developed software must be portable across many devices and architectures. As such, OpenCL (Open Computing Language) is chosen as the development framework for the parallelised mode matching methods. Unlike other frameworks, such as CUDA or Tensor, OpenCL is an open source and widely implemented API (Application Programming Interface) for the development of parallel routines. Some devices have architecture designs which can be better utilized by code developed specifically with that architecture in mind i.e. NVIDIA with CUDA. Each device may have a different underlying architecture, however, OpenCL employs a universal design pattern which is portable across all devices (Opencl 2009). Thus, portable programs can be developed that may use all resource available, regardless of architecture, potentially on a heterogeneous platform i.e. including a combination of CPUs, GPUs, FPGAs, etc. The OpenCL language is based on C99 but has many custom features to aid in the development of parallelised code (Opencl 2009).

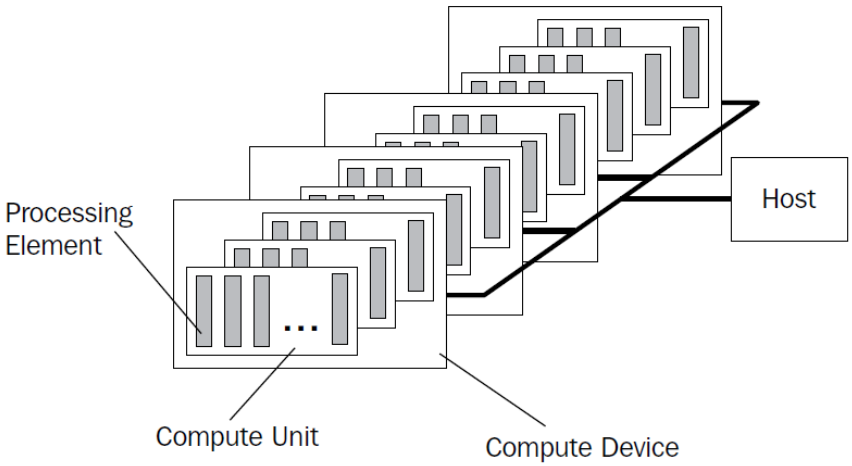

Figure 4-2: Overview of the OpenCL development framework; Each compute device (separate GPU's or CPU's) is made up of a number of compute units which operate in parallel and which contain a number of processing elements which too can operate in parallel. The number of parallel process which can take place on a compute device is governed by the device itself. Each compute device is scheduled and initialised by some host device (Opencl 2009).

Efficient development of parallel code relies on good knowledge of the hardware architecture available. However, OpenCL provides an abstraction of the architecture to provide a clearer

picture of the hardware device's execution cycle. The framework for OpenCL at its core is quite straightforward, but is governed by a strict set of rules that must be adhered to. In Figure 4-2, an overview of the development framework used for OpenCL is presented.

OpenCL handles the workflow across many devices through a dedicated *host* device. The host is used to manage and schedule the memory and execution operations on the available devices on the *platform*. Each of the non-host devices are available for computation operations and are referred to as *compute devices* which are sub-divided into *compute units* or *work groups* (Gaster et al. 2013). Work groups can be further sub-divided into *processing elements* or *work items*. This architecture is highlighted in framework overview shown in Figure 4-2. The problem is defined by an object known as the *kernel* which contains the code to be executed on the device, effectively it is the entry point of the OpenCL code i.e. its main function (Gaster et al. 2013). The kernel may be executed across one or many Compute Devices depending on the application. In this implementation only the operation for one compute device being utilized is considered. The architecture of OpenCL can also be seen in the memory map detailed in Figure 4-3.

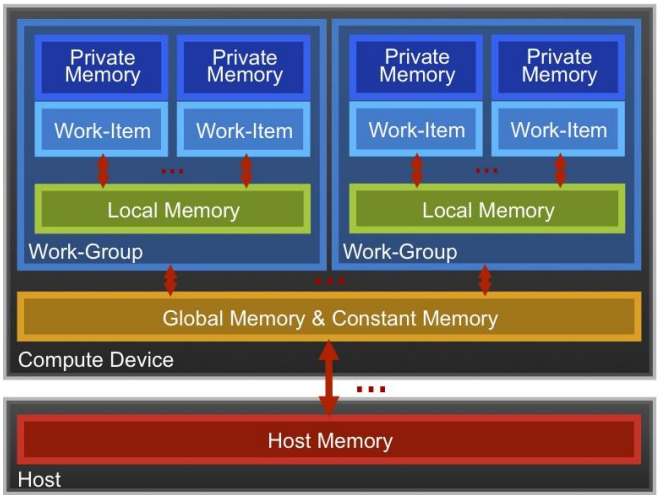

Figure 4-3 Shows an overview of the OpenCL memory model. The local memory banks for each work groups are separate from each other and must be scheduled to write to global memory such that the completed task can be required to the host device.

Memory management in OpenCL is left explicitly to the programmer, they must control the flow of data between the compute devices and host (Opencl 2009). There are three types of memory in OpenCL:

- *Global and Constant Memory* is visible to all work items. It is the largest and slowest of the memories available on the device. Constant memory is read only for the device.
    - 1-10 GB of Global Memory

    - 10-100 KB of Constant Memory
- *Local Memory* is shared memory within work groups. It is smaller but much faster than global memory.
    - 1-10 KB per work-group
- *Private Memory* is available to individual work items. It is also very limited in size but has rapid memory operations.
    - 10 bytes per work item

This memory allocation is shown in Figure 4-3, it can be seen that the global and constant memory banks are shared between the host and the computing device. Since these are separate devices there is clear a bottleneck where data must be transferred between them. The host device or *host context* defines all memory management and scheduling aspects of the execution. This context becomes especially important where multiple devices or kernels must operate concurrently. Scheduling and synchronisation in OpenCL is critical. Work items can be easily synchronised within individual work groups. However, between different work groups this is no longer possible as they operate on different local memory banks. Utilities such as barriers and memory fences provide a mechanism to synchronise operations between work groups during execution (Gaster et al. 2013). These tools ensure all local and global operations have been executed before proceeding any further. The theory introduced in this section gives the necessary tools to develop parallel scripts to tackle the coupling integral problem.

The OpenCL framework provides an abstraction from the individual architectures of different hardware devices. However, there are certain hardware aspects that must be considered which may influence the design choices made by the programmer or to gain the maximum performance from the compute devices. Each device will have a certain number of CPUs or *compute units* (CUs) in the case of GPUs, certain precision limits/speeds and amount of memory bandwidth. For example, in GPUs typically there are > 40 CUs, while CPUs typically have 4-8 Cores. Because of this GPUs are more suited towards parallel applications as the problem has many more available compute units. The main development device used in this work is an **AMD FirePro™ W9100** GPU, see Figure 4-4. The key features of this card are that:

- **Stream Processors and Compute Units:** 2816 and 44 CUs.
- **Peak Single (FP32)/Double Precision (FP64) Performance:** 5.24/2.62 TFLOPs.
- **Memory Size/Type:** 32 GB GDDR5

- **Memory Bandwidth:** 320 GB/s.

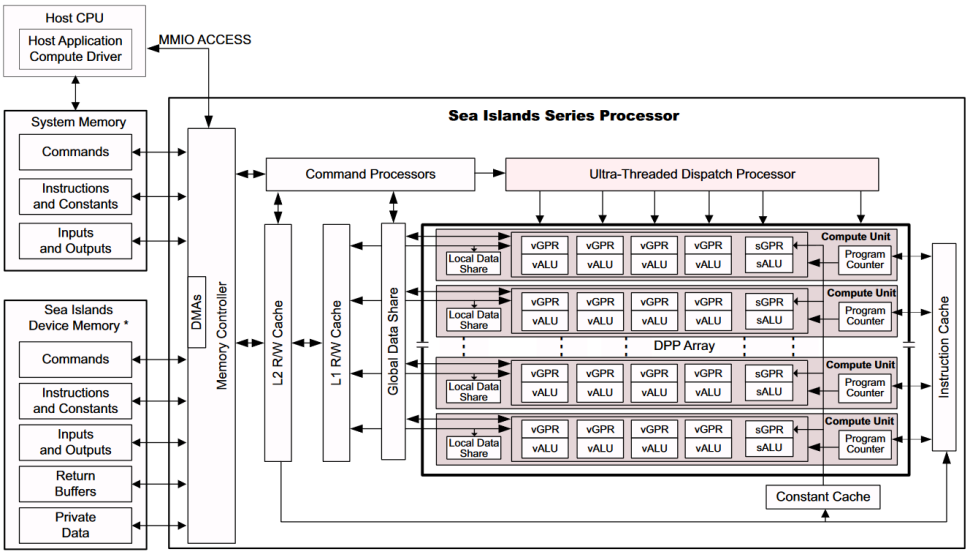

Figure 4-4: Overview of the AMD FirePro™ W9100 GPU architecture (AMD 2013)

The interface code used by the host device to perform the scheduling and memory management aspects of the program is typically written in a more modern accessible language. Here, the development language is Python and using the *PyOpenCL* module the parallel code can be easily integrated into existing code. The best way to understand the development of the OpenCL code is through example. In the following section the solution for the coupling integrals in parallel is presented with reference to the components introduced in this section to give a clear insight into the development and operation of OpenCL code.

4.1.1 Parallel Algorithm Solution to Numerical Coupling-Integrals

The networks introduced in Chapter's 2 and 3 rely on the solutions to the common coupling integrals type i.e. Type B, C or D. In many cases there are analytical solutions to these integrals, however, where no analytic solutions can be found the problem must be solved numerically. This section outlines an approach which can be applied to either rectangular or cylindrical geometries, however there is a particular focus on the offset cylindrical junctions as there exists no analytical solution to this scenario. As shown in Chapter 2, the surface integral for the common integrals can be reduced to contour integrals, which are more readily integrable, and interpolation methods can be exploited to deal with singularities in the contour integral approach. The common integral presented in Chapter 2 must be re-formulated to take advantage of the parallel capabilities of the GPU device.

Type	Surface Integral Form	Line Integral Form	
B	$B_{ij}^{kl}(S) = \int_S \nabla A_i^k \cdot \left(\nabla F_j^l \times \hat{\boldsymbol{z}}\right) dS$	$B_{ij}^{kl}(S) = \int_{dS} \left(A_i^k \nabla F_j^l\right) dl$	*(4.1.1)*
	$-B_{ji}^{lk}(S) = \int_S \nabla F_i^k \cdot \left(\nabla A_j^l \times \hat{\boldsymbol{z}}\right) dS$	$B_{ij}^{kl}(S) = -\int_{dS} \left(F_j^l \nabla A_i^k\right) dl$	
C	$C_{ij}^{kl}(S) = \int_S \nabla A_i^k \cdot \nabla A_j^l dS$	$C_{ij}^{RL}(S_L) = \frac{\left(\beta_{c,i}^{R,TM}\right)^2 \int_{dS} A_i^R \nabla A_j^L \cdot \hat{\boldsymbol{n}} dl}{\left(\beta_{c,i}^{R,TM}\right)^2 - \left(\beta_{c,j}^{L,TM}\right)^2}$	*(4.1.2)*
D	$D_{ij}^{kl}(S) = \int_S \nabla F_i^k \cdot \nabla F_j^l dS$	$D_{ij}^{RL}(S_L) = \frac{\left(\beta_{c,i}^{L,TE}\right)^2 \int_{dS} F_j^L \nabla F_i^R \cdot \hat{\boldsymbol{n}} dl}{\left(\beta_{c,j}^{L,TE}\right)^2 - \left(\beta_{c,i}^{R,TE}\right)^2}$	*(4.1.3)*

$$\int_{d\Omega} \boldsymbol{A} \cdot \nabla \boldsymbol{B}\, dl \qquad (4.1.4)$$

The contour integrals can be expressed in general as the inner product of the potentials of the two different modeset as shown in equation (4.1.4). This general form of the solution will be the foundation of the parallel formulation. Here Ω represents the intersection region between the two uniform guide sections that must be integrated over, **A** and **B** represent the potentials associated with each mode being considered. Collectively they span all the necessary coupling integrals for the normal (TE-TE, TM-TM) and tangential (TE-TM, TM-TE) mode coupling cases. The algorithm developed here works by breaking the problem into independent blocks which are divided among the available work groups.

To demonstrate the method, consider 4 workgroups and 8 modes on both sides of the interface between the guides. Each of the blocks works on a solving the coupling integrals for a particular sub-group of the modes, the outer-product of these modesets must be taken as the modes can couple in a bijective manner. The notation for the modal potentials for the left and right modesets **A** and **B** are defined. The work groups are split up such that the sub-groups of these modal potentials cover all cases of the outer product between the two sets of modal potentials as shown in Figure 4-5.

$$\boldsymbol{A} = \{A_0, \dots, A_7\}$$
$$\boldsymbol{B} = \{B_0, \dots, B_7\} \tag{4.1.5}$$

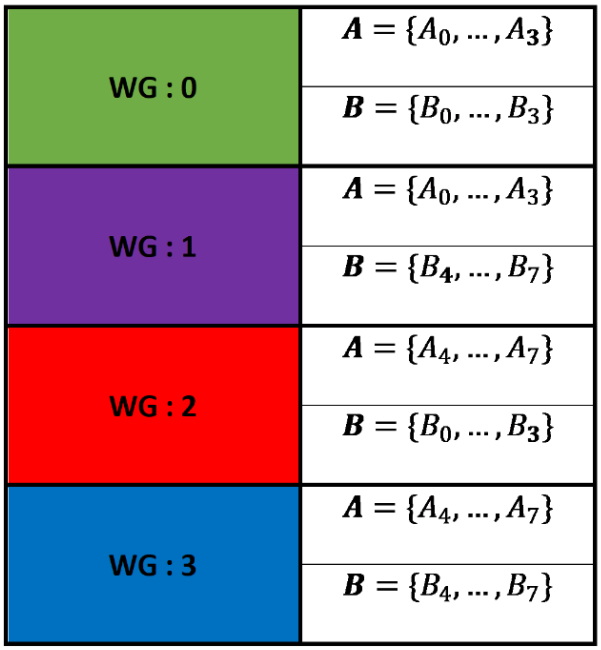

Figure 4-5: Division of modeset among workgroups, each workgroup will operate on a different subset of modes to produce a complete scattering matrix

The outer product of the modal potentials within each of these work groups gives all valid modal potentials that may exist. Set-up of the problem is handled strictly by the host device, the compute device operates on the mode data supplied. As such, any mode partitioning must be done externally to the OpenCL code. The complete set of coupling integrals will have the following form where the contribution from all the sub-groups are brought together to give the full result for the given modesets.

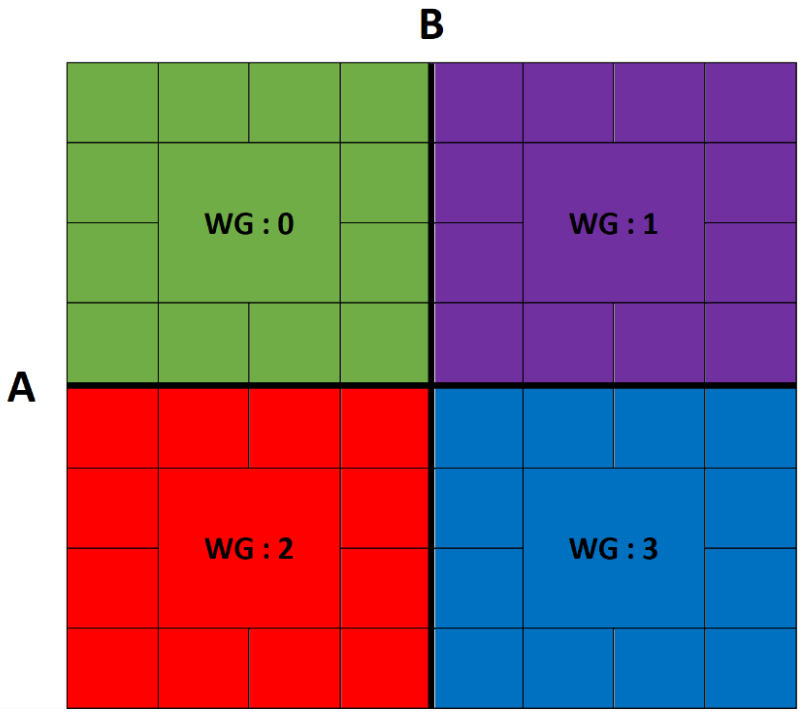

Figure 4-6: Joining of the results obtained from each workgroup, this has the form of the required scattering matrix composed of the modesets A and B

Within each work group the coupling integrals, which make up the set of modal combination shown in Figure 4-6, are solved using Riemann sums over the region of integration. Here these are all solved in parallel by the work items which are available in each work group, each combination gets a dedicated branch of local memory. By contrasting this splitting of the work load with the OpenCL code given in Figure 4-7. The work groups constituent work items generate the modal potentials **X** (which are by far the most computationally intensive part of the kernel call). After which, a barrier is placed to ensure that all potential have been determined before the outer product of the sub-group of modes is calculated. The solutions to the outer product are continuously summed **Y** such that by Riemann sums the coupling integral for the modes is calculated. These are then passed to global memory and read by the host **Z**. Each of the different cases for couple between the different mode types is also handled by the OpenCL code. This code scales cubically, such that for 16 work groups a similar pattern can be followed to determine the overall coupling integrals of the modes. The modeset solutions are padded to retain the square shape and pads can be removed after the execution cycle of the OpenCL code.

```
__kernel void blocks_scalar_normal(const my_circle circle,
                                   __global my_mode* modesL,__global my_mode* modesR,
                                   __local double* A,__local double* B,
                                   __local double* D,__global double* C,
                                   __global double* T,const int limit,
                                   const double dx,const double dy,
                                   const double alpha){
    int i,j,n;
    quple pt;

    int num_wrk_groups = get_global_size(0);
    int num_wrk_items  = get_local_size(0);
    int l_id       = get_local_id(0);
    int g_id       = get_group_id(0);

    double rowsteps = sqrt((double)num_wrk_groups/(double)(num_wrk_items*num_wrk_items));
    double step_size = (1.0/((double) limit));
    double t = 0.0;
    for(i =0;i<num_wrk_items;i++){
        for(j=0;j<num_wrk_items;j++){
            D[i*num_wrk_items + j] = 0;
        }
    }

    for(n = 0;n < limit; n++){
            /* Calculation Point t */
        t = n*step_size;
        pt = edgePoint(circle.start,circle.length,circle.radius,circle.centerA,circle.centerB,t);
            /* Index Mode Lists For WG */
        int Astart = (floor(g_id/rowsteps))*num_wrk_items;
        int Bstart = (g_id%(int)rowsteps)*num_wrk_items;

            /* Populate A and B with modes */
        A[l_id] = LHPOT(modesL[Astart + l_id], pt, dx, dy, alpha);
        B[l_id] = RHPOT(modesR[Bstart + l_id], pt, dx, dy, alpha);
        barrier(CLK_LOCAL_MEM_FENCE);

            /*Continuous sum of outer product of potentials*/
        for(i =0;i<num_wrk_items;i++){
            for(j=0;j<num_wrk_items;j++){
                D[i*num_wrk_items + j] += A[i]*B[j];
            }
        }
        barrier(CLK_LOCAL_MEM_FENCE);
    }
    /* Populate global array once complete*/
    int k = 0;
    for(k=0;k<num_wrk_items*num_wrk_items;k++){
        T[g_id*num_wrk_items*num_wrk_items + k] += D[k];
    }
    barrier(CLK_GLOBAL_MEM_FENCE);
}
```

X

Y

Z

*Figure 4-7: OpenCL code for the integrate scalar normal case core blocks are: **X** generates the modal potentials, **Y** continuously summed outer-products, **Z** passed to global memory and read by the host.*

The host is responsible for all of the set-up and execution calls as well as reading/building the OpenCL code and providing a context for the kernel execution. As well as this the argument types for the kernels can be predefined here as they are not expected to change once the code has been built. Here any common structures needed between Python and OpenCL can be defined such as mode structures and boundary shapes. These can be passed to the device once populated as a type which is dependent on the structure or as a None type. Calls to the kernel involve firstly determining the problem size and then assigning the appropriate amount of resources to the kernel call. Here the required memory assets local/global are assigned including any constant values such as the boundary. These assets are then given to the kernel where it is then queued and executed. The final result is fetched from the kernel and the device

memory assets are released. Finally, unwrapping and stacking of the data blocks highlighted in the previous section is performed. The final result is then passed where the scaling a refactoring can occur.

The correct scaling factors associated with the coupling integrals must be also applied to get correctly normalised results. These are generated at a mesh-grid which perform elementwise multiplication on the blocks of integral results. In some cases, padding of the mode-sets is performed to ensure *square* matrices are produced, these extra elements must be removed from the final result. These extra elements are pushed to the sides and bottoms of the blocks and require just the last few row and columns to be removed before progressing. Each of the results from the blocks algorithms are cast together using a concatenate function to assemble the TE-TE, TE-TM, TM-TE and TM-TM results. Lastly, this separation of the modes into their transverse electric and magnetic components is not natural when discussing cylindrical guide section. Instead, they should be ordered in terms of their azimuthal and radial orders. This requires refactoring the OpenCL result into this form. Test cases were performed to gauge the performance gain of the OpenCL implementation of the integration code. Two circular guide sections with dimensions $r = 1.4$ mm and $r = 1.7$ mm were cascaded together, with an offset *dx* (0.2 mm) & *dy* (0.2 mm) present. For the numerical coupling integrals PEC and generalised (lossy) single runs of the full modesets are performed and the timing is shown below.

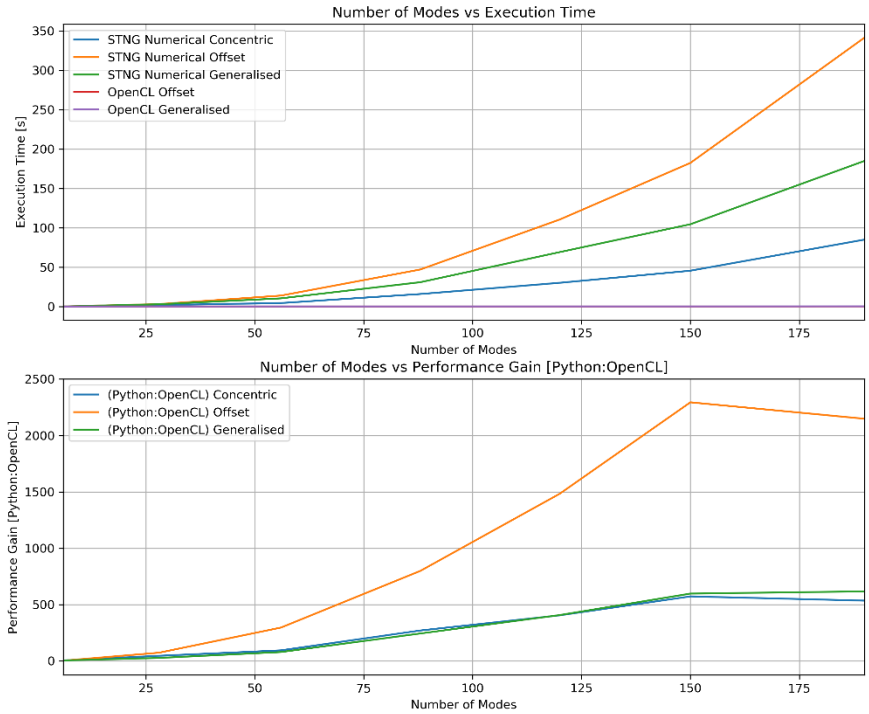

Figure 4-8:Shows the performance gain of parallel execution over serial execution: a) shows the raw simulation times of different networks using serial and parallel code b) gives the ratio of serial and parallel simulation times for identical systems.

Table 4-1 Gives the times of serial and parallel executions for varying number of modes included. Significant slowdown in serial execution with increasing modeset size is observed.

Type	No. Modes	Execution time (Python)	Execution time (OpenCL)
Coupling Integral (offset)	**6**	**0.07 (s)**	**0.0312 (s)**
	28	**3.06 (s)**	**0.042 (s)**
	56	**13.9 (s)**	**0.047 (s)**
	88	**47.04 (s)**	**0.0589 (s)**
	120	**110.5 (s)**	**0.0745 (s)**
	150	**182.4 (s)**	**0.0795 (s)**
	190	**341.6 (s)**	**0.159 (s)**
Generalised Integral (Lossy)	**6**	**0.13 (s)**	**0.0312 (s)**
	28	**2.9 (s)**	**0.11 (s)**
	56	**10.4 (s)**	**0.132 (s)**
	88	**30.9 (s)**	**0.127 (s)**
	120	**69.13 (s)**	**0.170 (s)**
	150	**104.5 (s)**	**0.175 (s)**
	190	**185 (s)**	**0.30 (s)**

4.1.2 Testing and Verification of the Parallelised Code

Verification of the method relies on CST Microwave Studio to produce reference estimates of the scattering parameters for identical systems as performed for the networks in Chapters 2 and 3. Considering the same test cases, the OpenCL implementation can be compared against identical CST simulation results. As before, very low wall conductivity is used to exaggerate the effect of the surface impedance, so that a significant deviation from the PEC case is observed. The following test cases are considered for the verification of the parallelised implementation.

- Junction of two cylindrical waveguide sections: the first of radius 1.4 mm and the second of radius 1.7 mm, both with length 1 mm and PEC walls (210 modes considered: 14 radial and 8 azimuthal orders).
    - With no offset (concentric case)
    - With a 0.2 mm offset in the *x*-direction of the second guide
- Junction of two cylindrical waveguide sections: the first of radius 1.4 mm and the second of radius 1.7 mm, both with length 1 mm and wall conductivity of $\sigma = 5.4 \times 10^4$ S/m (210 modes considered: 14 radial and 8 azimuthal orders).
    - With no offset (concentric case)
    - With a 0.2 mm offset in the *x*-direction of the second guide

The following figures demonstrate the correctness of the accelerated mode matching code over a frequency range of $30 - 300$ GHz and for a select set of modes the results the reflection (S_{11}) and transmission (S_{21}) results. For the both the concentric and offset PEC junctions there is excellent agreement between the two simulations as observed in Figure 4-9 and Figure 4-10.

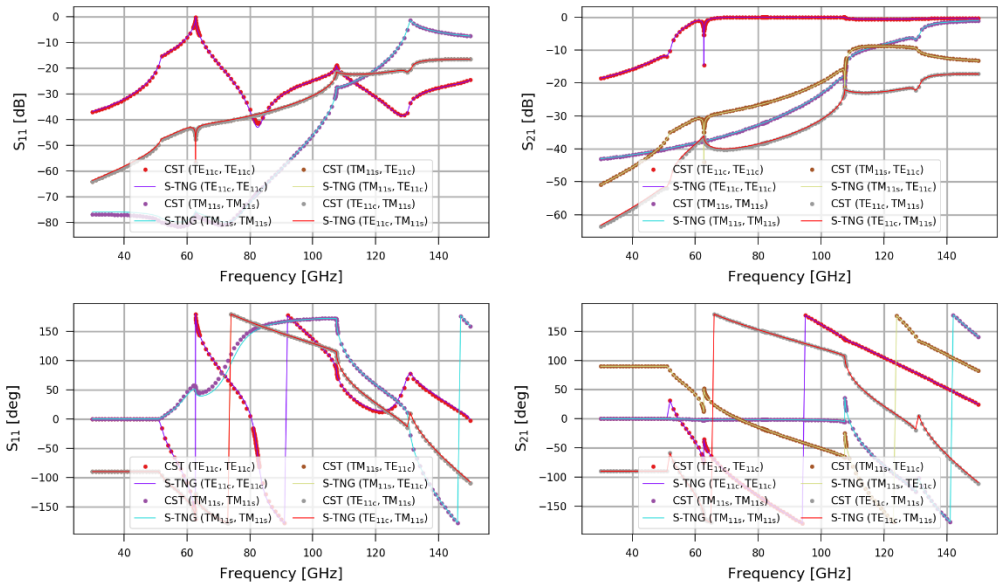

Figure 4-9: Results for selected modes in a 1.4mm circular to 1.7mm circular guide junction, with no offset. The OpenCL method is used in this case with 14 radial orders included.

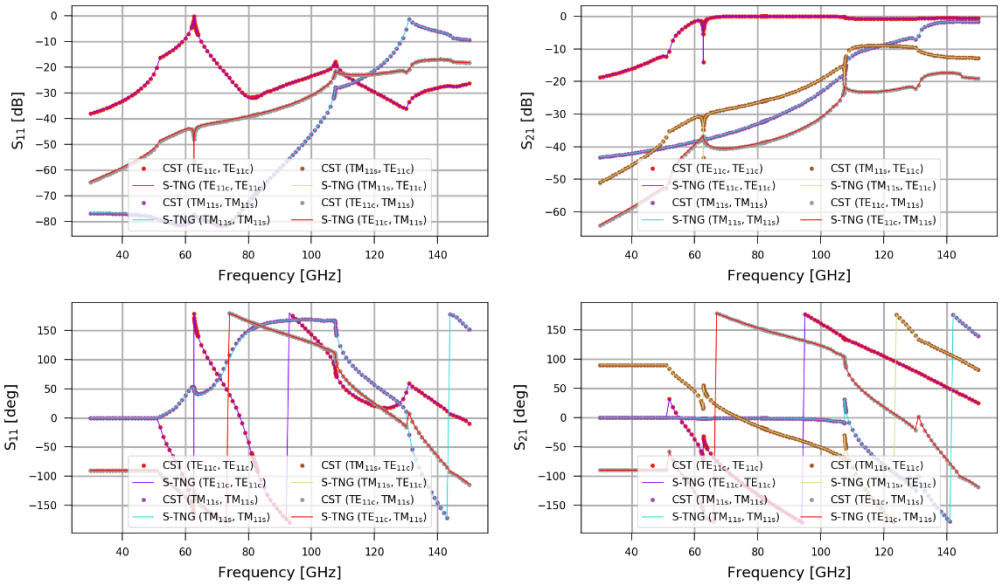

Figure 4-10 Results for selected modes in a 1.4mm circular to 1.7mm circular guide junction, with dx = 0.2 mm offset. The OpenCL method is used in this case with 14 radial orders included.

Furthermore, for the both the concentric and offset lossy junctions ($\sigma = 5.4 \times 10^4$ S/m) excellent agreement is also observed between the two simulations as shown in Figure 4-11 and Figure 4-12.

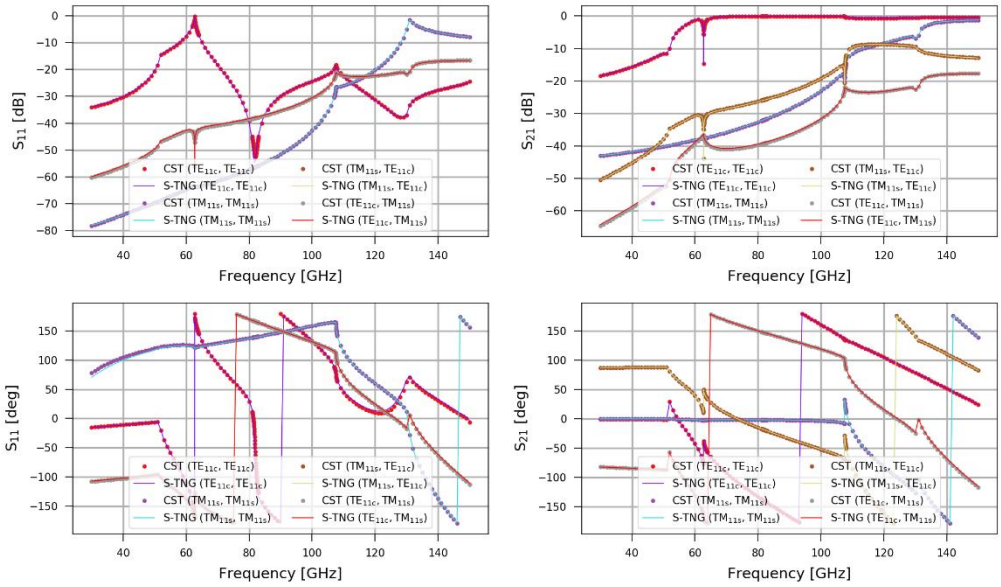

Figure 4-11 Results for selected modes in a 1.4mm circular to 1.7mm circular guide junction, with no offset, here lossy walls with conductivity of (5.8×10^4 S/m). The OpenCL method is used in this case with 14 radial orders included.

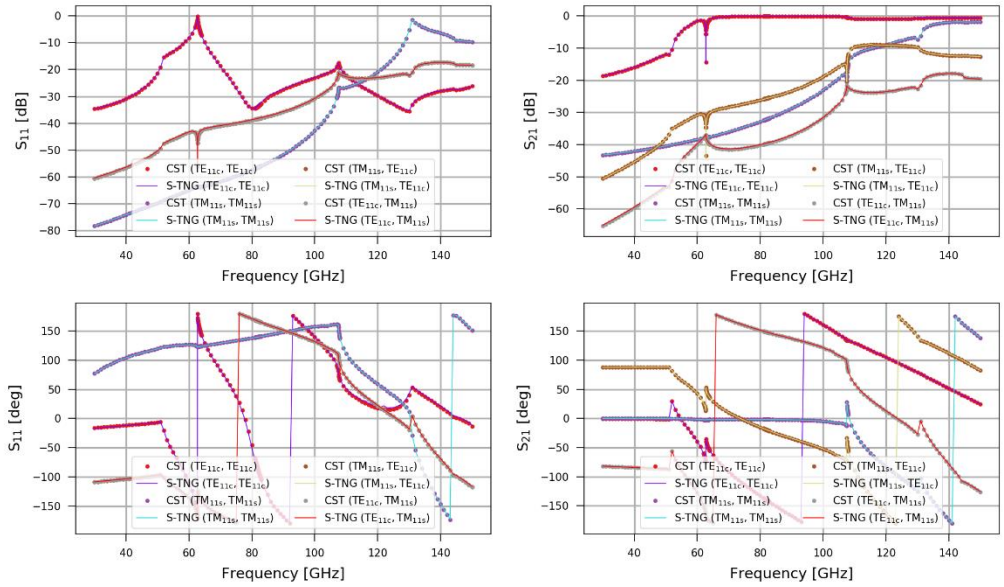

Figure 4-12 Results for selected modes in a 1.4mm circular to 1.7mm circular guide junction, with dx 0.2 mm offset, here lossy walls with conductivity of (5.8×10^4 S/m). The OpenCL method is used in this case with 14 radial orders included.

4.2 Power Monitoring Via Virtual Non-Reciprocal Port

Power monitoring within guide sections is an essential tool needed to accurately account for power absorption in waveguide systems, such as waveguide or cavity coupled absorber sections. Furthermore, with many mechanisms available for power loss i.e. absorber layers, lossy walls, free-space gaps, etc, the normal technique used to determine the power absorbed can become cumbersome and inaccurate. That is the *return loss* method, which accounts for power loss on each element by running the simulation multiple times with and without the structures of interest. Rather than determining the overall loss of the system, its scattering matrix can be augmented. The power dissipated by the lossy elements is accounted for through virtual modes on virtual non-reciprocal ports. The virtual modes are determined by enforcing conservation of total real power on networks including virtual ports. The scattering notation introduced in Chapter 2 is employed to describe the new 3-port network, as shown in Figure 4-13.

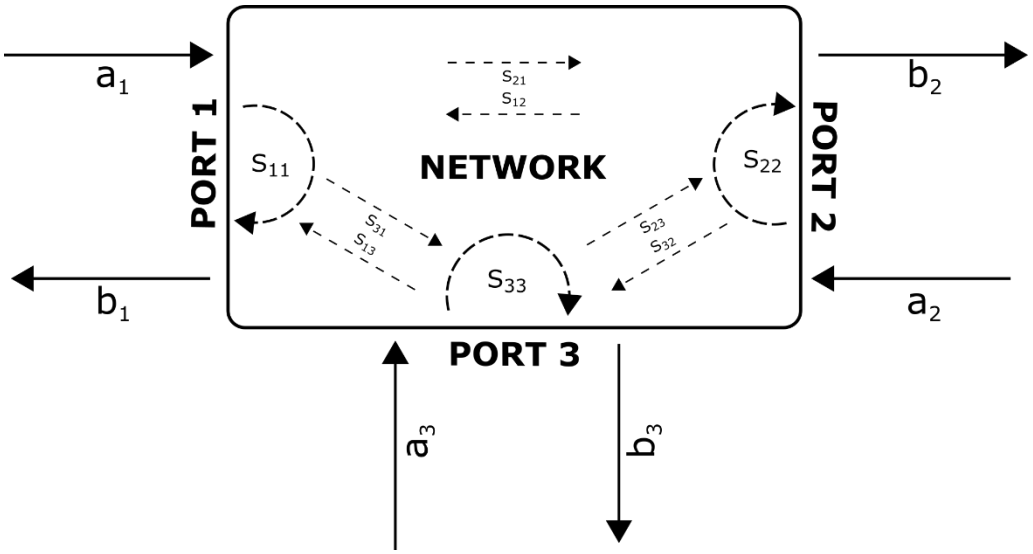

Figure 4-13 Schematic overview of the network arrangement of a three-port device. At each port there exist incoming and outgoing amplitudes "a" and "b" respectively.

The additional port will, at first, be treated as any other port and is assumed to have the same properties as the waveguide port before any restrictions are applied. As such, the scattering formulation of this network is given by:

$$\begin{bmatrix} \mathbf{b}_1 \\ \mathbf{b}_2 \\ \mathbf{b}_3 \end{bmatrix} = \begin{bmatrix} \mathbf{S}_{11} & \mathbf{S}_{12} & \mathbf{S}_{13} \\ \mathbf{S}_{21} & \mathbf{S}_{22} & \mathbf{S}_{23} \\ \mathbf{S}_{31} & \mathbf{S}_{32} & \mathbf{S}_{33} \end{bmatrix} \begin{bmatrix} \mathbf{a}_1 \\ \mathbf{a}_2 \\ \mathbf{a}_3 \end{bmatrix} \tag{4.2.1}$$

At this point the virtual modes at port 3 and their modal powers are not determined. The power at each port can be found by summing the square of the magnitudes of the modal amplitudes and the modal power over all the available modes at the port. The input power for the whole network is the sum of the input powers at all ports.

$$P_x = \sum_{i=1}^{N_x} \left|a_{x,i}\right|^2 P_{x,i} \text{ , for } x = 1,2,3 \qquad (4.2.2)$$

In a matrix formulation this is shown below:

$$P_{in} = [\mathbf{a}_1 \quad \mathbf{a}_2 \quad \mathbf{a}_3]^* \begin{bmatrix} \boldsymbol{P}_1 & \mathbf{0} & \mathbf{0} \\ \mathbf{0} & \boldsymbol{P}_2 & \mathbf{0} \\ \mathbf{0} & \mathbf{0} & \boldsymbol{P}_3 \end{bmatrix} \begin{bmatrix} \mathbf{a}_1 \\ \mathbf{a}_2 \\ \mathbf{a}_3 \end{bmatrix} \text{ or } P_{in} = < \mathbf{a} \left| \widetilde{\boldsymbol{P}} \right| \mathbf{a} > \qquad (4.2.3)$$

with P_1, P_2 and P_3 being diagonal modal power matrices.

The reflected power for the network or the individual ports can be obtained in a similar manner, here the amplitudes would be those of the reflected modes $\boldsymbol{b}$ i.e. $P_{out} = < \mathbf{b} \left| \widetilde{\boldsymbol{P}} \right| \mathbf{b} >$. If the conservation of power is to be maintained the input and output powers must be equal i.e. $P_{in} = P_{out}$. Furthermore, the relationship between the incident and reflected mode amplitudes gives $|\mathbf{b} >= \mathbf{S}|\mathbf{a} >$ and $< \mathbf{b}| =< \mathbf{a}|\mathbf{S}^+$ as shown below

$$|\mathbf{b} >= \mathbf{S}|\mathbf{a} > \Rightarrow \begin{bmatrix} \mathbf{b}_1 \\ \mathbf{b}_2 \\ \mathbf{b}_3 \end{bmatrix} = \begin{bmatrix} \mathbf{S}_{11} & \mathbf{S}_{12} & \mathbf{S}_{13} \\ \mathbf{S}_{21} & \mathbf{S}_{22} & \mathbf{S}_{23} \\ \mathbf{S}_{31} & \mathbf{S}_{32} & \mathbf{S}_{33} \end{bmatrix} \begin{bmatrix} \mathbf{a}_1 \\ \mathbf{a}_2 \\ \mathbf{a}_3 \end{bmatrix} \qquad (4.2.4)$$

$$< \mathbf{b}| =< \mathbf{a}|\mathbf{S}^+ \Rightarrow [\mathbf{b}_1 \quad \mathbf{b}_2 \quad \mathbf{b}_3]^* = [\mathbf{a}_1 \quad \mathbf{a}_2 \quad \mathbf{a}_3]^* \begin{bmatrix} \boldsymbol{S}_{11}^+ & \boldsymbol{S}_{21}^+ & \boldsymbol{S}_{31}^+ \\ \boldsymbol{S}_{12}^+ & \boldsymbol{S}_{22}^+ & \boldsymbol{S}_{32}^+ \\ \boldsymbol{S}_{13}^+ & \boldsymbol{S}_{23}^+ & \boldsymbol{S}_{33}^+ \end{bmatrix} \qquad (4.2.5)$$

By applying this relationship and enforcing the conservation of real power for arbitrary excitation it can be shown that:

$$\begin{bmatrix} \boldsymbol{S}_{11}^{+} & \boldsymbol{S}_{21}^{+} & \boldsymbol{S}_{31}^{+} \\ \boldsymbol{S}_{12}^{+} & \boldsymbol{S}_{22}^{+} & \boldsymbol{S}_{32}^{+} \\ \boldsymbol{S}_{13}^{+} & \boldsymbol{S}_{23}^{+} & \boldsymbol{S}_{33}^{+} \end{bmatrix} \begin{bmatrix} \boldsymbol{P}_1 & \boldsymbol{0} & \boldsymbol{0} \\ \boldsymbol{0} & \boldsymbol{P}_2 & \boldsymbol{0} \\ \boldsymbol{0} & \boldsymbol{0} & \boldsymbol{P}_3 \end{bmatrix} \begin{bmatrix} \mathbf{S}_{11} & \mathbf{S}_{12} & \mathbf{S}_{13} \\ \mathbf{S}_{21} & \mathbf{S}_{22} & \mathbf{S}_{23} \\ \mathbf{S}_{31} & \mathbf{S}_{32} & \mathbf{S}_{33} \end{bmatrix} = \begin{bmatrix} \boldsymbol{P}_1 & \boldsymbol{0} & \boldsymbol{0} \\ \boldsymbol{0} & \boldsymbol{P}_2 & \boldsymbol{0} \\ \boldsymbol{0} & \boldsymbol{0} & \boldsymbol{P}_3 \end{bmatrix} \quad (4.2.6)$$

and therefore $\boldsymbol{S}^{+}\widetilde{\boldsymbol{P}}\boldsymbol{S} = \widetilde{\boldsymbol{P}}$ where + denotes the conjugate transpose of a matrix.

This assumption of conservation of real power through the guide section includes any power that may be fed in at the additional port. With the generic scattering matrix for a 3-port network derived in equation (4.2.6) some restrictions can be imposed based on the requirements of the virtual port. Since this port is mapped to a non-radiating element in the network, unlike a traditional waveguide port, this port will have no mechanism for excitations as no stimulus can be applied. Thus, any scattering parameters originating from this port must be zero, i.e. $\boldsymbol{S}_{13} = \boldsymbol{S}_{23} = \boldsymbol{S}_{33} = 0$, while scattering paths from the waveguide ports to the virtual port are retained. Furthermore, there is no input power associated with the virtual port i.e. $P_3(\text{in}) = 0$. Applying this to the matrix system defined in equation (4.2.6), the scattering matrix can be significantly simplified:

$$\begin{bmatrix} K_1 & K_2 \\ K_3 & K_4 \end{bmatrix} = \begin{bmatrix} S_{11}^{+} & S_{21}^{+} & S_{31}^{+} \\ S_{12}^{+} & S_{22}^{+} & S_{32}^{+} \end{bmatrix} \begin{bmatrix} P_1 & 0 & 0 \\ 0 & P_2 & 0 \\ 0 & 0 & P_3 \end{bmatrix} \begin{bmatrix} S_{11} & S_{12} \\ S_{21} & S_{22} \\ S_{31} & S_{32} \end{bmatrix} = \begin{bmatrix} P_1 & 0 \\ 0 & P_2 \end{bmatrix} \quad (4.2.7)$$

At this point the matrix equation (4.2.7) can be expanded and a set of linear equations (4.2.8)-(4.2.11) are obtained:

$$K_1 = S_{11}^{+}P_1S_{11} + S_{21}^{+}P_2S_{21} + S_{31}^{+}P_3S_{31} = P_1 \quad (4.2.8)$$

$$K_2 = S_{11}^{+}P_1S_{12} + S_{21}^{+}P_2S_{22} + S_{31}^{+}P_3S_{32} = 0 \quad (4.2.9)$$

$$K_3 = S_{12}^{+}P_1S_{11} + S_{22}^{+}P_2S_{21} + S_{32}^{+}P_3S_{31} = 0 \quad (4.2.10)$$

$$K_4 = S_{12}^{+}P_1S_{12} + S_{22}^{+}P_2S_{22} + S_{32}^{+}P_3S_{32} = P_2 \quad (4.2.11)$$

By solving these linear constraints the required $\boldsymbol{S}_{31}$ and $\boldsymbol{S}_{32}$ scattering parameters can be determined. The most straight forward method to find a solution consistent with these constraints, is to impose a further restriction on the symmetry and reciprocity of the system. In this case, the virtual port is mapped to an absorber layer of zero length meaning the scattering parameters must be symmetric across the waveguide ports as shown in Chapter 3 i.e. $\boldsymbol{S}_{11} = \boldsymbol{S}_{22}$, $\boldsymbol{S}_{21} = \boldsymbol{S}_{12}$ and $P_1 = P_2$. Now there exists just two independent linear equations K_1 and K_2. It can also be shown that solutions of either satisfies the other for the symmetric case.

PROOF The relationship between the S_{11} and S_{21} scattering parameters for the infinitely thin absorber layer is that $S_{21} = (I + S_{11})$. Using this fact, it can be shown that if K_1 is satisfied then so is K_2:

Re-arranging $\boldsymbol{K_1}$ and $\boldsymbol{K_2}$:

$$K_1 \Rightarrow S_{11}^{+} P_1 S_{11} + S_{21}^{+} P_2 S_{21} + S_{31}^{+} P_3 S_{31} = P_1$$

$$K_2 \Rightarrow S_{11}^{+} P_1 S_{12} + S_{21}^{+} P_2 S_{22} + S_{31}^{+} P_3 S_{32} = 0$$

Enforcing symmetry relations:

$$K_1 \Rightarrow S_{11}^{+} P_1 S_{11} + S_{21}^{+} P_1 S_{21} + S_{31}^{+} P_3 S_{31} = P_1$$

$$K_2 \Rightarrow S_{11}^{+} P_1 S_{21} + S_{21}^{+} P_1 S_{11} + S_{31}^{+} P_3 S_{32} = 0$$

(4.2.12)

Applying the relation $\boldsymbol{S_{21} = (I + S_{11})}$ to $\boldsymbol{K_2}$:

$$S_{11}^{+} P_1 (I + S_{11}) + S_{21}^{+} P_1 (S_{21} - I) + S_{31}^{+} P_3 S_{32} = 0$$

$$S_{11}^{+} P_1 + S_{11}^{+} P_1 S_{11} + S_{21}^{+} P_1 S_{21} - S_{21}^{+} P_1 + S_{31}^{+} P_3 S_{32} = 0$$

$$S_{11}^{+} P_1 S_{11} + S_{21}^{+} P_1 S_{21} + S_{31}^{+} P_3 S_{32} + S_{11}^{+} P_1 - (I + S_{11})^{+} P_1 = 0$$

$$S_{11}^{+} P_1 S_{11} + S_{21}^{+} P_1 S_{21} + S_{31}^{+} P_3 S_{32} - P_1 = 0$$

$$\therefore K_1 \equiv K_2$$

From the derivation presented in equations (4.2.12), that if the constraints K_1 and K_2 are equivalent then $S_{31}^{+} P_3 S_{31} = S_{31}^{+} P_3 S_{32}$ if and only if $S_{32} = S_{31}$. Furthermore, the virtual port

scattering parameters S_{31} and S_{32} must be equivalent for the symmetric infinitely thin absorber layer. By enforcing this symmetry, the system is further simplified and its only required to solve a single linear equation (K_1) to find a set of virtual modes and modal powers which satisfy the conservation of power requirements. Through eigenvalue decomposition the virtual port scattering parameter (S_{31}) and powers (P_3) can be obtained. By enforcing the constraint:

$$K_1 : S_{31}^{+} P_3 S_{31} = P_1 - (S_{11}^{+} P_1 S_{11} + S_{21}^{+} P_2 S_{21}) \tag{4.2.13}$$

$$K_1 = Q \Lambda Q^{-1} \Rightarrow S_{31} = Q^{+} \text{ and } P_3 = \Lambda \tag{4.2.14}$$

Eigenvalue decomposition, as shown in equation (4.2.14), diagonalises the matrix (Strang 2013). K_1 is taken to be a normal-Hermitian matrix, with Λ a diagonal matrix of real valued eigenvalue entries and Q a unitary matrix ($Q^{-1} = Q^{+}$) giving the corresponding eigenvectors. The eigenvectors of Q corresponds to the virtual modes (channels for power dissipation) and likewise, the eigenvalues Λ give the real valued virtual port powers.

The virtual port method is first applied to an infinitely thin cylindrical absorber layer section, as seen in section 3.3, with a partially filling absorber to verify the correctness of the approach. To benchmark the virtual port method, the return loss results for the same system are obtained. As shown in Figure 4-14, this mechanism for obtaining the loss due to the absorber layer works perfectly with the return loss and power absorbed matching across the wavelength range.

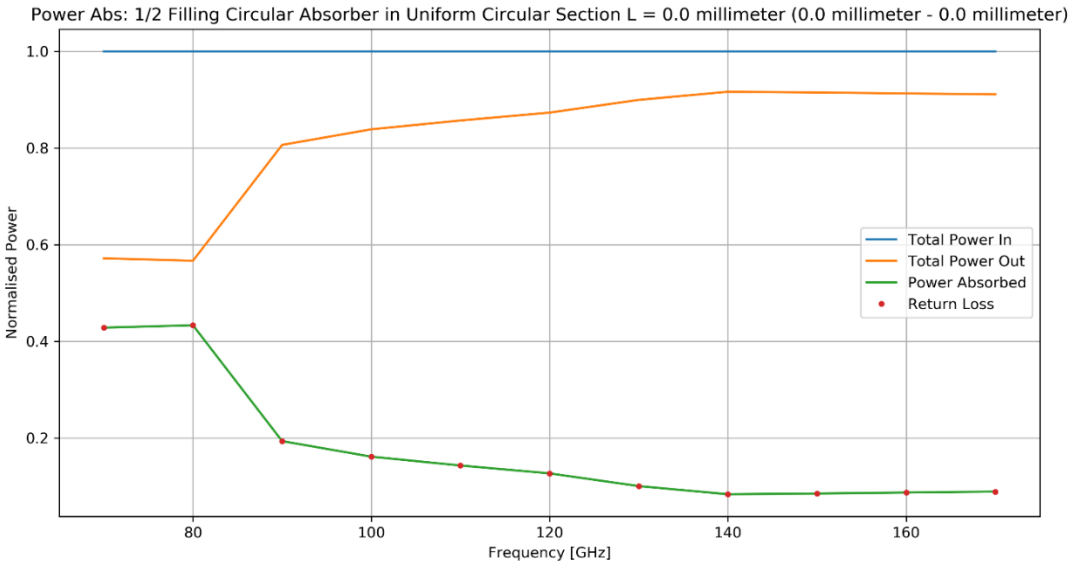

Figure 4-14: Measured power through the virtual port versus return loss value for zero length absorber segment network.

It is important to note that the method used here for an absorber layer will not be valid for all lossy cases, in particular where the loss cannot be localised or when reciprocity relations are not in place i.e. loss along a lossy uniform guide or junction section. Physical guide lengths leading to the absorber layer can be accounted for by either scaling the scattering parameters using phase factors consistent with the guide lengths, or by simply cascading additional guide sections where necessary to complete the system. The cascading procedure for such an arrangement is present in the following section.

4.2.1 Cascading a uniform section (2-port) with short absorber network (3-port)

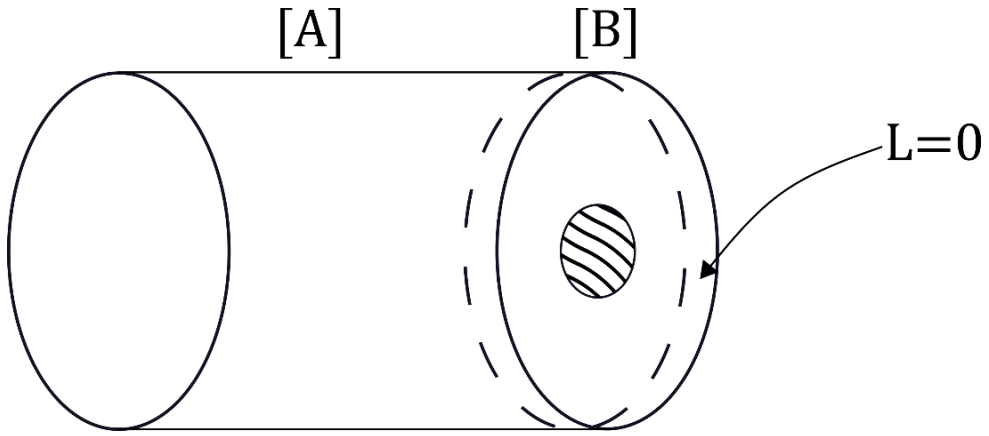

Figure 4-15: Uniform segment cascades with an infinitely short absorber segment.

Using the network and cascading theory developed in Chapter 2, an expression for the resulting S-matrix formed from the cascading of a 2-port and 3-port device can also be obtained. As shown in Figure 4-15, the two networks considered are network A (2-port uniform guide) and network B (3-port absorber layer). In a similar manner to the 2-port cascading example the remaining and vanishing modes are defined. The vanishing modes of network A ($N_{A,2} = N_{A,V}$) are mapped one-to-one to the modes in network B ($N_{B,1} = N_{B,V}$) such that $N_{A,V} = N_{B,V} = N_V$. The modal amplitudes of the input and outputs modes of the two networks will be linked as $\boldsymbol{a}^{B,V} = \boldsymbol{b}^{A,V}$ and $\boldsymbol{a}^{A,V} = \boldsymbol{b}^{B,V}$. The remaining modes of network A are $N_{A,1} = N_{A,R}$ and of network B are $N_{B,2} + N_{B,3} = N_{B,R}$.

$$\begin{bmatrix} \boldsymbol{b}^{A,R} \\ \boldsymbol{b}^{A,V} \end{bmatrix} = \begin{bmatrix} \boldsymbol{S}^{A}_{R,R} & \boldsymbol{S}^{A}_{R,V} \\ \boldsymbol{S}^{A}_{V,R} & \boldsymbol{S}^{A}_{V,V} \end{bmatrix} \begin{bmatrix} \boldsymbol{a}^{A,R} \\ \boldsymbol{a}^{A,V} \end{bmatrix} \tag{4.2.15}$$

$$\begin{bmatrix} \boldsymbol{b}^{B,R} \\ \boldsymbol{b}^{B,V} \end{bmatrix} = \begin{bmatrix} \boldsymbol{S}^{B}_{R,R} & \boldsymbol{S}^{B}_{R,V} \\ \boldsymbol{S}^{B}_{V,R} & \boldsymbol{S}^{B}_{V,V} \end{bmatrix} \begin{bmatrix} \boldsymbol{a}^{B,R} \\ \boldsymbol{a}^{B,V} \end{bmatrix} \tag{4.2.16}$$

For clarity the remaining and vanishing scattering parameters of network B are given explicitly:

$$\boldsymbol{S}^{B}_{R,R} = [\boldsymbol{S}^{\boldsymbol{B}}_{22} \quad \boldsymbol{S}^{\boldsymbol{B}}_{32}] \tag{4.2.17}$$

$$\boldsymbol{S}^{B}_{R,V} = [\boldsymbol{S}^{\boldsymbol{B}}_{21} \quad \boldsymbol{S}^{\boldsymbol{B}}_{31}] \tag{4.2.18}$$

$$\boldsymbol{S}^{B}_{V,R} = [\boldsymbol{S}^{\boldsymbol{B}}_{12} \quad \boldsymbol{S}^{\boldsymbol{B}}_{13}] \tag{4.2.19}$$

$$\boldsymbol{S}^{B}_{V,V} = [\boldsymbol{S}^{\boldsymbol{B}}_{11}] \tag{4.2.20}$$

To find the scattering matrix of the cascaded section, the individual scattering matrices are considered as shown in equation (4.2.15) – (4.2.16). The modal amplitudes of the input and outputs modes of the two networks will be linked as $\boldsymbol{a}^{B,V} = \boldsymbol{b}^{A,V}$ and $\boldsymbol{a}^{A,V} = \boldsymbol{b}^{B,V}$. Using the relationship between the modal amplitudes of the networks the matrices can be redefined as:

$$\begin{bmatrix} \boldsymbol{b}^{A,R} \\ \boldsymbol{b}^{A,V} \end{bmatrix} = \begin{bmatrix} \boldsymbol{S}^{A}_{R,R} & \boldsymbol{S}^{A}_{R,V} \\ \boldsymbol{S}^{A}_{V,R} & \boldsymbol{S}^{A}_{V,V} \end{bmatrix} \begin{bmatrix} \boldsymbol{a}^{A,R} \\ \boldsymbol{b}^{B,V} \end{bmatrix} \tag{4.2.21}$$

$$\begin{bmatrix} \boldsymbol{b}^{B,R} \\ \boldsymbol{b}^{B,V} \end{bmatrix} = \begin{bmatrix} \boldsymbol{S}^{B}_{R,R} & \boldsymbol{S}^{B}_{R,V} \\ \boldsymbol{S}^{B}_{V,R} & \boldsymbol{S}^{B}_{V,V} \end{bmatrix} \begin{bmatrix} \boldsymbol{a}^{B,R} \\ \boldsymbol{b}^{A,V} \end{bmatrix} \tag{4.2.22}$$

To solve for the new scattering matrix, an expression for the outgoing modal amplitudes $[\boldsymbol{b}^{A,R} \quad \boldsymbol{b}^{B,R}]$ in terms of the input amplitudes $[\boldsymbol{a}^{A,R} \quad \boldsymbol{a}^{B,R}]$ and the known scattering parameters from equations (4.2.21) and (4.2.22) must be found.

$$\begin{bmatrix} b^{A,V} \\ b^{B,V} \end{bmatrix} = \begin{bmatrix} \left(I - S^{A}_{V,V}S^{B}_{V,V}\right)^{-1}S^{A}_{V,R} & \left(I - S^{A}_{V,V}S^{B}_{V,V}\right)^{-1}S^{A}_{V,V}S^{B}_{V,R} \\ \left(I - S^{B}_{V,V}S^{A}_{V,V}\right)^{-1}S^{B}_{V,V}S^{A}_{V,R} & \left(I - S^{B}_{V,V}S^{A}_{V,V}\right)^{-1}S^{B}_{V,R} \end{bmatrix} \begin{bmatrix} a^{A,R} \\ a^{B,V} \end{bmatrix} \tag{4.2.23}$$

Moreover, these new linear equations can be expressed in matrix form as shown in equation (4.2.23). From (4.2.23) the required expressions for $[\boldsymbol{b}^{A,R} \quad \boldsymbol{b}^{B,R}]$ in terms of $[\boldsymbol{a}^{A,R} \quad \boldsymbol{a}^{B,R}]$ can be obtained by following the procedure outline in Appendix A.2. The scattering matrix of the joint network [AB] can be evaluated, where network [AB's] non-zero scattering parameters are found to be:

$$S_{11}^{AB} = S_{11}^{A} + S_{12}^{A}(I - S_{11}^{B}S_{22}^{A})^{-1}S_{11}^{B}S_{21}^{A} \tag{4.2.24}$$

$$S_{12}^{AB} = S_{12}^{A}(I - S_{11}^{B}S_{22}^{A})^{-1}S_{12}^{B} \tag{4.2.25}$$

$$S_{21}^{AB} = S_{21}^{B}(I - S_{22}^{B}S_{11}^{A})^{-1}S_{21}^{A} \tag{4.2.26}$$

$$S_{22}^{AB} = S_{22}^{B} + S_{21}^{B}(I - S_{22}^{B}S_{11}^{A})^{-1}S_{22}^{A}S_{12}^{B} \tag{4.2.27}$$

$$S_{31}^{AB} = S_{31}^{A} + S_{32}^{A}(I - S_{11}^{B}S_{22}^{A})^{-1}S_{11}^{B}S_{21}^{A} \tag{4.2.28}$$

$$S_{32}^{AB} = S_{32}^{A}(I - S_{11}^{B}S_{22}^{A})^{-1}S_{12}^{B} \tag{4.2.29}$$

4.2.2 Test and Verification of the Absorber Network Virtual Port

To verify the implementation of the virtual port power tracking and the cascading method's several test cases were considered. These test cases also aim to promote potential use cases of this tool. Firstly, a uniform cylindrical guide section of radius 1.4 mm, length 3 mm with partially filling circular absorber layer of radius 0.7 mm and $R_S = 200\ \Omega/\blacksquare$ was modelled. The network was excited by random amplitudes at both waveguide ports simultaneously and for number of different absorber positions along the length of the guide the power absorbed was computed.

In Figure 4-16, the results from this test case are shown. In all cases it can be seen that there is perfect agreement between the return loss method and the power absorbed through the virtual port. Using this method, the optimal position for an absorber layer within the guide across a frequency range can be determined.

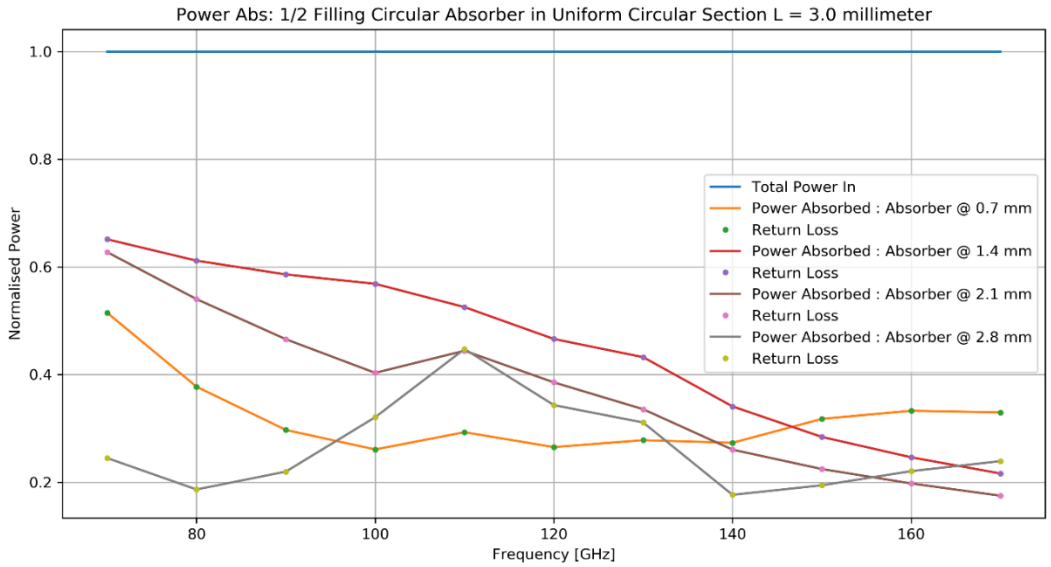

Figure 4-16: Tracking of power absorbed with varying absorber position in a uniform waveguide section with the virtual non-reciprocal port verified against the return loss method.

In a similar manner, the virtual port routine could be used to obtain the optimal position for a cavity coupled absorber layer. As in the previous test case, the absorber position can be easily varied and the power absorber through the virtual port can be tracked. By cascading the absorber network segment with a perfect reflector or *backshort* the 3 port network is collapsed to 2 ports. Here the remaining ports correspond to the waveguide/cavity opening and the virtual absorber port. In the following test case, a circular absorber layer of radius 0.7 mm and $R_S = 200\ \Omega/\blacksquare$ is contained within a uniform cylindrical cavity section with radius 1.4 mm and

length 3 mm. By varying the absorber layers position in steps of 0.25 mm the variation in absorption across the frequency range can be observed and optimised as shown in Figure 4-17.

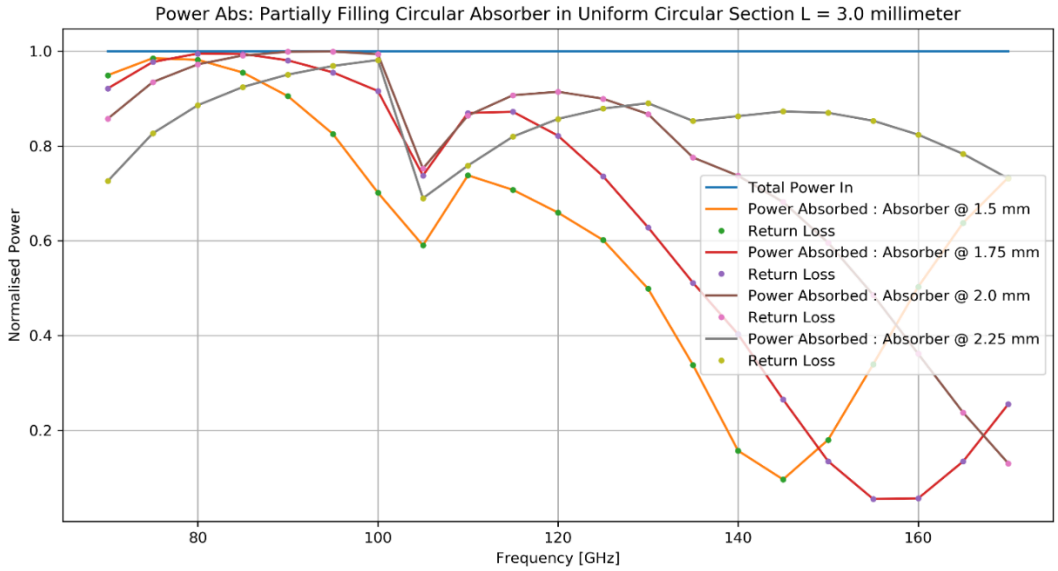

Figure 4-17: Tracking of power absorbed with varying position in a uniform cavity section with the virtual non-reciprocal port verified against the return loss method.

Likewise, using the same approach the shape of the absorber can be optimised for a particular position within the guide or cavity section. Assuming the range 100 – 120 GHz is desired for measurement, 2.0 mm is taken to be the optimal position as it is quite linear across this range and gives adequate power absorption. In Figure 4-18, the absorption patterns for absorber layers with varying radii and shapes are shown. From these different geometries it can be observed how the shape and size of the absorber can be optimised to improve the absorber efficiency.

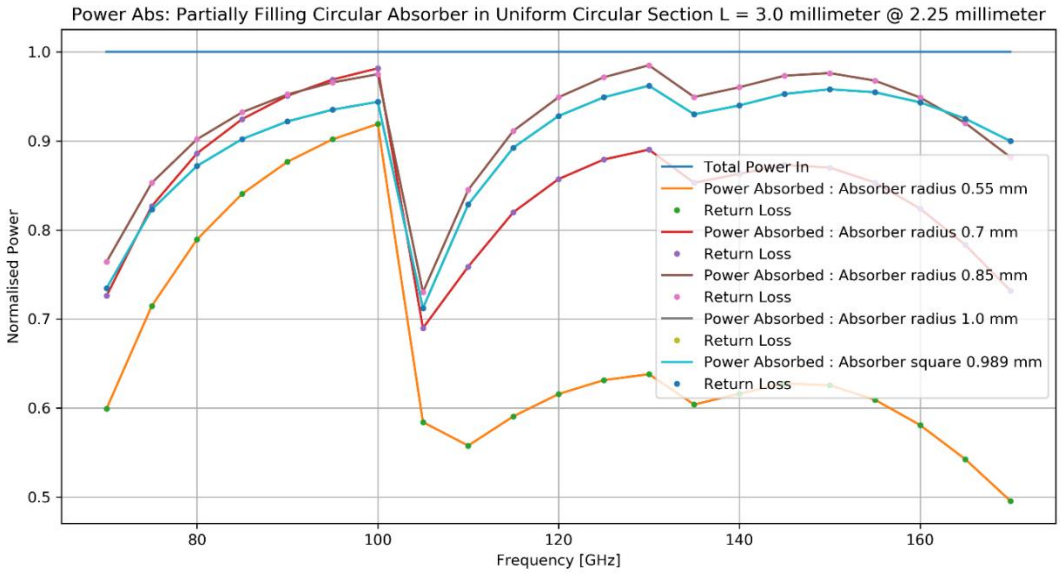

Figure 4-18: Tracking of power absorbed with varying absorber shape in a uniform cavity section with the virtual non-reciprocal port verified against the return loss method.

Finally, a test case is considered which highlights the advantage of this technique over traditional return loss mechanisms. Such a system could have multiple absorber elements, with more than a single mechanism for loss, traditional power extraction techniques require the simulation to be repeated with and without some elements for the effect of each to be accounted for. This method is inefficient and leaves scope for inaccuracies in power tracking. The single virtual port method is extended to multiple virtual ports with the aim to accurately track power lost through each lossy element. By attaching a virtual port to both of the absorber elements such that if the networks were separate there would be two independent 3-port devices. Cascading these elements together gives a single 4-port network with the additional ports associated with the lossy elements virtual ports. The cascading procedure is similar to the method for cascading a uniform section (2-port) with short absorber network (3-port) already outlined. Here the virtual ports retain the non-radiating condition which reduces the complexity cascading complexity.

Consider the following test case where there are two similar uniform sections, cylindrical with radius 1.4 mm, with virtual ports assigned to circular absorbers of radii 0.7 mm and $R_S = 200\ \Omega/\blacksquare$ placed within them. Figure 4-19 shows the power through these virtual ports which are placed asymmetrically in the system. Again both ports are excited and the corresponding return loss is shown.

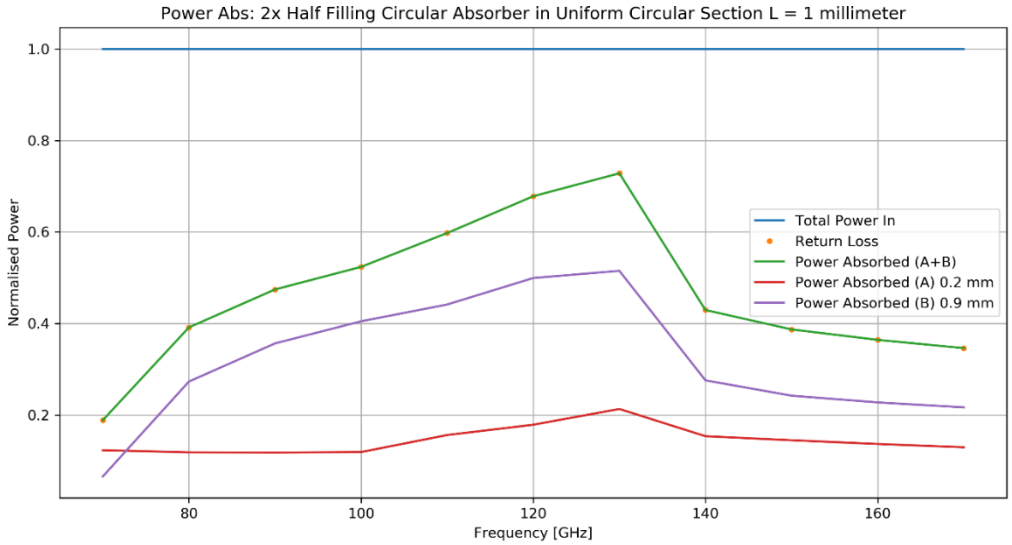

Figure 4-19: Tracking of power absorbed by multiple absorbers in a uniform waveguide section; here the return loss method can only give the total power lost in the system while the virtual port method can distinguish between the different paths of power loss.

Here, there is a clear difference in the power absorber by the two different absorber layers due to their different positions. While the return loss only gives the overall system loss, it is clear

that to retain information about the losses on individual elements that virtual port assignment can be a powerful tool.

As discussed, this method fails when the loss cannot be localised or when reciprocity relations are not in place, as stated earlier. To demonstrate this, the virtual port analysis is performed on a network made up of a circular absorber layer of radius 0.7 mm and $R_S = 200\ \Omega/\blacksquare$ placed at the midpoint of a lossy uniform cylindrical section ($\sigma = 5.8 \times 10^4$ S/m) with radius 1.4 mm and length 3 mm.

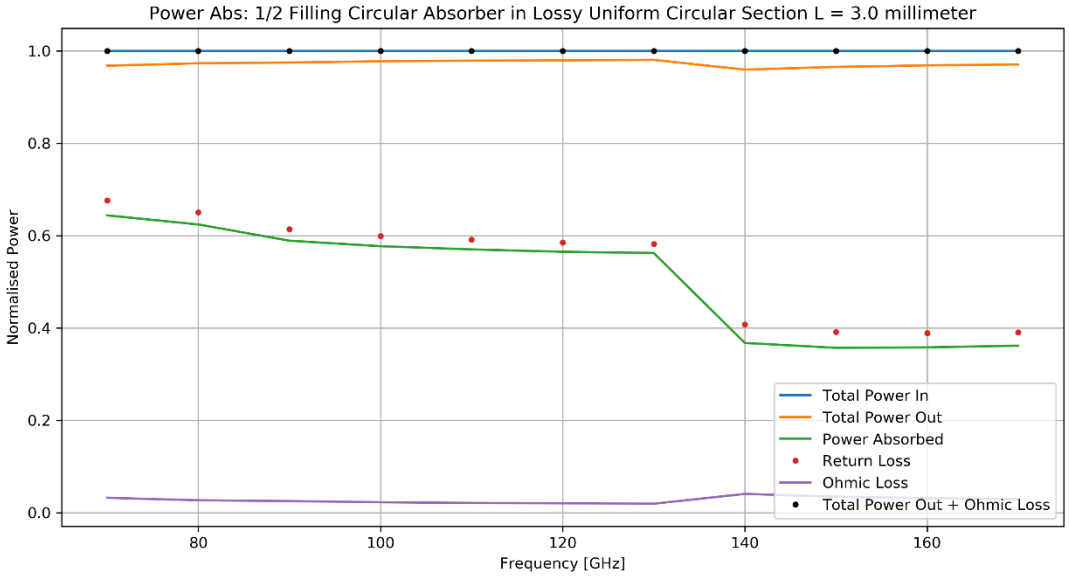

Figure 4-20: Tracking of power absorbed in a uniform lossy section with an absorber layer present: here the there is disagreement between the return loss and the virtual port methods which highlights the limitations of the virtual port method. However, power lost through the absorber layer and via ohmic losses can be distinguished

In Figure 4-20, the virtual port method fails to extract the correct amount of power lost when compared to the return loss mechanism. Although power is lost through the guide walls it cannot be localised to a single plane and as such a disagreement between the two methods is observed. While this example highlights the limitations of the virtual port method's ability to determine power loss from non-localised or non-reciprocal elements, it does allow for greater flexibility in isolating power loss per element. By using the return loss and virtual port methods in tandem increased granularity of the lossy elements can be achieved. In Figure 4-20, the difference between the return loss and power absorber through the virtual port can only be attributed to the power lost through the guide walls. Extracting this from the power tracking data the performance of the lossy guide section and absorber layer can be viewed separately.

4.3 Note on Free-Space Modes as Plane Waves

In Chapter 2, the method for obtaining radiation fields from waveguide apertures was introduced. Although correct, an important factor is omitted, that is the handling of the transition between waveguide aperture and free-space. Normally, in well-designed waveguides antennas, mode combinations at the aperture are well matched to the free-space impedance and thus the contribution of this transition is negligible. However, in more compact open ended waveguide devices (OEGs), such as probes, this impedance mismatch is no longer negligible and at the free-space interface there will be a non-zero reflection which must be captured to accurately model the device. A naïve approach to account for this reflection would be to determine the reflection coefficient from the impedance mismatch of the waveguide modes and free-space. However, this drastically underestimates the magnitude of reflection and provides no mechanism for accounting for the scattering between waveguide modes. This can be observed in the example test case of the reflection from the aperture of WR_{10} waveguide shown in Figure 4-21.

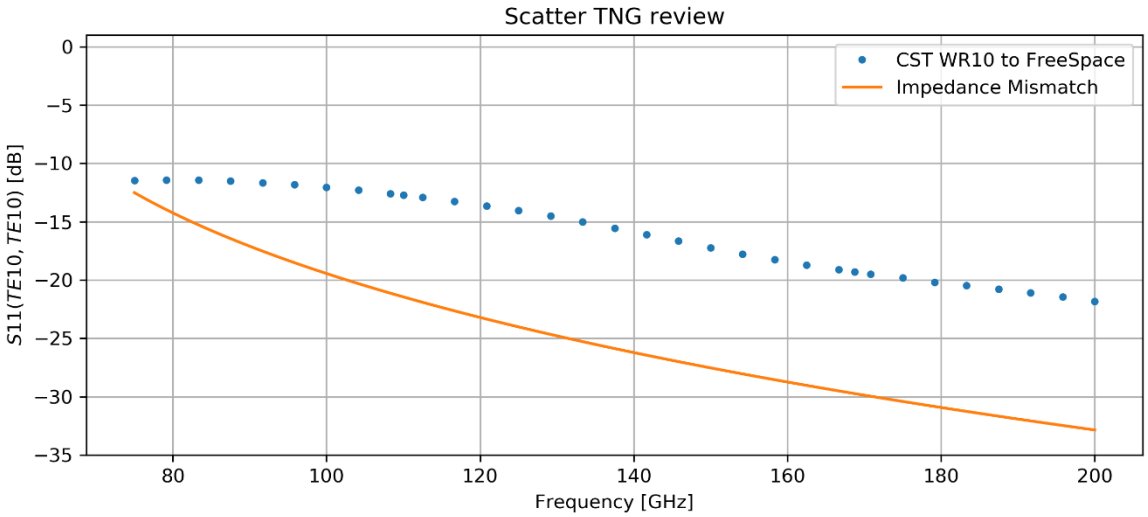

Figure 4-21 Refection coefficient of a $WR10$ guide section obtained from CST and the impedance mismatch of the fundamental mode and the intrinsic impedance of free-space.

To account for this an approximate method is proposed which model the free-space modes as a combination of plane waves which form a finite fan of angles radiating from the waveguide aperture. Using mode-matching techniques as introduced in previous chapters an estimate for the scattering parameters at this transition can be obtained. Here, the two modesets will be dissimilar. On one side conventional waveguide modes are considered and on the other a symmetric combination of free-space plane wave-like modes are used.

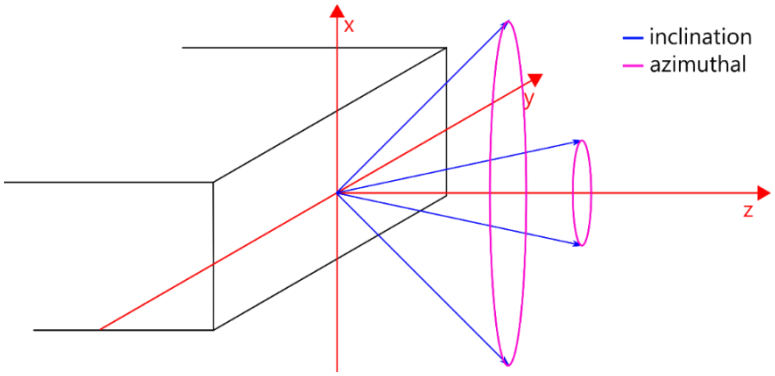

Figure 4-22 Shows the waveguide section with a fan of plane-waves radiating from the aperture

Uniform plane waves, with no rotations applied, propagate wholly along the *z*-axis in an unbounded medium (free-space). Initially two orthogonal plane waves, effectivity *y* and *x* polarisations, are defined by:

y-polarised field	**x-polarised field**
$\boldsymbol{E}^{+} = \hat{\boldsymbol{a}}_y E_0 \exp(-j\boldsymbol{\beta}^{+} \cdot \boldsymbol{r})$ $\boldsymbol{H}^{+} = -\hat{\boldsymbol{a}}_x H_0 \exp(-j\boldsymbol{\beta}^{+} \cdot \boldsymbol{r})$	$\boldsymbol{E}^{+} = \hat{\boldsymbol{a}}_x E_0 \exp(-j\boldsymbol{\beta}^{+} \cdot \boldsymbol{r})$ $\boldsymbol{H}^{+} = \hat{\boldsymbol{a}}_y H_0 \exp(-j\boldsymbol{\beta}^{+} \cdot \boldsymbol{r})$
$\boldsymbol{E}^{-} = \hat{\boldsymbol{a}}_y E_0 \exp(j\boldsymbol{\beta}^{-} \cdot \boldsymbol{r})$ $\boldsymbol{H}^{-} = \hat{\boldsymbol{a}}_x H_0 \exp(j\boldsymbol{\beta}^{-} \cdot \boldsymbol{r})$	$\boldsymbol{E}^{-} = \hat{\boldsymbol{a}}_x E_0 \exp(j\boldsymbol{\beta}^{-} \cdot \boldsymbol{r})$ $\boldsymbol{H}^{-} = -\hat{\boldsymbol{a}}_y H_0 \exp(j\boldsymbol{\beta}^{-} \cdot \boldsymbol{r})$

(4.3.1)

$$\boldsymbol{\beta}^{+} = (0,0,\beta), \boldsymbol{\beta}^{-} = (0,0,-\beta), \boldsymbol{r} = (0,0,z) \qquad (4.3.2)$$

Where $+/-$ indicate forward and backward travelling components. Of course only forward propagating plane waves are necessary to match the radiation from the waveguide aperture. When transformed by non-zero rotations of θ and ϕ these fields cover all possible directions and polarisations of plane waves. The appropriate Euler rotations which enable such projections are given by:

$$\mathrm{Rot}(\theta) = \begin{pmatrix} \cos\theta & 0 & \sin\theta \\ 0 & 1 & 0 \\ -\sin\theta & 0 & \cos\theta \end{pmatrix} \text{ and } \mathrm{Rot}(\phi) = \begin{pmatrix} \cos\phi & -\sin\phi & 0 \\ \sin\phi & \cos\phi & 0 \\ 0 & 0 & 1 \end{pmatrix} \qquad (4.3.3)$$

Applying these rotations to the orthogonal fields defined in equation (4.3.3) cause the plane wave fields to take the form of either transverse electric or magnetic plane wave-like modes as shown in Figure 4-23.

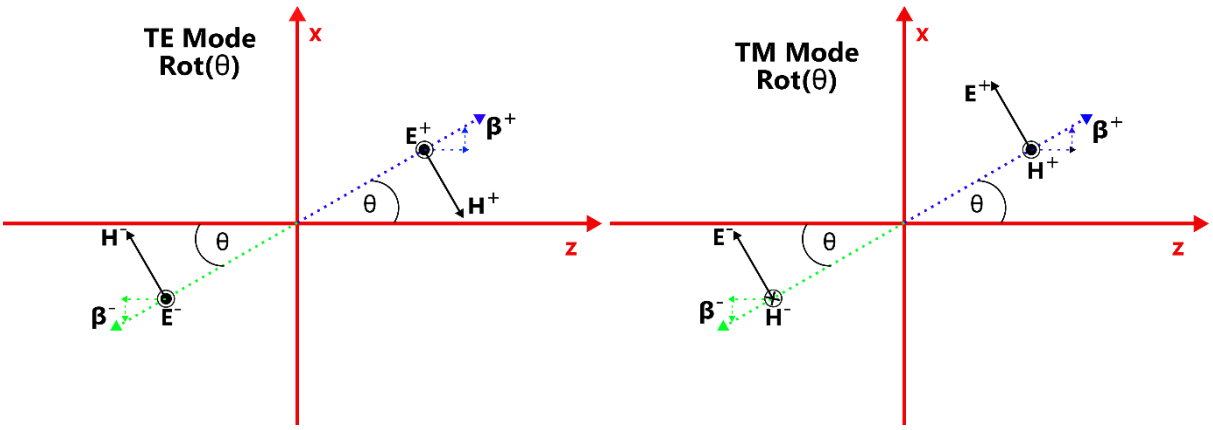

Figure 4-23 Shows the electric and magnetic field components of the y and x-polarised fields which give a) TE mode and b) TM mode upon θ rotation.

In practice such an implementation proved impractical, especially since it was proposed to provide an approximate and lightweight solution to the free-space interface problem. To accurately account for the reflection of the OEG, evanescent free-space modes had to be included in the analysis. The necessary density of the free-space modeset (which was effectively infinite (Bois, Benally, and Zoughi 1998)) meant that the computation of mode matching coupling integrals could not be completed in reasonable time. At the point of concession convergence could not be achieved for upwards of 10000 free-space modes included. In reality there exist a number of more practical solutions to the free-space problem (Selvan 2004), (Bois, Benally, and Zoughi 1998) and (McCarthy 2014) which provide much less intensive approaches to determining the correct aperture reflection from OEGs. The solution outlined in (McCarthy 2014) is used in Chapter 5 to account for the free-space transition in a prototype SAFARI pixel design.

4.4 Summary

In this chapter several tools have been developed to expand and enhance the modelling capabilities of the S-TNG software. In section 4.1, certain coupling-integral cases where no analytical solutions were identified i.e. offset cylindrical junctions. Significant work was done to develop a parallelised implementation of the numerical mode-matching method and to remove this obvious bottleneck. It was shown that through this parallelised implementation that there was significant performance gains, approaching simulation times close to purely analytic calculations, with little loss in accuracy. Furthermore, a method to model power dissipated through lossy elements is introduced. Here power loss is monitored through virtual modes on virtual non-reciprocal ports. This approach was verified using the standard return loss approach typically used to monitor power loss and in section 4.2.2 the advantages of such a power monitoring mechanism are shown.

Chapter 5 – SAFARI Instrument Investigations

The proposed far-infrared space telescope SPICA and more directly the SAFARI instrument were of particular interest to this project. Many of the mode matching tools presented in earlier chapters have been developed with aim of aiding in the design and analysis of SAFARI's detector arrays. In this chapter a number of the detector pixel designs are discussed and analysed using the developed routines. Furthermore, a potential focal plane solution for the SAFARI instrument is considered and analysed using in-house developed software MODAL (Maynooth Optical Design and Analysis Laboratory). The investigations presented in this chapter focus on:

- an Offner relay focal plane arrangement utilizing a beam steering mirror (BSM) to translate the instrument's point spread function (Hecht 2001) (PSF) between the different grating modules and to the high-resolution MP-interferometer,
- analysis of a modified SAFARI pixel testbed design,
- analysis of experimental results of a prototype SAFARI M-band subarray design, and
- analysis and optimisation of the S-band feed design of SAFARI 4.0.

As outlined in Chapter 1, one potential focal plane solution of the SAFARI instrument relies on an Offner relay arrangement. Here, a BSM is used to select between the different grating modules and resolution modes of the instrument. As part of an ongoing collaboration between Maynooth University and SRON, there was an involvement in a brief measurement campaign focused on the analysis of an Offner relay system. This work concentrated on the optical modelling of the system using MODAL. Most of the design and implementation of the system was performed as part of a Master's research project (Schallig 2015a). However, some unexplained irregularities in the measured beam pattern from the Offner relay were observed. In this chapter the Offner arrangement is introduced and the potential origin of these irregularities in the beam pattern is investigated. Furthermore, the Offner system is investigated using Gaussian Beam Mode analysis to better approximate the laboratory QCL source and the imaging of polychromatic sources is also considered.

Over the development cycle of the SAFARI, there have been a number of revisions to the pixel design. Using these prototype designs much of the necessary code was tested and developed, such that comprehensive analysis of SAFARI type pixels could be performed in a timely manner. A combination of physical optics (MODAL) and mode matching (S-TNG) are used to

determine the pixel's response to external stimulus. In previous investigations, detailed in (McCarthy 2014), the SAFARI pixels response to on-axis illumination has been studied. The work presented in this chapter focuses on an amended off-axis optical arrangement to illuminate the prototype SAFARI pixel. Here, the viability of such an arrangement to illuminate the SAFARI pixel is investigated.

A prototype subarray feed structure for SAFARI's M-band is considered and characterised. The prototype design was developed by Cardiff University and is the latest of the subarray feed designs to be realised. The subarray implementation is given in the technical description of SAFARI in chapter 1. To reconcile the measurement data with simulation results the routines developed in chapter 3 are utilized. The prototype feed design relies on novel manufacturing techniques and as such the surface impedance of the boundary walls play an important role. Simulations are performed with both finite conductivity and surface roughness included to model the structure more accurately.

Following on from the analysis of the prototype M-band SAFARI subarray design, work was commenced on the modelling of a new antenna design for the short wavelength band (S-band) of the SAFARI 4.0 instrument. The goal of this investigation was to use the roughness model to make informed design decisions from the very beginning. Here, free parameters such as the length, throat-aperture size and shape were investigated along with the response to varying levels of roughness. This allowed roughness losses to be mitigated and bounds to be set for the manufacturing tolerances of the feeds.

5.1 Offner Relay System

One focal plane solution for the proposed SAFARI instrument is an Offner relay system, which will make use of a beam steering mirror (BSM) to select the grating modules which span SAFARI's spectroscopic range. The optical arrangement of the Offner relay is comprised of two spherical mirrors concentric about their centres of curvature, see Figure 5-1. The primary mirror (M1) is concave, while the secondary mirror (M2) is convex and has a radius of curvature that is half that of M1. The mirrors are aligned to image in a plane containing a common centre, governed by M2, and perpendicular to the optical axis. This configuration offers unit magnification and image reproduction without the introduction of aberrations or astigmatisms (Fischer and Fischer 2003). By actuating M2, the BSM, the point spread function (PSF) can be translated in the focal plane where the detector array of the of the instrument is located.

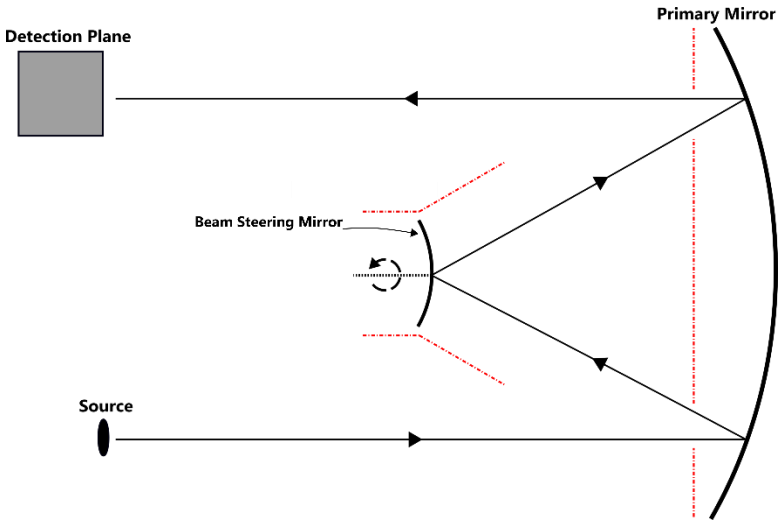

Figure 5-1 Overview of the Offner system optical arrangement, dashed red line indicates regions where absorber was placed to limited stray light reflections.

In an idealised optical system, the limiting shape of the PSF is an Airy pattern (Hecht 2001). By comparing the idealised result against the measured PSF in the focal plane, aberrations introduced by the optical system can be determined. The intensity pattern associated with the PSF is given by:

$$I(\theta,\lambda) = I(0,\lambda)\left[\frac{2J_1\left(\frac{\pi D}{\lambda}\sin\theta\right)}{\left(\frac{\pi D}{\lambda}\sin\theta\right)}\right]^2 \qquad (5.1.1)$$

where J_1 is the 1st order Bessel function, θ is the angle of observation, D is the aperture diameter and λ the wavelength (Hecht 2001).

5.1.1 Experimental Optical Arrangement

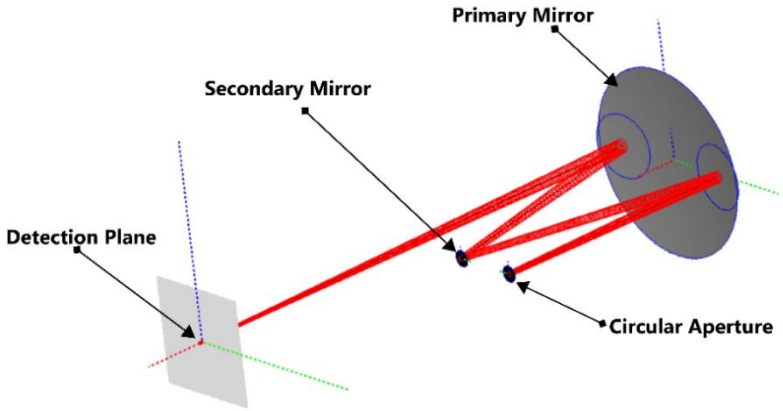

Figure 5-2: Overview of the implementation of the Offner system in MODAL

In the experimental Offner arrangement, M1 had a radius of curvature of 1000 mm, diameter of 350 mm giving a focal length of 500 mm. The BSM had a radius of curvature of 500 mm, diameter of 30 mm and a focus of 250 mm. This mirror was actuated via an attocube device (Schallig 2015a), a goniometer power by a piezo motor, allowing for positioning of the BSM's angle. The source (QCL) and detector (IRLabs Si Bolometer) are placed 1000 mm from M1 in the plane containing the optical centre of both mirrors. In Figure 5-2, which shows the system as modelled in the MODAL modelling software, M1 is shown with two smaller inner sections representing the active regions of the mirror. As indicated in Figure 5-1, M1 is partially masked away from these regions to limited stray light reflections. The source and detector are separated in the axis perpendicular to the optical axis by approximately 260 mm, where both the centre point of the source and detector are equidistant from the centre of curvature of the mirrors. This separation is governed by the size of the primary mirror and can cause issues with alignment which will be discussed later.

The QCL source operating at 3.91 THz provided a coherent narrowband source ($\lambda = 0.077$ mm $\pm\, 0.002$ mm (Thor Laboratories 2014)) which illuminates a limiting circular aperture with a diameter of 30 mm. The relatively large available power and coherent frequencies make this an appropriate source to test the response of the optical system. Although the QCL allows for testing of optical systems at terahertz frequencies, at these wavelengths alignment becomes critical and often more difficult. The bolometer detector has a spectral response of $[15 - 2000]$ μm and is sensitive to radiation produced by the QCL source.

Appropriate filters were available to remove noise from background sources. As standard the bolometer comes with 2 filters with either 13 or 100 µm cut-on (Infrared Laboratories 2015). Polychromatic measurements are made with the 100 µm and QCL measurements are made with the 13 µm filter.

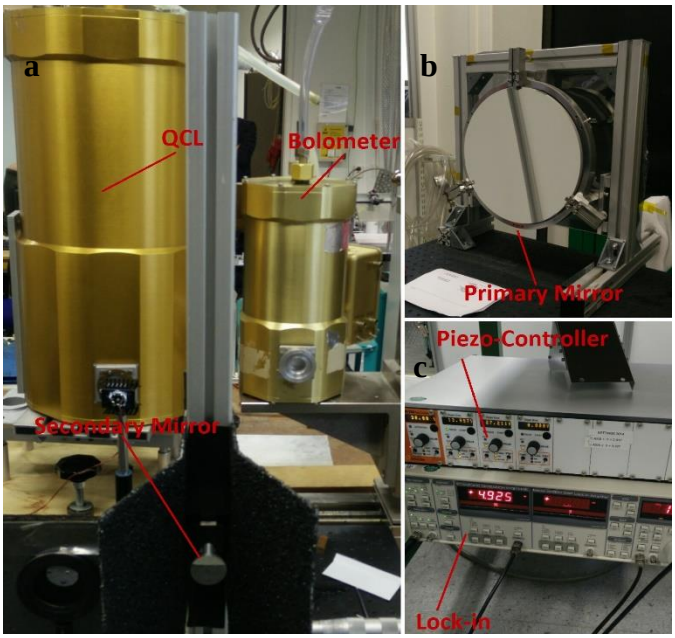

Figure 5-4: Shows the key apparatus used in the experimental Offner system: a) the cryostats of the QCL and bolometer detector along with the actuated secondary mirror, b) the large primary mirror is shown without its baffle present, c) the controller for the secondary mirror is shown.

5.1.2 Modelling

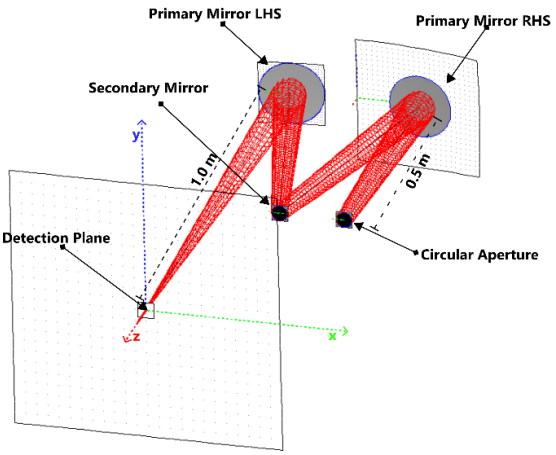

Figure 5-3: Simulation set-up in MODAL with the split primary mirror

The simulated Offner relay uses a uniformly illumined circular aperture as shown in Figure 5-3. This arrangement appears to differ somewhat from the experimental layout; however, this is superficial. The primary mirror M1 is split into two smaller mirror segments covering only the active regions (RHS and LHS). Segmenting of M1 allowed for a vast reduction in the total

mapping area improving the simulation time. The quality of the imaged PSF is assessed via direct comparison with the simulated results where both phase and amplitude are taken into consideration. Any deviations will indicate there are underlying issues with the optical system itself or that care has not been taken when performing the experiment.

5.1.3 System Alignment Analysis

For initial alignment and validation of the Offner relay measurements were made with the BSM in a fixed position. The detector bolometer was mounted on an XYZ stage and scans of the imaged PSF were made. This alignment must be completed for meaningful comparisons to be made with simulation results. Firstly, PSF must be centred in the detection plane which required zeroing of the BSM to its centred position. This was done using an optical laser, imaging screen and the known separation between the sources and detector about the optical axis. Secondly, the location of the imaged PSF's waist or focus must be determined. A series of measurements, varying in the *z*-direction, were made to find the optimal positon to place the bolometer. Scans of the detector moving in and out from the focal point of the optical system are shown in Figure 5-5.

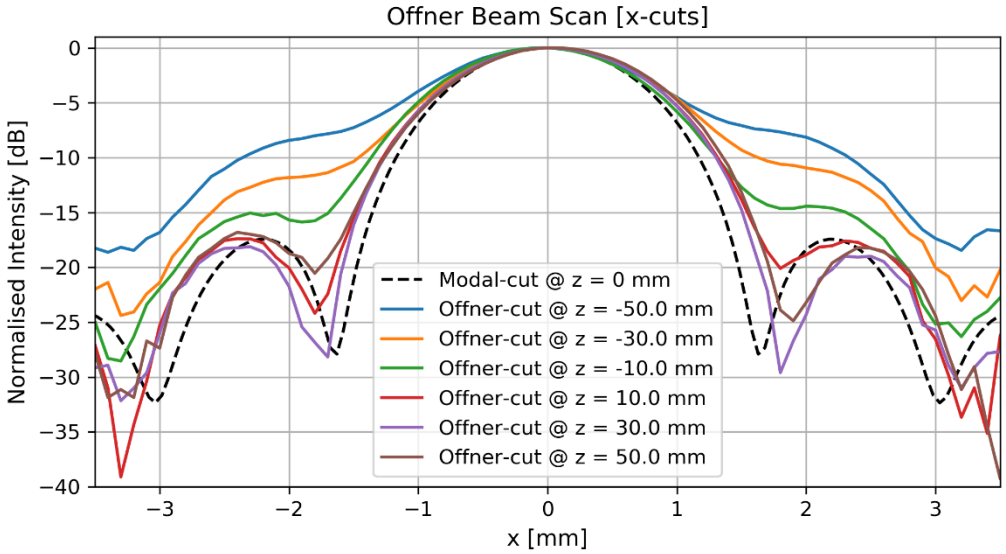

Figure 5-5: X-cuts of the experimental data for the detector moving into focus over a range of ±50 mm, Modal simulation results at the focus is used as a benchmark.

For all experimental result a pinhole of size 1 mm is placed in front of the bolometer detector to ensure there is no blurring of the imaged PSF. Detailed analysis on different pinhole sizes is given in (Schallig 2015a). There is a relatively narrow range of about [± 10 mm] to locate the position of the beam waist. In Figure 5-5, the experimental cuts are shown with the simulated MODAL result at the focus. By inspection, the focal point appears to occur at approximately

30 mm. The MODAL simulation predicts a slightly narrower Airy pattern so it is likely the exact focus lies within the 20 mm increment between 30 mm and 50 mm.

This conclusion is supported by further MODAL simulations, which show the spreading out of the beam as observations are made progressively further from the focus, see Figure 5-6. The

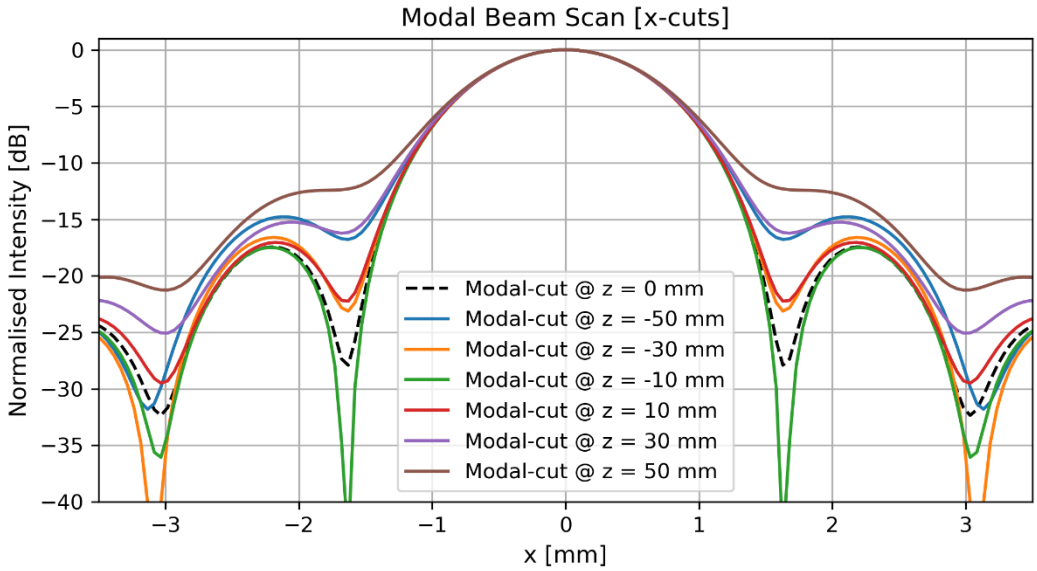

Figure 5-6:Modal simulation x-cuts of the detector plane moving into focus over a range of ±50 mm, clearly there is a spreading of the beam away from the focus at $z = 0$ mm.

importance of accurate determination of the focus position is clear, as deviation from the focus causes a loss in the definition of the imaged PSF. However, at these short wavelengths accurately finding the exact focus experimentally is difficult.

For both the experimental and simulated results there is a definite beam waist associated with the optical system. The same spreading of the PSF is observed away from the focus, i.e. an increase in the side-lobes is observed. Although the focus is difficult to find exactly due to the short wavelength, the structure of the PSF remains well defined near the waist, as illustrated in Figure 5-5 and Figure 5-6.

The initial alignment enabled the bolometer detector to be centred at the origin of the measurement plane. Operation of the Offner relay could then be investigated through translation of the PSF in the measurement plane. This was done using the attocube device to sweep the BSM through a range of angles. A number of scans of the PSF were made, in Figure 5-8 cuts of the imaged PSF's are shown alongside the simulated MODAL result. Here, the imaged PSF is in good agreement with the simulation result obtained from MODAL. However, there does appear to be an asymmetry present in the measured PSF. This feature is present in a number of the measurements made and also appears in results shown in (Schallig 2015a). To

investigate this further the performance of the Offner relay is investigated for varying angles of throw in MODAL.

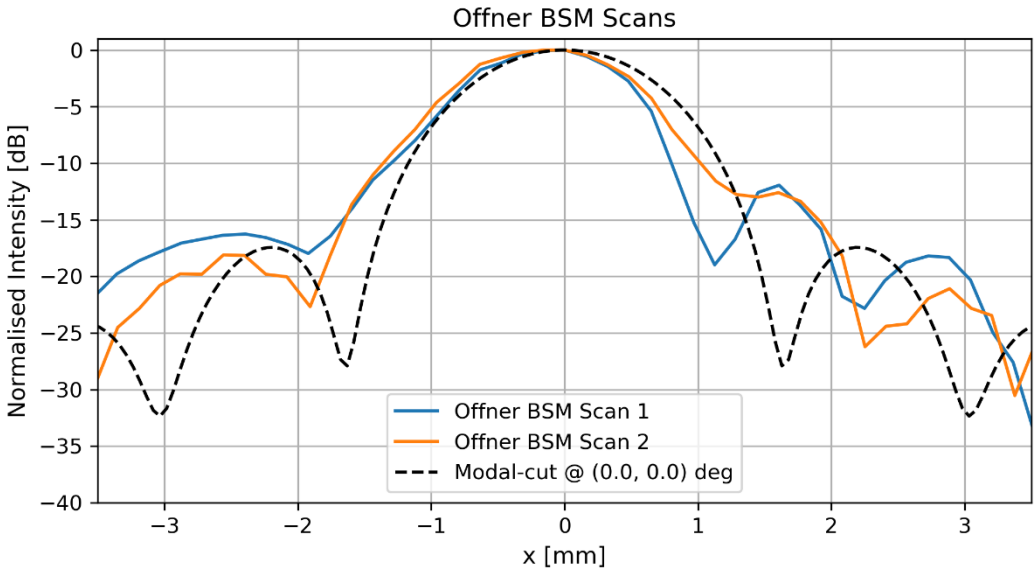

Figure 5-8: Modal simulation x-cuts of the Offner systems for the extremum angles of the secondary mirror.

The reliability of the Offner system is examined by observing the PSF of the Offner relay at the extremum angles of the secondary mirror (± 1.5 deg in both axes). Angles exceeding this range would cause the reflected beam to go beyond the mirror's active region. By investigating the simulation results at these extremum angles any inherent aberrations introduced by the rotation of the secondary mirror may be observed. For a range of angles, for which the reflected signal remains inside the LHS of the primary mirror, the PSF is examined.

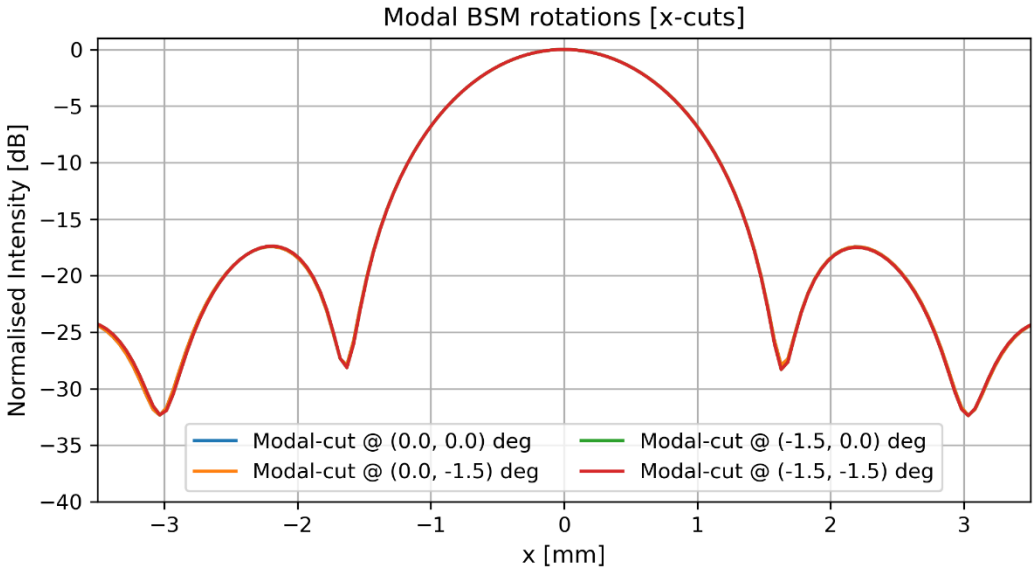

Figure 5-7: Modal simulation x-cuts of the Offner systems for the extremum angles of the secondary mirror.

In Figure 5-7, it can be observed that there is no deviation from the well aligned case at $(0°, 0°)$. Due to symmetry and clarity of expressing the result only the $-1.5°$ extremum angles are shown. Thus, for rotations of the secondary mirror kept at small angles, such that reflected beam remains inside the boundary of LHS of the primary mirror, the optical system introduces no aberrations to the resolved PSF. However, the BSM can achieve angles beyond this range and no limits were imposed on the controller software for the attocube.

In an effort to explain the asymmetry observed in Figure 5-8, the effect of the BSM's angle of throw being too severe is investigated. In such a scenario a portion of the beam reflected from the BSM would lie beyond the active region of the LHS of M1. To simulate this overlap with the masked region the BSM set with an angle of throw of $(2.1°, 2.1°)$. Due to this overlap of the reflected beam with the masked region of M1 part of the signal is lost resulting in an asymmetric PSF from the MODAL simulation as shown in Figure 5-9.

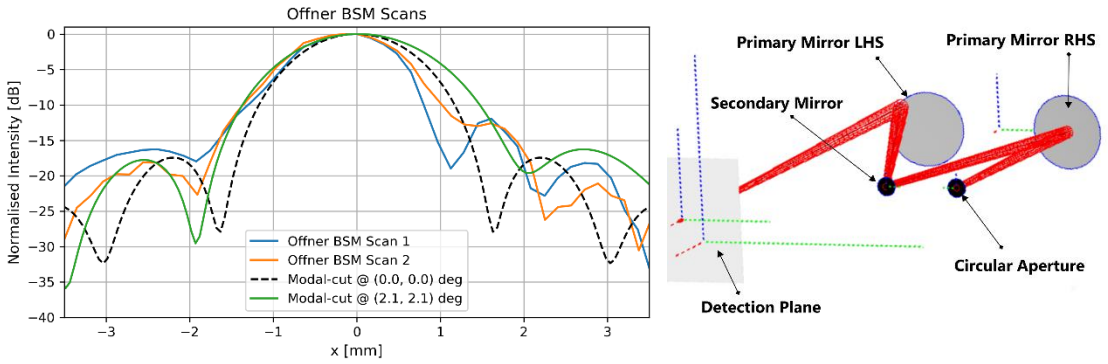

Figure 5-9: Shows the comparison between experimental data and the MODAL simulation where there is an overlap with the boundary of the primary mirror.

The mismatch in the side-lobe levels of the imaged PSF is quite similar to the simulated result where the overlap is present. This range of translation of the reflected ray is well within the angles achievable by the experimental set-up. It is possible that during the scanning of the BSM the reflected beam overlapped with the masked region of M1 causing this asymmetry. Furthermore, this could explain why acceptable result were obtained when the BSM was fixed, see Figure 5-5.

5.1.4 Gaussian Beam Source

Although the QCL does not produce a perfectly spherical wavefront, an attempt is made to capture the most spherically symmetric part of the wavefront when illumining the circular aperture ($D = 30$ mm). It is assumed that in the far-field this section of the QCLs beam pattern roughly provides uniform illumination of the aperture. Measurements were taken of the QCL's radiation field 20 cm from the opening window shown in Figure 5-10.

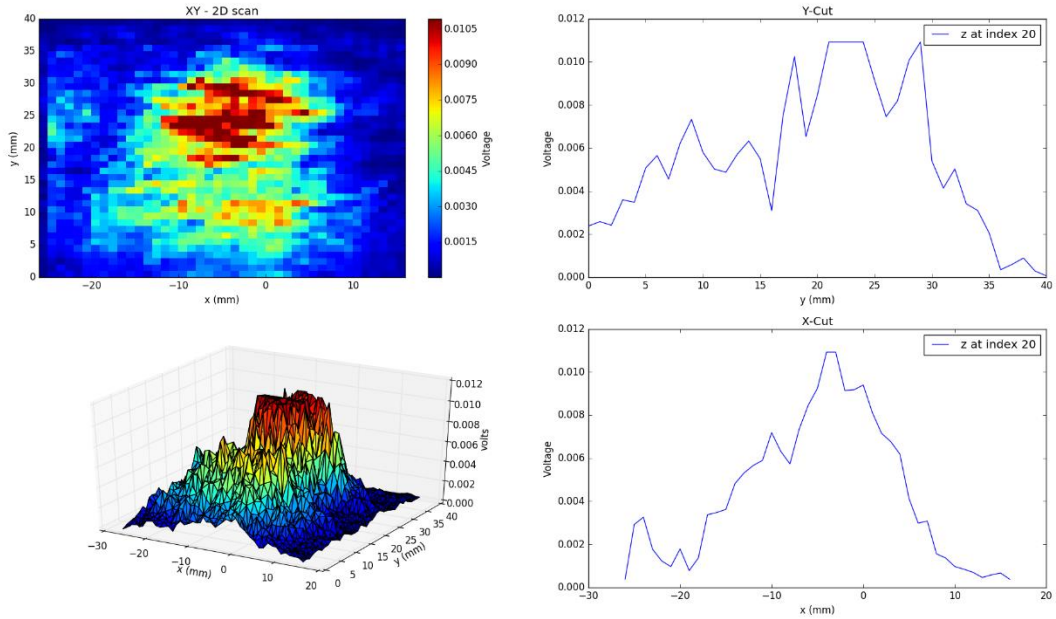

Figure 5-10 Plot of the beam pattern of the QCL with cuts taken through the maximum of the pattern.

From the measured radiation field, it can be seen that the main part of the beam covers a region well over $10 \text{ x } 10 \text{ mm}^2$ in size. Thus, the incident radiation field should provide reasonable illumination of the circular aperture. From (Fathololoumi et al. 2008) and (Adam et al. 2006) it is found that the most intense part of the QCL beam will have a somewhat Gaussian peak as shown in Figure 5-11.

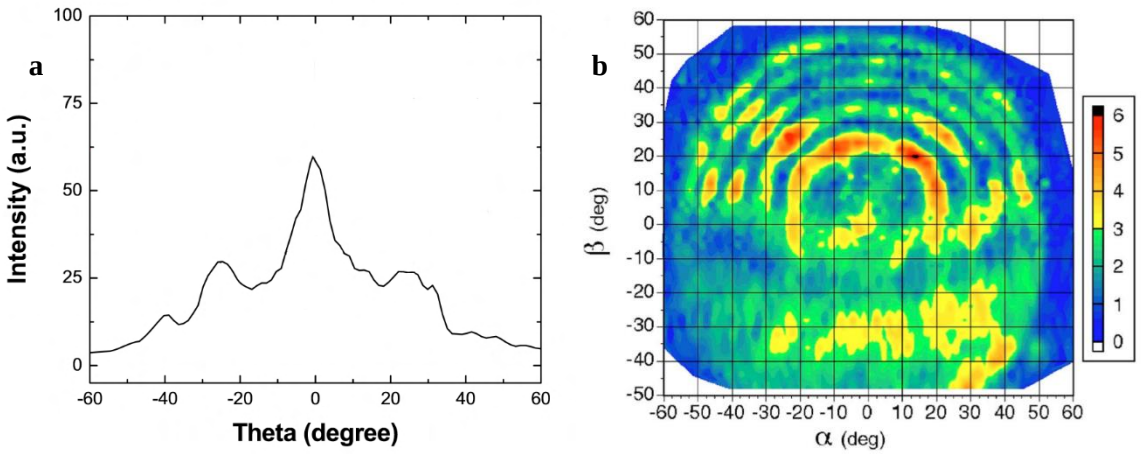

Figure 5-11: Plots of the beam profile and intensity pattern of a QCL a)(Fathololoumi et al., 2008) & b)(Adam et al., 2006).

Using this result, the uniformly illuminated aperture used in MODAL is replaced by a Hermite Gaussian source which illuminates an equivalent limiting aperture. This provides a better representation of the experimental Offner arrangement. The Gaussian source is defined with $f = 3.91$ THz and a phase radius of curvature of 0.5 m, which equals the propagation distance from the source to the limiting aperture. The beam waist of the source is set to $\omega_0 = 15$ mm such that it fully fills the limiting aperture. The system is imaged in a standard set-up with no offsets or rotations introduced as shown in Figure 5-12. The simulation result for the uniformly illuminated aperture is shown and here the shape of the two beams agrees quite well.

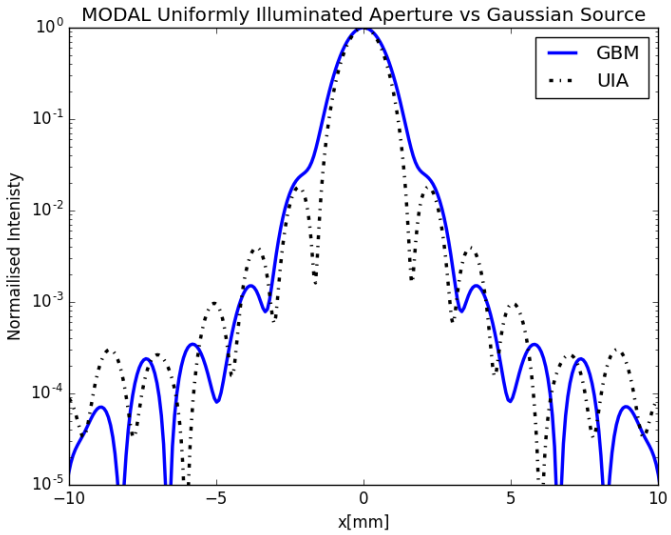

Figure 5-12: Shows a comparison between the PSF from a Gaussian and uniform source.

Furthermore, using this Gaussian approximation the effect of the QCL source not fully illuminating the aperture may also be investigated. In Figure 5-13, the imaged PSF from the Offner system is shown for progressively narrowing beam waists $\omega_0 = [15, 7.5, 3.75]$ mm.

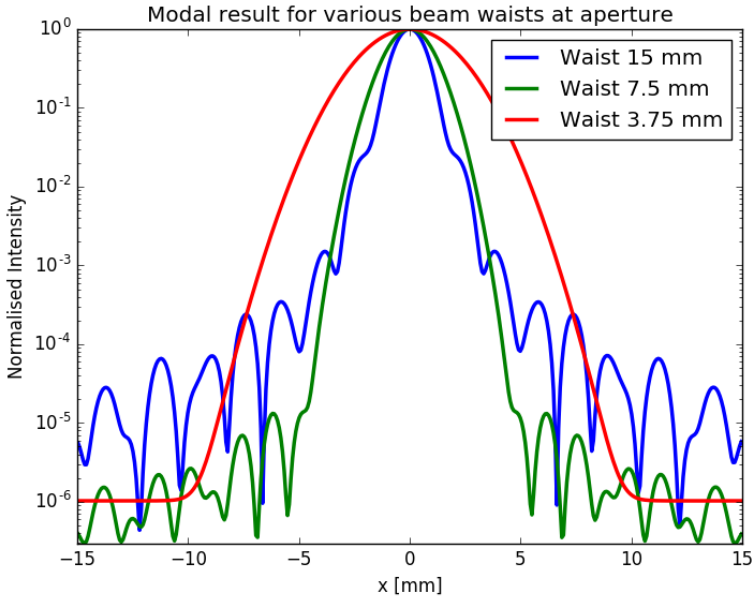

Figure 5-13: Resulting PSF for various beams waists at the source aperture.

The narrower beams do not provide sufficient illumination and as a result the Airy pattern shape is not present. For $\omega_0 = 3.75$ mm a simple Gaussian is observed and only when the waist begins to increase is the expected Airy pattern observed.

5.1.5 Polychromatic Airy pattern

A quasi-monochromatic QCL source provides an ideal test case for the Offner relay's performance to be tested against simulated results. However, in the instrument the system must also deal with polychromatic sources. The PSF for a polychromatic source is found by integrating the monochromatic PSF over the wavelength range of the source:

$$I(r) = I_0 \int_{\lambda_1}^{\lambda_2} \frac{1}{\lambda^2} \left[\frac{2J_1\left(\frac{\pi r}{F\lambda}\right)}{\frac{\pi r}{F\lambda}} \right]^2 d\lambda, \qquad (5.1.2)$$

where uniform intensity profile is assumed across the range.

The polychromatic source used was a DLS200X2224G2X IR – Emitter (700 ℃) with a wavelength range between 0.1 and 1 mm. A spectral analysis of the emission of this source was conducted by (Schallig 2015a), where the effects of atmospheric absorption can be clearly observed as can the frequency ranges where the maximum irradiance from the source is obtained. From Figure 5-14, the region where the maximum irradiance is obtained lies between 60 – 100 cm^{-1} (0.1 – 0.1667 mm). Below this there is significant absorption, and the maximum

irradiance is quite low. As a result, only the region of maximum irradiance is considered when performing simulations.

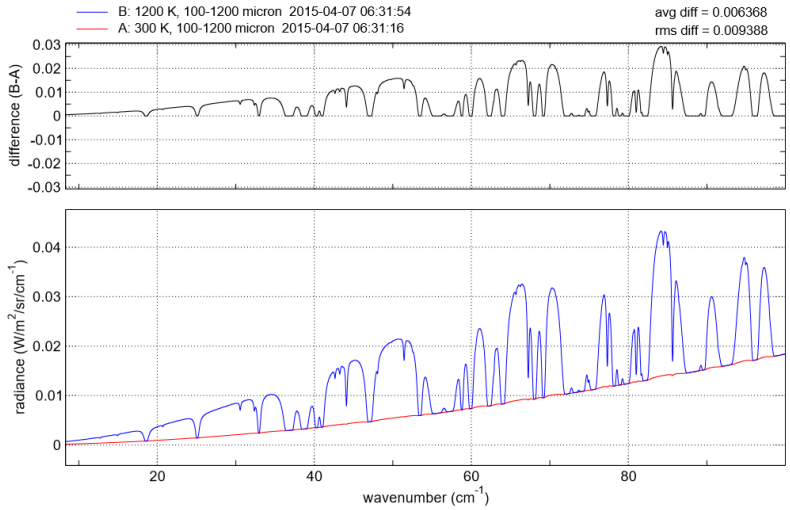

Figure 5-14:Theoretical spectra of black-body radiation with a pathlength of 3 m air between the globar and the detector (Schallig 2015a).

In the experimental arrangement the QCL and limiting aperture are removed and the polychromatic source is fixed in the same position. The polychromatic source is fitted with a pinhole of 0.63 mm to minimise any blurring due to the finite aperture sizes. As observed earlier the minima of the monochromatic PSF are in agreement with the roots of the first order Bessel function. However, for the polychromatic case these minima are no longer well defined due to the integration over the wavelength range. An example of this can be observed for in the polychromatic PSF in Figure 5-15a.

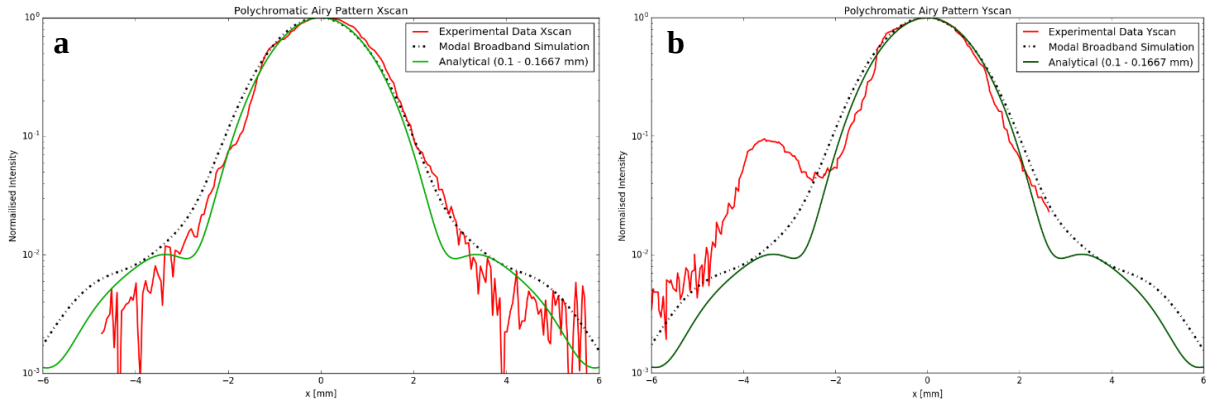

Figure 5-15: Shows the polychromatic measurements and the agreement with MODAL and the analytical result (0.1 – 0.1667 mm).

In the Figure 5-15a, there is good agreement between the experimental results and analytical result. The MODAL simulations were performed with a uniformly illuminated aperture (since

good agreement between this and the Gaussian source has been shown in Figure 5-12). The MODAL result predicts a wider PSF than the analytical result, this is potentially due to the number of samples taken between 0.1 and 0.1667 mm not being large enough. However, reasonable agreement is still observed. However, in Figure 5-15b although the beam width matches quite well extra features are observed in the experimental results. These anomalies may be attributed to stray light from background sources or from the improperly shielded regions of the experimental set-up or as before, over rotation of the BSM.

5.1.6 Conclusion

Through comprehensive PO simulations in MODAL the idealised Offner relay system was shown to translate the beam with minimal aberrations to the PSF as expected. Initial alignment of the experimental arrangement showed good agreement with the simulated results. However, full operation of the Offner relay, via actuation of the BSM, introduced irregularities to the imaged PSF. In practice the critical alignment of the system is challenging and as shown in section 5.1.3 an overlap of the reflected beam with the primary mirror shield offers some explanation to the observed irregularities in the PSF.

A strong assumption was made that the QCL source fills the Offner relay system's aperture. Scans of the QCL beam profile showed that the beam should provide adequate illumination of the aperture. Furthermore, simulations using GBA to illuminate the aperture for narrowing beam waist, showed the effect of an under-illuminated aperture on the resolved PSF. Finally, the Offner system was investigated using a polychromatic source. Experimental and simulated results were shown to be in good agreement with some potential beam irregularities again attributed to over rotation of the BSM.

5.2 Analysis of an Amended SAFARI Pixel Design

The work presented in this section summarises the computational modelling and analysis of a prototype SAFARI pixel, completed as part of contracted work for the European Space Agency (ESA). This study focuses on an amended optical arrangement to illuminate the SAFARI pixel. This arrangement is derived from an on-axis solution shown in Figure 5-16. Here, the pixel is coupled to a conical horn and is fed by a blackbody source through a number of intermediate limiting apertures.

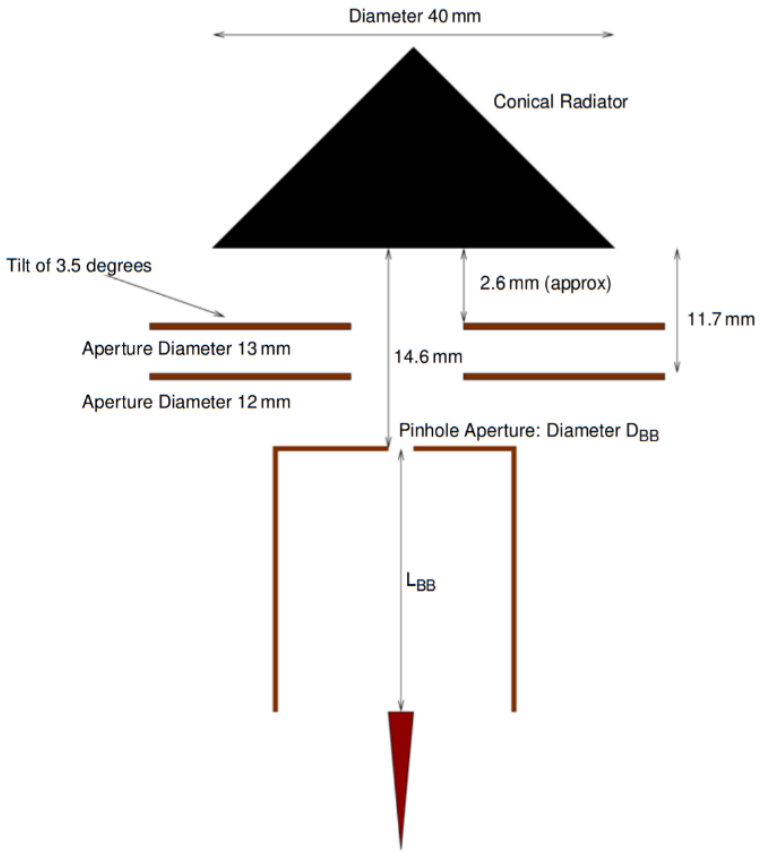

Figure 5-16: Layout of the previous SAFARI pixel design (McCarthy 2014).

Facilities at SRON, Groningen allowed for intermediate optics to be introduced in the test bed design. It was decided to extend this investigation further to consider an amended off-axis optical arrangement as shown in Figure 5-17. In this design the prototype SAFARI pixel was illuminated by an aperture limited blackbody source via a focusing elliptical mirror. The elliptical mirror was introduced to allow for greater flexibility in the optical test bed, improve coupling to the waveguide and potentially improve the pixel efficiency.

The blackbody source ($12 \times 12\ \mathrm{mm}^2$) illuminates the system over SAFARI's S-band ($35\ \mu\mathrm{m} - 70\ \mu\mathrm{m}$). The elliptical mirror has radii of curvature $R_1 = 30$ mm and $R_2 = 100$ mm, with the source and feedhorn positioned at the appropriate foci. The pixel feedhorn is defined by $L = 4.9$ mm, an opening aperture of $0.65 \times 0.65\ \mathrm{mm}^2$, an opening angle of 30° over the first 0.2 mm and an opening angle of 6° over the remainder of the geometry. In the detector plane the feedhorn is coupled to a TES cavity. This single horn forms part of the larger SAFARI subarray structure as discussed in chapter 1.

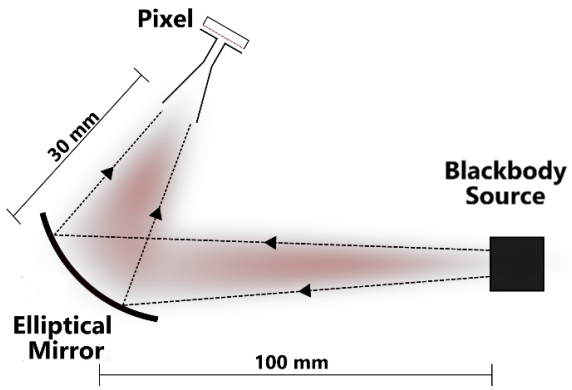

Figure 5-17 Proposed optical arrangement of the amended SAFARI pixel design.

A combination of physical optics (PO) and mode matching techniques was used to characterise the performance of the pixel design. For a range of inclination and azimuthal angles the blackbody source was rotated, and the response of the optical system was measured. The range of inclination and azimuthal angles used lie between $0 - 10$ deg and $0 - 180$ deg respectively. Furthermore, by rotating the source through 90 degrees the effect of the polarisation could be investigated. For modes up to and including a Cartesian order of 38 the amplitudes for each angular set was recorded. The simulated optical arrangement is shown in Figure 5-18, here a simple Gaussian beam illustrates the operation of the optical system.

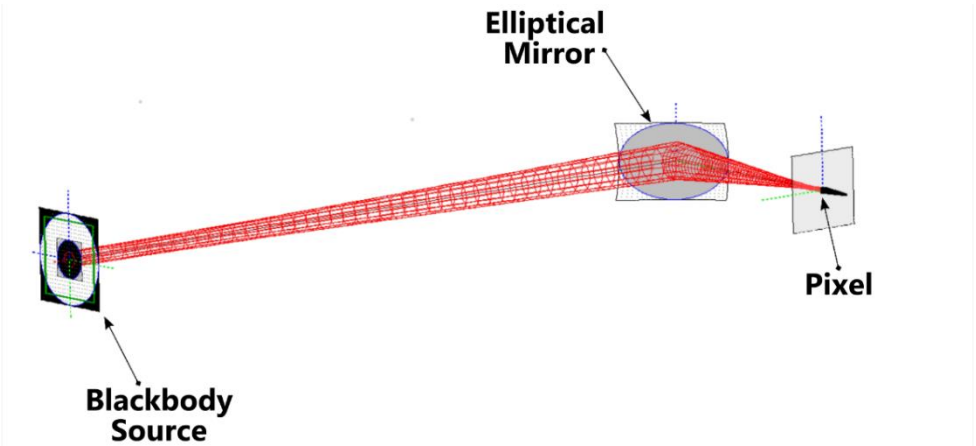

Figure 5-18: Schematic of the MODAL set-up of the amended SAFARI system

To reduce simulation time (which for the shortest wavelength can take ~70 hours) some optimisations of the model were implemented. Dynamic grid size mapping of the optical components was performed to ensure no oversampling. Furthermore, the appropriate ranges and step sizes for the beam sweep angles were investigated, such that there is sufficient resolution and all symmetries were exploited. The inclination angular range of $0 - 10$ deg offered adequate coverage (beyond 10 deg essentially no power is coupled to the detector). The azimuthal angular range of $0 - 180$ deg provided sufficient coverage. The symmetry conditions of the pyramidal horn meant that only half of the azimuthal range needed to be imaged.

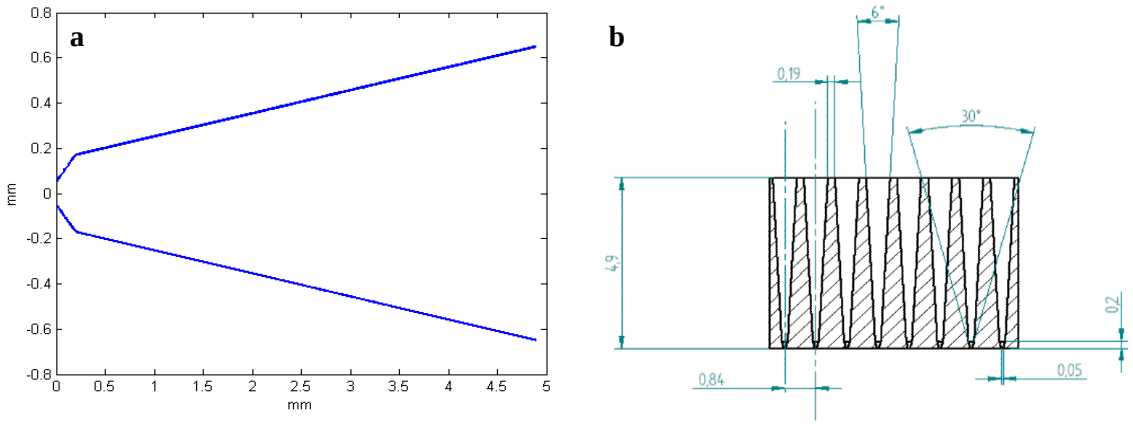

Figure 5-19: a) Geometry of S-Band pyramidal horns being modelled, b) Overview of the SAFARI horn array

5.2.1 Modelling the Prototype SAFARI Horn and Cavity Coupled Absorber

This section deals with the implementation of the mode matching techniques required to accurately model the prototype SAFARI pixel arrangement. Many of the mode matching routines presented in chapters 2 and 3 were developed as part of the ESA research contract in order to model these SAFARI type structures. The main advantage of the mode matching techniques, especially for multi-moded structures, is that the matrix description of scattering allows many modes to mutually scatter at a single frequency. In Finite Element Electromagnetic solvers, such as CST, each mode is propagated independently, and this is much more computationally intensive. For electrically large structures i.e. with lengths > 100 wavelengths and where many modes are included, such solvers are impractical.

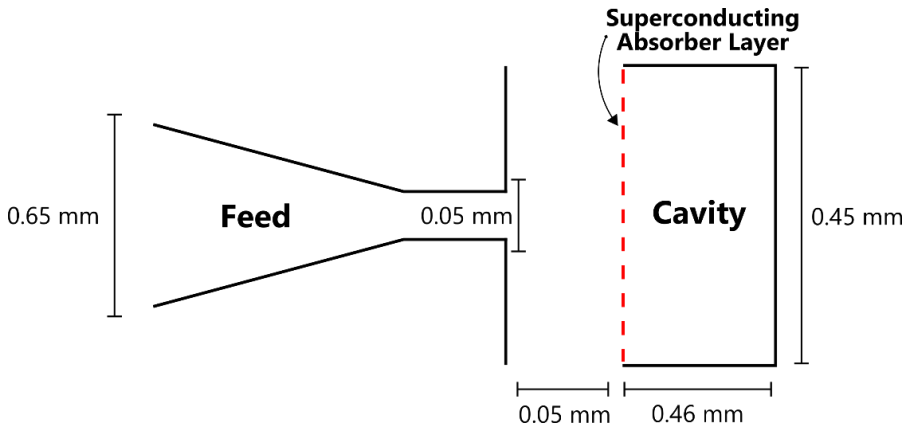

Figure 5-20 Representation of the geometry modelled using the developed rectangular mode matching code

In Figure 5-20, a schematic drawing of the pixel layout shows the different features of the complete pixel which must be modelled. The mode matching techniques are used to represent all possible scattering possibilities within the pixel with a waveguide and freespace mode set. This includes scattering in the feed, the exit through the freespace gap (including diffractive loss to the sides of the freespace gap) and the possible absorption at the absorber layer including reflection from backshort. The pixel's overall scattering matrix is obtained from the joining of the guide, absorber cavity and freespace network sections. In earlier chapters, the necessary mode matching routines required to model the guide and absorber cavity networks were introduced. However, the methods required to tackle the freespace gap network have yet to be discussed. Introduced in (McCarthy 2014), a freespace network model is summarised to describe the coupling of power across the pixels freespace region.

The waveguide modeset at the freespace interface is coupled to a representative set of freespace Hermite Gaussian modes:

$$\Psi_{l,m}(x,y,z) = u_l(x,z)u_m(y,z)\exp(-jkz) \tag{5.2.1}$$

The interface between the aperture and freespace is treated as a normal junction, such that the scalar product $\left(P = \int_S \boldsymbol{A}^{t^*} \cdot \boldsymbol{B}^t \, dS\right)$ can be defined for the transverse fields. The field in freespace is given by the sum of the Hermite Gaussian modeset, each scaled by their corresponding mode coefficients:

$$E_{in} = \sum A_n \Psi_n(W_{in}, R_{in}, \phi_{in}) \tag{5.2.2}$$

this field must now be propagated through a freespace gap distance *z* which will then excite the cavity coupled absorber section. Thus, the evolution of the field must be modelled as the field propagates through the freespace region to obtain the outgoing field:

$$E_{out} = \sum A_n \Psi_n(W_{out}, R_{out}, \phi_{out}) \tag{5.2.3}$$

Geometrical ray tracing methods are adapted to allow for the propagation of Gaussian beams (McCarthy 2014), within the paraxial limit, to be represented via ABCD matrices. Here, the method requires complex valued rays to be considered. Gaussian beams have waist positions which corresponds to a plane where the beam width and intensity are minimised and maximised respectively. It is assumed that the fundamental Gaussian beam is a spherical wave radiating from a complex source. If a point source is approximated to have field distribution given by:

$$E = \exp\left(\frac{-jkr^2}{2q}\right), \tag{5.2.4}$$

then this can be represented by allowing the field to have a complex radius of curvature, (Goldsmith 1998), given by:

$$\frac{1}{q} = \frac{1}{\mathrm{Re}(q)} - j\left(\frac{1}{\mathrm{Im}(q)}\right). \tag{5.2.5}$$

If this is to be constant with the fundamental Gaussian mode, the real component must represent the reciprocal of the phase radius of curvature and the complex component represents the Gaussian variation of off-axis amplitude:

$$\frac{1}{q} = \frac{1}{R} - j\left(\frac{\lambda}{\pi W(z)^2}\right) \tag{5.2.6}$$

Thus, the field distribution of the point source becomes:

$$E = \exp\left(\frac{-jkr^2}{2q}\right) = \exp\left(\frac{-jkr^2}{2R}\right)\exp\left(\frac{-\lambda}{\pi W(z)^2}\right) \tag{5.2.7}$$

The complex beam parameter therefore tracks the required Gaussian beam parameters and hence can be used to follow the evolution of the system. The complex beam parameter is transformed by an optical system (represented by an ABCD matrix) as follows:

$$q_{out} = \frac{Aq_{in} + B}{Cq_{in} + D} \tag{5.2.8}$$

Thus, the output phase radius of curvature and beam radius are given by:

$$\frac{1}{R_{out}} = \mathrm{Re}\left(\frac{1}{q_{out}}\right) = \mathrm{Re}\left(\frac{C + \frac{D}{R_{in}} - \frac{jD\lambda}{\pi W_{in}^2}}{A + \frac{B}{R_{in}} - \frac{jB\lambda}{\pi W_{in}^2}}\right) \tag{5.2.9}$$

$$W_{out} = \sqrt{\frac{-\lambda}{\pi \mathrm{Im}\left(\frac{1}{q_{out}}\right)}} = \sqrt{\frac{-\lambda}{\pi \mathrm{Im}\left(\frac{C + \frac{D}{R_{in}} - \frac{jD\lambda}{\pi W_{in}^2}}{A + \frac{B}{R_{in}} - \frac{jB\lambda}{\pi W_{in}^2}}\right)}} \tag{5.2.10}$$

For a known phase slippage at the input plane, the output phase slippage is given by:

$$\phi_{out} - \phi_{in} = -Arg\left(A + B\left(\frac{1}{q_{in}}\right)\right). \tag{5.2.11}$$

Thus, the evolution of the Gaussian beam through some optical system can be tracked via ABCD matrices. In the case of the free space gap the ABCD matrix is given by:

$$\begin{bmatrix} A & B \\ C & D \end{bmatrix} = \begin{bmatrix} 1 & d \\ 0 & 1 \end{bmatrix} \tag{5.2.12}$$

where d gives the propagation distance allowing the freespace section to be represented for the pixel.

Additionally, power leakage can occur at the sides of the freespace gap. To account for this truncating sections are placed on the freespace side of each transition plane. This truncates power loss beyond the pixel geometry and suppresses reflections. To achieve this, infinitely thin perfect absorbers form the truncating sections, with gaps made equal to that of the pixels' width. As reflections are modelled to be zero from the surrounding material on either side of the TES absorber, the transmission matrices are simply the overlap integrals between the Hermite Gaussian modes on either side of the TES absorber, across the area of the gap, as illustrated in Figure 5-21.

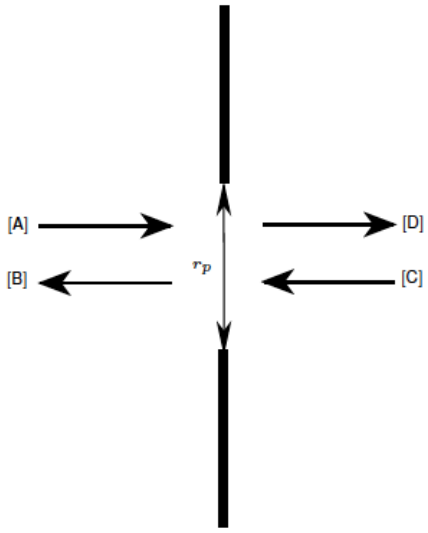

Figure 5-21 The introduction of loss due to diffractive loss in the free space gap of the waveguide pixel

The associated scattering matrices for this loss mechanism then become:

$$\boldsymbol{S} = \begin{bmatrix} \mathbf{0} & \boldsymbol{S_{12}} \\ \boldsymbol{S_{21}} & \mathbf{0} \end{bmatrix} = \begin{bmatrix} \mathbf{0} & \boldsymbol{P_2} \\ \boldsymbol{P_1} & \mathbf{0} \end{bmatrix} \tag{5.2.13}$$

with:

$$P_1 = \int_0^{r_p} e_n^- \, e_n^- dr \tag{5.2.14}$$

$$P_2 = \int_0^{r_p} e_n^- \exp\left(\frac{jkr^2}{2R}\right) e_n^- \, dr \tag{5.2.15}$$

On the back side of the horn array a reflective surface is implemented around the exit aperture of the horn to include reflections from this surface in the scattering regime. In order to verify this approach in terms of including the freespace section loss with the SRON rectangular horn a simpler, smaller waveguide geometry was analysed with the developed mode matching code and also analysed in CST to verify the approach. Finally, an SVD analysis is performed on S_{11} to determine the contributing modes in the scattering matrix. This is done to reduce the computational load related to determining the absorption modes of this pixel design.

5.2.2 Measuring Pixel Efficiency

Pixel efficiency is the ratio of the total power absorbed by the horn aperture to the total power arriving from the black body aperture. By performing an SVD analysis on the pixel's S_{11} matrix the individual eigenfields (both propagating and non-propagating) which comprise the aperture field of the pixel are found. Progressing to the far-field, the fields are normalised, such that they represent the fraction of power coupled to that eigenfield at a given angle of incidence compared to the total power coupled to the field from a uniformly illuminated antenna. The fraction of the total power arriving at the pixel entrance in each eigenfield can be calculated. This gives an aperture efficiency value for each angular set, represented by a data cube ($A[\theta, \phi]$) given by

$$A[\theta, \phi] = \frac{B[\theta, \phi]}{\cos(\theta) * P_{\max incident}} \tag{5.2.16}$$

$$B = \sum_i^{N_{modes}} r_i^2 * s_i \tag{5.2.17}$$

where the B represents the absorbed coupling sum, s_i are the singular values from the SVD analysis of the scattering matrix and r_i are the modulus of the dot product of the mode amplitudes at a particular combination of angles with the columns of the singular matrix. Using this technique, the effective aperture of the antenna (Γ_{app}), for each wavelength is obtained by integrating over the range of azimuthal and inclination angles:

$$\Gamma_{app} = 2 \times \iint_{0,0}^{\pi,\theta_{max}} A[\theta,\phi] \times \sin\theta \; d\theta d\phi \qquad (5.2.18)$$

where $\theta_{max} = 10°$ and the explicit factor of two accounts for the symmetry imposed by the azimuthal range defined earlier.

Finally, the total power absorbed by the pixel over the wavelength range can be calculated. The power density of the blackbody per unit wavelength, per unit area, per steradian is given by the Planck curve:

$$M_\lambda = \frac{2hc}{\lambda^5} \frac{1}{\exp\left(\frac{hc}{\lambda k_B T}\right) - 1} \qquad (5.2.19)$$

The spectral power absorbed (SPA) gives the absorbed power per unit frequency where $SPA = M_\lambda * \Gamma_{app}(\lambda)$. However, since the power is split into two polarisation channels, half the spectral irradiances lies with each, and $SPA = \frac{M_\lambda}{2} * \Gamma_{app}(\lambda)$ gives the absorbed power per unit frequency from an unpolarised blackbody source. The total absorbed power is obtained by integrating the spectral power absorbed over the wavelength band as shown below

$$P_{pixel} = \int_{\lambda_{min}}^{\lambda_{max}} SPA \; d\lambda \qquad (5.2.20)$$

5.2.3 Analysis of results

The pixel design is characterised over the wavelength range $40 - 70$ μm in 5 μm steps. Due to time and equipment constraints at SRON, it is unlikely that the corresponding experimental

measurements will be performed. However, the results from previous pixel designs can be used to make useful comparisons and comments on the overall performance of the amended pixel design.

From the results from previous measurements, given in Table 5-1, there appears to be only one set of results that could be used to draw comparisons to the new design. Based on the blackbody aperture alone comparisons are made with test #46, shown in Table 5-1, which has a radius of 12 mm which corresponds to an aperture area of $\approx 452\ \text{mm}^2$. In contrast the square (12×12 mm) blackbody aperture of the new pixel has an aperture area of $144\ \text{mm}^2$. The overall effect the aperture size has on radiation entering the system is negligible so effectively these test case apertures can be treated as equivalent. The path length to the opening aperture of the horn in previous design is a factor of 10 closer to the blackbody source. However, this factor is of little importance because of the focusing effect of the elliptical mirror. Below Table 5-1 shows the distance and aperture measurements along with values for the total absorbed power for the simulation and measurements.

Table 5-1 The measured and simulated power absorbed from test cases of original test bed design. Test #46 represents the most comparable arrangement of the previous design to the new arrangement.

Cool-down#	D_{BB}	L_{BB}	Measurement P_{abs} [fW]	Simulation P_{abs} [fW]
#46	12 mm	17 mm	47.2	76.1
#47	0.9 mm	10.77 mm	6.28	6.03
#48	0.5 mm	10.2 mm	2.44	2.33
#49	1.4 mm	10.2 mm	15	14.34

Here the values D_{BB} and L_{BB} refer to the diameter of the aperture and the distance to the horn from the aperture respectively.

Figure 5-22(a) shows a plot of the azimuthally averaged aperture efficiency values over an inclination angle range of 0 – 10 degrees for each wavelength with both 0 and 90 degrees polarisation. The azimuthal averaging is done for the purpose of illustration, as discussed earlier the aperture efficiency values which are referred to as $A[\theta, \phi]$, contains the aperture efficiency values for all combinations of angle for each wavelength. Averaging over the azimuthal range provides a sense of the system response to changing wavelength and inclination angle. In Figure 5-22(b) is the effective aperture values at each wavelength and again in both polarizations, the variation in these effective aperture values are discussed later.

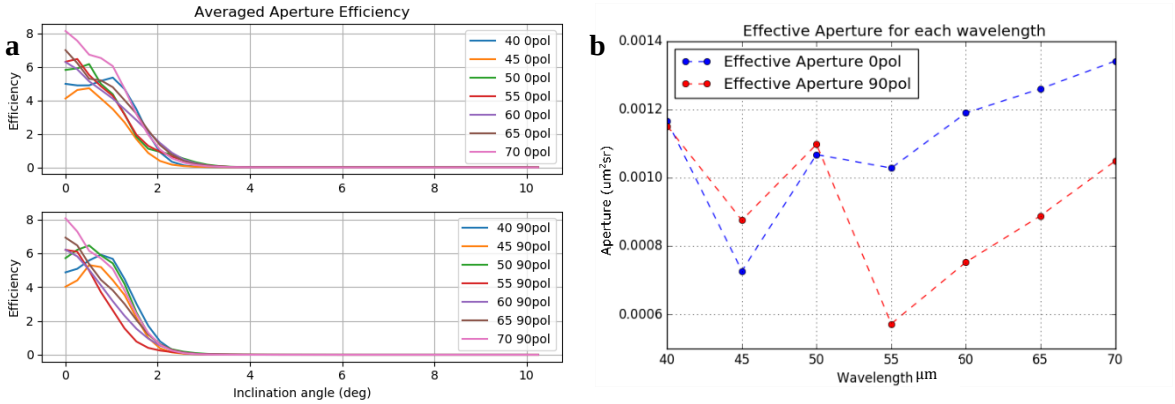

Figure 5-22 Shows (a) the azimuthally averaged aperture efficiency values over the inclination angle range and (b) the effective aperture for each wavelength at both 0 and 90 degrees polarisation.

Using these values along with the blackbody spectrum data shown in Figure 5-23 (a), with the appropriate filter present, values for the spectral power absorbed at each wavelength are obtained. The values for the spectral power absorbed at each wavelength are shown in Figure 5-23 (b), integrating over the wavelength range the power absorbed by the pixel is found to be 8.7 fW. There is a definite decrease in performance for this new pixel considering the relatively large blackbody aperture.

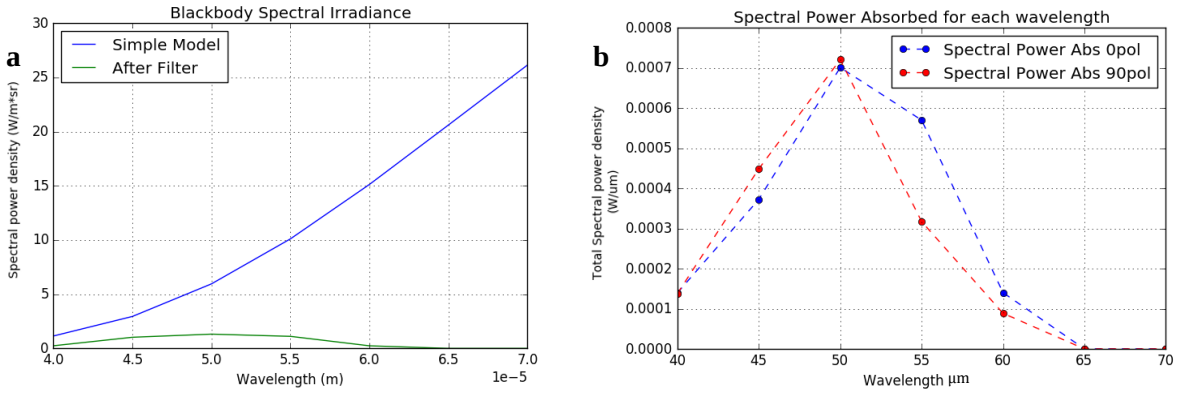

Figure 5-23 Shows (a) Blackbody spectral irradiance with and without filter applied (b) Spectral power absorbed at each wavelength for both polarisations.

Alongside the simulations of the amended pixel design, a 'benchmark' system with the aperture and mirror removed is defined i.e. just the blackbody is illuminating the horn. This benchmark allows for validation of the simulation result. However, the horn design will restrict the range of solid angles accepted to illuminate the pixel. In Table 5-2, the power absorbed by both the benchmark and the optical system is almost equivalent.

Table 5-2 Shows the benchmark and simulation results for the amended safari pixel system

Side Length	Length	Benchmark P_{abs} [fW]	Simulation P_{abs} [fW]
0.65 mm	130 mm	8.8	8.7

One would expect that the optical system would allow for much greater power absorption than just the plane illumination of the horn. The blackbody aperture for the benchmark provides essentially full illumination of the optical system, as such the same amount of power is present in both simulations. The brightness theorem (Quimby 2006) defines brightness or radiance as the optical power per unit solid angle per unit area of the emitting surface ($\mathrm{W/m^2 \cdot sr}$). Thus, a source is said to have a high brightness when it emits light in a narrow range of angles from a small surface area. One might think that by focusing the source to create an image with a smaller surface area that the brightness could be increased. However, the optics also changes the angular distribution of the light according to geometrical optics which reduces the apparent increase in brightness (Quimby 2006). To better understand the process which is occurring here the results from the benchmark test are illustrated in Figure 5-24.

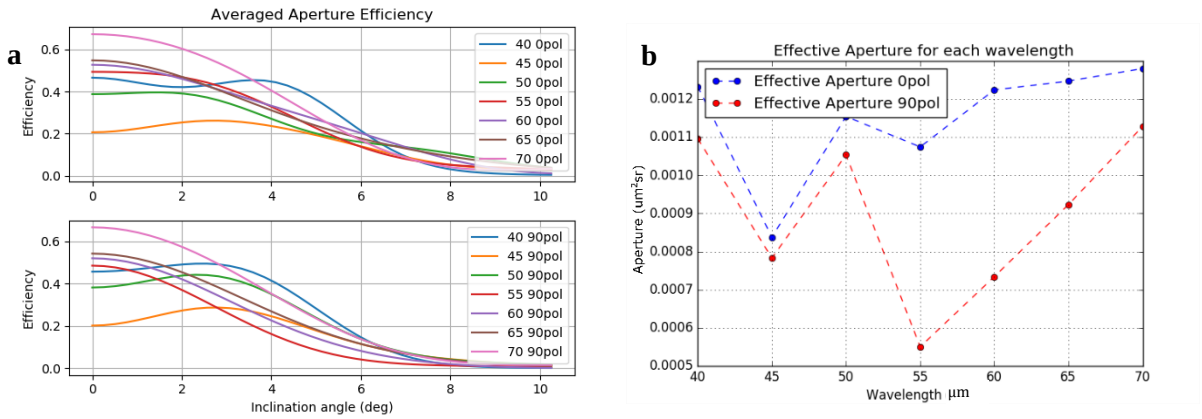

Figure 5-24 Shows (a) the azimuthally averaged aperture efficiency values over the inclination angle range and (b) the effective aperture for each wavelength at both 0 and 90 degrees polarisation for the benchmark tests.

In the benchmark results the loss in aperture efficiency with an increasing inclination angle is less dramatic. However, there is also a much-reduced peak efficiency. The elliptical mirror allows for the blackbody radiation to be focused directly onto the horn aperture. This gives an apparent increase in aperture efficiency but by inspecting the effective aperture values there is almost no change.

This effect becomes even more apparent when the efficiency values of individual modes are inspected. In Figure 5-25 the aperture efficiency values for both simulations are shown. It is clear the effect of the elliptical mirror has essentially focused the radiation onto a smaller region as described by the brightness theorem.

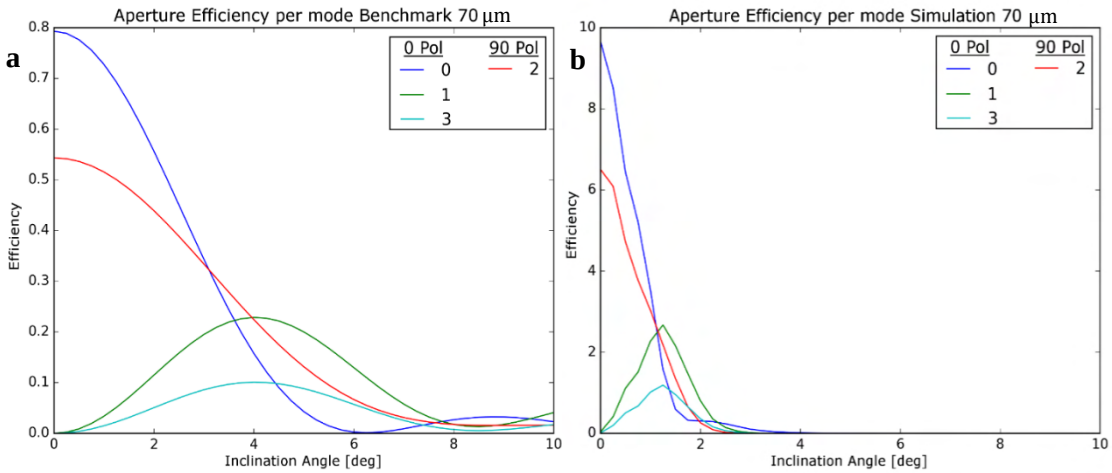

Figure 5-25 Shows the Aperture Efficiency values per individual mode for 70 µm a) the benchmark test case and b) the fully optical simulation. Both polarisations are included here and are labelled accordingly

There is a trend observed that the effective aperture values for the 90 degree polarisation values are lower than the 0 degree values. At the lower frequencies this effect is diminished so the contributing modes in the 90 degrees polarisation must be higher order modes and yet to fully cut on at these frequencies.

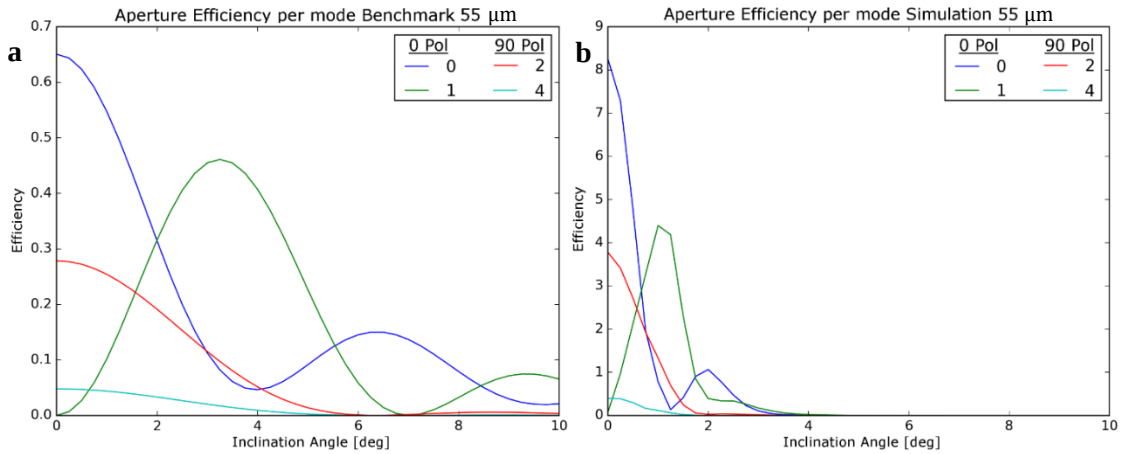

Figure 5-26: Shows the Aperture Efficiency values per individual mode for 55 µm: a) the benchmark test case and b) the fully optical simulation. Both polarisations are included here and are labelled accordingly

5.2.4 Conclusion

Both the benchmark test and the amended pixel design have overall performances which are equivalent in terms of power absorbed. This is due to the fact that there is only a limited amount of radiation emitted from the blackbody source that can be coupled to the horn detector per solid angle. The influence of the elliptical mirror does not lead to the capture of anymore radiation than emitted, it only focuses part of it. Compared to the previous testbed design, there is significant loss in performance and the power absorbed values are more comparable to test instances in Table 5-1 where a smaller blackbody aperture is present. As such, this type of optical arrangement is not entirely suited to the pixel design: if the horn which had a much reduced angle of acceptance the benchmark simulation would lose a large amount of power for the increasing inclination angles. In this scenario such an optical arrangement would allow more of the radiation to be focused into the horn's narrower angular acceptance range.

5.3 Analysis of a Prototype Pyramidal SAFARI M-band Horn

In this section the mode matching routines developed in chapters 2 and 3 are employed to aid in the accurate analysis and characterisation of a prototype sub-array feed block, as described in (Audley, de Lange, Gao, et al. 2018), for SAFARI's mid-wavelength band (60 – 110 μm). The prototype MW-feed array consists of 37 pixels realised through a combination of direct machining techniques, to form the split block, whereby individual platelets can be doweled together to form the complete sub-array block. Individual feeds are rectangular in shape, have an axial length of 9 mm, a throat aperture of 120×120 μm and an entrance aperture of 1350×650 μm.

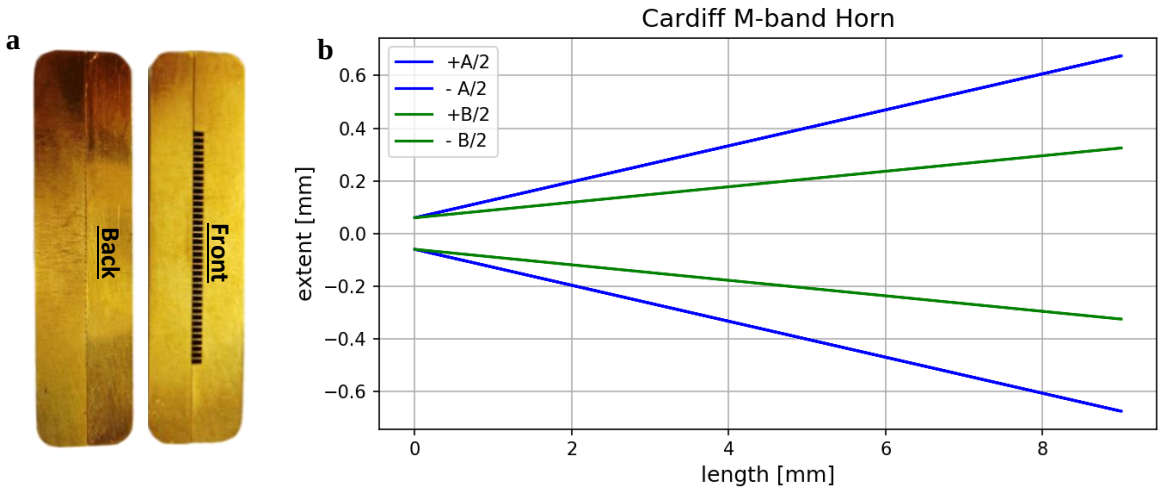

Figure 5-27 a) Image of the prototype sub-array structure b) Profile of the prototype M-band SAFARI horn where A and B define the horns x and y dimensions respectively.

The advantage of this fabrication method is that only one side of a platelet needs machining, via wire erosion cuts to form linearly tapered horn sections. Each feed is then closed by the flat wall of the adjacent platelet. The guide's surface finish, left by wire erosion techniques, affects the overall surface impedance along the wall (C. A. Balanis 2012).

Modal techniques are well established and have contributed greatly to the development of many mm and sub mm-wavelength instrument detector array systems (McCarthy 2014). Furthermore, it has been shown in this thesis and elsewhere that modal analysis is in excellent agreement with finite element methods and has significant advantages in terms of computational effort, especially for electrically large systems. Conventionally, treatment of the guide's boundary has been purely PEC, which provides more than adequate representation of low-loss guide structures. Upon analysis of the far-field measurement data obtained from the prototype SAFARI MW-feed, it was apparent that there was significant deviation from the

simulated result, assuming PEC walls. The main observation made was that a significant narrowing of the far-field pattern can be seen, consistent with a loss in power in higher order modes through ohmic dissipation in the guide walls (Olver et al. 2011). The lossy routines introduced in S-TNG are used to help characterise these effects.

5.3.1 Experimental Set-up and Results:

The experimental campaign was performed by Peter Ade and his team at Cardiff University. The preliminary results for the prototype MW-band horn are presented in here. The experimental arrangement, shown in Figure 5-28, was illuminated by a $7 \times 7\ \mathrm{mm}^2$ silicon carbide infrared source (with the appropriate MW-band filters) mounted on an x-y scanning stage allowing for the beam map of the prototype feed to be obtained. A vibrating vane modulator provides a near square modulation to the source aperture field at a frequency of 28 Hz and is fixed by the natural resonance of its torsion bar. A secondary aperture in front of the modulator limits the detector's field of view to the source aperture and thus prevents detection of stray power from the modulator arm. The prototype feed is placed within a cryogenic module, $25\ \mathrm{mm}$ from the cryostat's $30\ \mathrm{mm}$ diameter window, providing a scan range of $\pm 31°$. In order to scan the full range, without any vignetting by the aperture window, the scanner must be placed at least $250\ \mathrm{mm}$ from the cryostat window.

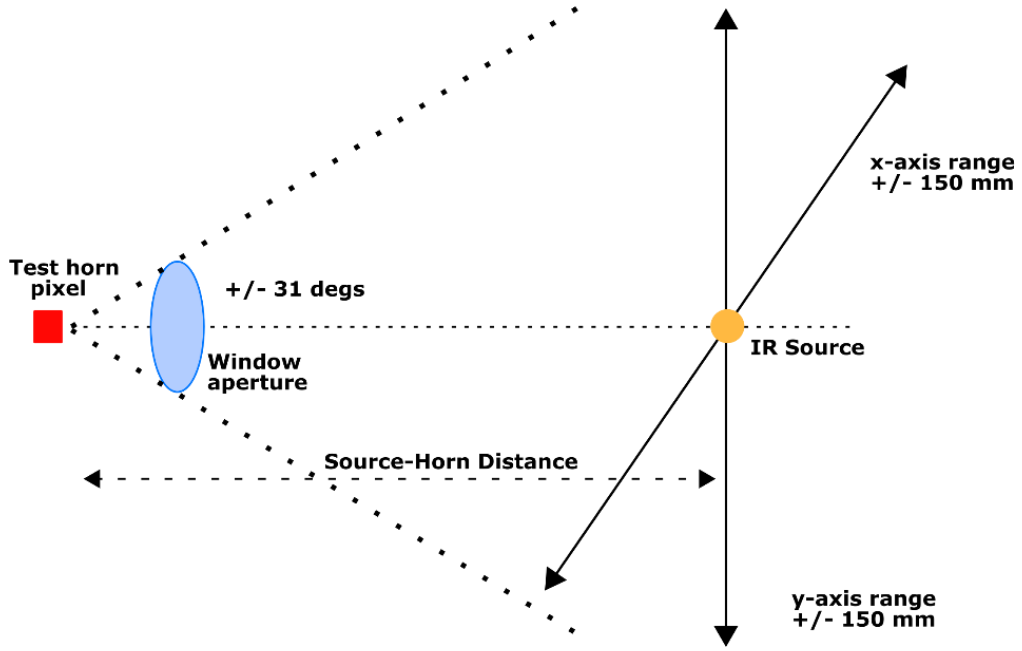

Figure 5-28 Schematic drawing of the experimental arrangement for the M-band horn test

To gather an understanding of the processes that occur within the prototype feed, simulations are performed at a single frequency only (2727.27 GHz – lower bound of the MW-band). Although this is not truly representative of the full characteristics of the feed, it does provide an insight into how the measured results perform against an idealised simulation. The measured beam pattern of the prototype feed is shown in Figure 5-29, alongside simulated results where PEC and smooth copper ($\sigma = 5.8 \times 10^7$ S/m) walls are used. By inspection it can be seen that there is poor agreement between the measured and simulated results in both the horizontal and vertical cuts. The measured results appear quite narrow indicating possibly that much of the power in the higher order modes has been lost, much less that can be explained by losses observed in the smooth copper simulation. The impact of surface impedance resulting from both the finite conductivity and surface roughness must be considered.

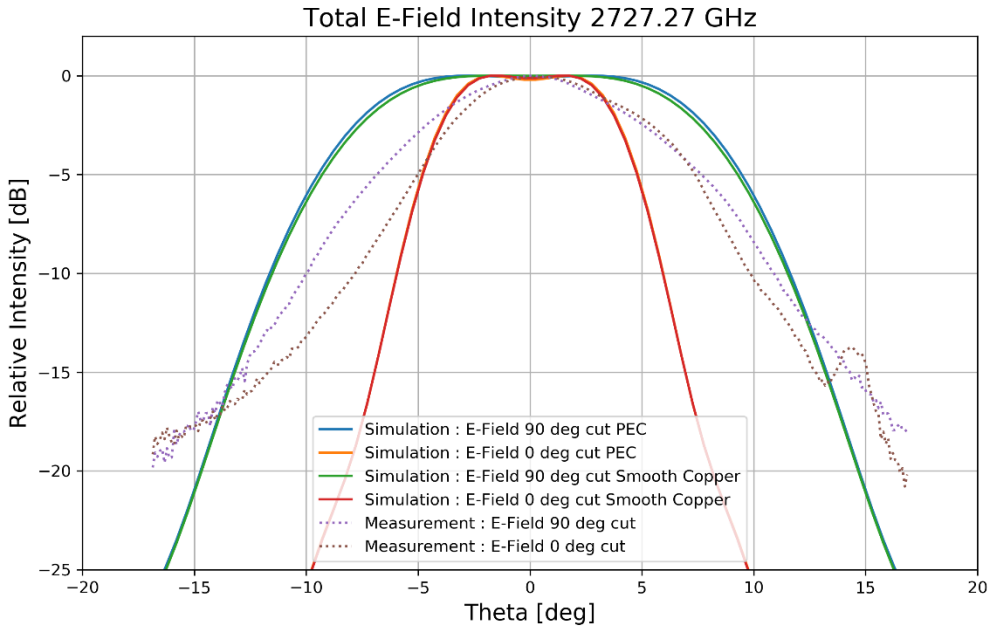

Figure 5-29 Simulation results for PEC and smooth non-PEC cases plotted with measurement data of the total electric field from Cardiff measurement campaign

5.3.2 Accounting for Losses in the SAFARI M-band horn

In Chapter 3, treatment of non-ideal guide's bounding walls gave rise to a modification of the boundary conditions. The tangential electric field along the boundary was shown to be no longer zero, instead $\boldsymbol{E}_{1t} \approx Z_s(\omega)(\hat{\boldsymbol{n}} \times \boldsymbol{H}_2)$. Furthermore, the coupling mechanism introduced due to interfering currents along the waveguide walls were discussed and justification that the PEC modeset provided an adequate representation of the fields was given. It was shown that for non-zero surface impedance, ohmic dissipation of power through the conducting walls occurs. These ohmic losses are expected to manifest themselves more significantly in higher

order modes. The rational being that their modal fields are distributed to a greater extent along the boundary, thus increasing the potential for power dissipation.

As shown in Figure 5-30, the field distributions of the cylindrical guide modes TE_{11} (fundamental mode) and TE_{31} (higher order mode) are clearly very different. The TE_{11} mode has the majority of its field localised in the centre of the structure, whereas the TE_{31} mode is present more towards the boundary.

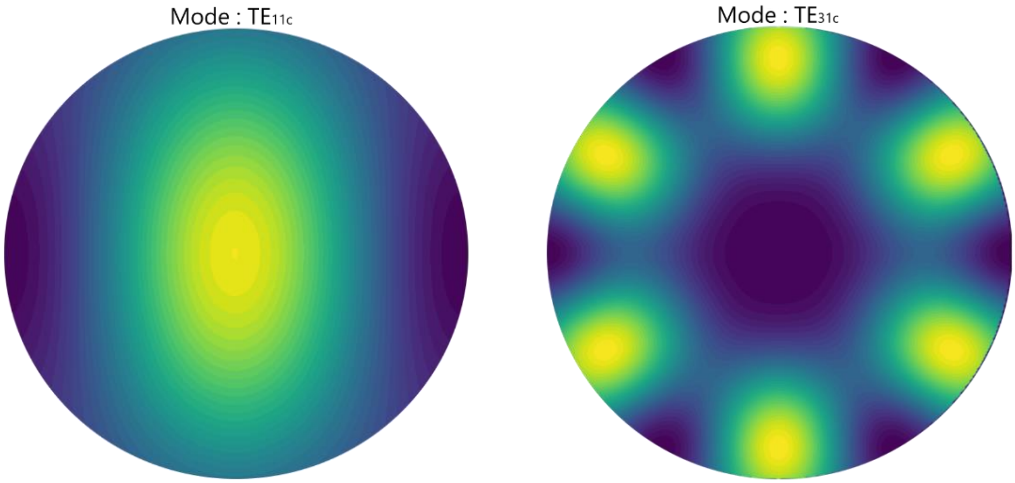

Figure 5-30 Modal field distributions for a) TE_{11} mode b) TE_{31} mode

This effect can be investigated further by modelling an over-moded cylindrical guide section where finite wall conductivity is considered. By varying the material conductivity, the effective surface impedance on the bounding walls can be controlled. The level of loss experienced by each mode is given by the ratio of the modes input and output powers i.e. $P_{out}: P_{in}$. Here, a uniform test guide structure ($r = 1.4$ mm, $L = 10$ mm) is modelled using S-TNG at $f = 150$ GHz for $\sigma = [1.0 \times 10^4, 1.0 \times 10^8]$ S/m.

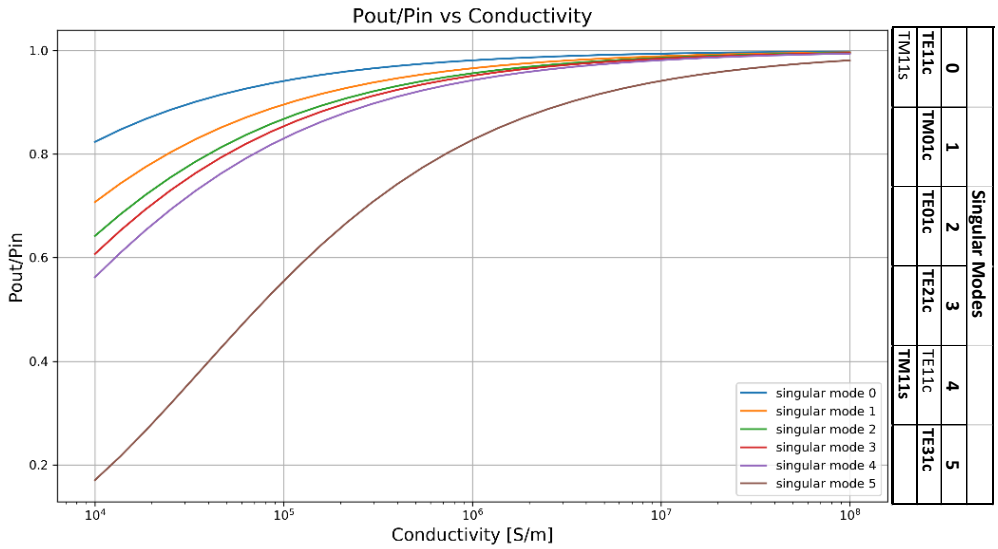

Figure 5-31 Plot of the propagation losses for singular modes considered in a uniform test guide structure $r = 1.4\ mm, L = 10\ mm$

As observed in Figure 5-31, there are losses associated with all modes propagating in the structure. However, the losses are more pronounced on the higher order modes (TE_{31}) compared to the fundamental mode (TE_{11}) as there is a dramatic decrease in the ratio of P_{out}: P_{in} as the impedance grows. The variation of surface impedance with roughness is shown in Figure 5-32, using the conductivity values in Figure 5-31 as upper and lower bounds.

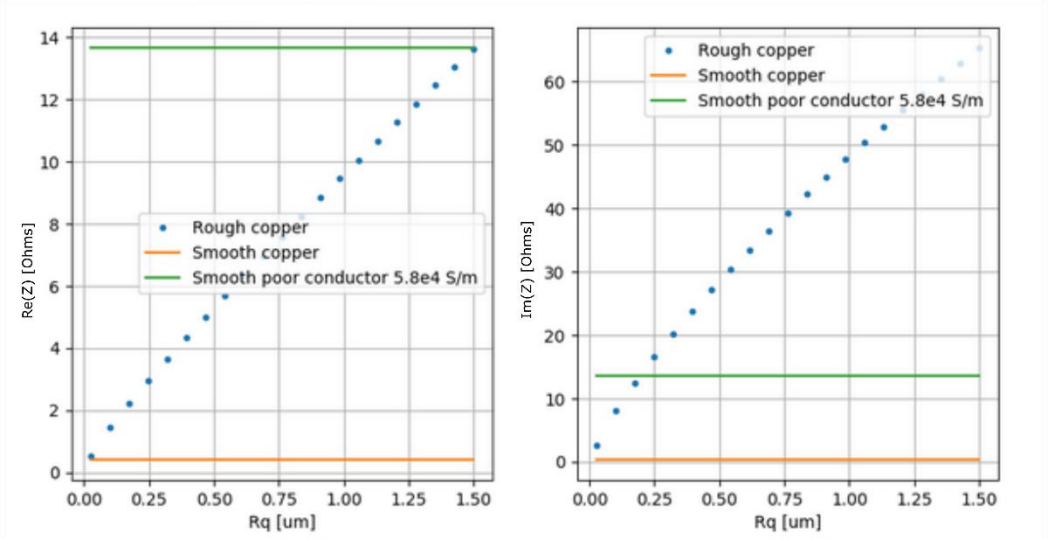

Figure 5-32 Effective wall impedance for varying values of roughness of copper material at 2727.27 GHz

For guide aperture dimensions of $120 \times 120\ \mu m^2$ surface imperfections of $0.1\% < R_q < 1.0\%$, do not seem unreasonable. Here R_q gives the rms-roughness of the surface. Simulations of the prototype SAFARI feed are repeated for copper like walls ($\sigma = 5.8 \times 10^7$ S/m) with surface roughness values within the range $R_q \approx [0.1, 1.0]$ μm. In each case, the simulated far-field patterns are compared against the measurement results. In Figure 5-33, convergence is observed for surface parameters $\sigma = 5.8 \times 10^7 \mathrm{S/m}, R_q = 0.25$ μm.

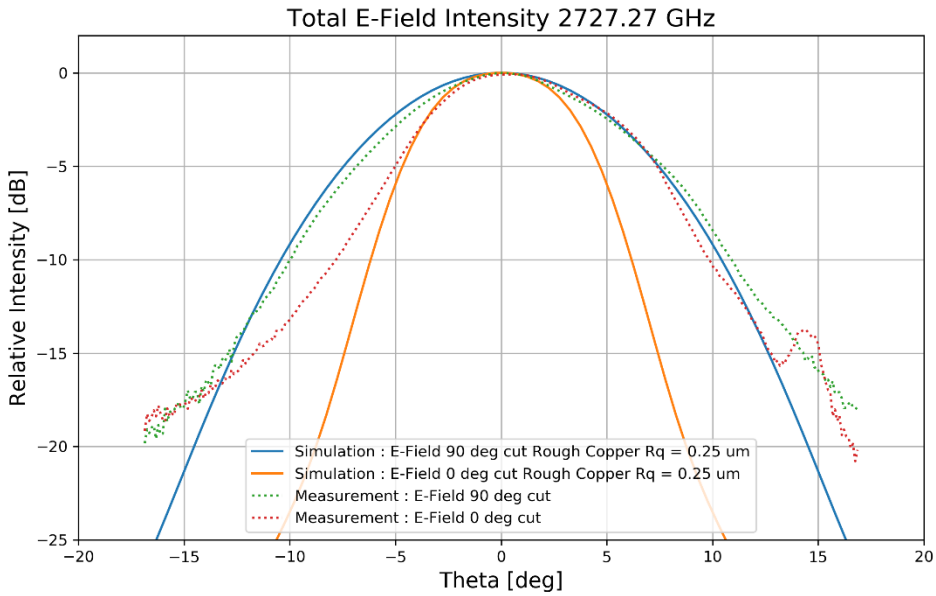

Figure 5-33 Simulation 0.25 μm roughness results plotted with measurement data of the total electric field from Cardiff measurement

Here, much improved agreement is observed between the simulated and measured results, the width of the vertical cuts match very well, and the horizontal cuts match well on one side only. Away from this set of surface parameters the beam was either too wide (indicating much of the higher order mode power had been retained) or too narrow (indicating the impedance is too great causing excessive reduction in higher order mode power). There appears to be an asymmetry in the measured horizontal direction cut, which is more apparent in the measured beam map shown in Figure 5-34(b). As this is not observed in the simulated beam map shown Figure 5-34(a), which may be due to some measurement errors or offsets in the horn geometry which were not considered.

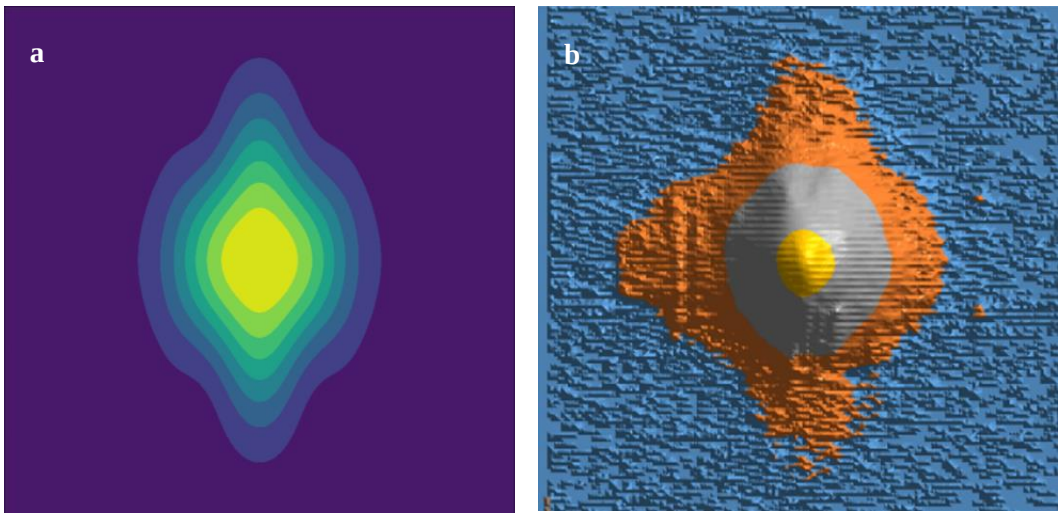

Figure 5-34 Total electric field for a) Rough non-PEC simulation and b) Experimental results

5.3.3 Conclusion

It is clear that the effects of surface roughness particularly at higher frequencies i.e. >1 THz can have significant impact on the performance of guide structures. For the prototype SAFARI feed, the majority of the contribution from the higher order modes power is lost resulting in a much narrower beam than expected. The loss mechanism investigated indicates that there is substantial roughness left by the wire erosion manufacture process. Clearly, the manufacturing techniques used must be refined if these structures are to perform as expected.

5.4 Redesign of SAFARI's Focal Plane

Following the departure of a key member of the SPICA consortium, the focal plane of the SAFARI instrument had to undergo a substantial redesign. This departure meant one of the four grating modules (GMs) had been lost, as such the desired spectral range had to be covered by the remaining GMs. SAFARI's (SAFARI 4.0) spectral range is now covered by three separate GMs with the default spectral resolution of R∼300 and cover short, medium, and long wavelength regions of the desired spectral range (SW $34-63.6$ μm, MW $61.8-115.6$ μm, LW $112.2-210$ μm). The instrument now consists of 3 detector sub-arrays per GM-band with each sub-array consisting of 5×48 pixels (144 spectral pixels and 5 spatial pixels per GM) giving a total pixel count of 2160 pixels. Each GM has 6 LC (inductor-capacitor) chips with 2 LC chips per sub-array. Finally, there are 18 readout channels, 6 per band, 2 per sub-array, giving MUX factor of 120 (total pixel count ÷ number of readout channels).

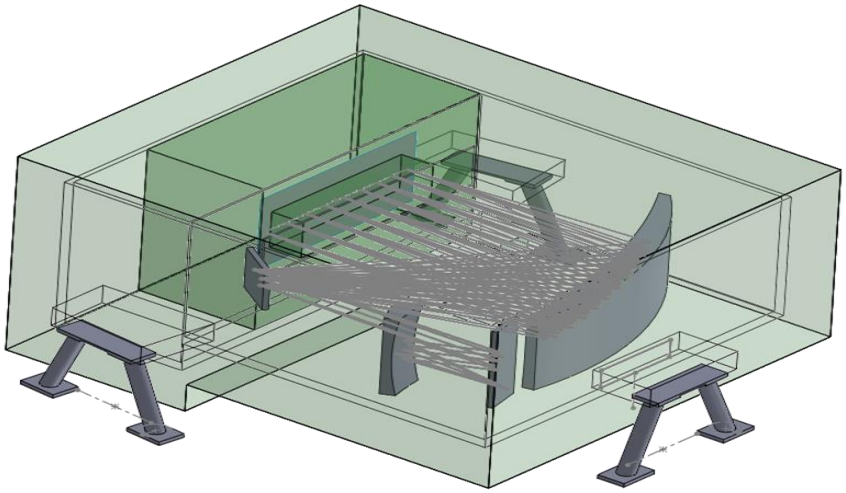

Figure 5-35 CAD drawing of the SAFARI-SW grating module

The SW-band ($34-63.6$ μm) of the SAFARI 4.0 design is of particular interest since this is a key requirement for the project. The band is divided into 3 logarithmically spaced sub-arrays SW [1-3], with apertures sizes given by the spectral and spatial direction values ($s_i \times p_i$) respectively. The horn blocks will be micro-machined as straight walled parts and must meet the desired performance levels if the project is to proceed. The SW-1 sub-array corresponds to the smallest and most challenging horn to design for the instrument ($s_1 = 0.899$ mm, $p_1 = 0.7$ mm). In this section the following questions will be investigated:

- What effect does surface roughness have on the efficiency of the feed?
- How does the length of the feed affect efficiency when non-PEC walls are considered?

- How does the throat-aperture geometry dictate the performance of the device?

The SW-1 feed is characterised at the central frequency of the band $6143.28\,\mathrm{GHz}$ and by examining the effects of each of these free parameters (aperture size and feed length) the design and tolerance levels required can be finalised. The feed length and aperture size are important parameters to tie-down as the instrument's mass and performance will ultimately be limited by these factors. The following test cases are considered to probe these questions.

Table 5-3 Test cases for SAFARI SW feed parameter investigation

Test.	**Description**
IA	Investigate effects of surface roughness on the SW-1 feed using the PEC result as a benchmark. Roughness values considered $R_q = [0.1,\ 0.3,\ 1.0\ \mu\mathrm{m}]$, which represent the best to worst case tolerance values for the machining equipment.
IB	Using the roughness values considered $R_q = [0.1,\ 0.3,\ 1.0\ \mu\mathrm{m}]$, investigate how the performance of three horn lengths for the SW-1 feed (short – 3.0 mm, medium – 5.0 mm. long – 7.0 mm) are affected by roughness.
II	In IA-B, a throat aperture of $100 \times 100\ \mu\mathrm{m}^2$ was used. The test cases are now repeated for $120 \times 120\ \mu\mathrm{m}^2$, $150 \times 150\ \mu\mathrm{m}^2$ and $100 \times 150\ \mu\mathrm{m}^2$ to see the effect of allowing more modes to propagate has on the feed's performance

5.4.1 IA – Investigation of Surface Roughness

The rms-roughness values considered are $R_q = [0.1,\ 0.3,\ 1.0\ \mu m]$ which give the upper and lower tolerance values for the machining equipment. In Figure 5-36, the impedance of the walls is shown for smooth and rough copper for 6143.28 GHz.

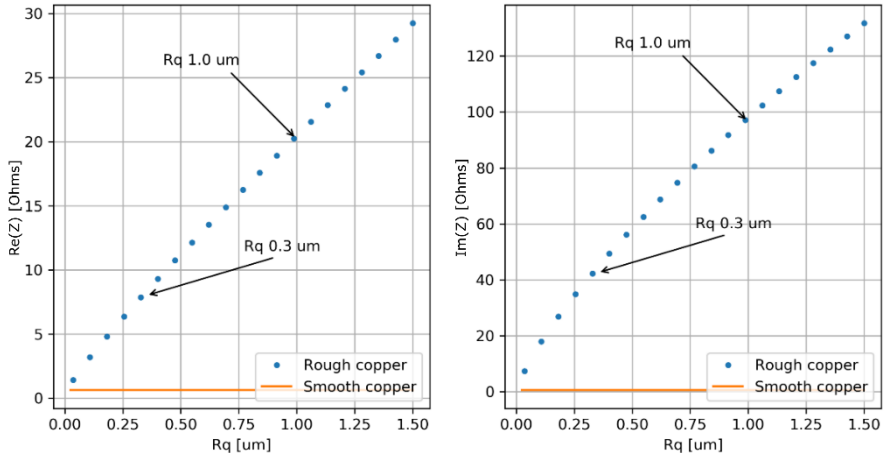

Figure 5-36 Shows the variation of impedance with increasing roughness at 6143.28 GHz

In chapter 3 the justification that PEC waveguide modes provide an adequate basis is presented. It was shown that for a good conductor the perturbation of the magnetic field near the wall is negligible and may be used to avoid explicit evaluation of the electric field along the boundary. It is apparent that there is a rapid increase in surface impedance for increasing frequency when relatively large surface roughness is considered. This can be observed by comparing the surface impedance plots at M-band and S-band frequencies shown in Figure 5-32 and Figure 5-36. At S-band frequencies it can no longer be assumed for roughness values which exceed 0.3 µm that the good conductor requirement holds true. An example the analysis failing for 1.0 µm surface roughness is shown in section 5.4.4.

To investigate the effect of surface roughness on the feed's performance the shortest ($L = 3$ mm) of the proposed SAFARI SW-1 feeds is considered, see Figure 5-37. Simulations are performed at the S-band's central frequency (6143.28 GHz) with 24 of 180 modes considered propagating in the horn's throat aperture ($100 \times 100\ \mu m^2$). The structure is modelled with both PEC and rough copper walls, with the PEC simulation providing a benchmark result.

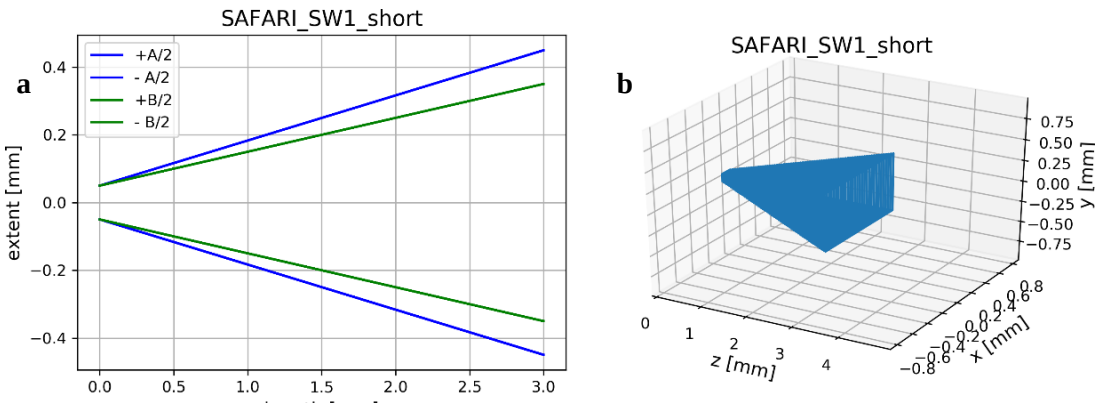

Figure 5-37 a) Profile of the prototype SW-1 horn, b) 3D view of prototype SW-1 horn

From Figure 5-38, it can be seen that for increasing surface roughness the peak electric field intensity decreases from the benchmark PEC result. For roughness values of 0.1 µm and 0.3 µm there is a −1.6 dB and −4.2 dB loss observed with respect to the baseline PEC result. Higher order modes, which in general have their field distributions more towards the guide boundaries, experience greater loss along the non-PEC boundary. It is clear from the narrowing of the 0.3 µm roughness cut that much more of the higher order mode power has been lost. However, the 0.1 µm roughness cut has retained much of the beam width of the PEC result.

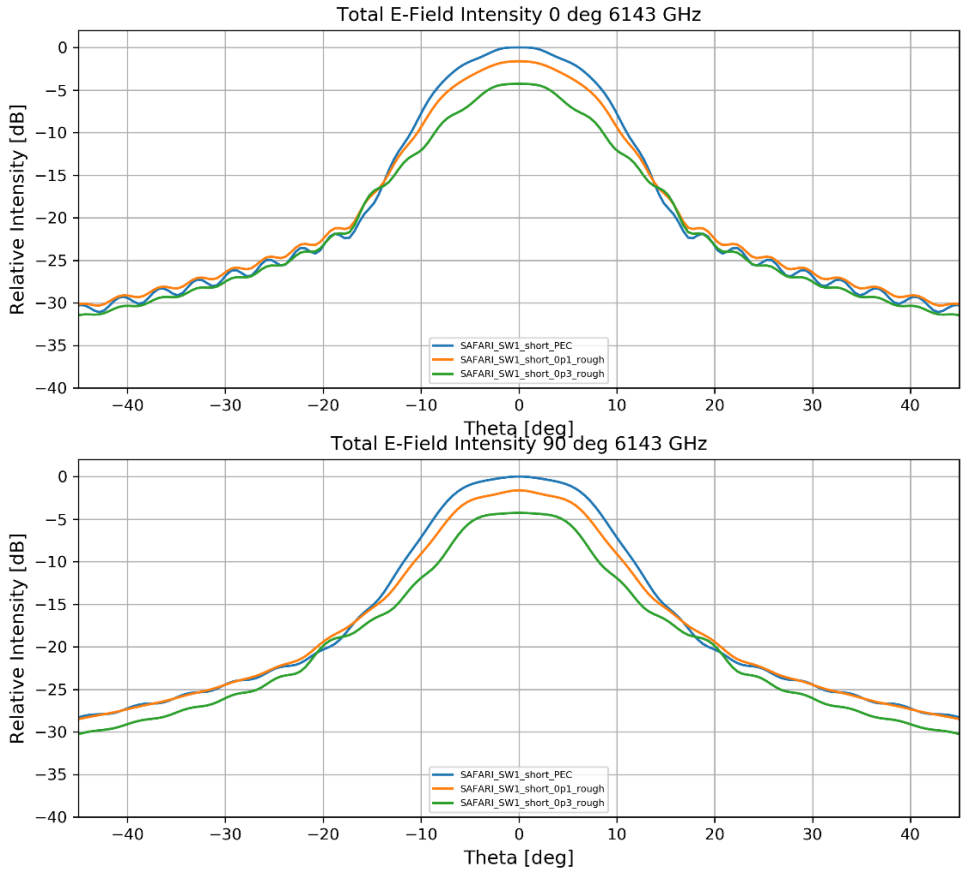

Figure 5-38 SAFARI SW-1 Short design far-field pattern taken at 6143 GHz for varying roughness values

5.4.2 IB – Investigation of Length with Surface Roughness

The simulation performed in the previous section are repeated for the medium ($L = 5$ mm) and long ($L = 7$ mm) feed designs of the SAFARI S-band. Investigating the medium and long horn designs, a similar pattern emerges with respect to the surface roughness. In general, the 0.1 μm roughness cuts are reasonable, with a loss of -2.4 dB for the medium feed and -3.1 dB for long feed. Moreover, in both feeds much of the PEC cuts shape is retained. However, for increasing roughness the performance of the feeds degrades rapidly.

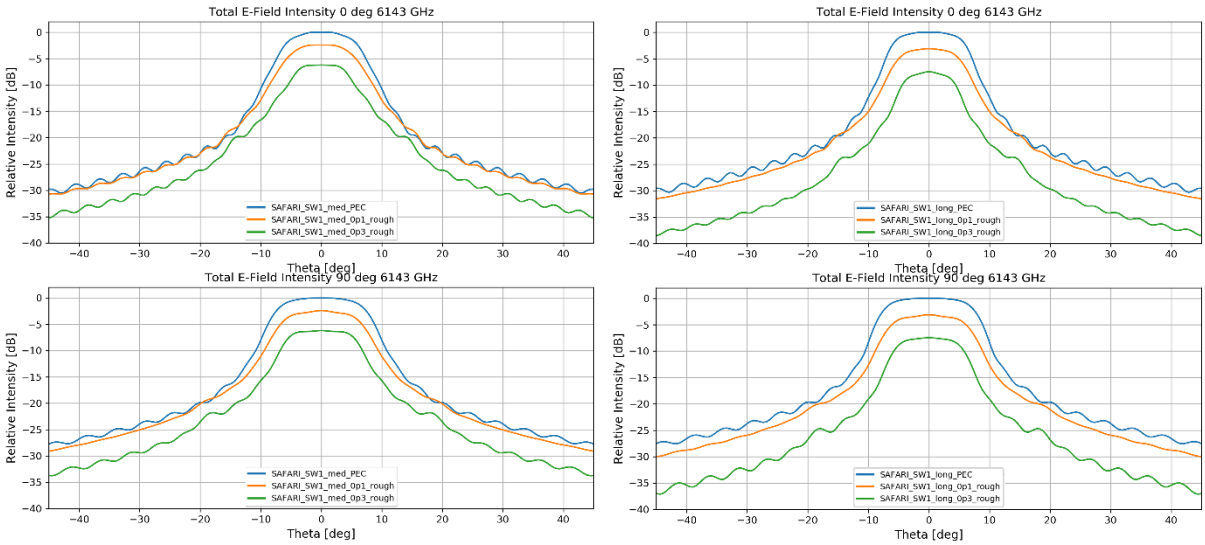

Figure 5-39 SAFARI SW-1 Medium and Long designs' far-field pattern taken at 6143 GHz for varying roughness values.

By inspecting the far-field plots of the three horn designs shown some remarks can be made:

A. It is clear that the length of the feed negatively impacts the throughput power with respect to the PEC result when rough walls are considered. Considering the 0.3 μm cuts, the short feeds peak intensity lies at -4.2 dB (see Figure 5-39) compared to the long feeds peak intensity which lies at -7.5 dB (see Figure 5-39).
B. Furthermore, by inspecting the shape of the rough beams for each length a number of comments can be made. For surface roughnesses of Rq $=$ 0.3 μm there is a substantial change in beam shape from the benchmark PEC results. Whereas for surface roughness's of Rq $=$ 0.1 μm this variation in shape is subtle. Here, the multimoded features observed in the PEC cuts are retained, meaning that the higher order modes were not as significantly affected by this type of surface. In terms of FWHM these parameters are summarised in Table 5-4.

Table 5-4 Summary of the key beam parameters for varying feed length and surface type

	3 mm			5 mm			7 mm		
Surface	**Peak I [dB]**	**FWHM 0°cut**	**FWHM 90°cut**	**Peak I [dB]**	**FWHM 0°cut**	**FWHM 90°cut**	**Peak I [dB]**	**FWHM 0°cut**	**FWHM 90°cut**
PEC	0	13.6	14.8	0	12.7	15.6	0	12.7	15.9
0.1 µm	-1.6	13.4	13.8	-2.4	12.0	14.0	-3.1	11.4	13.9
0.3 µm	-4.2	11.3	12.9	-6.2	10.1	12.8	-7.5	9.3	12.1

The point made in remark A can be investigated more thoroughly by looking at the singular modes efficiencies. In Figure 5-40, it can be seen that for increasing length there is a drop in all singular modes efficiencies. Furthermore, this can all be seen when inspecting the far-fields of the three different horn lengths with a roughness of $R_q = 0.3$ µm considered.

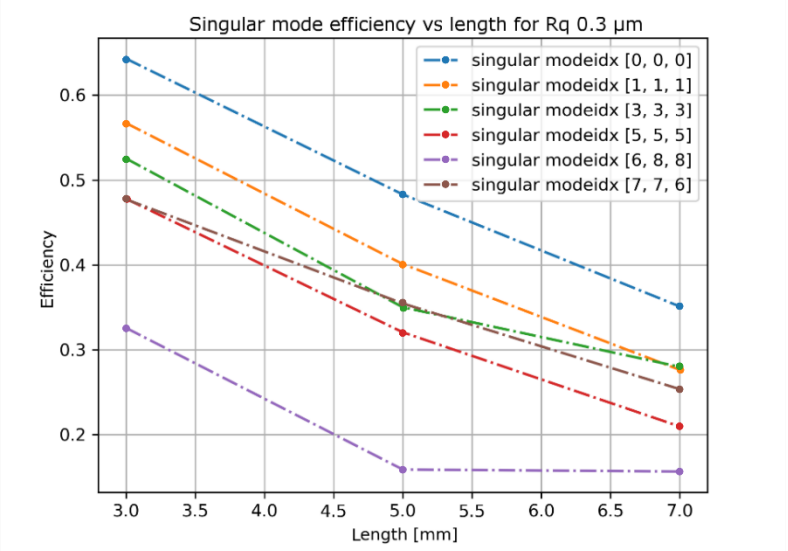

Figure 5-40 Plot of the singular modes efficiencies with increasing length of a lossy structure

It is important to observe how the beam cuts evolve with increasing feed length. Inspecting the PEC results for each horn length it is clear that there is a narrowing of the beam, particularly in the spectral direction (0 degree cut). The evolution of the beam when minimal surface roughness (0.1 µm) present is also examined, see Figure 5-41. Along with the narrowing of the beam, a reduction in peak on-axis intensity is observed and with a smoothing of the beam sidelobe, again due to the degradation of the higher order modes.

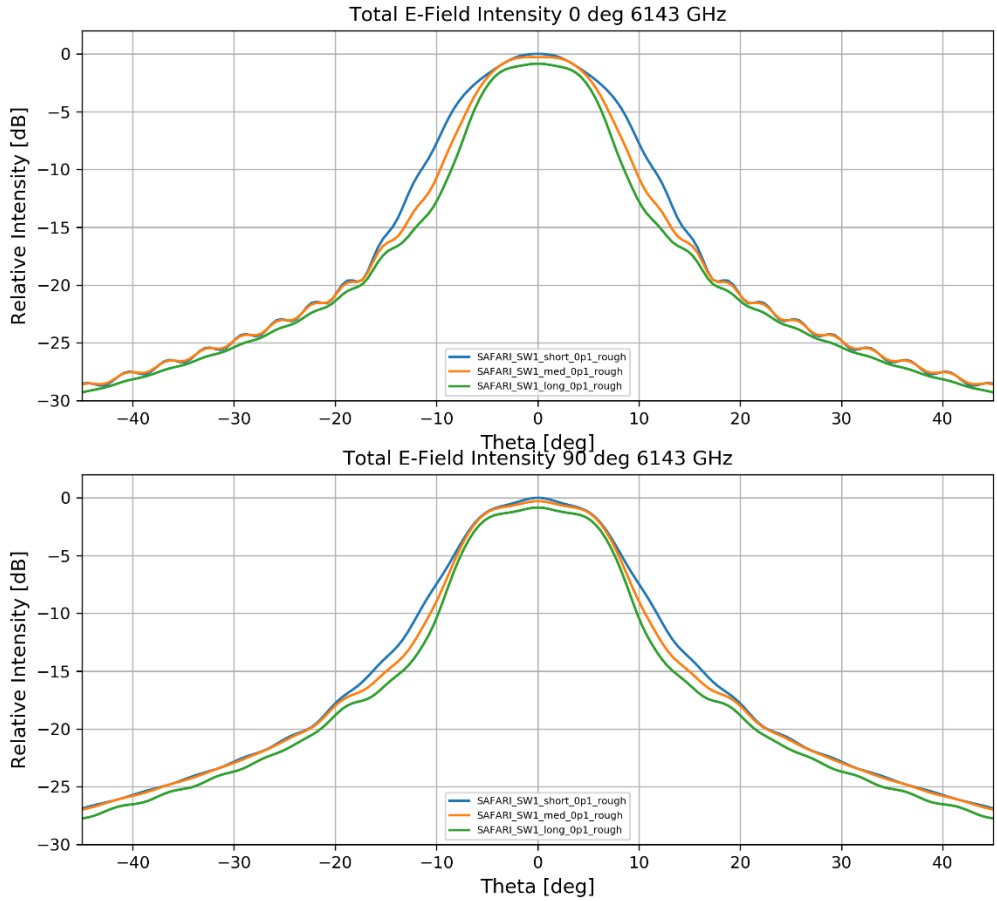

Figure 5-41 SAFARI SW-1 feed designs far-field pattern taken at 6143 GHz for $R_q = 0.1\ \mu m$

Because of this, the SAFARI instrument is likely to favour the medium length feed design. This feed design provides a compromise in terms of on-axis beam intensity, beam definition and weight constraints imposed on the instrument.

5.4.3 II – Investigation of the throat aperture dimensions

In this section the throat apertures of the three horn designs are expanded to increase throughput in an attempt to moderate the losses in the guide walls. The new aperture dimensions considered are $120 \times 120\ \mu m^2$, $100 \times 150\ \mu m^2$ and $150 \times 150\ \mu m^2$, which sees an increase in the number of the modes propagating in the $100 \times 100\ \mu m^2$ from 24 modes to at most 60 modes. The mode numbers for each throat aperture geometry are as follows:

- $120 \times 120\ \mu m^2$ - 34 modes propagating at 6143.28 GHz
- $100 \times 150\ \mu m^2$ - 40 modes propagating at 6143.28 GHz
- $150 \times 150\ \mu m^2$ - 60 modes propagating at 6143.28 GHz

The short feed design is again initially considered to gauge the effect of varying the aperture size. In Figure 5-42, a plot of the peak intensities for all the apertures with PEC walls considered is shown. Clearly, there is an increase in peak intensity for the larger aperture where more modes are propagating. This increase is of the order of ~0.7 dB from the $100 \times 100\ \mu m^2$ aperture to $150 \times 150\ \mu m^2$ peak. Moreover, the larger apertures see a widening and flattening of the beam compared to the original design. This is expected due to the inclusion of a greater number of higher order modes. The rectangular arrangement ($100 \times 150\ \mu m^2$) displays this trend in the spectral direction (0 degree cut) only.

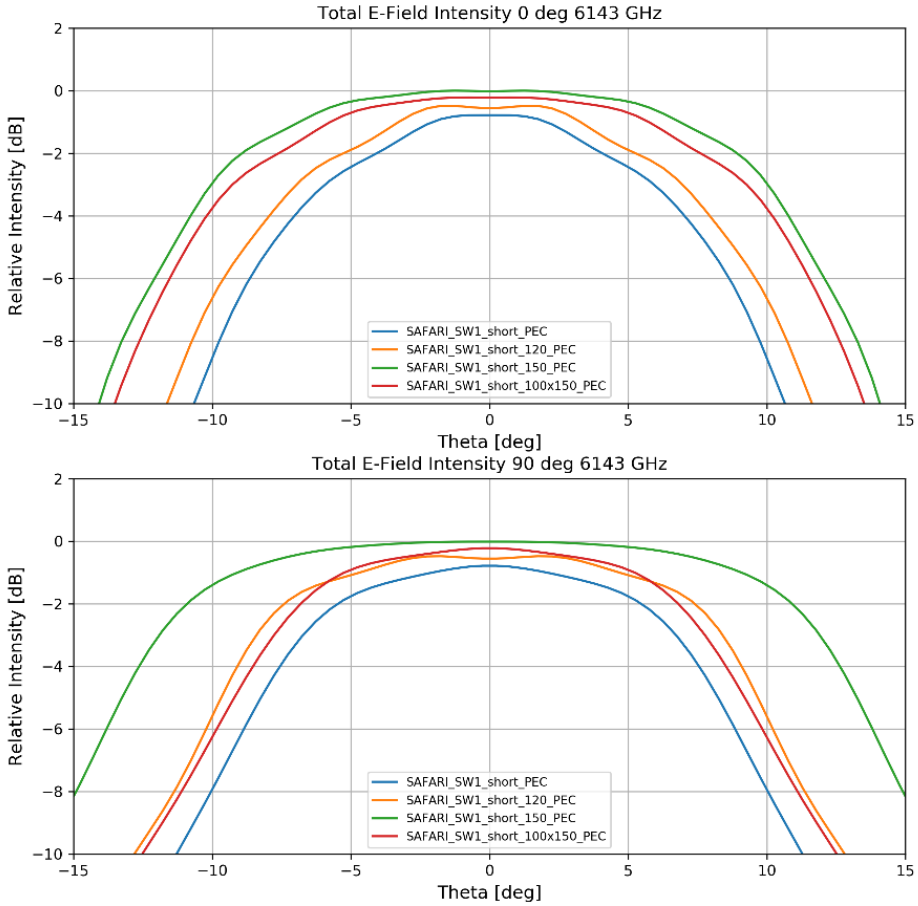

Figure 5-42 Far-field cuts of the different apertures with PEC walls considered

The PEC result of the short feed design with the $100 \times 100\ \mu m^2$ aperture is used as a baseline. This benchmark is compared to the results of the 0.1 µm and 0.3 µm roughness cuts for the different aperture sizes. In Figure 5-43, by observing the rough surface results it can be seen that there is an increase in peak on-axis intensity for increasing aperture size. With a maximum increase of 1 dB for the 0.1 µm surface and 1.7 dB for the 0.3 µm surface, see Table 5-5 for full results. Thus, for larger aperture sizes the peak intensity begins to approach that of the baseline PEC result of the $100 \times 100\ \mu m^2$ aperture. This trend continues to be observed for the medium and long feed designs.

Table 5-5 Summary of the peak intensities for each of the different aperture geometries for the short feed design.

	$100 \times 100\ \mu m^2$	$120 \times 120\ \mu m^2$	$100 \times 150\ \mu m^2$	$150 \times 150\ \mu m^2$
Surface	**Peak I [dB]**	**Peak I [dB]**	**Peak I [dB]**	**Peak I [dB]**
PEC	0	-	-	-
0.1 μm	−1.6	−1.1	−0.9	−0.6
0.3 μm	−4.2	−3.25	−3.0	−2.5

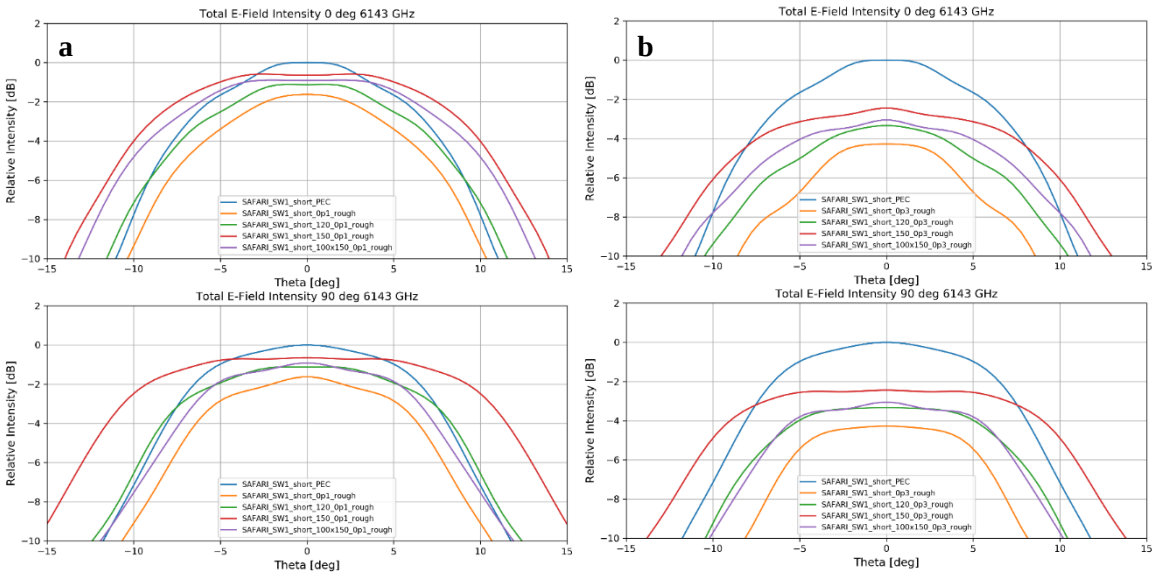

Figure 5-43 Far-field cuts of the different apertures for a) $Rq = 0.1\ \mu m$ and b) $Rq = 0.3\ \mu m$

It is clear that by increasing the aperture size and allowing more modes to propagate the throughput of the SAFARI SW-1 feed increases. However, for larger exit apertures comes a deterioration in the detectors' response time – larger apertures require larger absorbers leading to slower devices. The performance of the $100 \times 150\ \mu m^2$ rectangular aperture also sees an improvement over the $100 \times 100\ \mu m^2$ aperture. This design is considered as the SAFARI grating has high efficiency in one polarisation direction. The beam incident on the SAFARI detector plane arrives from a grating spectrometer and as such is ~80% polarised. Furthermore, the instrument team have further capitalised on that by using a polarising Fourier Transform Spectrometer (FTS) as a high-resolution option which is selected by the use of polarising elements in the optical chain. As such, in high resolution mode the input beam at the detector would be 100% polarised. This arrangement allows the absorber shape to have a reduced spectral footprint while a larger spatial extent enables better coupling to point like sources at no expense to detector time. This single polarisation implementation simplifies instrument design and allow for reduction in total system mass.

5.4.4 Limitations of the model

The original set of test cases shown in Table 5-3 included investigation of surface roughness up to 1.0 µm. However, at S-band frequencies the resulting surface impedance exceeds the good conductor limitation of this model. To illustrate this the long SAFARI-SW1 feed design with the largest aperture is modelled and the results are shown in Figure 5-44.

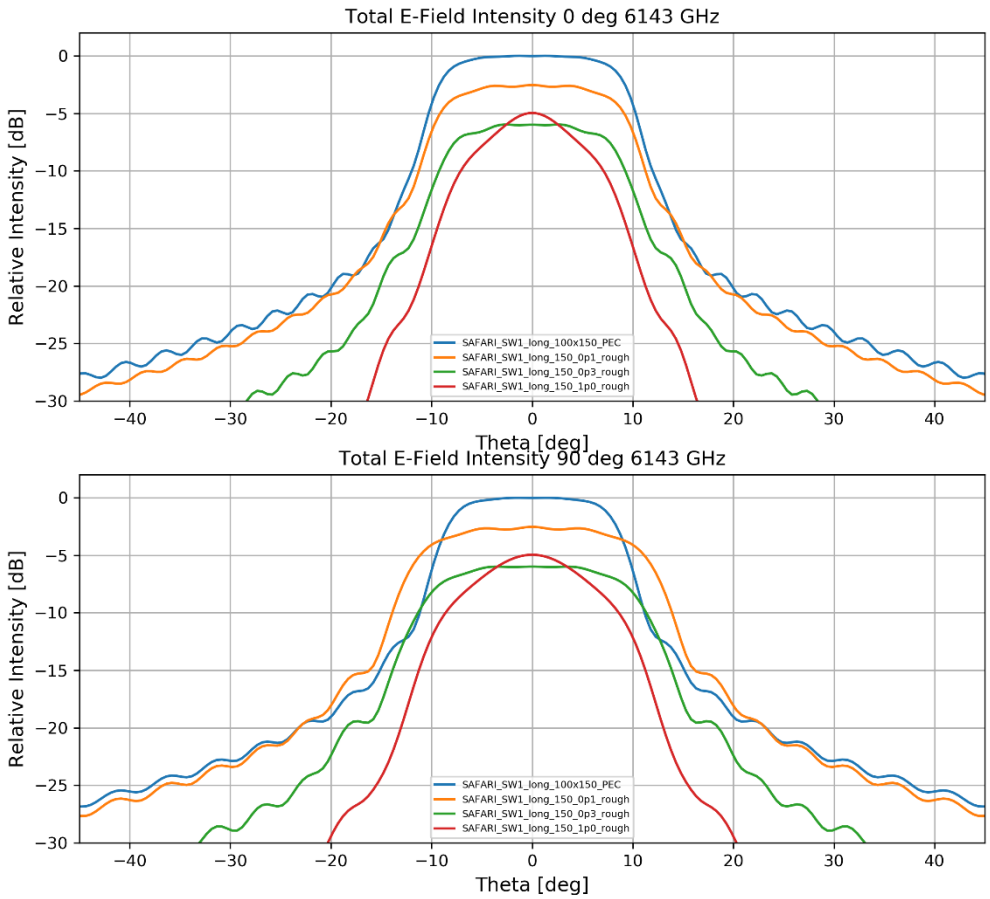

Figure 5-44 SAFARI SW-1 Long design aperture 150×150 *µm, far-field pattern taken at 6143 GHz for varying roughness values. Included to show the breakdown in simulation stability for very poor surfaces.*

The result shown here for the 1.0 µm surface roughness appears possibly non-physical, as it exceeds the peak on-axis intensity of the 0.3 µm result. This result is typical of those generated for this extreme level of roughness at SAFARI's S-band. By considering a section of the throat aperture of the original SAFARI feed ($100 \times 100\ \mu m^2, L = 0.2$ mm) the stability of the S-TNG mode matching ability for increasing poor surfaces can be investigated. Complementary simulations are performed in CST to benchmark the S-TNG results. In this test case the section is modelled with rough copper walls $R_q = [0.1, 0.3, 0.5, 1.0]$ µm.

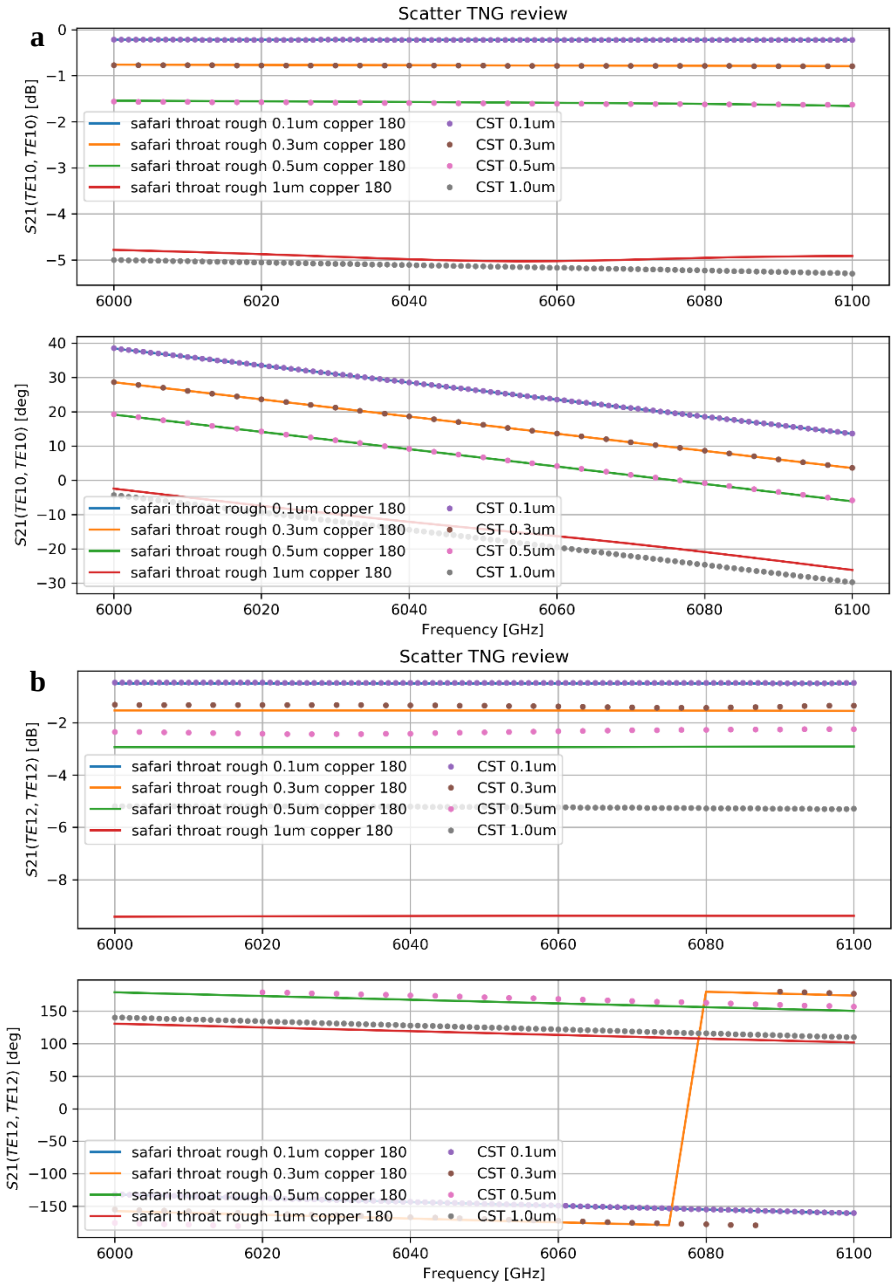

Figure 5-45 Transmission scattering coefficient through the SAFARI throat section for rough copper walls $R_q = [0.1, 0.3, 0.5, 1.0]$ μm a) TE_{10} mode b) TE_{12} mode

In Figure 5-45, results from S-TNG and CST are shown for two different modes TE_{10} and TE_{12}. Firstly, inspecting the results from the fundamental mode, Figure 5-45a, good agreement between the S-TNG and CST is observed for all surface roughnesses except for $R_q = 1.0$ µm. There is an obvious deviation from the corresponding CST result which indicates a failure of the model. Next, the results from the simulation of the higher order TE_{12}, Figure 5-45b, mode are inspected. In this case, one would expect the limitations of the model to be revealed more obviously since the higher order mode's field is present more towards the boundary. This is

observed in the complete failure of the S-TNG model for $R_q = 1.0$ μm and non-negligible deviations for roughness's 0.3 μm and 0.5 μm.

The example of the modal fields along the boundary from Chapter 3 is revisited. In this case the simulation is performed at S-band frequencies for an appropriate geometry. The electric and magnetic field components along the wall are shown for both PEC and rough copper with $R_q = [0.1, 0.3, 1.0]$ μm. As in Chapter 3 these results are obtained from CST.

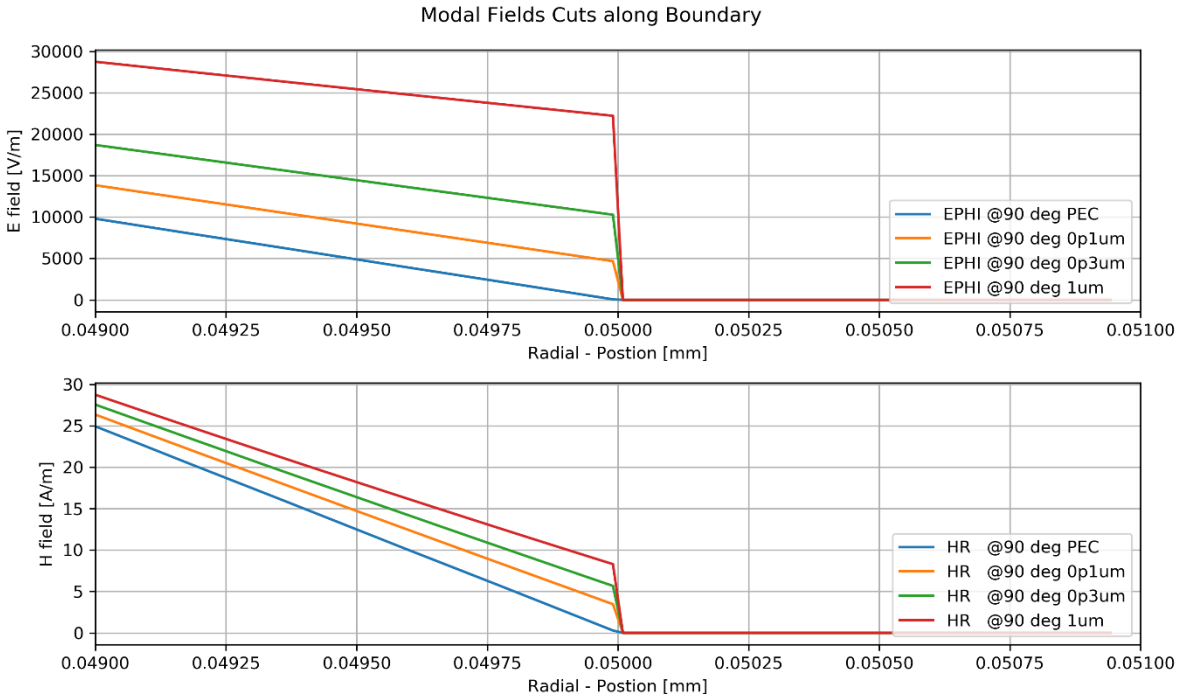

Figure 5-46 Electric and magnetic field components along the boundary for PEC and rough copper ($\sigma = 5.8 \times 10^7\ S/m$, $R_q = [0.1, 0.3, 1.0]\ \mu m$) walls generated from CST

The justification used in Chapter 3 is that for a good conductor the perturbation of the magnetic field near the wall is negligible and may be used to avoid explicit evaluation of the electric field along the boundary. However, this is quite arbitrary. An effort is made to tighten this assumption and give an estimate for an upper valid limit for the non-PEC mode matching method.

One potential mechanism to impose an upper limit is to quantify the deviation of the electric field along the wall compared to the known PEC result. The CST simulation results from Figure 5-46 are used to determine the electric field magnitude along the wall as a percentage of the on-axis maximum electric field ($\approx 3.2 \times 10^5$ V/m). With knowledge that the S-TNG result begins to breakdown beyond $R_q = 0.3$ μm the percentage deviation along the walls should be limited to ~3% of the on-axis electric field.

Table 5-6 Percentage of on-axis electric field present along the guide wall

	PEC	0.1 µm	0.3 µm	1.0 µm
$\Delta E_{wall}\%$	0	1.5%	3.2%	6.5%

Moreover, by no longer enforcing PEC modes at waveguide ports in the CST simulation the true field patterns within lossy guides can be inspected. Using these results the assumption that PEC guide modes provide an adequate basis can be gauged for increasing surface impedance with the fundamental TE_{11} mode shown as an example. As seen in Figure 5-47, the field distributions for the 0.1 µm and 0.3 µm are approximated quite well by the PEC field. However, for roughness values beyond this the field distribution of the fundamental TE_{11} mode becomes unrecognisable. Clearly, PEC guide mode basis approximation where excessive roughness is present is insufficient.

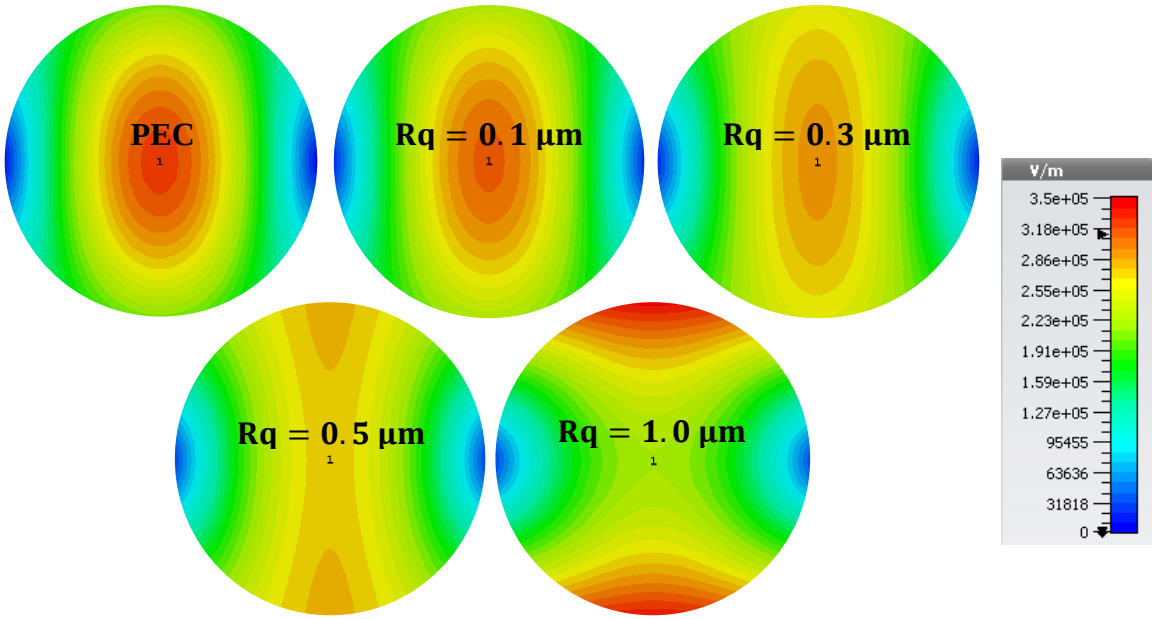

Figure 5-47 Field distribution of the TE_{11} waveguide mode for increasing surface roughness.

5.5 Summary

This chapter covered a series of investigations which contributed to the development of the SAFARI instrument. Many of the techniques which were developed in earlier charters are employed to aid in the analysis of the instrument components of interest. In sections 5.1 and 5.2, some of the proposed focal plane arrangements of the instrument were studied. The Offner relay arrangement, combined with the beam steering mirror, was simulated to explain some of disagreement between measurement and theory. A potential source of these irregularities was identified as the over rotation of the beam steering mirror which resulted in an overlap with a masked region of the primary mirror. Moreover, an off-axis arrangement was considered to allow for a compact and optically efficient testbed. However, it was found that this arrangement offered no performance advantage when coupled to the SAFARI pixel.

The developed S-TNG software was also applied in the design and analysis of the prototype antenna designs for SAFARI short and medium wavelength bands. In the analysis of the M-band SAFARI horn it was evident that ideal treatment of the boundary walls did not accurately model the experimental results. The measured beam profile was much narrower than the idealised simulation. This narrowing was indicative of power loss in the higher order modes and these losses could be accounted for by including non-PEC boundary walls in the simulations. Finally, the S-TNG software was employed to study the effects of varying lengths, aperture sizes and surface roughness values in the design of the shortest of the SAFARI prototype horn designs. The results from these simulations were used to guide the manufacturing of the optimal horn design with aperture size and feed length selected to moderate the throughput and beam profile of the horn when non-PEC surfaces were considered.

Conclusions

In this thesis, significant emphasis is placed on the further development and reformulation of traditional mode matching routines. This work was motivated by ESA contracted work to develop modelling software for the design and analysis of sensitive pixel devices for future millimetre and sub-millimetre instruments. Modelling such structures in commercial software solutions, which rely on finite element methods, often becomes impractical due to the large volumetric size relative to the wavelength. The mode matching method offers an alternative, more computationally efficient method while maintaining good accuracy. This development cycle has also seen the extension of the methods to modelling of non-PEC walls, allowing for a more comprehensive model of pixels where ohmic and surface roughness losses may be important (i.e. high frequency and multi moded cases). Application of these routines has proved particularly useful to the design and analysis of the prototype feed structures of the SAFARI (SPICA Far-Infrared Instrument) instrument.

The introductory thesis chapter is used to provide context to the chapters that follow, as often the modelling and software development focus is far removed from the overall aim. Here, a general overview of terahertz astronomy field is given with a focus on legacy, the Herschel space observatory, and ongoing experiments at ALMA (Atacama Large Millimetre Array) detailing the observation that can be performed in this portion of the electromagnetic spectrum. These missions also provide a platform to discuss the proposed far-infrared mission SPICA (Space Infrared Telescope for Cosmology and Astrophysics), whose science goals must complement those of ALMA and advance on the legacy of Herschel. The focal plane arrangement of the SAFARI instrument is covered in good detail as much of the developed software presented in this thesis deals explicitly with this region. Detailed analysis of the proposed optical arrangement of the focal plane and of the sensitive pixel designs are presented in later chapters. Furthermore, a review of the state-of-the-art in detection and source technologies is presented, with a focus on many of the superconducting technologies which are emerging.

In Chapter 2 the main focus was on the reformulation of a number of key elements of the mode matching routines. This reformation can be summarised by three key changes. Firstly, the fundamental description of the fields within waveguides was changed to be represented by auxiliary vector potentials. Secondly, the modal normalising method was completely overhauled allowing for a more natural transition between evanescent and propagating states through the mode's cut-off frequency. Now the mode is normalised to a unit power magnitude asymptotically, far from its cut-off frequency, by passing the magnitude of modal power through zero as the frequency passes through the cut-off – improving stability of the numerical representation. Finally, the necessary coupling integrals for the mode matching routines were identified (i.e. the common B, C and D types presented in Chapter 2) and expressed in terms of contour integrals. Furthermore, an interpolation routine was implemented to avoid explicit calculation of the surface integrals where normal evaluation via contour integral definition is not directly possible. This contour integral implementation also allowed for more efficient formulation of the scattering problem between mixed and offset geometries i.e. rectangular to circular, which were previously challenging to model.

The remaining portion of this chapter is focused on the verification of the newly developed mode matching methods and implementing the necessary techniques to allow for modelling of complete waveguide structures. Industry standard software CST Microwave Studio is used to verify the essential correctness and accuracy of the mode matching formulation. In a series of verifying test cases, near perfect agreement was observed between CST and SCATTER-TNG software packages. Agreement to the level of -80 dB was shown in the comparison of the scattering parameters plots. The standard cascading routines that are necessary for building up complete waveguides are introduced and for completeness, routines necessary for the characterisation of radiation properties of feed structures (aperture field calculations, Fourier transforms and singular value decomposition) are discussed and implemented. Using all the methods presented in this chapter typical aperture antenna designs are described, modelled and evaluated.

The material presented in Chapter 3 represents a significant advancement in the modelling capabilities of the mode matching method. Most important is the more rigorous treatment of the boundary walls; by including large yet finite conductivity in the description of the mode-matching method the effects of non-zero surface impedance along the boundary can be accurately modelled. This more comprehensive treatment is necessary for the accurate analysis

of high frequency and multimoded waveguides. The essential building blocks presented in Chapter 2 had to be derived again while allowing for the inclusion of non-PEC walls. Likewise, a series of verifying test cases were performed with near perfect agreement between CST and S-TNG maintained i.e. to a level of -80 dB. In uniform guide section it was observed that in multimoded operation, due to the effects of interfering currents at the bounding wall, coupling between guide modes can occur. In contrast, in uniform PEC sections guide modes couple bijectively to themselves only.

The non-PEC wall method was extended to allow for some surface roughness to be included. This was enabled by a simple but powerful Gradient Model, which could be extended to account for physical surface roughness as well as finite conductivity. Finally, a model of an absorber layer section as an infinitely thin sheet was revisited and adapted to the new formulation of the mode matching routine. Here, application of the contour integral approach allowed for trivial realisation of arbitrary absorber layer shapes. This is demonstrated for a number of test cases including mixed geometries and annulus shaped absorber layers, with excellent agreement with CST maintained.

In Chapter 4, a number of the novel routines developed as part of the SCATTER-TNG software package are introduced. Firstly, the first steps towards a truly parallel implementation of the mode matching methods are introduced. In most cases the common coupling integrals identified for the mode matching routines can be solved analytically drastically reducing the computational load. However, for offset cylindrical sections no analytical solutions can be obtained making tolerance analyses of cylindrical waveguides challenging. Hardware acceleration techniques are implemented to overcome this limitation. Here, the common coupling integrals are reformulated to take advantage of the parallel capabilities of the GPU device. The parallel implementation results are verified for the same test cases as posed in previous chapters with comparable accuracy achieved.

Secondly, a method for monitoring power loss in a system is discussed. Here, the network's scattering matrix is augmented such that the power dissipated by the lossy elements is accounted for through virtual modes on virtual non-reciprocal ports. Ultimately it was shown that this was limited to infinity short symmetric elements, but made an interesting application to monitoring power absorption by absorber layers. This approach was verified using the standard return loss approach typically used to monitor power loss. Furthermore, the cascading

routines are used to derive the scattering matrix of this novel 3-port arrangement when cascaded with typical waveguide sections.

Chapter 5 reports on a series of investigations into the focal plane arrangement of the SAFARI instrument. As part of a short research placement with SRON (Netherlands institute for space research) an investigation was performed into feasibility of an Offner reimaging system as a focal plane solution for the SAFARI instrument. This arrangement would allow for switching between different grating modules or between standard and high resolution modes. However, in the measured PSF (point spread function) from the experimental Offner system unexplained irregularities were observed. The system was modelled using in-house software MODAL (Maynooth Optical Design and Analysis Laboratory), where during normal operation the same irregularities could not be recreated. A potential source of these irregularities was identified as the over rotation of the BSM (beam steering mirror) of the Offner system which resulted in an overlap with a masked region of the primary mirror. An extended analysis was also preformed into the adequacy of the uniformly illuminated aperture initially used in the model. Here, a number of Gaussian beam profiles were used to show the effect of an under illuminated aperture and also confirmed the assumption that the QCL (Quantum Cascade Laser) provided uniform illumination of the aperture. Finally, the response of the Offner system to a polychromatic source was modelled and was found to be in good agreement with measured data where no irregularities in the PSF were observed.

An off-axis SAFARI pixel arrangement was considered to allow for a more compact test-bed arrangement and achieve greater optical efficiency. Comparing this to a previous iteration of the design, there was significant loss in performance, with the power absorbed values are more comparable to the previous design test case where there was a smaller blackbody aperture present. It was found that the elliptical mirror offers no performance advantage when coupled to the SAFARI pixel. The influence of the elliptical mirror does not capture any more radiation than was emitted, it only focuses part of it. This type of optical arrangement would be more suited to a feed design with a much-reduced angle of acceptance. Here, the benchmark simulation would lose a large amount of power for the increasing inclination angles. In such an arrangement use of this off-axis arrangement would be beneficial.

In the analysis of a prototype feed for the medium wavelength band (M-band) of the SAFARI instrument, it was found that the measured beam profile was much too narrow when compared to the simulated results. This indicated that much of the power in the higher order modes had been lost. By including the effects due to the physical surface properties (i.e. finite wall conductivity and surface roughness) in the analysis of multi-moded structures a better understanding of the losses experienced by the higher order modes due to the non-PEC boundary walls can be obtained. As applied to the SAFARI M-band structure, it was observed that by performing this type of analysis the lossy simulations allowed for much improved agreement with the measurement results compared to the PEC simulation. Furthermore, if the values considered for surface roughness are within the tolerance of the wire erosion technique finish it is clear that much refinement is required in order to mitigate the losses due to surface roughness left behind by the machining process.

As part of an ongoing collaboration with Cardiff University a significant investigation into the design and analysis of the shortest wavelength band (S-band) of the SAFARI instrument was performed. Here, the focus was on determining the feed's performance for varying lengths, aperture sizes and surface roughness values. This analysis enabled tolerances values to be set for the manufacturing of the SAFARI type waveguides. An upper surface roughness limit of $R_q = 0.3$ μm was determined, with an aim to achieve surface roughness values approaching $R_q = 0.1$ μm. Furthermore, the trade-off between different horn lengths was investigated, with a more directive and top-hat shaped beam profile desired. The medium (5 mm) and long (7 mm) length horns provided the desired profile, while the medium length horn allowed for a reduction to the overall weight of the instrument (which was a key consideration in this early design stage). Lastly, a number of aperture geometries were considered. While the larger square apertures did indeed increase throughput such an arrangement may compromise the detector response time. The results from the rectangular aperture simulation indicate an increase in horn throughput and such an arrangement complements the highly polarised field incident at the SAFARI detector plane.

The package of work presented in this thesis extends the capabilities of the mode matching methods beyond what could previously be achieved. Fundamentally, this implementation of the mode matching method can address more physical systems rather than assuming concentric, PEC structures. The extensive validation work performed against CST ensured that systems with mixed geometries, offset geometries and non-PEC surfaces could be confidently modelled

– using either numeric or analytic results. Moreover, work presented on the parallelisation of the numerical routines ensures the method is not badly bottlenecked where no analytic solutions are available and lays the foundation of a fully parallel mode matching approach. As shown in the final section of Chapter 5, the non-PEC model begins to breakdown for excessively poor surfaces. Although not as accurate as finite element analysis, such modelling can still provide a valuable insight into the multi-moded operation in the presence of extremely poor surfaces.

References

Abbas-Azimi, M., Farhad M., and Fereidoon B. 2009. 'Design of Broadband Constant-Beamwidth Conical Corrugated-Horn Antennas'. *IEEE Antennas and Propagation Magazine* 51 (5): 109–14. https://doi.org/10.1109/MAP.2009.5432055.

Adam, A., Kašalynas I., Hovenier J., et al. 2006. 'Beam Patterns of Terahertz Quantum Cascade Lasers with Subwavelength Cavity Dimensions'. *Applied Physics Letters* 88 (15): 2006–8. https://doi.org/10.1063/1.2194889.

Akyildiz, I.F., Jornet J.M., and Chong H. 2014. 'Terahertz Band: Next Frontier for Wireless Communications'. *Physical Communication* 12: 16–32. https://doi.org/10.1016/j.phycom.2014.01.006.

'ALMA - ESO'. 2013. https://www.eso.org/public/teles-instr/alma/.

'ALMA - ESO Receiver Bands'. 2016. https://www.eso.org/public/teles-instr/alma/receiver-bands/.

AMD. 2013. 'Sea Islands Series Instruction Set Architecture Reference Guide'. www.amd.com.

Archibald, E. N., Jenness T., Holland W. S., Coulson I. M., et al. 2002. 'On the Atmospheric Limitations of Ground-Based Submillimetre Astronomy Using Array Receivers'. *Monthly Notices of the Royal Astronomical Society* 336 (1): 1–13. https://doi.org/10.1046/j.1365-8711.2002.05582.x.

Audley, M D, de Lange G, Jackson B, Roelfsema P, Withington S, Ade P, Bradford C, et al. 2018. 'The SAFARI Detector System' 31 (0): 18. https://doi.org/10.1117/12.2313361.

Audley, M D., de Lange G., Gao J., Jackson B., et al. 2018. 'The SAFARI Detector System'. In *Millimeter, Submillimeter, and Far-Infrared Detectors and Instrumentation for Astronomy IX*, edited by Jonas Zmuidzinas and Jian-Rong Gao, 10708:45–51. SPIE. https://doi.org/10.1117/12.2313361.

Balanis, C. 2016. *Antenna Theory: Analysis and Design, Fourth Edition*. *John Wiley & Sons, Inc.* https://doi.org/10.2307/j.ctvfxvc64.18.

Balanis, CA. 2012. *Advanced Engineering Electromagnetics, 2nd Edition*. Wiley.

Bois, K., Benally A., and Zoughi R. 1998. 'A Multi-Mode Solution for Analysis of the Reflection Coefficient of Open-Ended Rectangular Waveguides Radiating into a Dielectric Infinite Half-Space'. *Review of Progress in Quantitative Nondestructive Evaluation*, 705–11. https://doi.org/10.1007/978-1-4615-5339-7_91.

Bouchet, F. R., de Bernardis P., Maffei B., and Martinez-Gonzalez E. 2010. 'A Cosmic ORigins Explorer (COrE) Satellite Mission for Probing Cosmic Origins , Neutrinos Masses and the Origin of Stars and Magnetic Fields through a High-Sensitivity Survey of the Microwave Polorization on the Full Sky Contents'. *Strategy*, 1–64.

Bracken, C. 2015. 'Electromagnetic Techniques for Analysis and Design of Ultra Sensitive Receivers for Far-Infrared Astronomy'

Chattopadhyay, G., Alonso-delPino M., Chahat N., González-Ovejero D., Lee C., and Reck T. 2018. *Terahertz Antennas and Feeds*. *Signals and Communication Technology*. https://doi.org/10.1007/978-3-319-62773-1_10.

Cheon, H. 2019. 'Potential Clinical Applications of Terahertz Radiation'. *Journal of Applied Physics* 190901 (November 2018). https://doi.org/10.1063/1.5080205.

Collin, R E, IEEE Antennas, and Propagation Society. 1991. *Field Theory of Guided Waves*. IEEE Press.

Day, P.K., Leduc H.G., Mazin B.A., Vayonakis A., and Zmuidzinas J. 2003. 'A Broadband Superconducting Detector Suitable for Use in Large Arrays' 425 (October): 12–14. https://doi.org/10.1038/nature01981.1.

Doherty, S. 2012. 'Optical and Quasi-Optical Design and Analysis of Astronomical Instrumentation Including a Prototype SAFARI Pixel'

Dole, H., Fernández-Conde N., Pérez-González P.G., Papovich C., Rieke G.H. et al. 2006. 'The Cosmic Infrared Background Resolved by Spitzer'. *Astronomy & Astrophysics* 451 (2): 417–29. https://doi.org/10.1051/0004-6361:20054446.

'ESA - Andromeda Galaxy (M31)'. 2011. https://sci.esa.int/web/herschel/-/48182-multiwavelength-images-of-the-andromeda-galaxy-m31.

Fathololoumi, S., Ban D., Luo H., Grant P., Laframboise S.R., Wasilewski Z., Buchanan M., and Liu H.C. 2008. 'Beam Pattern Investigation of Terahertz Quantum Cascade Lasers'. *PIERS Online* 4 (2): 267–70. https://doi.org/10.2529/PIERS070905092309.

Ferlet, M., Geis N., Goicoechea J., Griffin D.K., Heras A.M., Isaak K., Nakagawa T., et al. 2010. 'SPICA Revealing the Origins of Planets and Galaxies',

Figlia, G., and Gentili G. 2002. 'On the Line-Integral Formulation of Mode-Matching Technique'. *IEEE Transactions on Microwave Theory and Techniques* 50 (2): 578–80.

Fischer, J, and Fischer J. 2003. 'ASTROCAM: Offner Re-Imaging 1024 X 1024 InSb Camera for near-Infrared Astrometry on the USNO 1.55-m Telescope'. *Proceedings of SPIE* 4841 (2003): 564–77. https://doi.org/10.1117/12.461033.

Francesco, J. Di, Johnstone D., Matthews B.C., Bartel N., Bronfman L., Casassus S., Chitsazzadeh S., et al. 2013. 'The Science Cases for Building a Band 1 Receiver Suite for ALMA', no. October. http://arxiv.org/abs/1310.1604.

Fuller, G.A., Avison A., Beltran M., Casasola V., Caselli P., Cicone C., Costagliola F., et al. 2016. 'The Science Case for ALMA Band 2 and Band 2+3'. http://arxiv.org/abs/1602.02414.

Gaster, B., Howes L., Kaeli D., Mistry P., and Schaa D. 2013. *Heterogeneous Computing with OpenCL*. *Heterogeneous Computing with OpenCL*. https://doi.org/10.1016/C2012-0-03322-4.

Gleeson, E. 2004. 'Single and Multi-Moded Corrugated Horn Design for Cosmic Microwave Background Experiments'.

Gold, G, and Helmreich K. 2017. 'A Physical Surface Roughness Model and Its Applications'. *IEEE Transactions on Microwave Theory and Techniques* 65 (10): 3720–32. https://doi.org/10.1109/TMTT.2017.2695192.

Gold, G, and Helmreich K. 2017. 'A Physical Surface Roughness Model and Its Applications' 65 (10): 3720–32.

Goldsmith, P F. 1998. *Quasioptical Systems: Gaussian Beam Quasioptical Propagation and Applications*. https://doi.org/10.1109/9780470546291.

Granet, C., Bolton R., and Moorey G. 2004. 'A Smooth-Walled Spline-Profile Horn as an Alternative to the Corrugated Horn for Wide Band Millimeter-Wave Applications'. *IEEE Transactions on Antennas and Propagation* 52 (3): 848–54. https://doi.org/10.1109/TAP.2004.825156.

Harris, A I. 1990. 'Coherent and Incoherent Detection'. *In ESA, From Ground-Based to Space-Borne Sub-Mm Astronomy p 165-169 (SEE N91-21986 13-89)*, 368.

Hecht, E. 2001. 'Optics 4th Edition'. *Optics 4th Edition by Eugene Hecht Reading MA AddisonWesley Publishing Company 2001*. https://doi.org/10.1119/1.3274347.

Höhne, J., Altmann M., Angloher G., Hettl P., Jochum J., Nüssle T., Pfnür S., et al. 1999. 'High-Resolution x-Ray Spectrometry Using Iridium - Gold Phase Transition Thermometers'. *X-Ray Spectrometry* 28 (5): 396–98. https://doi.org/10.1002/(SICI)1097-4539(199909/10)28:5<396::AID-XRS374>3.0.CO;2-Q.

Hübers, H W. 2008. 'Terahertz Heterodyne Receivers'. *IEEE Journal on Selected Topics in Quantum Electronics* 14 (2): 378–91. https://doi.org/10.1109/JSTQE.2007.913964.

Huray, P.G., Hall S., Pytel S., Oluwafemi F., Mellitz R., Hua D., and Ye P. 2007. 'Fundamentals of a 3-D "Snowball" Model for Surface Roughness Power Losses'. *Proceedings - 11th IEEE Workshop on Signal Propagation on Interconnects, SPI 2007*, 121–24. https://doi.org/10.1109/SPI.2007.4512227.

Jackson, J D. 1998. *Classical Electrodynamics*. Wiley.

Kalinauskaitė, E. 2018. 'Electromagnetic and Quasi-Optical Analysis of Cavity Coupled Bolometers for Far-Infrared and Terahertz Receivers.

Kirley, M.P., Booske J. et al. 2015. 'Terahertz Conductivity of Copper Surfaces' 5 (6): 1012–20.

De Korte, P., Mauskopf P., Bruijn M P., and Cros A. 2012. 'The SPICA-SAFARI Detector System : TES Detector Arrays with Frequency Division Multiplexed SQUID Readout', no. May 2014. https://doi.org/10.1109/TTHZ.2011.2177705.

De Maagt, P. 2007. 'Terahertz Technology for Space and EARTH Applications'. *Conference Proceedings - 2007 IEEE International Workshop on Antenna Technology: Small and*

Smart Antennas Metamaterials and Applications, IWAT 2007, 111–15. https://doi.org/10.1109/IWAT.2007.370091.

Ferenc M., and Marki C. 2010. 'Mixer Basics Primer'. *Marki Microwave*, 1–11. http://www.markimicrowave.com/menus/appnotes/mixer_basics_primer.pdf%0Apapers2://publication/uuid/0E08CAA3-7180-4BC4-904D-D65937266CCB%0Ahttp://www.markimicrowave.com/assets/appnotes/mixer_basics_primer.pdf.

McCarthy, D. 2014. 'Investigation of Horn Optimisation, Simulation and Measurement Techniques, with Application to Integrating Cavity Based Pixel Design'. Maynooth University.

Mei, S., Shi Y., Jonasson O., and Knezevic I. 2017. 'Quantum Cascade Lasers: Electrothermal Simulation'. *Handbook of Optoelectronic Device Modeling and Simulation: Lasers, Modulators, Photodetectors, Solar Cells, and Numerical Methods* 2: 235–59. https://doi.org/10.4324/9781315152318.

'NRAO - ALMA Band 10'. 2018. 2018. https://public.nrao.edu/news/2018-alma-band10/.

O'Sullivan, C M., and Murphy J.A. 2012. *Field Guide to Terahertz Sources, Detectors, and Optics*. SPIE.

Olver, A. D., Shafai L., Kishk A. A., and Clarricoats, P. J. 2011 'Corrugated Horns'. In *Microwave Horns and Feeds*. https://doi.org/10.1049/pbew039e_ch9.

Olver, C., Kishk, A.A., and Shafai, L. 2011. *Microwave Horns and Feeds*. https://doi.org/10.1049/pbew039e.

Olver, F W., Lozier D W., Boisvert R F., and Clark C W. 2017. 'The NIST Handbook of Mathematical Functions'. *NIST*, February. https://www.nist.gov/publications/nist-handbook-mathematical-functions.

Opencl, Khronos. 2009. 'OpenCL Specification'. *ReVision*, 1–385. https://doi.org/10.1016/j.actamat.2006.08.044.

Orfanidis, S J. 2008. 'Waves and Antennas Electromagnetic'. *Media* 2: 525–70. http://www.ece.rutgers.edu/~orfanidi/ewa/.

Pilbratt, G. L., Riedinger J. R., Passvogel T., Crone G., Doyle D., Gageur U., Heras A. M., et al. 2010. 'Herschel Space Observatory'. *Astronomy and Astrophysics* 518 (7–8). https://doi.org/10.1051/0004-6361/201014759.

Quimby, R S. 2006. *Photonics and Lasers: An Introduction*. https://doi.org/10.1002/0471791598.

Rangwala, N., Maloney P. R., Christine, J.G., Wilson D., Rykala A., Isaak K., Baes M., et al. 2011. 'Observations of Arp 220 Using Herschel-Spire: An Unprecedented View of the Molecular Gas in an Extreme Star Formation Environment'. *Astrophysical Journal* 743 (1). https://doi.org/10.1088/0004-637X/743/1/94.

Roelfsema, P.R. 2018. 'SPICA M5 Proposal'.

Schallig, E. 2015a. 'A Far-Infrared Beam-Steering Offner Relay for SAFARI'.

Scully, S., Burke D., O'Sullivan C., Gayer D., Gradziel M., Murphy J. A., De Petris M., et al. 2016. 'Optical Design and Modelling of the QUBIC Instrument, a next-Generation Quasi-Optical Bolometric Interferometer for Cosmology'. *Millimeter, Submillimeter, and Far-Infrared Detectors and Instrumentation for Astronomy VIII* 9914: 99142S. https://doi.org/10.1117/12.2231717.

Selvan, K T. 2004. 'Approximate Formula for the Phase of the Aperture-Reflection Coefficient of Open-Ended Rectangular Waveguide'. *IEEE Transactions on Antennas and Propagation* 52 (1): 318–21. https://doi.org/10.1109/TAP.2003.822449.

Shafii, J., and Vernon R. J. 2002. 'Investigation of Mode Coupling Due to Ohmic Wall Losses in Overmoded Uniform and Varying-Radius Circular Waveguides by the Method of Cross Sections'. *IEEE Transactions on Microwave Theory and Techniques* 50 (5): 1361–69. https://doi.org/10.1109/22.999151.

Shafii, J/, and Vernon R. J. 2002. 'Investigation of Mode Coupling Due to Ohmic Wall Losses in Overmoded Uniform and Varying-Radius Circular Waveguides by the Method of Cross Sections' 50 (5): 1361–69.

Siegel, P H. 2002. 'Terahertz Technology'. *IEEE Transactions on Microwave Theory and Techniques* 50 (3): 910–28. https://doi.org/10.1109/22.989974.

Strang, G. 2013. ‘Linear Algebra and Its Applications Fourth Edition’. *Pressure Vessel Design Manual*. https://doi.org/10.1016/B978-0-12-387000-1.01001-9.

Van Der Tak, F. 2012. ‘The First Results from the Herschel-HIFI Mission $’, 1–32.

Wade, J., and Macphie R. H. 1990. ‘Conservation of Complex Power Technique for Waveguide Junctions with Finite Wall Conductivity’. *IEEE Transactions on Microwave Theory and Techniques* 38 (4).

Walker, C K. 2015. *Terahertz Astronomy*. https://doi.org/10.1201/b19111.

Wiltse, J C. 1984. ‘History of Millimetre and Submillimetre Waves’, 1118–27, *IEEE Transactions on Microwave Theory and Techniques 32*

Withington S, Trans, P., and Lond R. 2014. ‘Terahertz Astronomical Telescopes and Instrumentation : One Contribution of 16 to a Discussion Meeting ’ The Terahertz Gap : The Generation of Far-Infrared Radiation and Its Applicati ... Terahertz Astronomical Telescopes and Instrumentation’, no. February 2004. https://doi.org/10.1098/rsta.2003.1322.

Yang, Y., Shutler A., and Grischkowsky D. 2011. ‘Long Tube Precise THz-TDS Measurement of the Transmission of the Atmosphere from 0.2 to 2 THz’. *Optics InfoBase Conference Papers* 19 (9): 8830–38. https://doi.org/10.1364/cleo_si.2011.cthee6.

Appendix A

A.1 Type B, C and D integrals

The analytical solutions for the common coupling integrals (B, C and D) required for the mode matching method are presented for cylindrical and rectangular guide geometries.

Cylindrical Geometry:

The scalar potentials $F_z^+(\rho,\phi,z)$ and $A_z^+(\rho,\phi,z)$ can be expressed in the form of two orthogonal solutions given by:

$$F_z^+(\rho,\phi,z) = A_{mn}J_m(\beta_\rho\rho)\begin{pmatrix}\cos(m\phi)\\ \sin(m\phi)\end{pmatrix}e^{-j\beta_z z} \quad (A.1.1)$$

$$A_z^+(\rho,\phi,z) = B_{mn}J_m(\beta_\rho\rho)\begin{pmatrix}\cos(m\phi)\\ \sin(m\phi)\end{pmatrix}e^{-j\beta_z z} \quad (A.1.2)$$

where $\rho = \sqrt{x^2+y^2}$ and $\phi = \tan^{-1}\frac{y}{x}$ are given by.

Both scalar potentials can be expressed in terms of polar coordinates by setting one of the solutions to be imaginary and using the common Euler relation. This is shown for the scalar potential $F_z^+(\rho,\phi,z)$

$$F_z^+(\rho,\phi,z) = A_{mn}J_m(\beta_\rho\rho)[\cos(m\phi) + i\sin(m\phi)]e^{-j\beta_z z} \quad (A.1.3)$$

$$F_z^+(\rho,\phi,z) = A_{mn}J_m(\beta_\rho\rho)e^{im\phi}e^{-j\beta_z z} \quad (A.1.4)$$

Effectively two valid solutions are combined to account for this a normalisation factor must be included:

$$F_z^+(\rho,\phi,z) = \frac{A_{mn}}{\sqrt{N}}J_m(\beta_\rho\rho)e^{im\phi}e^{-j\beta_z z} \quad (A.1.5)$$

where $N = 1$ for zero azimuthal orders m (corresponding to the case where only one solution exists) and $N = 2$ otherwise (corresponding to the case where the sine solution is not trivial in (2.4.50)). Likewise, the same procedure can be applied to $A_z^+(\rho, \phi, z)$.

The following integral solution below appears in the derivation of the common integrals:

$$\int_0^{2\pi} e^{i(m_i - m_j)\phi} d\phi = \left[\frac{e^{i(m_i - m_j)\phi}}{i(m_i - m_j)} \right]_0^{2\pi} \tag{A.1.6}$$

which only has non-zero value for $m_i = m_j$. For $k = R$ and $l = L$ the B-type integral has the following analytical solution:

$$B_{ij}^{RL}(S) = \int_{\partial S} \left(A_i^R \nabla F_j^L \right) d\boldsymbol{l} \tag{A.1.7}$$

$$\nabla F_j^L = \beta_{\rho,j}^L J'_{m_j}\left(\beta_{\rho,j}^L \rho\right) e^{im_j\phi} \hat{\boldsymbol{r}} + \frac{1}{\rho} i m_j J_{m_j}\left(\beta_{\rho,j}^L \rho\right) e^{im_j\phi} \hat{\boldsymbol{\phi}} \tag{A.1.8}$$

$$A_i^R = J_{m_i}\left(\beta_{\rho,i}^R \rho\right) e^{im_i\phi} \tag{A.1.9}$$

$$\begin{aligned} B_{ij}^{RL}(S) = \frac{1}{N} \rho^L \int_0^{2\pi} J_{m_i}\left(\beta_{\rho,i}^R \rho^L\right) e^{im_i\phi} \Big(& \beta_{\rho,j}^L J'_{m_j}\left(\beta_{\rho,j}^L \rho^L\right) e^{im_j\phi} \hat{\boldsymbol{r}} \\ & + \frac{1}{\rho} i m_j J_{m_j}\left(\beta_{\rho,j}^L \rho^L\right) e^{im_j\phi} \hat{\boldsymbol{\phi}} \Big) d\phi \end{aligned} \tag{A.1.10}$$

$$= \frac{1}{N} \left(\alpha \int_0^{2\pi} e^{i(m_i - m_j)\phi} d\phi + \kappa \int_0^{2\pi} -ie^{i(m_i - m_j)\phi} d\phi \right) = \frac{\alpha 2\pi - i\kappa\alpha 2\pi}{N} \tag{A.1.11}$$

$$\alpha = \rho^L J_{m_i}\left(\beta_{\rho,i}^R \rho^L\right) \beta_{\rho,j}^L J'_{m_j}\left(\beta_{\rho,j}^L \rho^L\right), \kappa = J_{m_i}\left(\beta_{\rho,i}^R \rho^L\right) m_j J_{m_j}\left(\beta_{\rho,j}^L \rho^L\right) \tag{A.1.12}$$

The integration procedure for the remaining common integrals follows directly the method used in the B-type form. As such, the detail is excluded and only the result is given. For $k = R$ and $l = L$ the (ii) C-type integral has the following analytical solution:

$$C_{ij}^{RL}(S_L) = \frac{\left(\beta_{c,i}^{R,TM}\right)^2 \int_{dS} A_i^R \nabla A_j^L \cdot \hat{\boldsymbol{n}} dl}{\left(\beta_{c,i}^{R,TM}\right)^2 - \left(\beta_{c,j}^{L,TM}\right)^2} \tag{A.1.13}$$

$$C_{ij}^{RL}(S_L) = \frac{\left(\beta_{c,i}^{R,TM}\right)^2}{\left(\beta_{c,i}^{R,TM}\right)^2 - \left(\beta_{c,j}^{L,TM}\right)^2} \frac{\alpha 2\pi}{N}, \text{for } \alpha = \rho^L \beta_{\rho,j}^L J_{m_i}\left(\beta_{\rho,i}^R \rho^L\right) J'_{m_j}\left(\beta_{\rho,j}^L \rho^L\right) \tag{A.1.14}$$

Likewise, the (iii) C-type integral has the following analytical solution:

$$C_{ij}^{RL}(S_L) = \left(\beta_{c,j}^{L,TM}\right)^2 \int_S A_i^R A_j^L dS \tag{A.1.15}$$

$$C_{ij}^{RL}(S_L) = X_{m_j n_j}^2 \frac{\pi}{N} \left[-J'_{m_j}\left(X_{m_j n_j}\right)\right]^2 \tag{A.1.16}$$

Finally, for $k = R$ and $l = L$ the (ii) D-type integral has the following analytical solution:

$$D_{ij}^{RL}(S_L) = \frac{\left(\beta_{c,i}^{L,TE}\right)^2 \int_{dS} F_j^L \nabla F_i^R \cdot \hat{\boldsymbol{n}} dl}{\left(\beta_{c,j}^{L,TE}\right)^2 - \left(\beta_{c,i}^{R,TE}\right)^2} \tag{A.1.17}$$

$$D_{ij}^{RL}(S_L) = \frac{\left(\beta_{c,i}^{L,TE}\right)^2}{\left(\beta_{c,j}^{L,TE}\right)^2 - \left(\beta_{c,i}^{R,TE}\right)^2} \frac{\alpha 2\pi}{N}, \text{for } \alpha = \rho^L \beta_{\rho,i}^R J_{m_j}\left(\beta_{\rho,j}^L \rho^L\right) J'_{m_i}\left(\beta_{\rho,i}^R \rho^L\right) \tag{A.1.18}$$

and the (iii) D-type integral has the following analytical solution:

$$D_{ij}^{RL}(S_L) = \left(\beta_{c,j}^{L,TE}\right)^2 \int_S F_i^R F_j^L dS \tag{A.1.19}$$

$$D_{ij}^{RL}(S_L) = \left(X'^2_{m_j n_j} - m_j^2\right)\frac{\pi}{N}\left[J_{m_j}^2\left(X'_{m_j n_j}\right)\right]^2 \qquad (A.1.20)$$

Rectangular Geometry:

In the rectangular case the surface integral form of the B, C and D-type integral solved as this form allows for offsets to be easily considered. Transformations $(\Delta x, \Delta y)$ are explicitly applied to the right hand potential, effectively offsetting the position right hand guide section. For $k = R$ and $l = L$ the B-type integral has the following analytical solution

$$B_{ij}^{RL}(S) = \int_S \nabla A_i^R \cdot \left(\nabla F_j^L \times \hat{\boldsymbol{z}}\right) dS \qquad (A.1.21)$$

$$\begin{aligned} F_j^L(x,y) &= \cos\left(\beta_{x,j}^L\left(x + \frac{a_L}{2}\right)\right)\cos\left(\beta_{y,j}^L\left(y + \frac{b_L}{2}\right)\right) \\ A_i^R(x,y) &= \sin\left(\beta_{x,i}^R\left(x + \frac{a_R}{2} + \Delta x\right)\right)\sin\left(\beta_{y,i}^R\left(y + \frac{b_R}{2} + \Delta \mathrm{y}\right)\right) \end{aligned} \qquad (A.1.22)$$

$$\nabla F_j^L = \frac{\partial F_j^L}{\partial x}\hat{\boldsymbol{x}} + \frac{\partial F_j^L}{\partial y}\hat{\boldsymbol{y}} \text{ and } \left(\nabla F_j^L \times \hat{\boldsymbol{z}}\right) = \frac{\partial F_j^L}{\partial y}\hat{\boldsymbol{x}} - \frac{\partial F_j^L}{\partial x}\hat{\boldsymbol{y}} \qquad (A.1.23)$$

$$\begin{aligned} B_{ij}^{RL}(S) = -\beta_{y,j}^L\beta_{x,i}^R \int_S &\cos\left(\beta_{x,i}^R\left(x + \frac{a_R}{2} + \Delta x\right)\right)\sin\left(\beta_{y,i}^R\left(y + \frac{b_R}{2} + \Delta \mathrm{y}\right)\right) \\ &\cos\left(\beta_{x,j}^L\left(x + \frac{a_L}{2}\right)\right)\sin\left(\beta_{y,j}^L\left(y + \frac{b_L}{2}\right)\right) dS \\ +\beta_{x,j}^L\beta_{y,i}^R \int_S &\sin\left(\beta_{x,i}^R\left(x + \frac{a_R}{2} + \Delta x\right)\right)\cos\left(\beta_{y,i}^R\left(y + \frac{b_R}{2} + \Delta \mathrm{y}\right)\right) \\ &\sin\left(\beta_{x,j}^L\left(x + \frac{a_L}{2}\right)\right)\cos\left(\beta_{y,j}^L\left(y + \frac{b_L}{2}\right)\right) dS \end{aligned} \qquad (A.1.24)$$

The integral is split such that $\int_S \nabla A_i^R \cdot \left(\nabla F_j^L \times \hat{\boldsymbol{z}}\right) dS = (\alpha) + (\gamma)$, with α and γ given by:

$$(\alpha) = -\beta_{y,j}^L \beta_{x,i}^R \int_{-\frac{a_L}{2}}^{\frac{a_L}{2}} \cos\left(\beta_{x,i}^R \left(x + \frac{a_R}{2} + \Delta x\right)\right) \cos\left(\beta_{x,j}^L \left(x + \frac{a_L}{2}\right)\right) dx \times \int_{-\frac{b_L}{2}}^{\frac{b_L}{2}} \sin\left(\beta_{y,i}^R \left(y + \frac{b_R}{2} + \Delta y\right)\right) \sin\left(\beta_{y,j}^L \left(y + \frac{b_L}{2}\right)\right) dy \quad \textit{(A.1.25)}$$

$$(\gamma) = \beta_{x,j}^L \beta_{y,i}^R \int_{-\frac{a_L}{2}}^{\frac{a_L}{2}} \sin\left(\beta_{x,i}^R \left(x + \frac{a_R}{2} + \Delta x\right)\right) \sin\left(\beta_{x,j}^L \left(x + \frac{a_L}{2}\right)\right) dx \times \int_{-\frac{b_L}{2}}^{\frac{b_L}{2}} \cos\left(\beta_{y,i}^R \left(y + \frac{b_R}{2} + \Delta y\right)\right) \cos\left(\beta_{y,j}^L \left(y + \frac{b_L}{2}\right)\right) dy \quad \textit{(A.1.26)}$$

$$\text{notice: } \frac{\beta_{x,i}^R a_R}{2} = \frac{m_i \pi}{2}, \frac{\beta_{y,i}^R b_R}{2} = \frac{n_i \pi}{2} \text{ and } \frac{\beta_{x,j}^L a_L}{2} = \frac{m_j \pi}{2}, \frac{\beta_{y,j}^L b_L}{2} = \frac{n_j \pi}{2} \quad \textit{(A.1.27)}$$

Integrals involving the product of sine's and cosine's appear throughout the derivation of the common B, C and D-type integrals. For clarity these trigonometric integral results are functionalised. Using the *x*-derivative as basis the trigonometric integral solutions are given as:

$$CC_x(u_x, v_x, a_L) = \int_{-\frac{a_L}{2}}^{\frac{a_L}{2}} \cos(u_x)\cos(v_x) dx = \frac{1}{2} \int_{-\frac{a_L}{2}}^{\frac{a_L}{2}} \cos(u_x - v_x) + \cos(u_x + v_x) dx \quad \textit{(A.1.28)}$$

$$u_x - v_x = \left(\beta_{x,i}^R - \beta_{x,j}^L\right)x + \frac{\pi}{2}\left(m_i - m_j\right) + \beta_{x,i}^R \Delta x$$
$$u_x + v_x = \left(\beta_{x,i}^R + \beta_{x,j}^L\right)x + \frac{\pi}{2}\left(m_i + m_j\right) + \beta_{x,i}^R \Delta x \quad \textit{(A.1.29)}$$

$$CC_x(u_x, v_x, a_L) = \frac{1}{2}\left[\frac{\sin(u_x - v_x)}{\frac{d(u_x - v_x)}{dx}} + \frac{\sin(u_x + v_x)}{\frac{d(u_x + v_x)}{dx}}\right]_{-\frac{a_L}{2}}^{\frac{a_L}{2}} \quad \textit{(A.1.30)}$$

$$SS_x(u_x, v_x, a_L) = \int_{-\frac{a_L}{2}}^{\frac{a_L}{2}} \sin(u_x)\sin(v_x)dx = \frac{1}{2}\int_{-\frac{a_L}{2}}^{\frac{a_L}{2}} \cos(u_x - v_x) - \cos(u_x + v_x)dx \quad \textit{(A.1.31)}$$

$$SS_x(u_x, v_x, a_L) = \frac{1}{2}\left[\frac{\sin(u_x - v_x)}{\frac{d(u_x - v_x)}{dx}} - \frac{\sin(u_x + v_x)}{\frac{d(u_x + v_x)}{dx}}\right]_{-\frac{a_L}{2}}^{\frac{a_L}{2}} \quad \textit{(A.1.32)}$$

Similar results can be obtained for $CC_y(u_y, v_y, b_L)$ and $SS_y(u_y, v_y, b_L)$. Thus, the solution to the B-type integral can be expressed as:

$$(\alpha) = -\beta_{y,j}^{L}\beta_{x,i}^{R}[CC_x \times SS_y] \quad \textit{(A.1.33)}$$

$$(\gamma) = -\beta_{y,j}^{L}\beta_{x,i}^{R}[SS_x \times CC_y\ ] \quad \textit{(A.1.34)}$$

The same approach is taken for the C and D-Type integrals, with analytic solutions given by:

$$C_{ij}^{RL}(S) = \int_S \nabla A_i^R \cdot \nabla A_j^L dS = (\alpha) + (\gamma) \quad \textit{(A.1.35)}$$

$$(\alpha) = -\beta_{x,j}^{L}\beta_{x,i}^{R}[CC_x \times SS_y] \quad \textit{(A.1.36)}$$

$$(\gamma) = -\beta_{y,j}^{L}\beta_{y,i}^{R}[SS_x \times CC_y\ ] \quad \textit{(A.1.37)}$$

and:

$$D_{ij}^{RL}(S) = \int_S \nabla F_i^R \cdot \nabla F_j^L dS = (\alpha) + (\gamma) \tag{A.1.38}$$

$$(\alpha) = -\beta_{x,j}^L \beta_{x,i}^R [SS_x \times CC_y] \tag{A.1.39}$$

$$(\gamma) = -\beta_{y,j}^L \beta_{y,i}^R [CC_x \times SS_y] \tag{A.1.40}$$

A.2 Cascading Procedure

The cascading technique considers two N-port networks A and B, both of which can be represented by their own scattering matrices which take the form:

$$\boldsymbol{b}^A = [\boldsymbol{S}^A]\boldsymbol{a}^A \tag{A.2.1}$$

$$\boldsymbol{b}^B = [\boldsymbol{S}^B]\boldsymbol{a}^B \tag{A.2.2}$$

where $\boldsymbol{a}^X = [a_i^X]$ represents the amplitudes of the incident modes, $\boldsymbol{b}^X = [b_i^X]$ represents the amplitudes of the outgoing modes and X gives the network element of interest. Ports in the two constituent networks that are connected to each other will vanish in the resulting network, while the remaining will become its external ports. The number of modes considered in each network is given by N_X. These modes can be separated into *remaining* (in the external ports; denoted by **R**) and *vanishing* (those in the vanishing internal ports of the complete network; denoted by **V**). The scattering matrix for each network can be correspondingly refactored using the remaining and vanishing notation introduced:

$$\begin{bmatrix} b^{A,R} \\ b^{A,V} \end{bmatrix} = \begin{bmatrix} \boldsymbol{S}_{R,R}^A & \boldsymbol{S}_{R,V}^A \\ \boldsymbol{S}_{V,R}^A & \boldsymbol{S}_{V,V}^A \end{bmatrix} \begin{bmatrix} a^{A,R} \\ b^{B,V} \end{bmatrix} \tag{A.2.3}$$

$$\begin{bmatrix} b^{B,R} \\ b^{B,V} \end{bmatrix} = \begin{bmatrix} \boldsymbol{S}_{R,R}^B & \boldsymbol{S}_{R,V}^B \\ \boldsymbol{S}_{V,R}^B & \boldsymbol{S}_{V,V}^B \end{bmatrix} \begin{bmatrix} a^{B,R} \\ b^{A,V} \end{bmatrix} \tag{A.2.4}$$

$\begin{bmatrix} \boldsymbol{b}^{A,R} \\ \boldsymbol{b}^{B,R} \end{bmatrix}$ must be expressed wholly in terms of the amplitudes of the remaining input modes $\begin{bmatrix} \boldsymbol{a}^{A,R} \\ \boldsymbol{a}^{B,R} \end{bmatrix}$.

$$b^{A,V} = \boldsymbol{S}^{A}_{V,R} a^{A,R} + \boldsymbol{S}^{A}_{V,V} b^{B,V} \tag{A.2.5}$$

$$\Rightarrow b^{A,V} - \boldsymbol{S}^{A}_{V,V} b^{B,V} = \boldsymbol{S}^{A}_{V,R} a^{A,R} \tag{A.2.6}$$

$$b^{B,V} = \boldsymbol{S}^{B}_{V,R} a^{B,R} + \boldsymbol{S}^{B}_{V,V} b^{A,V} \tag{A.2.7}$$

$$\Rightarrow -\boldsymbol{S}^{B}_{V,V} b^{A,V} + b^{B,V} = \boldsymbol{S}^{B}_{V,R} a^{B,R} \tag{A.2.8}$$

In matrix form:

$$\begin{bmatrix} I & -\boldsymbol{S}^{A}_{V,V} \\ -\boldsymbol{S}^{B}_{V,V} & I \end{bmatrix} \begin{bmatrix} b^{A,V} \\ b^{B,V} \end{bmatrix} = \begin{bmatrix} \boldsymbol{S}^{A}_{V,R} & 0 \\ 0 & \boldsymbol{S}^{B}_{V,R} \end{bmatrix} \begin{bmatrix} a^{A,R} \\ a^{B,R} \end{bmatrix} \tag{A.2.9}$$

$$\begin{bmatrix} b^{A,V} \\ b^{B,V} \end{bmatrix} = \begin{bmatrix} I & -\boldsymbol{S}^{A}_{V,V} \\ -\boldsymbol{S}^{B}_{V,V} & I \end{bmatrix}^{-1} \begin{bmatrix} \boldsymbol{S}^{A}_{V,R} & 0 \\ 0 & \boldsymbol{S}^{B}_{V,R} \end{bmatrix} \begin{bmatrix} a^{A,R} \\ a^{B,R} \end{bmatrix} \tag{A.2.10}$$

The inverse of the block matrix is:

$$\begin{bmatrix} I & -\boldsymbol{S}^{A}_{V,V} \\ -\boldsymbol{S}^{B}_{V,V} & I \end{bmatrix}^{-1} = \begin{bmatrix} \left(I - S^{A}_{V,V} S^{B}_{V,V}\right)^{-1} & \left(I - S^{A}_{V,V} S^{B}_{V,V}\right)^{-1} S^{A}_{V,V} \\ \left(I - S^{B}_{V,V} S^{A}_{V,V}\right)^{-1} S^{B}_{V,V} & \left(I - S^{B}_{V,V} S^{A}_{V,V}\right)^{-1} \end{bmatrix} \tag{A.2.11}$$

Therefore:

$$\begin{bmatrix} b^{A,V} \\ b^{B,V} \end{bmatrix} = \begin{bmatrix} \left(I - S^{A}_{V,V} S^{B}_{V,V}\right)^{-1} & \left(I - S^{A}_{V,V} S^{B}_{V,V}\right)^{-1} S^{A}_{V,V} \\ \left(I - S^{B}_{V,V} S^{A}_{V,V}\right)^{-1} S^{B}_{V,V} & \left(I - S^{B}_{V,V} S^{A}_{V,V}\right)^{-1} \end{bmatrix} \begin{bmatrix} \boldsymbol{S}^{A}_{V,R} & 0 \\ 0 & \boldsymbol{S}^{B}_{V,R} \end{bmatrix} \begin{bmatrix} a^{A,R} \\ a^{B,R} \end{bmatrix} \tag{A.2.12}$$

$$\begin{bmatrix} b^{A,V} \\ b^{B,V} \end{bmatrix} = \begin{bmatrix} \left(I - S^A_{V,V}S^B_{V,V}\right)^{-1}\boldsymbol{S}^A_{V,R} & \left(I - S^A_{V,V}S^B_{V,V}\right)^{-1}S^A_{V,V}\boldsymbol{S}^B_{V,R} \\ \left(I - S^B_{V,V}S^A_{V,V}\right)^{-1}S^B_{V,V}\boldsymbol{S}^A_{V,R} & \left(I - S^B_{V,V}S^A_{V,V}\right)^{-1}\boldsymbol{S}^B_{V,R} \end{bmatrix} \begin{bmatrix} a^{A,R} \\ a^{B,R} \end{bmatrix} \quad \textit{(A.2.13)}$$

The remaining expressions for outgoing modes are obtained by expanding equations (A.2.3)-(A.2.4) and applying the results of the obtained for the vanishing modes $b^{A,V}$ and $b^{B,V}$ from equations (A.2.12)-(A.2.13)(A.2.8):

$$b^{A,R} = \boldsymbol{S}^A_{R,R}a^{A,R} + \boldsymbol{S}^A_{R,V}b^{B,V} \quad \textit{(A.2.14)}$$

$$= \boldsymbol{S}^A_{R,R}a^{A,R} + \boldsymbol{S}^A_{R,V}\left(I - S^B_{V,V}S^A_{V,V}\right)^{-1}S^B_{V,V}\boldsymbol{S}^A_{V,R}a^{A,R} + \boldsymbol{S}^A_{R,V}\left(I - S^B_{V,V}S^A_{V,V}\right)^{-1}\boldsymbol{S}^B_{V,R}a^{B,R} \quad \textit{(A.2.15)}$$

$$b^{B,R} = \boldsymbol{S}^B_{V,R}a^{B,R} + \boldsymbol{S}^B_{V,V}b^{A,V} \quad \textit{(A.2.16)}$$

$$= \boldsymbol{S}^B_{V,R}a^{B,R} + \boldsymbol{S}^B_{V,V}\left(I - S^A_{V,V}S^B_{V,V}\right)^{-1}\boldsymbol{S}^A_{V,R}a^{A,R} + \boldsymbol{S}^B_{V,V}\left(I - S^A_{V,V}S^B_{V,V}\right)^{-1}S^A_{V,V}\boldsymbol{S}^B_{V,R}a^{B,R} \quad \textit{(A.2.17)}$$

Rearranging this to the form:

$$\begin{bmatrix} \boldsymbol{b}^{A,R} \\ \boldsymbol{b}^{B,R} \end{bmatrix} = \boldsymbol{S}^{AB}\begin{bmatrix} \boldsymbol{a}^{A,R} \\ \boldsymbol{a}^{B,R} \end{bmatrix} \quad \textit{(A.2.18)}$$

Thus the new cascaded matrix S^{AB} is given by:

$$= \begin{bmatrix} S^A_{R,R} + S^A_{R,V}\left(I - S^B_{V,V}S^A_{V,V}\right)^{-1}S^B_{V,V}S^A_{V,R} & S^A_{R,V}\left(I - S^B_{V,V}S^A_{V,V}\right)^{-1}S^B_{V,R} \\ S^B_{R,V}\left(I - S^A_{V,V}S^B_{V,V}\right)^{-1}S^A_{V,R} & S^B_{R,R} + S^B_{R,V}\left(I - S^A_{V,V}S^B_{V,V}\right)^{-1}S^A_{V,V}S^B_{V,R} \end{bmatrix} \quad \textit{(A.2.19)}$$